Chemical Looping Propane Oxidative Dehydrogenation Studies as an Alternative Route for Propene Production

Caitlin Moffat

Submitted in fulfilment of the requirements for the degree of Doctor of Philosophy

School of Chemistry

College of Science and Engineering

University of Glasgow

November 2022

Abstract

Propene production has suffered drastically over the years since conventional steam cracking and fluidized catalytic cracking units have been refined to maximise ethene, diesel and gasoline yields. This has led to a significant gap between propene supply and demand, and the chemical industry has looked to alternative on-purpose propene production technologies, like propane dehydrogenation, to bridge this gap. Despite the selectivity benefits, the process is endothermic and requires high operational temperatures, where the catalyst is susceptible to fast deactivation. Alternatively, propane oxidative dehydrogenation is an exothermic process, which occurs in an oxidative atmosphere thus providing the potential to overcome these constraints.

Unfortunately, the commercialisation of the oxidative route is not currently feasible due to undesired combustion reactions, which subsequently hamper propene yields. There also exists many drawbacks when considering the operational logistics due to the requirement of C_3H_8 and O_2 co-feeds, since O_2 production is costly and energy intensive and there is difficulty in controlling the mixtures to keep them under explosive limits. In order to combat these challenges, interest has shifted to systems which use alternative, softer N_2O and CO_2 oxidants as a co-feed, as well as adopting a chemical looping approach. Chemical looping propane oxidative dehydrogenation (CL-PODH) tests are carried out in an O_2-free atmosphere, by utilising the lattice oxygen within metal oxide catalysts as the oxygen source, where a separate regeneration step is subsequently performed.

Consequently, this work has investigated the efficacy of γ-Al_2O_3 supported VO_x, MoO_x and VO_x-MoO_x catalysts for propene production in a series of novel CL-PODH redox cycling tests. Benchmark CL-PODH tests were performed in a combined microreactor and mass spectrometer system and consisted of ten propane dehydrogenation-catalyst regeneration redox cycles, utilising O_2 as the oxidant. Such tests provided valuable insight into the relationship between the activity of vanadia and molybdena species as a function of varying vanadium loading and increased molybdenum incorporation. The use of N_2O and CO_2 within the catalyst regeneration step was also explored to establish catalyst regenerability throughout the cycles when using alternative, softer oxidants.

Fresh $VO_x/\gamma\text{-}Al_2O_3$ and $MoO_x/\gamma\text{-}Al_2O_3$ catalysts were synthesised via the incipient wetness impregnation technique with varying vanadium loadings of 5.0, 7.5 and 10.0 wt.% and a fixed molybdenum loading of 9.4 wt.%. $VO_x\text{-}MoO_x/\gamma\text{-}Al_2O_3$ catalysts were synthesised via the co-impregnation technique, where the vanadium loading was fixed to 10.0 wt.% and molybdenum loadings of 3.2, 4.7 and 9.4 wt.%, which gave V:Mo molar ratios of 6:1, 4:1 and 2:1, respectively. Various characterisation techniques were used to establish the catalysts properties, including MP-AES, ICP-OES, BET, H_2-TPR, O_2 chemisorption, Raman spectroscopy and XRD.

Throughout the $VO_x/\gamma\text{-}Al_2O_3$ catalyst series, the most promising results for propene production were obtained in tests using 10 wt.% V catalyst. Propene selectivities of up to 40.8 % were achieved, at 15.8 % propane conversion upon completion of the 10^{th} PDH step. A long duration PDH step was also performed, revealing a substantial 30 % loss in catalyst activity after 3 h time on stream. Post-reaction Raman analysis revealed significant coke formation, thus highlighting the need for successive catalyst regeneration steps.

Alternative N_2O and CO_2 oxidants were also employed in CL-PODH tests using the 10VAl catalyst. In comparison to using O_2, an increase in propene selectivity was observed, reaching 47.6 % at a similar propane conversion of 15.4 %. A significant decline in catalyst activity is observed when using CO_2 as the oxidant however, as propene selectivities of only 36.5 % were achieved, at 9.2 % propane conversion upon completion of the 10^{th} PDH step. Post-reaction characterisation tests were conducted to probe the surface vanadia species present in the 10VAl catalyst removed at different stages throughout the ten cycles. Results from BET, Raman and XPS suggest the formation and removal of carbonaceous deposits with successive dehydrogenation and regeneration steps, thus reinforcing the regenerative ability of the O_2 and N_2O oxidant for coke removal. The inability of the CO_2 oxidant to remove carbon laydown and regenerate activity is highlighted further in the post-reaction Raman with prominent features attributed to coke formation.

A significant observation in CL-PODH redox cycling tests was the rise in propene production during the 6^{th} PDH step, which was performed after holding the catalyst overnight under argon following the O_2 regeneration step of cycle 5. The 10VAl catalyst was similarly removed and characterised after this overnight argon purge. XPS results reveal an increase in surface V^{4+} species at this stage, which agrees with findings from the thermodynamics and post-reaction Raman that surface vanadia sites are oxidising and

removing residual low-level carbonaceous deposits, hence the surface vanadium is in a more reduced state. An increase in propene selectivity due to the presence of this reduced species establishes a potential for tuning specific V^{5+}/V^{4+} ratios, which may be crucial in overcoming the selectivity limitations to enhance propene production.

The use of 9.4 wt.% $MoO_x/\gamma\text{-}Al_2O_3$ in the benchmark CL-PODH redox cycling test produced significantly lower propene selectivities in comparison to the 10VAl catalyst. The incorporation of molybdenum as a promotor in the 10VAl catalyst however, yielded an enhancement in catalyst activity, where an increase in propane conversion was observed with increasing molybdena loading across the $VO_x\text{-}MoO_x/\gamma\text{-}Al_2O_3$ series. The presence of V-O-Mo domains was implied in the pre-reaction Raman of all three $VO_x\text{-}MoO_x/\gamma\text{-}Al_2O_3$ catalysts, which showed a promotional effect on catalyst activity. In comparison to 10VAl and 9.4MoAl catalysts, a higher activity is observed in tests utilising the 10V9.4MoAl sample. Upon completion of the 10^{th} PDH step, propene selectivities of 32.5 % were obtained at a propane conversion of 22.9 %. Despite the lower selectivity towards propene, this increase in activity results in an overall higher propene yield.

Acknowledgements

It gives me great pleasure to acknowledge the many wonderful people who were instrumental to the completion of my PhD.

First and foremost, I'd like to express my sincere gratitude to Professor David Jackson and Dr. Emma Gibson. I am so grateful to you both for giving me the opportunity to be part of such amazing research groups. Thank you for always being only a knock-on-the-door away and for making me feel like no problem was ever too big or small.

To all of the past and present members of the Heterogeneous Catalysis section, thank you for some of the best times of my life! The endless laughs that we shared during our tea breaks really were the highlight of the day. You all well and truly made my PhD the most enjoyable time and I'm so glad to have made friends for life.

I would also like to express my appreciation to all of the technical support staff within the School of Chemistry, especially Andy Monaghan. What a guy! Thank you for always making time to help with the *many* problems that the HetCat section had. Monday mornings were definitely made that little bit easier hearing all about your weekend antics. I would also like to thank Dr. Chris Kelly, Dr June Callison and Dr David Morgan - your assistance with the acquisition and analysis of ICP-OES, MP-AES and XPS data is greatly appreciated.

To my fiancé Michael, thank you for always going above and beyond when I've struggled to detach from PhD life. I'm so beyond grateful to have had you by my side every step of the way. A huge thank you is also due to my amazing family and friends. Celebrating all the highs with you really kept me going, thank you for always pushing me to be the best that I can be.

Finally, to my beloved Nana and Granda. I know how much you would've loved to have shared all of these special moments with me - I hope I've made you both proud.

Declaration

The work contained in this thesis is submitted for the degree of Doctor of Philosophy and has not been submitted for any other degree at the University of Glasgow or any other institution. Furthermore, the work contained is the result of my own work, except where reference is made to the contribution of other authors.

Table of Contents

1 Introduction

1.1 The Propene Gap

Propene is ubiquitous in the petrochemical industry, where its high versatility stems from the ability to functionalise both the allylic methyl group and the olefinic bond existing within the monomer unit. [1] The primary use of propene is its use as a feedstock in the production of various intermediary and polymeric compounds, where the chain polymerisation route to afford polypropene holds the largest market share, accounting for ~68 % of the total global propene demand in 2018. [2]

Owing to its extraordinary chemical properties, polypropene has become an excellent candidate for packaging, textile, cosmetic and medicinal goods. Other key derivatives include propene oxide, acrylic acid, the oxo-alcohols, cumene and acrylonitrile, which are primarily used for automotive, coating and plasticizer goods for applications within the aviation, automotive and construction sectors. [1-3] These sectors have suffered in recent years due to the catastrophic social and economic effects brought about by the Covid-19 pandemic, which resulted in significantly lower demand for various key propene derivatives. Contrary to this, the demand for polypropene for use within packaging, hygiene and medical applications has exponentially increased throughout the pandemic, counteracting, to some extent, the initial decline in propene demand. [4]

Global demand for chemical and polymer grade propene was approximately 129.8 mtpa in 2019, with significant growth expected and propene production forecast to reach 191.8 mtpa by 2030. [5] This growth has caused mounting concern as to how the petrochemical industry will meet demand and alleviate strain on propene resources via conventional steam cracking and fluidized catalytic cracking technologies. The steam cracking of ethane, LPG and naphtha has been the principal route for the production of light olefinic compounds since its commercialisation in the 1950's. [6] Conventionally, the process is carried out in a tubular reactor, where the hydrocarbon feed is mixed with steam at elevated temperatures and subsequently cracked into smaller entities. [3] This process is highly endothermic and requires operational temperatures ranging from 750-900 °C, making it one of the most energy intensive processes existing within the petrochemical industry. [3, 7] Propene forms merely as a by-product in the steam cracking process, where its production relies heavily on the type of hydrocarbon feedstock used e.g., an increase in propene yield results when feedstocks trend heavier from ethane to LPG to naphtha. [8, 9]

Furthermore, the type of feedstock utilised in steam cracking operations is centred around feedstock availability and profitability. Since ethene currently dominates the petrochemical market and pure ethane-based feeds are in abundance due to developments in shale gas fracking technologies, modern-day steam crackers have shifted to using ethane-based feeds, where propene yields are minimised. [3, 7-10]

Accounting for around 30 % of global propene production, the chemical industry has looked to the fluidized catalytic cracking (FCC) process as an alternative route to provide additional propene supply. [8] Propene production via FCC operations utilise selective zeolite-based catalysts to convert heavy distillate feedstocks into valuable gasoline and olefinic mixtures. The process is far more economically sustainable than steam cracking, with typical operational temperatures below 550 °C. [11, 12] Unfortunately, propene production from FCC units has faced similar limitations over the years, as the focus has shifted on maximising diesel and gasoline yields to meet the rise in demand from the transportation industry. [11]

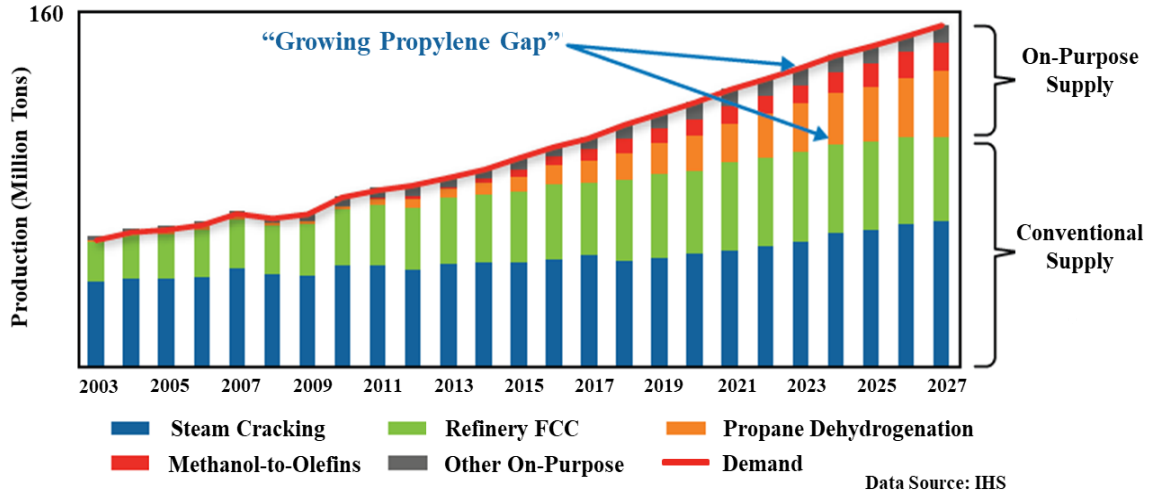

Figure 1: Global propene production versus demand. Adapted from [2]

The refinement of steam cracking and FCC processes has resulted in a gap between propene supply and demand, and there is mounting concern as to how the chemical industry overcomes this shortfall. As seen in Figure 1, industrial developers have made significant advancements in developing alternative on-purpose propene production methods in a bid to bridge the emerging gap between propene supply and demand. [1, 10] In 2020, IHS Markit projected that steam crackers and FCC would produce 46 % and around 30% of global propene supply respectively, with the remainder accounted for via on-purpose propene methods such as methanol-to-olefins and propane dehydrogenation. [2]

1.2 On-purpose Propene Production

1.2.1 Methanol-to-Olefins

The development of alternative production methods has attracted considerable interest within the chemical industry in a bid to meet the growing demand for propene. Notably, alternative routes, which steer towards natural gas resources and avoid the use of oil reserves, are deemed far more economical and environmentally sustainable. In particular, methanol derived from the steam reforming of natural gas is far more accessible and inexpensive in comparison to crude oil feedstocks, and is therefore an excellent candidate for light olefin production. [13] Current methanol-to-olefins (MTO) technologies start with a methanol dehydration step to produce an equilibrated mixture of methanol, water and dimethyl ether. This equilibrated mixture is further converted into lighter olefins, where ethene dominates the product mixture. [14]

The MTO process has existed for quite some time, however, it did not originally attract much attention due to the cheap and easy accessibility of light olefins from crude oil resources. [15] Interest in using methanol as a feedstock was re-ignited in the early 1970's, stemming from the 1973 oil crisis and the rising uncertainty of crude oil availability. [13, 15] Earlier MTO studies report the quantitative transformation of methanol into light hydrocarbons at temperatures ranging from 300-500 ℃ by using zeolite-based molecular sieves. In the 1980's, the discovery of the zeolite-based silicoaluminophosphate catalyst (SAPO-34) and its efficiency for MTO was led by the Molecular Sieve Division based within Union Carbide. [13]

This division was to merge forces with UOP in 1988 and subsequently developed the first MTO process in partnership with Norsk Hydro. [13, 16] The process utilised a SAPO-34 type catalyst and a fluidised bed reactor, where the selectivity of methanol to ethene and propene was around 80 %. [16] The main component of SAPO-34 that is integral for the conversion of methanol to light olefins is its structural ~3.8 Å pore diameter. A pore diameter of this size limits the diffusion of bulkier and heavier hydrocarbons, ultimately leading to higher selectivities to the desired olefin product. [17] Furthermore, the use of a fluidized bed reactor enables the continuous regeneration of spent catalyst by heating catalyst portions in the presence of air to remove coke deposition, subsequently preserving catalyst activity and product composition. This type of reactor also enables the adjustment of operational conditions and the modification of the propene to ethene weight ratio, an

adaptation vital to meeting the changing market demands which govern the desired product composition. [18]

The process was first made available for license in 1995, and has been operational at demonstration scale since, in a unit based in the Norwegian Hydro Research Centre. [13] Significant advancements of the UOP/Norsk MTO process were accelerated through the partnership of UOP and Total Petrochemicals in 2000, where both companies strategized to integrate the process with olefin cracking technology developed by Total Petrochemicals. [18] The integration of the olefin cracking unit enhances the selectivity of methanol to ethene and propene to around 90 % by additionally transforming the C_4 to C_6^+ olefins produced within the MTO unit. This advancement has led to the start-up of a fully integrated MTO demonstration plant in Belgium, with a capacity thirteen times larger than that of Hydro's MTO unit based in Norway. [13]

Advancements to optimise propene in the MTO process have also been established in Lurgi's methanol-to-propene process (MTP), which uses a catalyst based around the selective aluminosilicate zeolite, H-ZSM-5, which has a pore diameter of around 5.5Å. [19] The strong acidic sites existing within the micropores of the H-ZSM-5 framework allows control over olefin selectivity, ensuring that propene is formed as the primary product. [20] The first step in the MTP process is methanol dehydration to produce an equilibrated mixture of methanol, dimethyl ether and steam. The mixture is transformed to propene over the ZSM-5 catalyst in a fixed bed reactor at temperatures ranging from 400-500 °C, with LPG, gasoline and fuel gas forming as by-products. [13, 20] Despite the benefits that Lurgi's MTP process offers when it comes to combatting the growing propene gap, the high formation of coke observed when using the active ZSM-5 catalyst remains a huge drawback and presents many challenges. The deposition of carbonaceous material leads to the blockage of microporous catalytic sites, subsequently restricting the movement of reactants and products, ultimately rendering the catalyst inactive. [16]

1.2.2 Propane Dehydrogenation

Amongst the on-purpose propene production methods that currently exist, propane dehydrogenation (PDH) is by far the most promising, as it offers a highly selective route, producing propene as the sole olefin product. [3] An additional benefit that PDH holds is the accessibility to cheap and abundant propane feeds, which have resulted from the recent advancements made within the hydraulic fracking sector and the rise in shale gas production. [21, 22]

The chemical equation of PDH, which illustrates the one-step conversion of propane into propene and hydrogen, is presented in Equation 1. Notably, propane dehydrogenation is highly endothermic, where elevated reaction temperatures above 600 ºC are typically required to overcome thermodynamic limitations.

Equation 1: Chemical equation of PDH

$$C_3H_8 \longleftrightarrow C_3H_6 + H_2 \quad (\Delta H°_{298K} = +124.3 \text{ kJ mol}^{-1})$$

Several PDH technologies have been patented and commercialised for propene production, including Oleflex, CATOFIN, STAR and FBD. In order to limit the extent of catalyst deactivation and to maximise propene yields, reactor design, catalyst employed, and operating conditions vary between processes, with the most widely used being Oleflex (developed by UOP) and CATOFIN (developed by Lummus Technology). [21-23]

The Oleflex process was made commercially available by UOP in 1990 and the first plant, with a propene capacity of over 300 ktpa, commissioned in Thailand. [24, 25] The technology is centred around a continuous operation, with a reactor configuration comprising several fluidised moving bed reactors, in conjunction with independent product recovery and catalyst regeneration units. The process uses a Pt-Sn/Al_2O_3 catalyst with typical pressures ranging from ~1-3 bar and temperatures from 525-705 ℃, resulting in propane conversions of up to 40 % and propene selectivity of up to 88 %. [22] At these temperatures, coke formation is favoured and catalyst activity is inevitably lost, therefore, the requirement for a catalyst regeneration section is crucial. The regeneration of the catalyst takes place simultaneously to the dehydrogenation process occurring in the reactor section. In the catalyst regeneration unit, the coke is burned off and the catalyst is exposed to a mixture of chlorine and air to facilitate the re-dispersion of active platinum sites before it is recycled back to the reactor units. [21-23, 26]

Lummus Technologies CATOFIN process varies significantly to the Oleflex technology described above. The process stems from the work pioneered by Eugene Houdry, which was initially designed and commercialised for butane dehydrogenation, however, propene production via the CATOFIN process was first commissioned in 1986 in Texas, with a capacity of ~250 ktpa. [21, 27] Nowadays, CATOFIN is employed in over thirty PDH plants worldwide with a propene capacity of over 22 mtpa, yielding a propane conversion of up to 45 % and propene selectivities of between 82-87 %. [28] The process comprises a reactor configuration of several parallel fixed bed reactors connected horizontally, and utilises an alkali promoted CrO_x/Al_2O_3 catalyst with typical pressures ranging from 0.3-0.5 bar and temperatures of between 565 and 650 °C. [22] The reactors operate in short cycles lasting approximately 15-30 min, where the PDH reaction is subsequently followed by inert purge and regeneration steps. In the regeneration stage, carbonaceous deposits are burned off and the heat released is recycled and used as energy for the endothermic PDH step. The cycles occur intermittently between the reactors, therefore, up to 8 reactors are required to ensure continuous propene production. [21-23]

The STAR process, developed and commissioned in 1992 by Phillips Petroleum for isobutene production, similarly implements a cyclic configuration. The capacity for propene production was fulfilled following the acquirement of STAR technology by Uhde in 1999, who commissioned three PDH plants totalling a propene capacity of 1.3 mtpa in 2021. [21] The process comprises two adiabatic reactors, one for dehydrogenation and the other for oxydehydrogenation, loaded with Pt-Sn based catalysts supported on calcium and zinc aluminates. Typical temperatures ranging from 550-600°C and pressures ranging from 5-6 bar are utilised, yielding a propane conversion of up to 35 % and propene selectivity of up to 90 %. [22] Propane dehydrogenation occurs in the first reformer-type dehydrogenation reactor in the presence of steam to combust carbonaceous deposits. The effluent is then directed into the secondary oxydehydrogenation reactor, where oxygen is injected to ultimately shift the thermodynamic equilibrium towards even higher propene yields. [21-23]

The FBD process, commissioned by Yarsintez-Snamprogett, implements a continuous operation and regeneration system similar to Oleflex and utilises a chromia based alumina catalyst akin to CATOFIN. [21] The technology centres around a series of dehydrogenation and regenerating fluidised bed reactors, where the catalyst bed moves fluidly throughout the configuration in a liquid-like manner. After the catalyst particles are successfully re-oxidised in the regeneration unit, they are transferred to a “stripping” section situated at the bottom of the reactor, where the catalyst material is reduced to strip the surface of any

adsorbed oxygenated compounds. [21, 22] Comparably, FBD technology yields less coke than observed in the Oleflex process, however, the high level of catalyst mixing ultimately results in the breakdown of catalyst particles, which is the main deactivation route. To prevent loss in catalyst activity and sustain propene yields, fresh catalyst material is added to the regeneration section. [21] Operational temperatures range from 535-590 °C at pressures between 0.5-1.5 bar, obtaining a propane conversion of up to 50 % and propene selectivity of up to 80 %.[22]

Several other PDH technologies, existing at different development stages, have been established in the last ten years, including PDH (Linde-BASF), FBR (Sabic), FCDh™ (Dow), FLOTU (Tsinghua) and K-PRO™ (KBR). Despite these recent advances, the thermodynamic constraint of the endothermic reaction means that harsh operational temperatures are required. At these temperatures, undesirable side reactions are favoured, which ultimately results in fast catalyst deactivation and limited propene yields. [4, 23] Moreover, the catalysts used typically revolve around precious platinum and highly toxic chromium metals, which inevitably drives up costs and steers away from the movement towards environmentally sustainable processes. As a result, propene production from alternative on-purpose technologies is required to bridge the ever-growing gap between propene supply and demand.

1.3 Oxidative Dehydrogenation: A Promising Alternative

Propane dehydrogenation can also proceed through an oxidative pathway, which has many advantages over the direct dehydrogenation route previously discussed. For instance, propane oxidative dehydrogenation (PODH) is an exothermic reaction and does not suffer from the same thermodynamic limitations, permitting the use of lower reaction temperatures (typically 450-550 °C). Another benefit is that the need for a catalyst regeneration step is eliminated since the presence of oxygen limits the extent of carbon laydown. [29-31]

The chemical equation of PODH is presented in Equation 2, which illustrates the conversion of propane and oxygen into propene and water.

Equation 2: Chemical equation of PODH-O_2

$$C_3H_8 + \frac{1}{2}O_2 \longrightarrow C_3H_6 + H_2O \quad (\Delta H°_{298K} = -117.6 \text{ kJ mol}^{-1})$$

The generalised reaction pathway for PODH is shown in Figure 2. [32] Involved in the pathway are two parallel oxidation steps, where propane converts to propene and carbon oxides (CO_x) and the desired propene product can also undergo further combustion in a sequential over-oxidation step. [33] Although the thermodynamics of PODH make it a promising technique for additional propene production, undesired combustion reactions remain a huge drawback as they have a damaging effect on propene yields. [33-35]

Carbon oxide formation occurs primarily due to the greater reactivity of propene in comparison with propane. When considering the bond energies, the weakest C-H bond in propane, at the primary methyl group, has a stronger bond energy than the allylic C-H bond in propene, allowing the over-oxidation of propene at similar temperatures required to activate propane. [34] Unfortunately, strategies to poison the catalyst sites responsible for the activation of propene C-H bonds have failed as they are the same sites as those required to active propane C-H bonds. [33, 36] Studies into similar oxidation reactions have reported a significant loss in yield when the weakest bond energy in the product molecule is around 40 kJ mol^{-1} less than the weakest bond energy in the reactant molecule. [33, 37] Bond energies for the primary C-H bond in propane and the allylic C-H bond in propene are presented in Table 1. [34]

Figure 2: Generalised reaction pathway for PODH

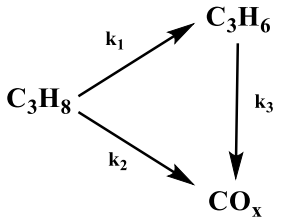

Table 1: Bond energies for primary and allylic C-H bonds in propane and propene

Bond	Bond Energy (kJ mol^{-1})
Primary C-H	420
Allylic C-H	361

Notably, the difference in bond energy is not the only factor which dictates the over-oxidation reaction to carbon oxides. The ratio of rate constants, k_3/k_1, is directly affected by various parameters, including the structure of the active catalyst species. Differences in this ratio have also been observed when there is a change in local structure, indicating that the acid-base characteristics and interaction between the metal oxide and support also have an effect. [33] If PODH is to become a viable route for propene production in the near-future, it will require propene yields of ~65 % to be competitive with current routes. [38] To achieve this, the discovery of catalyst systems which can activate propane C-H bonds whilst inhibiting the over-oxidation of propene is essential. Research into various metal oxide catalysts has been explored, the majority of which have focused on catalyst systems containing vanadium and molybdenum oxide species. [39, 40]

1.4 Active Catalysts for Propane Oxidative Dehydrogenation

1.4.1 Vanadia-based Catalysts

Supported vanadium oxide catalysts have been studied extensively for PODH reactions, with investigations centring around the optimal species and nature of the active site. [41] In order to elucidate the role of active vanadia sites for PODH, Bell and co-workers conducted a series of isotopic tracer reactions over V_2O_5/ZrO_2. [33, 42] Competitive reactions of C_3H_6 and $CH_3{}^{13}CH_2CH_3$ implied that CO production occurs via the secondary combustion of propene intermediates. Results suggest that CO_2 is also produced this way, in addition to the direct oxidation of propane. Furthermore, $^{18}O_2/C_3H_8$ reaction mixtures were directed over supported $V_2{}^{16}O_5$ species, and the early appearance of lattice ^{16}O atoms in oxygen-containing products were observed, implying that lattice oxygen sites within the vanadia catalyst are required for C-H bond activation. The authors concluded from their studies that the PODH mechanism is consistent with a Mars-van Krevelen type reaction, shown in Figure 3. [43] This mechanism is analogous to various other oxidation reactions, where the alkane interacts with lattice oxygen sites, followed by the desorption of the product, resulting in surface vacancies which are subsequently re-oxidised by dissociatively adsorbed oxygen. Investigations of PODH using supported vanadia catalysts have also been conducted via DFT calculations. In this study, a Mars-van Krevelen redox mechanism is also proposed, where the rate-limiting step is the activation of chemisorbed propane through the hydrogen abstraction of the methylene $-CH_2$ group. [44]

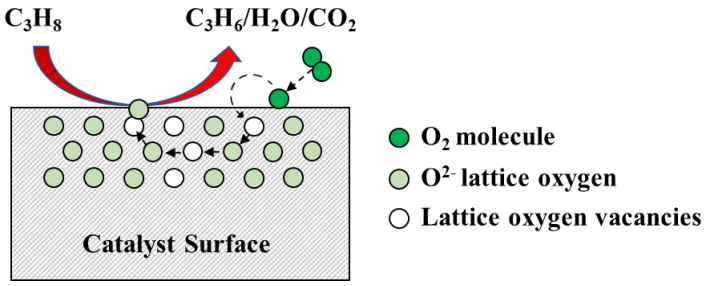

Figure 3: Mars-van Krevelen mechanism for propane oxidation in PODH. Adapted from Ref [43].

The sequential steps of the Mars-van Krevelen pathway required to complete one PODH cycle, proposed by Bell and co-workers, are shown below:

1. Propane adsorbs associatively on the lattice oxygen sites present in the metal oxide:

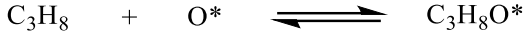

2. Neighbouring lattice oxygen sites cleave the propane C-H bond via hydrogen abstraction which forms a propoxide bonded to V-O domains:

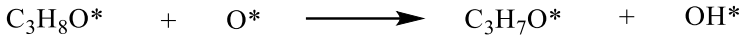

3. The absorbed propoxide species undergoes hydride elimination to allow the desorption of propene from surface vanadia vacancies:

4. The hydroxyl groups adsorbed on the surface vacancies combine to form water. Consequently, vanadia centres are reduced:

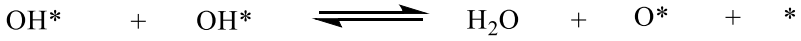

5. Dissociatively chemisorbed O_2 molecules re-oxidise reduced vanadia centres:

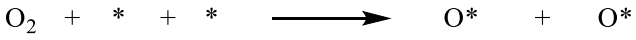

Notably, * is a free surface vacancy that may arise from either one V^{4+} site or two V^{3+} sites, O* is lattice oxygen species present in either vanadyl (V=O) or in polyvanadate bonds (V-O-V) and $C_3H_7O^*$ is an absorbed propoxide species bonded to a vanadium site via an oxygen atom (V-O-C_3H_7).

Contrary to this, recent investigations performed by Schlögl *et al.* utilised isotopic tracer and alternative *operando* Raman studies to deduce the mechanism of propane oxidation on V_2O_5. Using mixed C_3H_8-$^{18}O_2$ feeds, only the vanadyl bond (V=^{16}O) of the V_2O_5 sample was partially exchanged over an extensive reaction time of 2 h. A slight variation in the Raman spectra was observed as a result, where propene and CO_2 production reached steady state prior to the spectral changes. The absence of significant isotopic exchange and

variation in the Raman spectra of the vanadia species questions whether Mars-van Krevelen is the predominant reaction pathway in lower temperature (400 °C) PODH studies. [45]

As well as having an understanding of the reaction mechanism, it is also desirable to understand the structure-activity relationship regarding the configuration of vanadium oxide species present on the support surface. [46] Keller and Weckhuysen proposed the four possible molecular arrangements of supported vanadium oxides, which are presented in Figure 4. [47] Figure 4(a) shows isolated monovanadate species, coordinating to four oxygen molecules, three of which are V-O-support bonds with the other being a terminal vanadyl (V=O) bond. Figure 4(b) shows a polyvanadate dimer, where two vanadia centres are bridged via an oxygen atom. Figure 4(c) shows two-dimensional polyvanadate oligomeric chains, and Figure 4(d) shows bulk V_2O_5 crystallites.

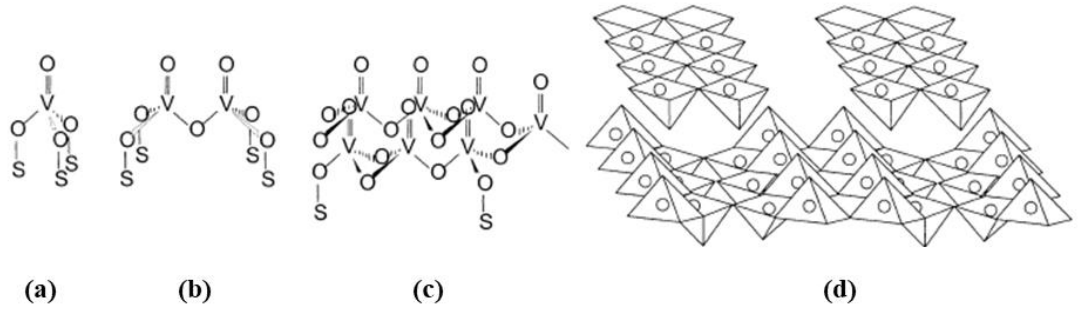

Figure 4: Possible arrangements of supported VO_x [47]

The arrangement of VO_x species on the support surface relies heavily on the dispersion of the metal, which is directly related to metal loading and surface density. Iglesia *et al.* reported that bulk V_2O_5 crystallites were the predominant species at surface densities above 7.5 V nm^{-2}. Polyvanadates dominated at surface densities between 2.3-7.5 V nm^{-2}, whilst the predominant species observed on the surface at densities below 2.3 V nm^{-2} were highly dispersed monovanadates. [37] The formation of these species is presumed to occur during calcination, where the intermediately formed VO_x species interacts chemically with the support material, forming V-O-support bonds. The strength of this bond relies heavily on the support properties and surface coverage, where a low coverage comprises of thin vanadate layers and strong vanadia-support interactions. As the surface coverage increases, the vanadia-support interaction ultimately weakens, leading to the agglomeration of bulk V_2O_5 crystallites, as observed in Figure 5. [29, 48]

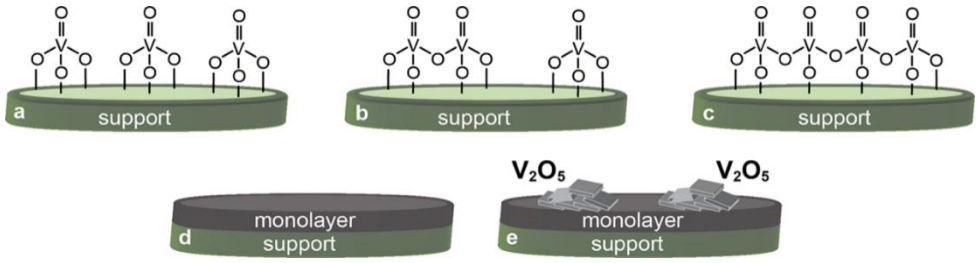

Figure 5: VO_x species reaching and exceeding the monolayer coverage [48]

Raman spectroscopy has previously been used to interpret surface vanadia species. Reports suggest that isolated, monovanadates (VO_4) are characterised by a sharp band at 1018 cm^{-1} and a broad band at ~910 cm^{-1}, assigned to the symmetric vibration of vanadyl (V=O) species and V-O-Al anchoring bonds, respectively. [49, 50] As surface density increased, the band at 1018 cm^{-1} shifts to 1035 cm^{-1}, accompanied by the addition of broad bands at ~750, 550, 450 and 350 cm^{-1}. Since an increase in surface density results in a higher degree of polymerisation, the shift from ~1018 to 1035 cm^{-1} is attributed to the symmetric stretch of terminal vanadyl (V=O) bonds present in polyvanadate species. Raman bands at ~750 and 550 cm^{-1} were assigned to the symmetric and asymmetric vibrational modes, whilst bands at ~450 and 350 cm^{-1} were assigned to symmetric and asymmetric bending modes of oxygen bridged polyvanadates (V-O-V). [49, 51] Furthermore, bulk V_2O_5 crystallites are characterised by bands at ~994, 701, 525, 409, 295, 285, and 143 cm^{-1}. [52]

It is widely accepted in literature that supported vanadia systems containing highly dispersed, isolated monovanates, are the most active for alkane ODH reactions. [46, 53] Many believe this behaviour is ascribed to the V-O-support bonds present within these structures since they are a central factor in the acid-base properties and the reducibility of the catalyst. [46] Studies performed by Sam *et al.*, [54] however, explored the use of V-Mg-O catalysts for PODH, where the α-$Mg_2V_2O_7$ phase exhibited a higher selectivity towards propene than $Mg_3V_2O_8$ and α-$Mg_2V_2O_6$ phases. When α-$Mg_2V_2O_7$ was utilised in the PODH reaction, a propene selectivity of 53.5 % was obtained at a propane conversion of 5.6 %. The authors concluded that this observation was due to the characteristic vanadyl (V=O) bond present in α-$Mg_2V_2O_7$, which was crucial for the hydrogen abstraction step. [54]

Later studies performed by Corma *et al.* [55] investigated vanadia systems impregnated on an array of supports (SiO_2, Al_2O_3, TiO_2, and MgO) and found that the dispersion of vanadia exhibited a strong dependence on the acid-base properties and vanadium loading, which had a direct impact on the catalyst activity and selectivity towards propene. A reduction in vanadia dispersion was observed when utilising acidic supports e.g., SiO_2. which resulted

in increased V_2O_5 domains even at low vanadium loadings. The authors inferred that VOV pairs present in V_2O_5 domains were active for propene formation. However, a loss in selectivity was also observed, as these domains facilitate the over-oxidation of propene. A higher presence of VOV pairs results in a higher concentration of vanadyl, VO^{2+} species, which they report as exhibiting a stronger affinity for propene adsorption, ultimately leading to the consecutive oxidation of the olefin to undesired carbon oxides. Contrary to the reports of Sam *et al.*, the investigations performed by Corma and co-workers concluded that V-O-S bonds in tetrahedral vanadium complexes exhibit a higher selectivity to propene than vanadyl bonds, which re-oxidise the desired propene product. [55]

Similarly, PODH studies utilising VO_x/Al_2O_3 catalysts were conducted by Zhang *et al.*, [56] where vanadium loadings ranged between 3 and 15 wt.%. The characterisation results reveal that both V-O-Al and V=O domains exist on the 3 and 6 wt.% VO_x/Al_2O_3 catalysts, indicating the presence of equally dispersed vanadia species. These domains were also observed in the remaining 9, 12 and 15 wt.% VO_x/Al_2O_3 catalysts, in addition to V-O-V bonds, suggesting the presence of V_2O_5. PODH reaction tests performed at 500 °C, utilising the 3 wt.% VO_x/Al_2O_3 catalyst, resulted in a propane conversion of 75.9 % and a propene selectivity of 12.5 %. When the 15 wt.% VO_x/Al_2O_3 catalyst was employed in PODH reaction tests, a propane conversion of 67.3 % and a propene selectivity of 10.7 % was obtained. This decay in both catalyst activity and selectivity towards propene highlights the importance of maintaining high dispersion in supported vanadia catalysts for PODH reactions. [56]

Lastly, a review conducted by Wachs *et al.* [57] also concluded that vanadyl bonds were not the critical bond for hydrocarbon oxidation reactions based on investigations which show a lack of correlation between alkane turnover frequency (TOF), and the presence of V=O bonds in butane ODH. A significant change in TOF is observed when altering the specific oxide support however, inferring that the critical oxygen bond required for alkane ODH reactions is the bridging V-O-support bond. [41] It is evident that the nature of the active site in supported vanadia catalysts remains a complex matter. Several contributing factors exist which impact the catalytic behaviour in alkane ODH reactions, including vanadium coordination number, acid-base properties, and the dispersion and reducibility of active vanadia sites, which are dictated by both the vanadium loading and type of oxide support used in the catalyst preparation. [57]

1.4.2 Molybdena-based Catalysts

Supported molybdenum oxide catalysts, currently used in important hydrodenitrogenation and hydrodesulphurisation catalytic processes, are also active for PODH. [58, 59] Bell and co-workers carried out similar isotopic tracer experiments, as discussed previously, for PODH reactions catalysed by MoO_x/ZrO_2. [60] The kinetic data obtained was analogous to the results observed in their previous work using V_2O_5/ZrO_2 catalysts, therefore, the Mars-van Krevelen type reaction pathway presented previously is also applicable. The first step involves the activation of the C-H bond within the adsorbed propane molecule by hydrogen abstraction, to form a surface bound propoxide species. Beta-hydride elimination occurs, and propene desorbs from the surface leaving behind surface bound hydroxyl groups. These hydroxyl groups combine to form water, resulting in either one Mo^{4+} or two Mo^{5+} surface vacancies, which are consequently re-oxidised via the dissociative chemisorption of molecular oxygen. When comparing the activity of ZrO_2-supported VO_x and MoO_x, the authors report an increase in activity when catalysing the PODH reaction with V_2O_5/ZrO_2, which reflects the lower activation energy of C-H bond activation when using vanadia based catalysts compared to those molybdena based. [60]

In order to probe the possible molybdenum oxide configurations that can form on the support surface, Christodoulakis *et al.* utilised operando-Raman spectroscopy on MoO_x/Al_2O_3 catalysts with various metal loadings during ethane ODH. [61] The four different MoO_x arrangements presented in Figure 6 were observed, all exhibiting a high dependency on metal loading. Figure 6(a) shows an isolated molybdenum ion coordinating to four oxygen molecules, two of which are Mo-O-Al bonds with the other two being Mo=O bonds. Figure 6(b) shows an isolated octahedral complex, with one bond being Mo=O and the other four bonds being Mo-O-Al. Figure 6(c) and (d) show the polymerisation of molybdenum oxides where the metal centres are bridged via an oxygen atom. [61]

Similar to VO_x species, the configuration of MoO_x on the support surface relies heavily on the dispersion of the metal, which is directly related to metal loading and surface density. In MoO_x/Al_2O_3 catalysts, Iglesia *et al*. found that both polymeric and monomeric species were generally present at low molybdenum loadings, where an increase in the metal loading led to a growth in polymeric Mo-O-Mo oligomers. As the surface density exceeded 4.5 Mo nm^{-2}, MoO_3 crystallites were observed, which co-existed with polymeric molybdenum domains. [62]

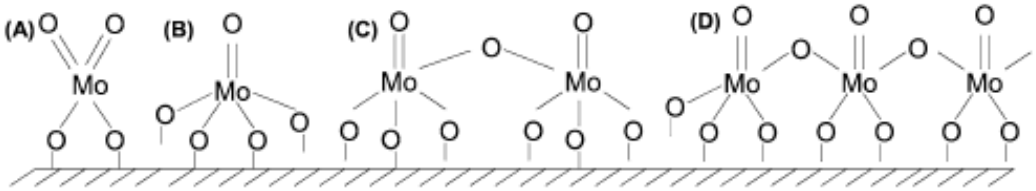

Figure 6: Possible arrangements of alumina supported MoO_x: (a) MoO_4 in a tetrahedral complex, (b) MoO_5 in an octrahedral complex and (c) and (d) Polymeric MoO_x species. [61]

At low molybdenum loadings, the observation of Raman bands at ~996 cm^{-1} and ~850 cm^{-1} have been reported and assigned to the stretching vibration of terminal molybdenyl (Mo=O) and Mo-O-Mo functionalities, respectively. [61] It should be noted that terminal Mo=O modes within polymeric molybdate species also contribute to the band at ~996 cm^{-1} since tetrahedral/octahedral, monomeric/polymeric species tend to overlap. As molybdenum loading increases, the bands at ~996 and ~850 cm^{-1} are shifted to ~1005 and ~870 cm^{-1}, in addition to an increase in intensity of the 850-870 cm^{-1} band, characteristic of oxygen-bridged Mo-O-Mo species. [61] Upon exceeding the monolayer coverage, bulk MoO_3 crystallites are observed, characterised by bands at ~999, 820, 672, 383, 342, 290, 250 and 163 cm^{-1}. [52, 61]

With regards to the structure-activity relationship of supported molybdenum oxide catalysts, Bell and co-workers reported an increase in reaction rates with increasing molybdenum surface density in PODH studies utilising MoO_3/ZrO_2 catalysts. Optimal ODH activity was observed when two-dimensional MoO_x oligomers were present, which was attributed to the higher reducibility of MoO_x domains existing in the Mo^{6+} oxidation state. As the surface density increased and the monolayer coverage exceeded however, three-dimensional molybdenum trioxide (MoO_3) crystallites were formed, leading to inaccessible sites and a subsequent decrease in PODH rates. [60, 62] The authors concluded that molybdenyl bonds (Mo=O) are crucial for activating the propane C-H bond for hydrogen abstraction, whilst Mo-O-support bonds facilitate the over-oxidation reaction, combusting propene to undesired carbon oxides. The strength of the molybdenyl bond also plays a role in the reactivity of the catalyst, which is directly related to the molybdenum surface density. As molybdenum domains increase significantly, the strength of the molybdenyl bond also increases, resulting in a lower activity in PODH reactions. [63]

Additionally, studies performed by Høj *et al.* focused on MoO_x/Al_2O_3 catalysts with varying molybdenum loadings, ranging between 2 and 15 wt.%. [64]

Characterisation results reveal that only small amounts of crystalline MoO_3 species were observed at 15 wt.% Mo loading, indicating the presence of highly dispersed molybdena species in catalyst samples containing lower molybdenum loadings of 2, 4, 7 and 10 wt.%. PODH reaction tests performed at 500 °C, utilising the 2 wt.% MoO_x/Al_2O_3 catalyst, resulted in a propane conversion of 36 % and a propene selectivity of 17.5 %. When the 15 wt.% MoO_x/Al_2O_3 catalyst was utilised in PODH reaction tests, a propane conversion of 24 % and a propene selectivity of 30.8 % was obtained. The decay in the catalyst activity for higher loading Mo catalysts, which exhibit a higher degree of polymerisation and three dimensional MoO_3 crystallites, is combatted by an increase in selectivity towards propene. These results agree with the findings of Bell *et al.*, thus demonstrating the importance of the molybdenyl bond on the catalyst activity. On the other hand, low molybdenum loadings with a higher presence of Mo-O-Al domains contribute significantly to the over-oxidation reaction, thus lowering propene selectivity and yield. [63, 64]

1.4.3 Role of modifiers and promoters

Whilst supported molybdena and vanadia are both active catalysts for PODH, propene yields remain lower than those required for the process to become commercially viable. An inverse selectivity-conversion relationship results due to the difference in bond energies of propane and propene, where an increase in propane conversion decreases the selectivity to propene. One method that has been considered to resolve this issue, is to promote active vanadia catalysts with secondary metal oxide modifiers e.g. MoO_x, CrO_x and WO_x. [48, 65-67] The role of the modifier can either be interactive or non-interactive, where interactive modifiers directly affect the performance as they chemically co-ordinate to surface vanadium oxide species. Non-interactive modifiers however, do not chemically co-ordinate to surface vanadium oxide species but can still affect the performance. [66, 68]

Research into the use of promoted V_2O_5/Al_2O_3 catalysts for PODH reactions has been explored by Mitra *et al.* [66] In their studies, vanadia catalysts were promoted with molybdenum, chromium and tungsten oxide ions via a co-impregnation technique. The samples were characterized by Raman spectroscopy, which revealed that only uniform surface metal oxide species were present on the catalyst. The absence of Mo-V-O, Cr-V-O and W-V-O species implies that the modifiers do not chemically alter the structure of vanadium oxide domains and are therefore classed as non-interactive. The same study also reports that PODH activity over V_2O_5/Al_2O_3 catalysts was significantly enhanced with the addition of the secondary modifiers. The activity of both MoO_x and WO_x promoted

V_2O_5/Al_2O_3 catalysts was approximately double that of the non-promoted V_2O_5/Al_2O_3 catalyst, whilst the CrO_x promoted catalyst exhibited an activity over six times higher. The authors proposed that this improvement was due to the presence of a larger pre-exponential factor relating to the equilibrium adsorption constant of propane. They concluded that the relatively inactive MoO_x and WO_x promoters enable the weak adsorption of propane in a precursor state, which is then supplied to the active vanadia sites for the activation of propane. In the case of the CrO_x modifier, which exhibits a higher activity than VO_x, the improvement in PODH activity is attributed to ability of VO_x domains to supply weakly adsorbed propane to active CrO_x sites. [66]

PODH reactivity tests utilising molybdena promoted VO_x/Al_2O_3 catalysts were also performed by Dai *et al*. [69] Their studies, however, report the formation of V-O-Mo domains, where the MoO_x species co-ordinates chemically to VO_x sites. In this case, the Mo promoter behaves as an interactive modifier, where it exists as an interlayer between vanadia sites and the alumina support. The results obtained from their PODH tests reveal that, at a given propane conversion, the molybdena promoted VO_x/Al_2O_3 catalyst exhibits a higher selectivity towards propene, in comparison to the unpromoted catalyst. Kinetic analysis was also conducted in this study, which shows a significantly lower ratio between the rate constant associated with the combustion of propane to propene. The authors conclude that the observed enhancement in propene selectivity and lower propane to propene combustion rate constant ratios is due to the formation and promotional effect of V-O-Mo bonds. [69]

1.5 Oxidants for Propane Oxidative Dehydrogenation

Another approach that has been taken in order to enhance propene yields is the use of alternative oxidants. Typically, PODH is carried out in the presence of molecular oxygen to retain the exothermicity of the reaction, however, its strong oxidising character contributes to the deep oxidation of propene and the over oxidation of the alkane feed. To overcome this barrier, the idea of using "softer" oxidants like CO_2 and N_2O has attracted considerable interest in recent years. [70]

1.5.1 PODH-CO_2

Developing processes that utilise CO_2 is highly beneficial from an ecological perspective, as it would significantly reduce the large contribution to the greenhouse gas effect that it currently holds. [71] However, CO_2 molecules are thermodynamically stable and kinetically inert, therefore, it's use as a "mild" oxidant in PODH reactions is limited, exhibiting an even higher endothermicity than the direct PDH reaction ($\Delta H°_{298K}$ = +164.0 kJ mol^{-1}). [72] As a result, high-energy reactants, effective catalyst systems and severe reaction conditions are required for PODH-CO_2 operations, resulting in a trade-off between the ecological benefit of using of CO_2 and the operation of the PODH-CO_2 reaction at temperatures exceeding 550 °C. [30, 73]

PODH studies using O_2 and CO_2 oxidants over a series of VO_x/SiO_2 catalysts were conducted by Kang *et al*. [71] The PODH-CO_2 reaction, performed over the moderately loaded 7 wt % VO_x/SiO_2 catalyst, demonstrated a propane conversion of 25 %. This was lower in comparison to the PODH test utilising O_2 as the oxidant, which exhibited a propane conversion of 27.3 %. An improvement in propene selectivity is observed however, where initial propene selectivities of 45.1 % and 41.6 % were obtained in PODH-CO_2 and PODH-O_2 tests, respectively. [71]

The mechanistic pathway for the PODH-CO_2 reaction has not yet been thoroughly elucidated, however, several studies conducted in recent years propose different reaction pathways and side reactions, depending on the conditions and type of catalyst used. [70] The reaction pathways that have been proposed include the conventional ODH Mars-van Krevelen mechanism, in addition to an alternative two-step reaction pathway revolving around a direct PDH step (Equation 1), in conjunction with the reverse water gas shift (RWGS) reaction shown in Equation 3. [73] Notably, both mechanisms are centred around the same net reaction. In the two-step pathway, the production of hydrogen from the direct

PDH reaction limits propane conversions, as the equilibrium shifts towards the reactants. When coupling the PDH reaction with the RWGS reaction, the hydrogen produced can react with the CO_2 oxidant to produce CO and water, which ultimately shifts the PDH reaction towards the product side, thus enhancing propene yields at lower reaction temperatures.

Equation 3: Chemical equation of the RWGS reaction

$$CO_2 + H_2 \longleftrightarrow CO + H_2O \quad (\Delta H°_{298K} = +41.0 \text{ kJ mol}^{-1})$$

Recent studies performed by Hess *et al*. focused on obtaining mechanistic information of the PODH-CO_2 reaction over silica supported vanadia catalysts by utilising *in-situ* Raman measurements. [74] A direct PDH step was performed on VO_x/SiO_2 catalysts without the CO_2 oxidant, which resulted in the formation of insignificant amounts of CO. A notable amount of CO was detected in the CO_2 assisted PODH reaction however, which indicated the successful activation of the CO_2 molecule. This observation was coupled with a significant decrease in hydrogen production, implying that the two-step dehydrogenation and RWGS mechanism was in play during the reaction. The Raman spectra shows the predominance of small vanadia oligomers during the reaction, where the vanadyl bonds exist in a partially reduced state. The study shows the ability to re-oxidise the vanadyl bond with CO_2, where an increase in intensity for the vanadyl Raman shift is observed after re-oxidation. Therefore, the authors conclude that both the ODH, and two-step dehydrogenation and RWGS reaction pathway, are possible and may occur in parallel. [74]

1.5.2 PODH-N_2O

The use of N_2O has been considered as an alternative oxidant for PODH, which would also be highly advantageous from an environmental standpoint. N_2O is a greenhouse gas with a global warming potency over 300 times that of CO_2, therefore, the use of atmospheric N_2O as an oxidant in industrial processes is highly desirable. Similar to PODH reactions utilising O_2 as the oxidant, the use of N_2O is exothermic and does not suffer any thermodynamic limitations (Equation 4). [75]

Equation 4: Chemical equation of PODH-N_2O

$$C_3H_8 + N_2O \longrightarrow C_3H_6 + H_2O + N_2 \quad (\Delta H°_{298K} = -199.3 \text{ kJ mol}^{-1})$$

Studies which exploit the use of N_2O as a mild oxidant in PODH reactions are relatively scarce and the reaction mechanism has not yet been thoroughly elucidated. It is understood, however, that the desired route for propene production similarly occurs via a Mars-van Krevelen pathway [76], which involves the chemisorption of N_2O (1) and the removal of surface bound oxygen species by adsorbed propane (2), as shown below:

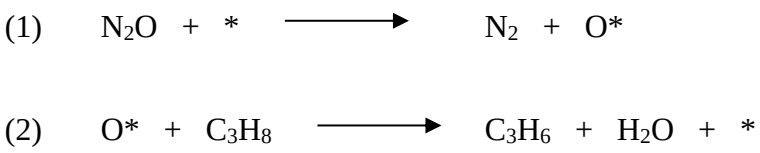

Earlier studies conducted by Kondratenko and Baerns employed O_2 and N_2O oxidants and a series of VO_x/Al_2O_3 catalysts with varying vanadium loadings in PODH reactions. [77] The authors report a decrease in activity when utilising the milder N_2O oxidant, whilst the selectivity towards propene increased at similar propane conversions. Characterisation results reveal a lower concentration of V^{5+} species when performing PODH-N_2O, indicating that the catalyst material is in a more reduced state than when using O_2 as the oxidant. These findings correlate with the previous work performed by Baerns, which revealed that the selectivity towards propene was dictated by the extent of surface reduction, where an increase in reduction resulted in an increase in propene selectivity. [78] This observation has been attributed to lower lattice oxygen concentrations when using N_2O versus O_2, which occurs due to the slower decomposition of N_2O in comparison to O_2. As a result, active lattice oxygen species are more isolated on the catalyst surface, which subsequently inhibits the over-oxidation reaction to produce carbon oxides.

Further research into the role of peroxovanadate and vanadyl species in PODH reactions when using N_2O as opposed to O_2 has been carried out using DFT methods. The authors concluded that enhanced selectivity towards propene occurs because N_2O can only successfully re-oxidise reduced V^{3+} sites, whilst molecular O_2 holds the ability to re-oxidise both reduced V^{3+} and V^{4+} sites. The re-oxidation of both sites forms a precursor containing peroxovanadate species, which are more active for the over-oxidation of propene, consequently decreasing propene yields. [77]

1.6 Chemical Looping PODH (CL-PODH)

Various challenges exist when considering the implementation PODH-O_2 at the industrial scale. These relate to the exothermicity of the reaction, the methods of controlling the consecutive combustion reaction and the means of co-feeding molecular oxygen with flammable propane gas. [79] As a result, recent oxidative dehydrogenation studies have shifted towards using O_2-free atmospheres and chemical looping PODH (CL-PODH) systems, where the lattice oxygen sites of metal oxide catalysts are used as the oxygen source, and a separate catalyst regeneration step is performed. For this to be achievable, metal oxide catalysts that can provide lattice oxygen species at the temperatures necessary for the PODH reaction are required. [31, 80-82] Chemical-looping oxidation technologies typically comprise of dual-reactor systems, which exploit metallic oxygen carriers for the transfer of lattice oxygen species for the partial or full oxidation of the reactant species (1), before being regenerated back to their original state (2), as shown below [83, 84] :

$$(1) \qquad C_3H_8 + MO_x \longrightarrow C_3H_6 + MO_{x-1} + H_2O$$

$$(2) \qquad MO_{x-1} + \frac{1}{2}O_2 \longrightarrow MO_x$$

This model has been employed in PODH studies conducted by S. Rostom and H. I. de Lasa by utilising a CREC Riser Simulator and transition metal oxide catalysts in the hopes of maximising propene selectivities. [80] The configuration of their dual bench-scale reactor was invented in 1992 by de Lasa and involves both a PODH downer and a mini-fluidized bed reactor. [80, 85] In their studies, ten consecutive propane injections were fed over fluidizable $VO_x/\gamma Al_2O_3$ and VO_x/ZrO_2-γAl_2O_3 catalysts, with varying vanadium loadings, at 550 °C. Lattice oxygen sites acted as the oxygen source for catalyst regeneration between propane injections, however, an increase in cracking products and low propene selectivities were observed after the 10th injection due to a lack of surface oxygen species. A catalyst re-oxidation step was consequently employed at this point to regenerate the catalyst and restore PODH activity. [80] From this study, the authors proposed that varied oxygen reactivities were in play during the consecutive propane injections. Specifically, labile oxygen played a vital role in propane oxidation during the first injection, where propene selectivity was extremely low and the bulk of the propane combusted to carbon oxides. During the second injection, inhibition of propene formation remained significant, since a large fraction of propane converted to carbon oxides. Labile oxygen seemed to be

consumed from the third injection onwards, where propene selectivities gradually increased, reaching 93 % at 25 % propane conversion for the 7.5 wt.% VO_x/ZrO_2-γAl_2O_3 catalyst. This is a substantial enhancement in comparison to the propene selectivities obtained during the first and second injection, which implies to some extent that a degree of surface reduction is required to maximise propene selectivity. [80]

Alternatively, CL-PODH studies using mixed Mo-V-O oxides have been performed in a fixed bed reactor, which utilise various propane dehydrogenation-catalyst regeneration cycles. [86] This alternative chemical looping approach yielded propane conversions of 36 % and propene selectivities of 89 %, which remained stable over 100 consecutive propane dehydrogenation-catalyst regeneration cycles performed at 500 °C. The stability of the catalyst throughout the cycles showcases the ability to successfully regenerate vanadia based catalyst systems in CL-PODH reactivity tests. These results highlight the possibility of eradicating co-fed molecular oxygen in PODH studies, which ultimately eliminates the extensive safety precautions that are required to keep propane and oxygen feeds under explosive limits, and prevent reaction run-aways. [86]

2 Project Aims

The main objectives throughout the scope of this research are as follows:

1. The preparation of γ-Al_2O_3 supported VO_x, MoO_x and VO_x-MoO_x catalysts

    - VO_x/γ-Al_2O_3 and MoO_x/γ-Al_2O_3 catalysts will be prepared via the incipient wetness impregnation technique with varying vanadium loadings of 5.0, 7.5 and 10.0 wt.% and a fixed molybdenum loading of 9.4 wt.%

    - VO_x-MoO_x/γ-Al_2O_3 catalysts will be prepared via the co-impregnation technique, where the vanadium loading was fixed to 10.0 wt.% and molybdenum loadings varied from 3.2, 4.7 and 9.4 wt.% as a function of varied V:Mo molar ratio of 6:1, 4:1 and 2:1, respectively.

2. To investigate the chemical and structural properties of the freshly prepared catalysts, various techniques were employed which include MP-AES, ICP-OES, BET, H_2-TPR, O_2 chemisorption, Raman spectroscopy and XRD.

3. The development of CL-PODH redox cycling tests, which will be performed over the prepared catalysts to probe the efficacy for propene production in addition to catalyst regenerability and stability, when using O_2 as an oxidant. As a result, the effect of varying vanadium loading and incorporation of the molybdenum promotor at various V:Mo ratios on CL-PODH reactions will be analysed.

4. The most promising catalyst will be studied further in CL-PODH redox cycling tests using softer N_2O and CO_2 to establish the catalyst regenerability and stability in comparison to tests using O_2 as the oxidant.

5. A series of propane pulsing tests will be employed to provide further insight into the reaction chemistry taking at key points within the CL-PODH redox cycling tests.

6. Post-reaction characterisation of catalysts removed at various stages of the CL-PODH redox cycles will be conducted to investigate any chemical and structural changes brought about by reaction tests.

3 Experimental

3.1 Catalyst Synthesis

3.1.1 Materials

Detailed in Table 2 and Table 3 are the materials used for the synthesis of catalysts studied throughout this work. Several alumina-supported vanadium oxide, molybdenum oxide and mixed vanadium-molybdenum oxide catalysts were prepared and are denoted as VAl, MoAl and VMoAl respectively.

Table 2: Precursors used in the synthesis of VAl, MoAl and VMoAl catalysts

Material	Phase	Purity	Manufacturer
NH_4VO_3	Solid	99.0%	Alfa Aesar
$(NH_4)_6Mo_7O_{24}.4H_2O$	Solid	99.0%	Alfa Aesar
$C_2H_2O_4 \cdot 2H_2O$	Solid	99.5%	Fischer Scientific

Table 3: Support used in the synthesis of VAl, MoAl and VMoAl catalysts

Material	Size (mm)	Shape	Surface Area ($m^2\ g^{-1}$)	Pore Volume ($cm^3\ g^{-1}$)	Avg. Pore Diameter (nm)	Manufacturer
γ-Al_2O_3	3.2	Sphere	270	0.77	8.1	Saint-Gobain

3.1.2 Preparation of VAl Catalysts

VAl catalysts with varying vanadium loadings (5.0, 7.5 and 10.0 V wt.%) were prepared via incipient wetness impregnation shown below in Figure 7, where the γ-Al_2O_3 support was impregnated with solutions of NH_4VO_3 in volumes corresponding to the pore volume of the support. Due to the poor solubility of NH_4VO_3, aqueous solutions were achieved by adding the precursor to solutions of oxalic acid, such that the stoichiometric molar ratio was NH_4VO_3:oxalic acid = 0.5. The solutions were stirred and heated to 343 K, which resulted in a colour change from orange to brilliant blue, suggesting a change in vanadium oxidation state. The reaction is shown in Equation 5, where the oxalic acid acts as a reducing agent to form the readily soluble ammonium oxalate vanadate complex with vanadium in the +4 oxidation state. [87]

Equation 5: Chemical equation for the reaction between oxalic acid and the NH_4VO_3 precursor

$$2NH_4VO_3 + 4H_2C_2O_4 \rightleftharpoons (NH_4)_2[V_2O_2(C_2O_4)_3] + H_2O + CO_2$$

Once CO_2 evolution had ceased, pre-calculated amounts of γ-Al_2O_3 support were added to the solutions under continuous stirring. The resulting solids were dried overnight at 353 K before calcining for 12 h at 823 K at a ramp rate of 10 K min^{-1}. Catalyst spheres were then crushed and sieved to a particle size of 250-425 µm.

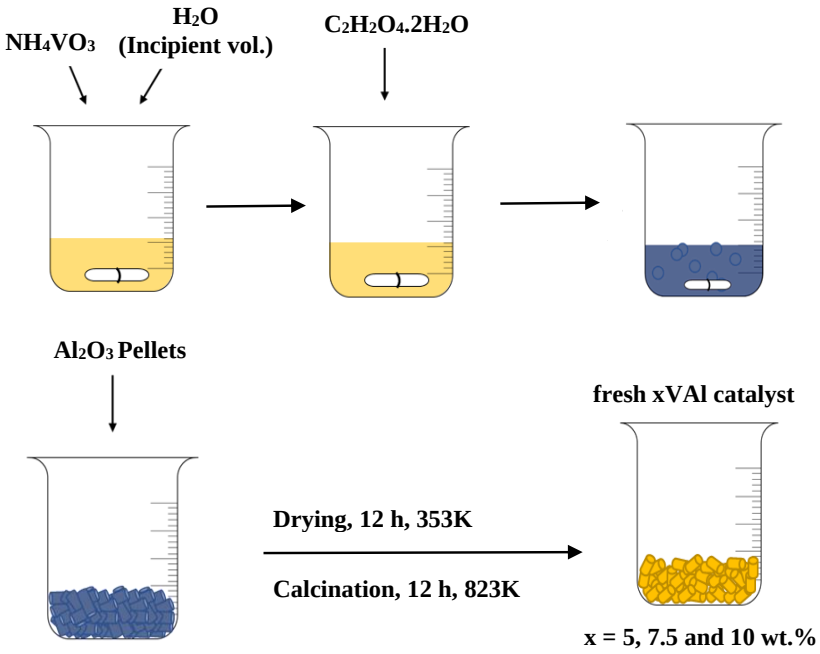

Figure 7: Incipient wetness impregnation technique of fresh VAl catalysts

3.1.3 Preparation of VMoAl Catalysts

The co-impregnation technique was used for the preparation of VMoAl catalysts, where the γ-Al_2O_3 support was impregnated simultaneously with solutions of both NH_4VO_3 and $(NH_4)_6Mo_7O_{24}.4H_2O$ precursors. The vanadium metal loading in VMoAl catalysts was fixed to 10.0 wt.%, and molybdenum metal loadings varied from 3.2, 4.7 and 9.4 wt.% as a function of varied V:Mo molar ratios of 6:1, 4:1 and 2:1, respectively. Aqueous solutions of both precursors were prepared as those described above in Section 3.1.2, with the addition of $(NH_4)_6Mo_7O_{24}.4H_2O$ to the vanadium solution occurring once CO_2 evolution had ceased. Due to the poor solubility of both precursors, additional volumes of deionised water were required for complete dissolution, resulting in solutions that no longer corresponded to the pore volume of the support. The solutions were added slowly to pre-calculated amounts of the γ-Al_2O_3 support under continuous stirring in a beaker. The mixture was stirred at 343 K for 30 mins to slowly evaporate excess water off and reduce the solution down until the incipient wetness point had been reached. The resulting solids were dried, calcined and crushed as described above in Section 3.1.2.

3.1.4 Preparation of MoAl Catalysts

A 9.4 wt.% MoAl catalyst was prepared via the incipient wetness impregnation technique, where the aqueous solution of the molybdenum precursor was prepared by dissolving a pre-calculated amount of $(NH_4)_6Mo_7O_{24}.4H_2O$ in deionised water. The solution was stirred and heated to 343 K to accelerate the dissolution, before slowly adding to the γ-Al_2O_3 support under continuous stirring in a beaker. The resulting solid was dried, calcined and crushed as described above in Section 3.1.2.

A summary of VAl, MoAl and VMoAl catalysts is presented in Table 4, which details the desired vanadium and molybdenum wt.% and the corresponding V:Mo molar ratios where applicable. The actual quantities of NH_4VO_3, $(NH_4)_6Mo_7O_{24}.4H_2O$, oxalic acid, support and deionised water that were utilised for each catalyst preparation are summarised in Table 5.

Table 4: Summary of prepared VAl, MoAl and VMoAl catalysts

Catalyst	Desired wt.% of Vanadium	Desired wt.% of Molybdenum	Molar Ratio (V:Mo)
5VAl	5.0	-	-
7.5VAl	7.5	-	-
10VAl	10.0	-	-
10V3.2MoAl	10.0	3.1	6:1
10V4.7MoAl	10.0	4.7	4:1
10V9.4MoAl	10.0	9.4	2:1
9.4MoAl	-	9.4	-

Table 5: Summary of support, precursor, oxalic acid and deionised water quantities utilised in the preparation of VAl, VMoAl and MoAl catalysts (on the 5 g scale)

Catalyst	Mass of Al_2O_3 (g)	Mass of NH_4VO_3 (g)	Mass of $(NH_4)_6Mo_7O_{24}.4H_2O$ (g)	Mass of Oxalic Acid (g)	Volume of H_2O (mL)
5VAl	4.75	0.576	-	1.239	3.6
7.5VAl	4.63	0.861	-	1.856	3.5
10VAl	4.52	1.149	-	2.475	3.4
10V3.2MoAl	4.47	1.148	0.289	2.535	6.0
10V4.7MoAl	4.27	1.151	0.435	3.095	6.5
10V9.4MoAl	4.03	1.150	0.871	3.717	7.5
9.4MoAl	4.529	-	0.868	-	3.5

3.2 Catalyst Characterisation

3.2.1 Brunauer-Emmett-Teller Surface Area Determination

The Brunauer-Emmett-Tellet (BET) method is frequently used to determine the specific surface area, pore volume and average pore diameter of solid-state materials by studying the physisorption interaction between nitrogen adsorbate gas molecules and the solid surface.

The BET adsorption isotherm equation is shown below in Equation 6,

Equation 6: The BET Equation,

$$\frac{P}{V(P_o - P)} = \frac{C - 1}{V_m C}\left(\frac{P}{P_o}\right) + \frac{1}{V_m C}$$

The parameters are detailed below:

- P is the equilibrium pressure of the adsorbate gas,
- P_o is the saturated vapor pressure of the adsorbate gas,
- V is the volume of adsorbate gas at equilibrium pressure P,
- V_m is the volume of adsorbate gas required for a complete monolayer coverage,
- C is the BET constant.

Plotting $\frac{P}{V(P_o - P)}$ against $\frac{P}{P_o}$ yields a straight line where the gradient of the slope equals $\frac{C-1}{V_m C}$ and the intercept equals $\frac{1}{V_m C}$. Thereby, gradient and intercept values can be used to determine the monolayer gas quantity, V_m and the BET constant, C. These parameters can be used to calculate the total surface area and the specific surface area S_{BET} by using Equations 7 and 8.

Equation 7: Total Surface Area Equation

$$S_{Total} = \frac{V_m N A_{cs}}{V_0}$$

Equation 8: Specific Surface Area Equation

$$S_{BET} = \frac{S_{Total}}{m}$$

The parameters are detailed below:

- V_m is the volume of adsorbate gas required for a complete monolayer coverage,
- N is Avogadro's constant,
- A_{cs} is the cross-sectional area of the adsorbate gas molecule,
- V_0 is the molar volume of adsorbate gas
- m is the mass of the sample.

A number of assumptions are used when deriving the BET Equation: (1) gaseous molecules behave ideally, (2) multiple adsorbate molecules can be adsorbed on each site, (3) all surface sites are equivalent, (4) each adsorbed molecule provides an available site for an adsorbate molecule in the layer above it, (5) there is no adsorbate-adsorbate interaction, and (6) adsorbate molecules in the second and subsequent layers are assumed to be in a liquid-like state.

BET measurements were performed on fresh and spent VAl, MoAl and VMoAl catalysts using a Quadrasorb Evo Gas Sorption Surface Area and Pore Size Analyser at 77 K where nitrogen was the adsorbent gas and helium was the calibrant gas. Prior to analysis, approximately 0.1 g of each sample was dried and degassed for 16 h at 383 K under a constant flow of nitrogen.

3.2.2 Laser Raman Spectroscopy

Laser Raman Spectroscopy (LRS) is a technique, which focuses on the interaction between a monochromatic laser source and the vibrations within a molecule. Raman scattering (or inelastic scattering) occurs when the laser photons interact inelastically with the target sample by exciting an incident photon from the ground vibrational level into a new "virtual state". This excitation is merely transient, where the photon returns to a lower vibrational level in the form of an inelastically scattered photon which possesses a different frequency with respect to the incident photon. The extent to which the frequencies of the photons are shifted is indicative of the vibrational modes of the molecule (Figure 8). When the frequency of the scattered photon is greater than that of the incident photon, anti-Stokes scattering occurs and when the frequency of the scattered photon is less than that of the incident photon, Stokes scattering occurs. Rayleigh scattering (or elastic scattering) can also occur, where the scattered photon returns to the original ground vibrational level with a frequency corresponding to the incident photon.

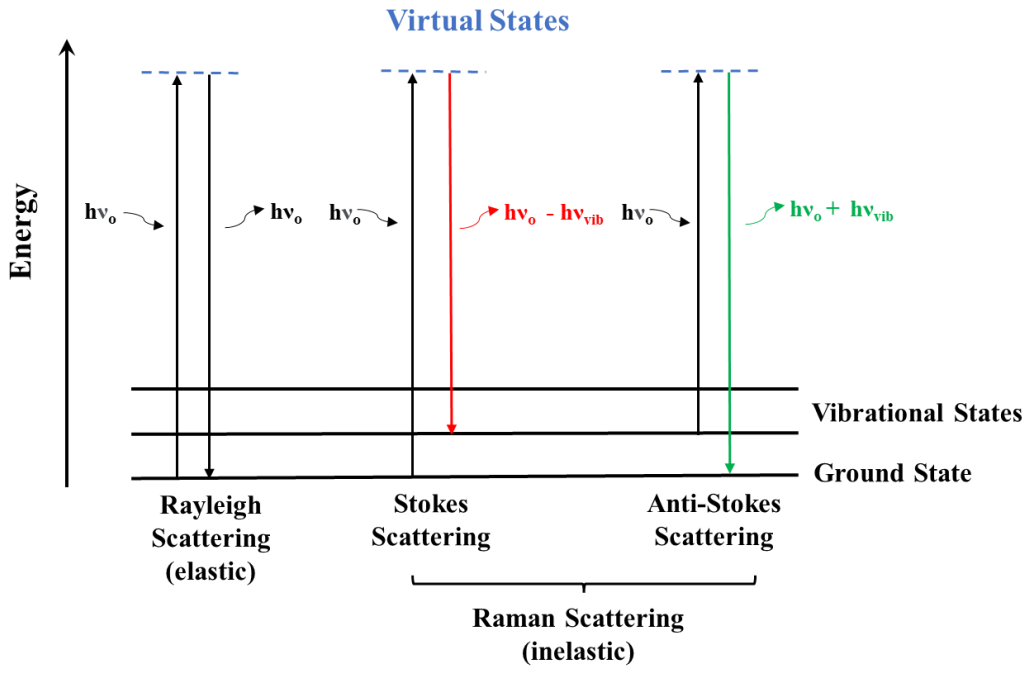

Figure 8: Energy transition diagram for Rayleigh and Raman scattering

There must be a change in polarizability in order for a vibrational mode within a molecule to be Raman active. In Raman spectroscopy, this change in polarizability occurs when the external field of the laser beam distorts the electron cloud surrounding the molecule. This polarizability induces a dipole moment where oscillating dipoles produce the electromagnetic radiation required for photon scattering. Raman spectroscopy has provided

valuable insight into supported metal oxide catalysts, including information regarding monolayer coverage and the structure of the active complex for reactions catalysed by metal oxide species. [88]

Laser Raman Spectroscopy was utilised to probe the vanadium and molybdenum oxide species within the various fresh and spent VAl, MoAl and VMoAl catalysts. Spectra were collected in the spectral range 100-1800 cm^{-1} at ambient temperatures by using a Horiba LabRAM HR Spectrometer equipped with a 532 nm green visible laser. The parameters used varied depending on whether the sample was a fresh or spent catalyst. The-parameters are detailed in Table 6.

Table 6: Parameters used in LRS measurements

Sample	Laser (nm)	Filter (%)	Hole Size (µm)	Grating (I/mm)	Exposure Time (s)	Accumulation Number
Fresh VAl, MoAl, VMoAl	532	100	200	600	10	5
Spent VAl, MoAl, VMoAl	532	25	200	600	10	10

3.2.3 X-Ray Diffraction

X-Ray Diffraction (XRD) offers the ability to probe the internal structure of catalyst material by irradiating a powdered sample with X-Rays that have wavelengths in the Angstrom range. The generation of X-Rays occurs by heating a tungsten filament to produce electrons. A voltage is then applied to accelerate these electrons and give them sufficient energy to remove the core, inner shell electrons of the target material upon bombardment. Filtering by monochrometers is required to produce monochromatic X-rays which are then collimated and directed towards the sample. When conditions satisfy Bragg's law (Equation 9), constructive interference results from the interaction between the sample and the incident rays resulting in diffracted rays. These are detected and counted by scanning the sample through a range of angles where all diffraction directions within the lattice are attained. The diffraction peaks can then be converted to d-spacings, allowing us to identify the compound since each compound has a set of d-spacings unique to that compound.

Equation 9: Braggs Equation

$$n\lambda = 2dsin\theta$$

The parameters are detailed below:

- n is an integer,
- λ is the wavelength of the generated X-rays,
- d is the interplanar distance between atomic layers
- θ is the scattering angle which corresponds to the angle of incidence.

X-Ray diffraction patterns of both fresh and spent VAl, MoAl and VMoAl catalysts were obtained by using an X'Pert Pro X-Ray Diffractometer, which is equipped with a Cu K_α radiation source, (wavelength = 0.15406 nm, 40 kV, 40 mA). Each pattern was produced using a scan rate of 80 seconds per step in the 5-85º 2θ scale with a step size of 0.02º.

3.2.4 Thermogravimetric Analysis

Thermogravimetric analysis (TGA) provides the ability to measure the physical change in sample mass as a function of temperature and time. The instrumentation typically comprises of a precision balance housed within a furnace, whereby a sample pan is placed inside and exposed to various temperature conditions and gaseous atmospheres. Two commonly used types of analysis, which branch from TGA, are temperature programmed reduction (TPR) and temperature programmed oxidation (TPO) where the catalyst is exposed to reducing and oxidising atmospheres, respectively.

Throughout this work specifically, TPR has played an integral role in the characterisation of our metal oxide catalysts, providing information regarding the nature of the reducible sites within the catalyst sample and at which temperature the reduction occurs. TPO analysis has also been particularly useful in investigating the extent of catalyst deactivation, where the carbon deposited on spent catalysts combusts due to the oxidising atmosphere and increasing temperature. The change in sample mass results directly from the loss of carbon deposited on the sample, thus allowing us to quantitively determine the extent of carbon deposition.

TGA analysis was carried out on fresh and spent VAl, MoAl and VMoAl catalysts using the TA Instruments TGA/DSC SDT Q600 thermal analyser which is coupled to an online ESS Evolution mass spectrometer. Approximately 15 mg of sample was heated to 1073 K at a ramp rate of 10 K min^{-1} under a continuous 100 mL min^{-1} flow of either 5% H_2 in nitrogen or 2% O_2 in argon for TPR or TPO analysis, respectively. Evolved gas analysis was monitored by the mass spectrometer which recorded the following mass fragments: 44 (CO_2), 32 (O_2), 28 (CO and CO_2), 18 (H_2O), 2 (H_2).

3.2.5 Microwave Plasma Atomic Emission Spectroscopy

Atomic Emission Spectroscopy (AES) is commonly used to quantify the elements present in a sample by measuring the wavelength and the intensity of the emitted photons produced by excited atoms as they fall from higher energy levels down to lower energy states. Microwave Plasma-Atomic Emission Spectroscopy (MP-AES) uses microwave induced plasma as the excitation source in this described atomic emission phenomena. The plasma is obtained using a high frequency generator to produce microwaves, which are directed towards a torch situated in the centre of a cavity. The electromagnetic microwaves are then coupled with a stream of carrier gas, before igniting to form a high energy plasma. Liquid samples are injected into a nebuliser to create an aerosol spray, which is then introduced to the core of the plasma. The high energy microwave plasma is adequate for sample atomisation and excitation, which produces high intensity emission lines characteristic of specific elements, that can be measured and compared with standard solutions to allow for the quantitative analysis of samples.

The vanadium wt.% loading present in fresh VAl and VMoAl catalysts were determined by MP-AES at the Catalysis Hub Research Complex in Harwell, performed by June Callison. Solid catalyst samples were digested using the Anton Paar multiway 3000 and analysed using an Agilent 4100 Microwave Plasma-Atomic Emission Spectrometer.

3.2.6 Inductively Coupled Plasma Optical Emission Spectroscopy

ICP-OES is an important analytical tool primarily used to detect and quantify elements present in a sample. Similar to the MP-AES technique, ICP-OES fundamentally relies on plasma as the ionisation source, where the excited atoms emit light at specific wavelengths upon transitioning to a lower vibrational level. Analyte determination begins by pumping the aqueous sample into a nebulizer to produce an aerosol. The aerosol is then directed to the core of a high energy argon plasma, reaching up to 10,000 K, where complete sample atomisation occurs with minimal chemical interference. Like MP-AES, the emission spectrum is then measured and compared with standard solutions to quantitively determine the elements concentration.

The molybdenum wt.% loading present in fresh MoAl and VMoAl catalysts were determined by ICP-OES, performed by Christopher Kelly. Solid catalyst samples were prepared via a standard acid digestion, where the sample was digested in ~5 mL quantities of aqua regia at 393 K for approximately 30 min. The resulting solutions were cooled, filtered, and diluted accordingly for their analysis using the Agilent 5900 ICP-OES instrument.

3.2.7 X-Ray Photoelectron Spectroscopy

X-Ray Photoelectron Spectroscopy (XPS) is based upon the photoelectric effect shown in Figure 9. In XPS, the X-Ray excitation source has sufficient energy to excite and eject core photoelectrons with a quantitative kinetic energy (E_K) relating to the energy of incident radiation ($h\nu_0$). This relationship is shown in Equation 10, where E_B is the binding energy of the photoelectron and Φ is the work function of the material, also known as the atomic ionisation threshold.

Equation 10: Kinetic Energy Equation for Ejected Photoelectrons

$$E_K = h\nu - E_B - \Phi$$

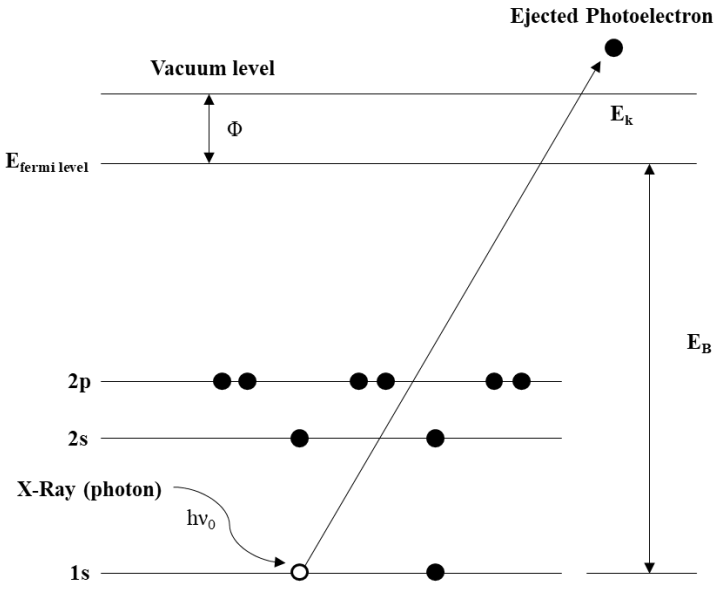

Figure 9: The photoelectric effect in XPS

Once ejected, a detector collects the emitted photoelectrons. Since each set of binding energies for a given photoelectron are element specific, the measurement of oxidation state, electronic configuration, and elemental composition is possible by analysing the resulting kinetic energies of the emitted photoelectrons. XPS must also be performed under ultra-high vacuum (UHV) conditions since the detector is situated approximately one metre away from the target material. XPS is classified as a surface sensitive technique and cannot be used to probe the bulk structure of materials since the photoelectrons emitted below the surface have a greater path length and cannot be ejected from the sample towards the vacuum level.

X-ray photoelectron spectroscopy (XPS) was performed on various 10VAl catalyst samples in order to probe the oxidation state and elemental composition of the vanadia species at various stages within our propane redox cycles. The samples were analysed on a Thermo Fisher Scientific K-alpha^{+} spectrometer. The spectrometer houses a micro-focused monochromatic Al X-ray source (72 W) using the "400-micron spot" mode, which provides an analysis defining elliptical X-ray spot of ca. 400 x 600 microns. Data was recorded at pass energies of 150 eV for survey scans and 40 eV for high resolution scan with 1 eV and 0.1 eV step sizes respectively. Charge neutralisation of the sample was achieved using a combination of both low energy electrons and argon ions.

XPS data collection was performed at the EPSRC National Facility for XPS ('HarwellXPS'), operated by Cardiff University and UCL, under contract No. PR16195. Data analysis was performed by David Morgan using CasaXPS v2.3.24 after calibrating the data to the lowest C(1s) component taken to have a value of 284.8 eV.[89] Quantification was made using a Shirley type background and Scofield cross sections, with an electron energy dependence of -0.6.

3.3 Experimental Procedures for Catalyst Testing

3.3.1 CATLAB Microreactor

Oxygen chemisorption measurements and catalyst reactivity tests were performed in the combined CATLAB microreactor and mass spectrometer system developed by Hiden Analytical (Figure 10). [90] The Hiden CATLAB unit is a modular, bench-top system which is made up of three major components:

1. Gas feeding system comprising of four mass flow controllers (MFC's), valves and switches, allowing for continuous flow or pulsing measurements. The four MFC's deliver flow rates from 2-100 mL min^{-1} where the minimum gauge pressure is 3 bar. Port connections to the MFC's are 1/8" Swagelok and the gases used throughout this study were connected via Swagelok tubing.

2. Microreactor unit comprising of a powerful, low thermal mass furnace with the capability to reach 1273 K at a heating ramp rate range up to 20 K min^{-1}. Housed within the furnace is the quartz microreactor tube which has an inner diameter of 7 mm, a length of 185 mm and a 1 mm bored hole at the base to allow the movement of gas from the inlet to the outlet. The quartz sample tube was packed with quartz wool at the base of the tube prior to loading the catalyst sample, where an "in-bed" K-type thermocouple was inserted through the tube and onto the catalyst bed, allowing for the direct measurement of the sample temperature ± 1°C.

3. Hiden's QGA mass spectrometer system comprising of an inert, quartz lined sampling capillary which draws in post-reaction gas from the reactor outlet at fast response times below 500 ms. The sampling capillary directs the post-reaction gas towards the Hiden HAL 201 RC MS for analysis by a dual Faraday/Scanning Electron Multiplier (SEM) detector with a mass range of 200 amu.

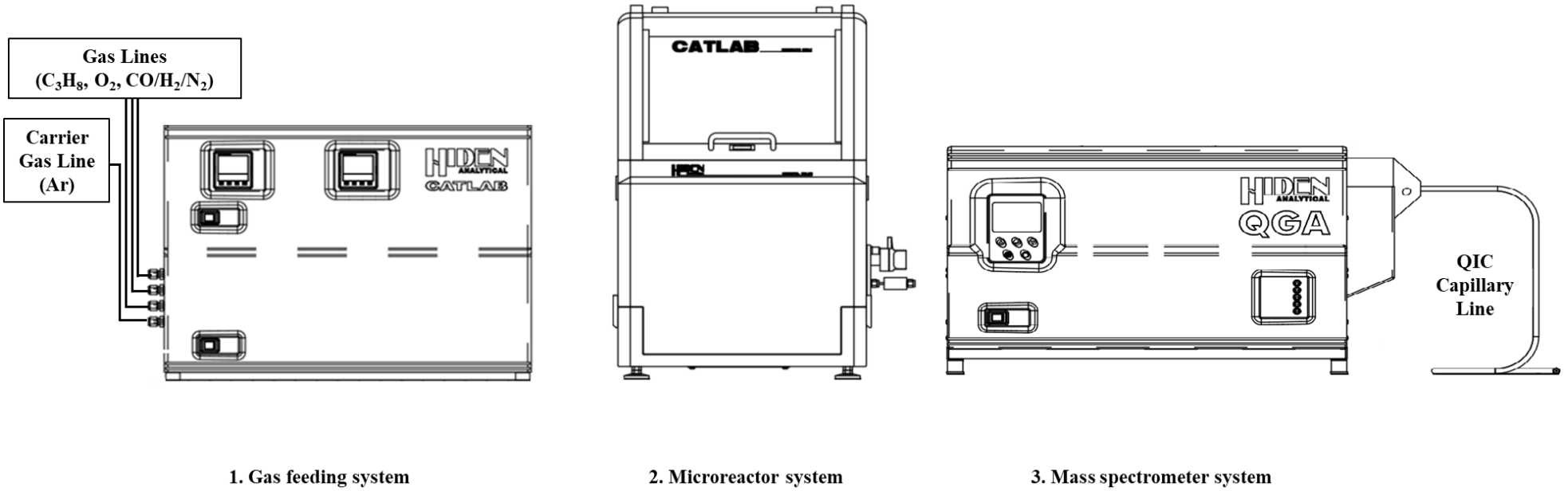

Figure 10: Schematic diagram of Hiden's CATLAB combined microreactor/mass spectrometer system. [90]

3.3.2 Oxygen Chemisorption

Chemisorption is a widely used technique in the field of catalysis and provides the means of quantitatively determining the number of active sites available on the catalyst surface. Whilst the technique is relatively simple, difficulties can arise when analysing metal oxide catalysts, as bulk reduction may occur if the reduction step is not properly controlled. The oxygen adsorption step must also be carried out at sufficient temperatures to ensure that the metal oxide surface has been entirely re-oxidised back to its original state. Oxygen chemisorption measurements were carried out on fresh VAl, MoAl and VMoAl catalysts by utilising the dynamic pulsing mode in Hiden's CATLAB system. The pulsing mode enables a fixed quantity of gas, in this case oxygen, to pulse through the microreactor system at a chosen dosing and loading interval of 45 s. Oxygen was directed through the pulse line towards the gas switching valve which incorporates a 100 uL sample loop. The activation of the pulse mode allows the sample loop to be filled before it is pushed out of the loop towards the reactor tube by a flow of inert carrier gas.

Prior to the oxygen adsorption step, approximately 30 mg of catalyst powder was loaded into the quartz sample tube and reduced in a continuous flow of hydrogen (5 mL min^{-1}) and argon (45 mL min^{-1}) for 2 h at 643 K before subsequently flushing for 1 h with a pure argon flow. Oxygen uptake measurements were performed at 643 K and monitored using Hiden's QGA MS, following the m/z 32 ion fragment with the SEM detector at 70 eV and 400 uA. Once the uptake plateaued and three successive peaks with a similar area were detected, the measurement was deemed complete, and the pulses were stopped.

3.3.3 Chemical Looping PODH Reaction Tests

Chemical looping propane oxidative dehydrogenation (CL-PODH) redox cycles, summarised in Figure 11, were carried out utilising the continuous flow mode in Hiden's CATLAB system. The microreactor was charged with 0.4 mL of VAl, MoAl or VMoAl and several propane dehydrogenation-regeneration redox cycles were carried out at 773 K at atmospheric pressure, switching between propane and oxygen flows during the tests.

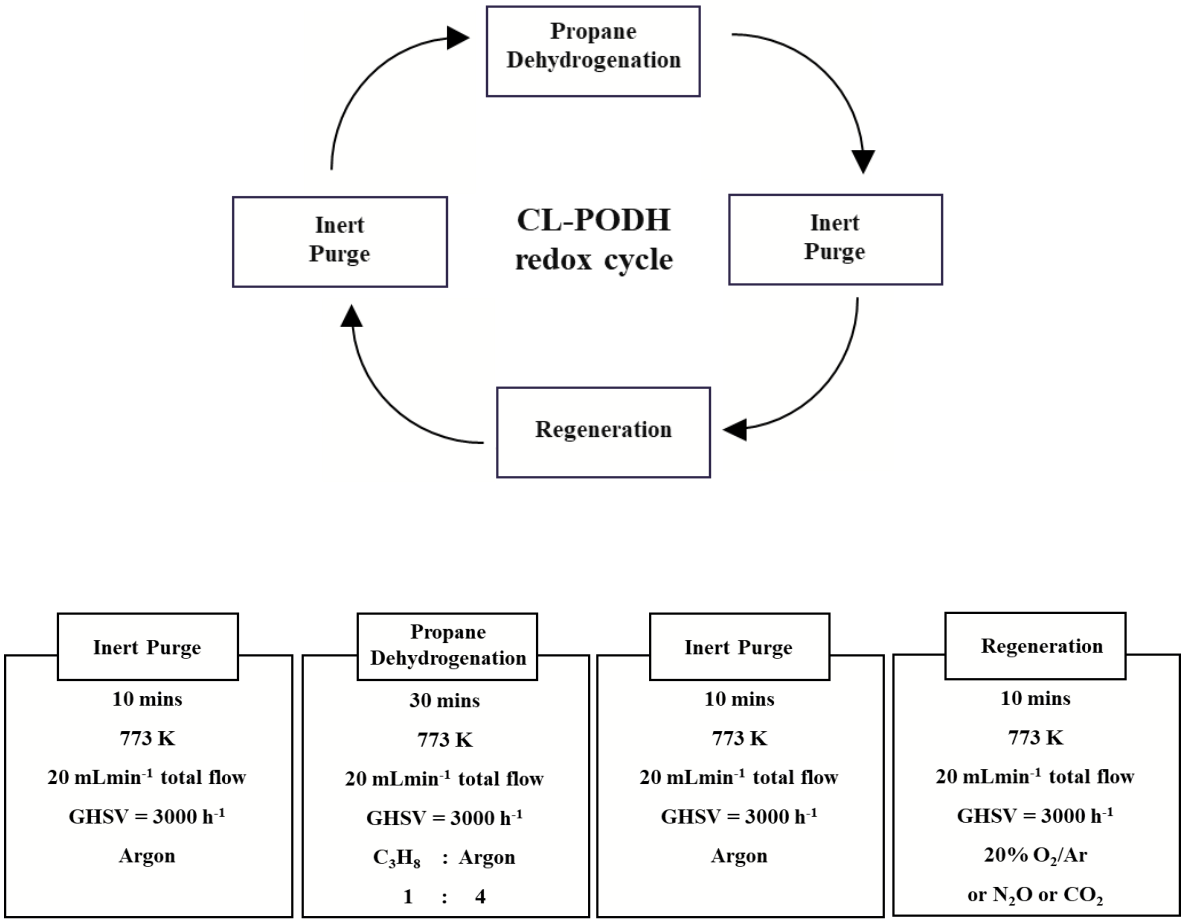

Figure 11: CL-PODH redox cycles

A typical redox cycle is shown in Figure 11 and is described as follows: a catalyst sample was loaded into the microreactor and heated to 773 K under a constant argon flow of 20 mL min^{-1}. Once at 773 K, VAl, MoAl and VMoAl catalysts were reduced for 30 min using mixed propane (4 mL min^{-1}) and argon (16 mL min^{-1}) feeds, at a GHSV of 3000 h^{-1}. Catalyst re-oxidation was carried out for 10 min using a mixed oxygen (4 mL min^{-1}) in argon (16 mL min^{-1}) feed where an inert purge of argon (20 mL min^{-1}) was employed for 10 mins between the reduction and reoxidation step to prevent the mixing of propane and oxygen feeds. A total of ten redox cycles were carried out over a two-day period for each catalyst, where the catalyst was held under argon (20 mL min^{-1}) overnight after the fifth cycle before resuming the sixth cycle the following day. The effect of using alternative softer oxidants, N_2O and CO_2, was also studied in the catalyst re-oxidation step.

Propane pulsing tests were performed to investigate key reactivity zones within the performed CL-PODH redox cycles. These were achieved by utilising the dynamic pulsing mode, as described above in Section 3.3.2, where propane pulses were directed over the catalyst bed at specific times in a continuous flow experiment before resuming a continuous flow of propane or regeneration step, where required.

3.4 Data Analysis

3.4.1 Mass Spectrometry

Mass spectrometry (MS) has played a pivotal role in the field of catalysis with capabilities spanning from various characterisation to kinetic analysis in reaction studies. Principally, MS centres around the ability to ionise species into a range of ion fragments which are then separated depending on their mass-to-charge ratio (m/z).

The technique provides the ability to continually monitor evolved species in real-time over a high dynamic range, making it an excellent analytical tool, both quantitatively and qualitatively, for a wide variety of temperature dependent, oxidation and reduction reactions.

A mass spectrometer typically encompasses three main components:

1. Ion Source: this is where the sample is ionised to produce and accelerate ion fragments towards the mass analyser. Various ionisation methods exist but it is the electron ionisation technique which is used throughout this study. Electron ionisation occurs via the collision of gaseous analyte molecules with high energy electrons (typically 70 eV), which are produced from a heated filament. These high energy electrons are sufficient in overcoming the ionisation potentials of most compounds, allowing fragmentation to molecular ions at relatively high ion currents.

2. Mass analyser: this is where the ion fragments are separated based on their m/z ratio. When the ions are accelerated towards the mass analyser, a magnetic field is applied which produces a force and ultimately changes the ions trajectory. The extent of deflection is dependent on an ion's m/z value, an observation that is described by Newtons second law (Equation 11).

Equation 11: Newton's Second Law

$$F = ma$$

Whereby, F is the applied force, m is the ions mass, and a is the acceleration of ions.

A wide array of mass analysers are available for MS and the appropriate one depends on several parameters, including the mass of the sample molecule and the required m/z range that is desired. Hiden's QGA mass spectrometer houses a quadrupole mass analyser, shown below in Figure 12. A quadrupole mass analyser is made up of four parallel and cylindrical rods, where only selected resonant ions with specific m/z values are directed towards the detector by applying a specific voltage setting across each rod pair. Unselected, non-resonant ions have unstable trajectories at these voltages and will be neutralised by the rods and removed via the vacuum system.

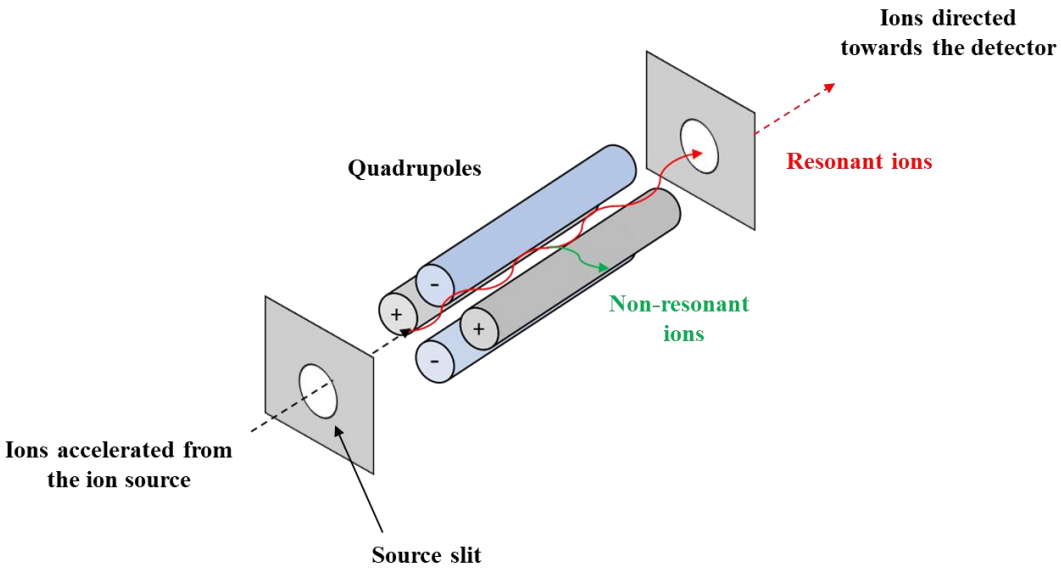

Figure 12: Schematic diagram of a quadrupole mass analyser

3. Detector: this is where resonant ion fragments with different m/z ratios are detected and counted, resulting in a measurable ion current. Hiden's QGA mass spectrometer comprises a dual Faraday cup and Scanning Electron Multiplier (SEM) detector system, which are both commonly used in MS and operate as follows. In a Faraday cup detector, resonant ion fragments strike the inner walls of the conductive cup to produce secondary electrons. These secondary electrons are captured by the cup and the electron current that is produced is then amplified and measured. In a SEM detector, ion fragments collide with a surface that is specifically engineered with emissive material in order to yield a cascade of secondary electrons from only one incident ion. Higher voltages (~ 1 kV) are required to promote the measurable ion current, allowing for lower detection limits than those achieved with the Faraday cup detector.

3.4.2 Mass Spectrometry Calibrations

The product compositions from all CL-PODH redox cycles and propane pulsing tests were analysed using Hiden's QGA MS.

In order to quantitively determine the compounds present during CL-PODH redox cycles, MS calibrations were performed by feeding various flows of propane, propene and carbon dioxide, each made up to 20 mL min^{-1} with argon, in an empty reactor. The set flow rates were converted to number of moles using the ideal gas law (Equation 12).

Equation 12: Ideal Gas Law

$$PV = nRT$$

The parameters are detailed below:

- *P* is the pressure,
- *V* is the volumetric flow rate,
- *n* is the number of moles
- *R* is the gas constant
- *T* is the temperature

Resulting ion currents of specifically selected fragments from each gas were averaged and plotted against the number of moles, giving a calibration factor used to determine the number of propane, propene, and carbon dioxide moles during the reaction.

Calibration graphs for propane, propene and carbon dioxide flows are detailed in Figures 13-15, respectively.

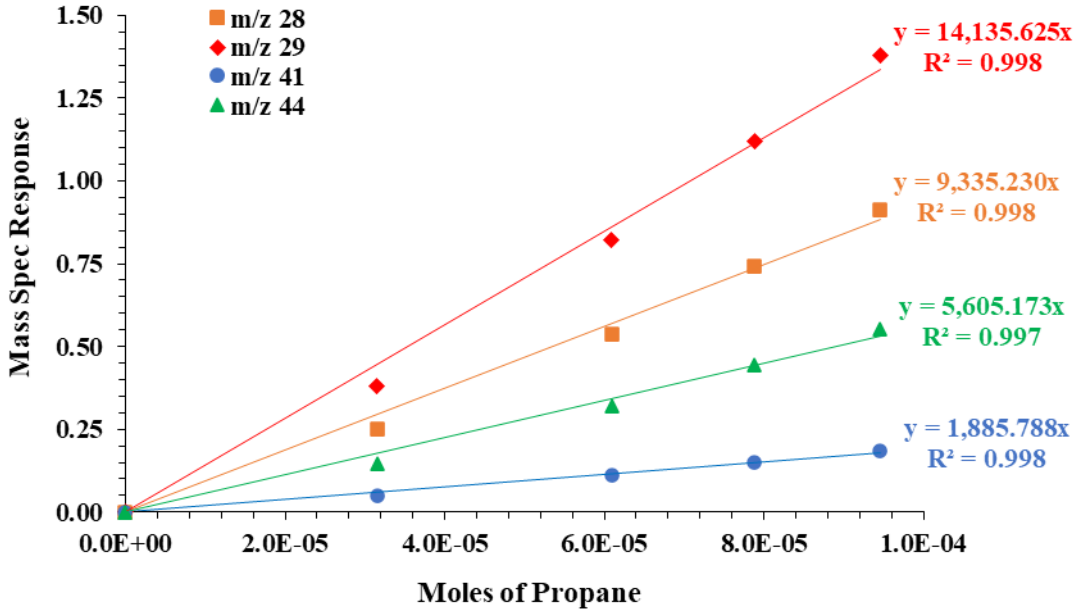

Figure 13: MS Calibration Graph for Propane

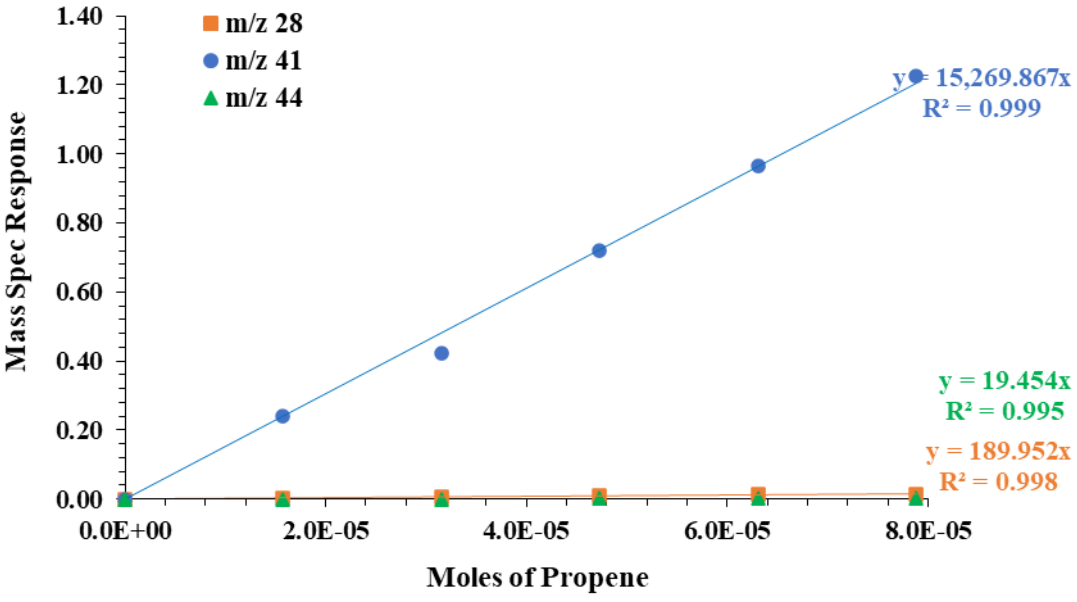

Figure 14: MS Calibration Graph for Propene

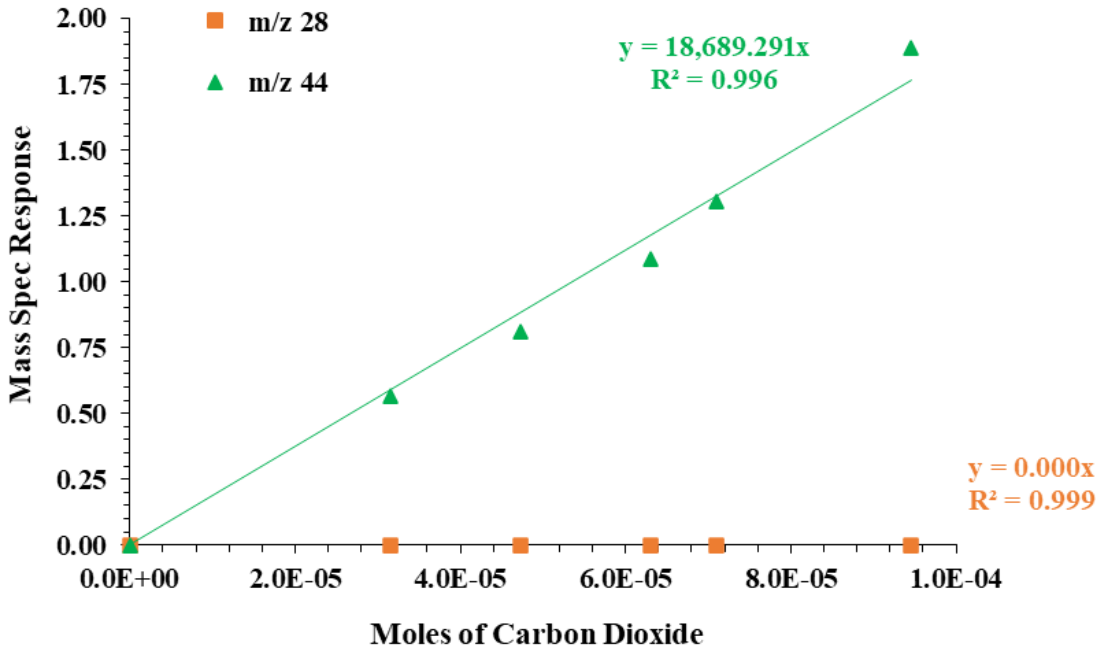

Figure 15: MS Calibration Graph for Carbon Dioxide

The mass spectral data from CL-PODH redox cycles are complex since the compounds of interest have fragmentation patterns of ions with common m/z ratios. As such, it is important to choose specific m/z ratios to identify each product and then subtract any contribution that other products may have towards the signal of the common m/z ratio.

Table 7 details the fragmentation pattern of each compound and the m/z ratio chosen to identify them. These m/z ratios were chosen since they have the largest relative intensities for that compound in their typical mass spectra obtained from the NIST chemical webbook. [91]

Table 7: Mass fragments and the chosen identifier for each compound

Compound	Ion Fragments, m/z	Chosen Identifier
Propane	45, 44, 43, 42, 41, 40, 39, 38, 37, 36, **29**, 28, 27, 26, 25, 24, 21, 20, 19, 16, 15, 14, 13, 12	29
Propene	44, 43, 42, **41**, 40, 39, 38, 37, 36, 28, 27, 26, 25, 24, 21, 20, 19, 16, 15, 14, 13, 12, 2, 1	41
Carbon Dioxide	46, 45, **44**, 29, 28, 22, 16, 12	44

These identifiers allow us to quantify the amount of propane, propene and carbon dioxide present throughout our CL-PODH redox cycles. For example, the mass fragment chosen as the identifier for propene is m/z 41, however, this signal will also have a contribution from propane. Since the chosen identifier for propane, m/z 29, is exclusive, the ratio of signal intensities between m/z 29 and 41 can be calculated for each propane sample taken from the calibrations. In our propane calibrations, the signal of the m/z 41 fragment is approximately 13.4 % of the signal belonging to m/z 29. This allows us to estimate the amount of propene produced during the reaction by calculating 13.4 % of the signal of the m/z 29 fragment and subtracting this value from the overall signal produced by the m/z 41 fragment.

In order to quantitively determine the compounds present during propane pulsing tests, MS calibrations were performed by pulsing five consecutive propane, propene and carbon dioxide pulses through an empty reactor and recording the MS signal from the chosen identifier ion fragments, m/z 28, 29, 41 and 44. The maximum peak height of chosen m/z fragments which resulted from each pulse were determined and subsequently averaged.

The pulsing loop volume was converted to number of moles using the ideal gas law shown previously in Equation 12. The average peak heights for each chosen m/z fragment were then related to the calculated number of moles present in the sample loop to obtain a one point conversion factor. This conversion factor was then used to determine the number of reactant or product moles from the maximum peak height of m/z fragments, with contributions from other compounds subtracted, as described above, for analysis of products during our CL-PODH redox cycles.

Calibration graphs for propane, propene and carbon dioxide pulses are detailed in Figures 16, 17, and 18, respectively.

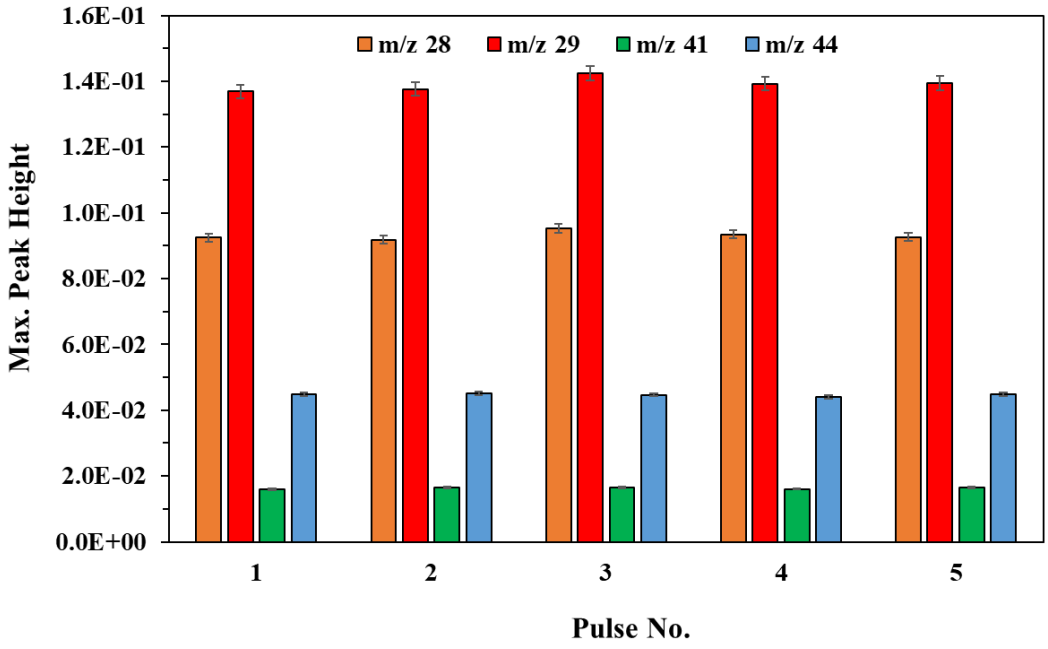

Figure 16: MS Calibration Graph for Propane Pulses

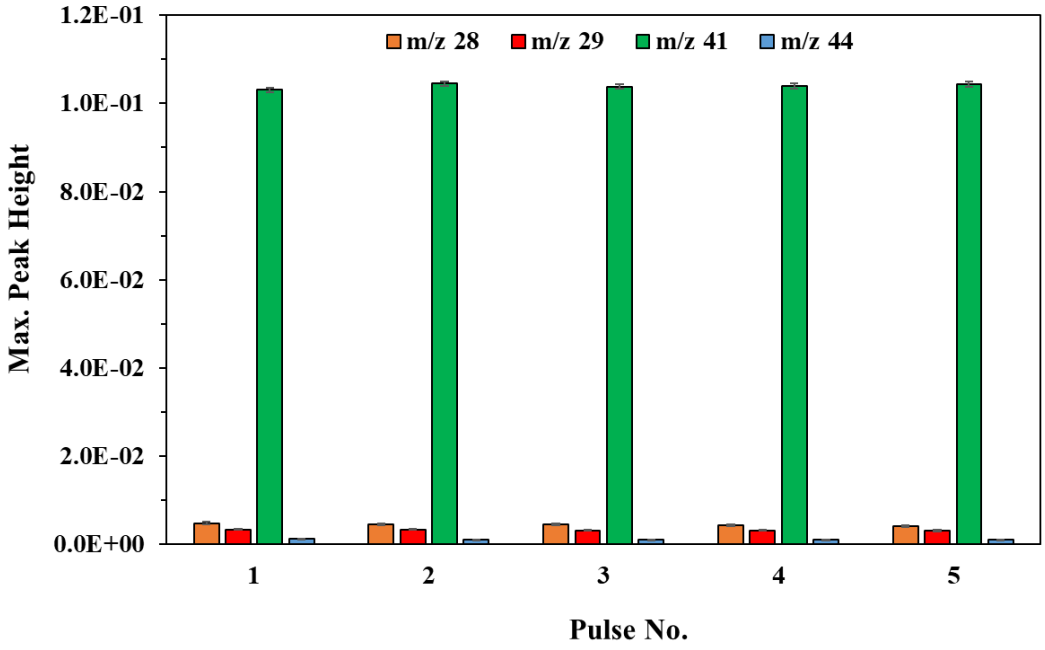

Figure 17: MS Calibration Graph for Propene Pulses

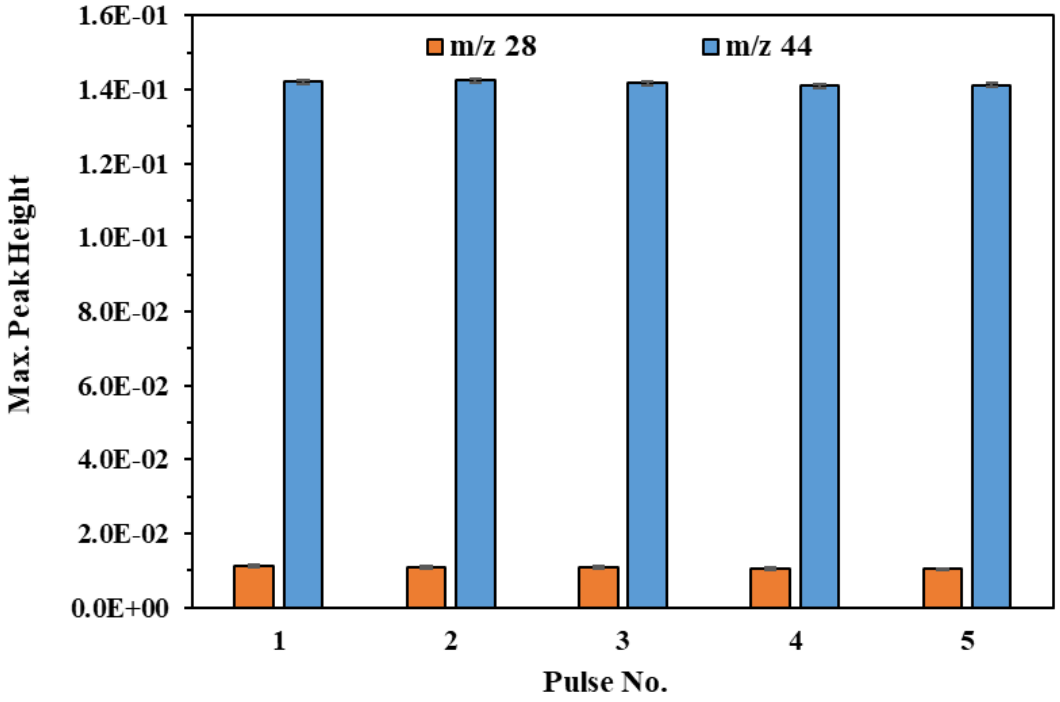

Figure 18: MS Calibration Graph for CO_2 Pulses

3.4.3 Product Analysis Calculations

The performance of catalysts during CL-PODH tests were investigated based upon the conversion of propane, the selectivity to propene and CO_2 and the resulting yield of propene and CO_2 products. Propane conversion and propene/CO_2 selectivity and yield were calculated as follows,

Equation 13: Calculation of propane conversion

$$\%\ Propane\ Conversion = \frac{C_3H_{8_{in}} - C_3H_{8_{out}}}{C_3H_{8_{in}}} \times 100\%$$

Equation 14: Calculation of propene and CO_2 selectivity

$$\%\ Selectivity = \frac{x \times n_{out}}{3 \times (C_3H_{8_{in}} - C_3H_{out})} \times 100\%$$

Equation 15: Calculation of propene yield

$$\%\ Propene\ Yield = \frac{n_{C_3H_6}}{n_{C_3H_{8_{in}}}} \times 100\%$$

Equation 16: Calculation of CO_2 yield

$$\%\ CO_2\ Yield = \frac{n_{CO_2}}{n_{C_3H_{8_{in}}}} \times 100\%$$

Where, *n* is the number of moles of the product and *x* is the number of carbon atoms present in the product.

4 Vanadium Oxide

4.1 Pre-Reaction Characterisation

This section details the characterisation results of fresh VAl catalysts, carried out prior to CL-PODH redox cycling and pulsing tests. The techniques employed include MP-AES, BET, H_2-TPR, O_2 chemisorption, Raman spectroscopy and XRD.

4.1.1 MP-AES

MP-AES was performed to determine the vanadium content in fresh VAl catalyst samples. The results detailing the vanadium loadings that were achieved via the incipient wetness impregnation technique are summarised in Table 8.

Table 8: MP-AES results for fresh VAl catalysts

Sample	Weight (mg)	V ppm	V wt.%
Fresh 5VAl	103.4	49.6	4.8
	100.0	50.6	5.1
Fresh 7.5VAl	100.9	73.0	7.2
	97.9	71.3	7.3
Fresh 10VAl	96.0	93.7	9.8
	103.4	49.6	9.6

An average V wt.% of 4.9, 7.3 and 9.7 was achieved for 5, 7.5 and 10VAl catalysts, respectively, indicating that the incipient wetness impregnations had been performed successfully for the fresh VAl catalyst series.

4.1.2 BET Surface Area Determination

BET adsorption-desorption isotherms for the γ-Al_2O_3 support and fresh VAl catalysts are shown in Figure 19. According to IUPAC classifications, the isotherms obey the Type IV model which features a characteristic H1-Type hysteresis loop. [92]

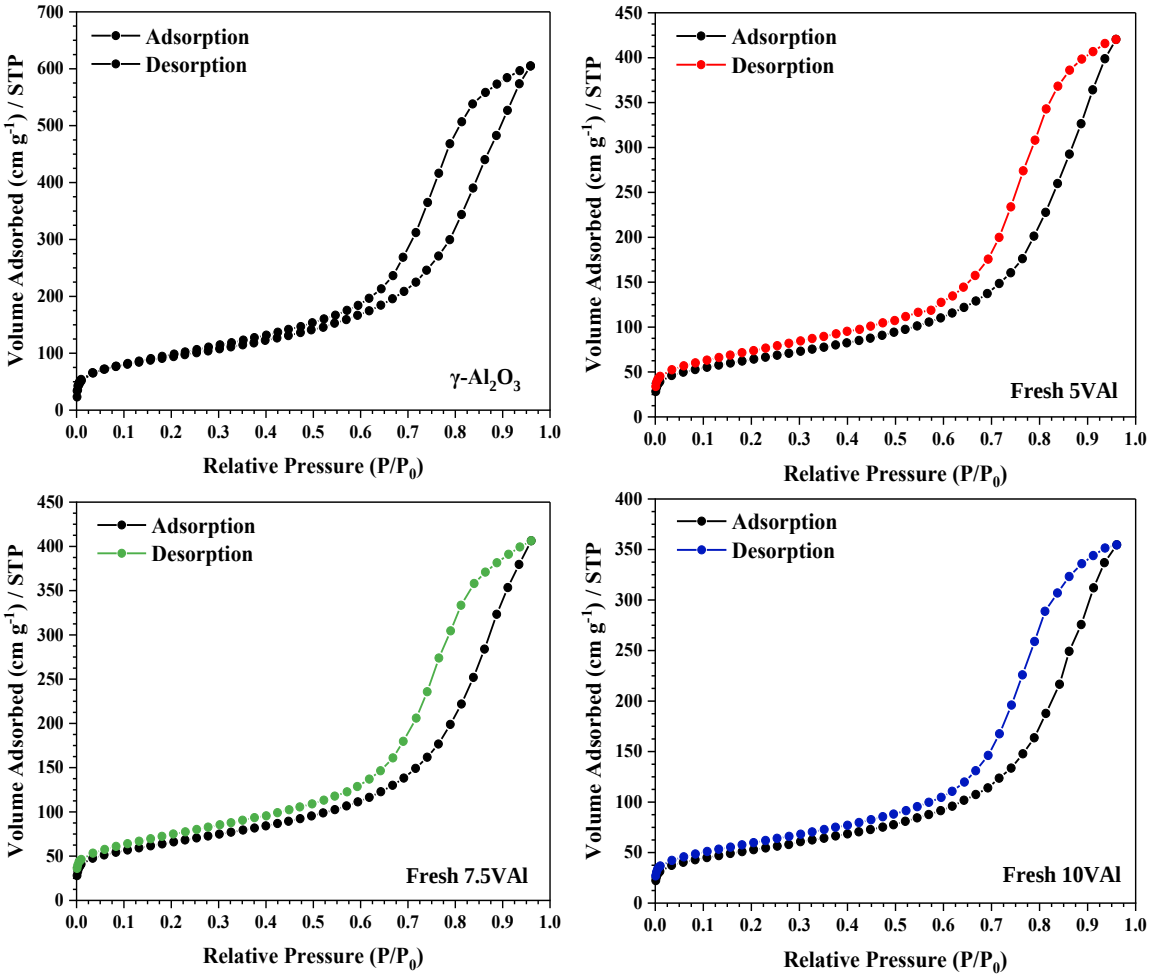

Figure 19: N_2 adsorption-desorption isotherms for fresh VAl catalysts

Table 9 details the surface area, pore volume and average pore diameter of the γ-Al_2O_3 support and fresh VAl catalysts. The surface area of γ-Al_2O_3 was 258 $m^2\ g^{-1}$, which decreased with increasing vanadium loading and calcination at 823 K for 12 h. When going from 5 to 7.5 V wt.%, the average pore diameter was unaffected with only a modest reduction in surface area and pore volume. Upon loading the γ-Al_2O_3 support with 10 wt.% vanadium however, the change in the surface area, pore volume and average pore diameter was more significant.

This observation can be explained when considering the surface density of vanadium on the alumina support. The surface density is calculated from the vanadium content and the BET surface area of each corresponding catalyst (Equation 17) and is expressed as the number of vanadium atoms per nm^2 of the catalyst sample. Surface densities are particularly useful in providing information regarding the extent of dispersion of the metal atoms by the support and the structure of VO_x species that is present on the surface.

Table 9: Surface area, pore volume and average pore diameter of the γ-Al_2O_3 support and fresh VAl catalysts

Sample	S_{BET} ($m^2\ g^{-1}$)	V_{pore} ($cm^3\ g^{-1}$)	Avg. pore diameter (Å)	Surface Density (V nm^{-2})
γ-Al_2O_3	258	0.93	54	-
Fresh 5VAl	175	0.64	48	3.3
Fresh 7.5VAl	171	0.62	48	5.0
Fresh 10VAl	145	0.55	43	7.9

Equation 17: Vanadium Surface Density Calculation

$$Vanadium\ Surface\ Density = \frac{(\frac{V\ wt.\%}{100}) \times\ N_A}{M_W\ \times\ S_{BET} \times 10^{18}}$$

Whereby,

- N_A is Avogadro's constant ($6.02x10^{23}\ mol^{-1}$)
- M_w is the molar weight of vanadium ($50.94\ g\ mol^{-1}$)
- S_{BET} ($m^2\ g^{-1}$) is the specific surface area of the catalysts

4.1.3 H_2-TPR

H_2-TPR measurements were performed in order to probe the nature of reducible sites as the vanadium loading increased in fresh VAl catalysts. The resulting H_2-TPR profiles and corresponding peak maxima are presented in Figure 20 and Table 10, revealing two distinct reduction events above 500 K.

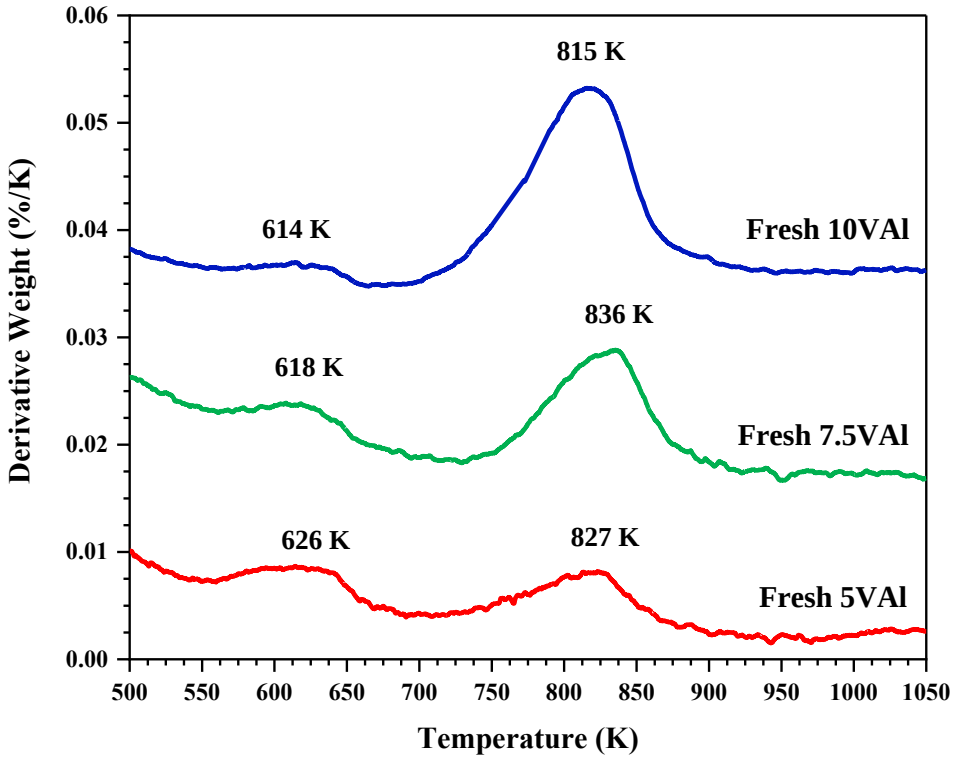

Figure 20: H_2-TPR profile of fresh VAl catalysts

Table 10: H_2-TPR data summarising T_{max} of reduction peaks in fresh VAl catalysts

Sample	T_{max} (K)	
	A	**B**
Fresh 5VAl	626	827
Fresh 7.5VAl	618	836
Fresh 10VAl	614	815

Lower temperature reduction peaks, T_{max} = 614, 618 and 626 K, are ascribed to the reduction of amorphous monomeric and polymeric VO_x surface species. The extent of vanadia polymerisation grows with increasing vanadium loading. This is depicted in the H_2-TPR spectra as reduction peaks shift to lower temperatures on going from the 5 to the 10VAl catalyst. [93]

A second reduction event is observed at T_{max} = 815, 836 and 827 K in the H_2-TPR spectra of fresh 5, 7.5 and 10VAl catalysts. Reduction events at these temperatures have previously been established in literature as the reduction of crystalline V_2O_5 surface species. [94] Notably, the intensity of this peak increases with respect to first reduction event as the vanadium loading increases. The total weight loss associated with H_2O evolution at the higher temperature reduction event was determined for each VAl catalyst and is tabulated in Table 11. The results show that approximately one oxygen atom was lost per one vanadium atom, which implies the reduction of V_2O_5 to V_2O_4.

Table 11: Weight loss associated with H_2O evolution at the higher temperature reduction event in VAl catalysts

Sample	Weight Loss[a] (mg)	O moles (µmol)	V moles[b] (µmol)	O/V Ratio
Fresh 5VAl	0.13	8.1	8.1	1.00
Fresh 7.5VAl	0.17	10.8	10.6	1.02
Fresh 10VAl	0.28	17.5	17.8	0.98

[a]Oxygen weight loss from H_2O evolution, [b]V moles present in the sample used for each TPR measurement

4.1.4 Oxygen Chemisorption

Oxygen chemisorption measurements were performed as described in Section 3.3.2 to investigate the active sites available in reduced VAl catalysts. Figure 21 presents the cumulative oxygen uptake plotted as a function of pulse number. It should be noted that the oxygen uptake of the γ-Al_2O_3 support at the same conditions was negligible.

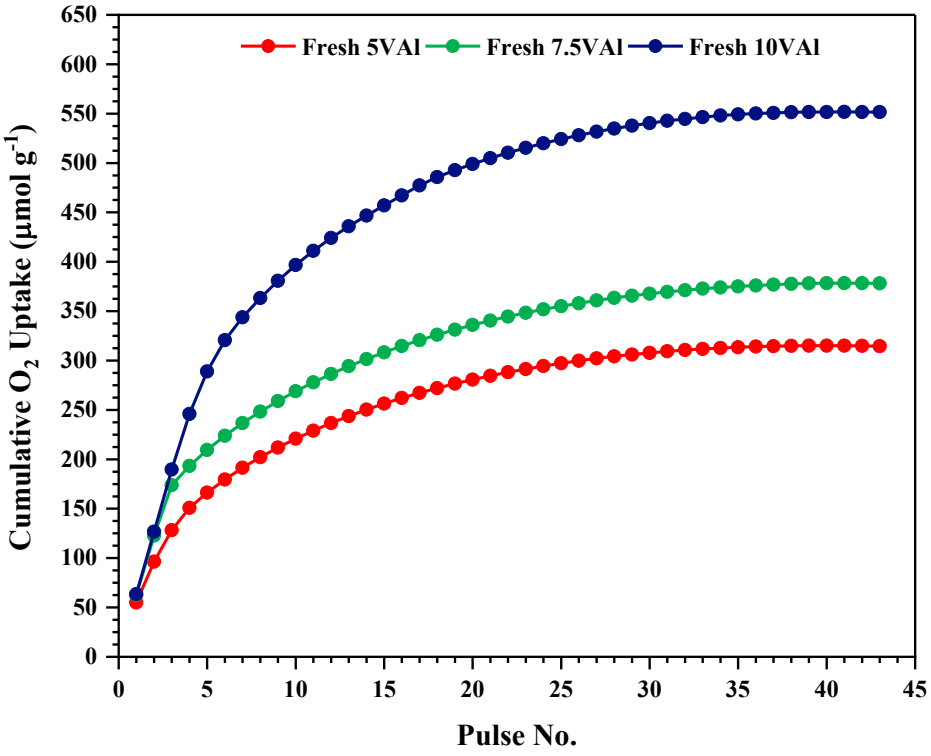

Figure 21: Cumulative oxygen uptake of fresh VAl catalysts

The resulting oxygen uptake capacity allows us to obtain the oxygen atom site density and metal dispersion of reduced VAl catalysts. Oxygen atom site densities were calculated as the ratio of oxygen atoms to the specific BET surface area of the corresponding catalyst, and the dispersion was determined by taking the ratio of adsorbed oxygen to total vanadium atoms, assuming $O_{ads}/V_{atoms} = 1$.

Oxygen uptake, atom site density and the vanadium dispersion of fresh VAl catalysts are summarised in Table 12 and Figure 22 displays the trend in oxygen uptake and metal dispersion as the vanadium loading increases. Despite an increase in oxygen uptake as the vanadium loading increases from 5 to 10 wt.%, the metal dispersion is observed to decrease on going from the fresh 5 to 7.5VAl before subsequently increasing for the fresh 10VAl catalyst. Oxygen chemisorption measurements where repeated to probe the accuracy of the results and the same findings were obtained.

Table 12: Oxygen uptake, atom site density and dispersion of fresh VAl catalysts resulting from oxygen chemisorption measurements

Sample	S_{BET} ($m^2\ g^{-1}$)	Oxygen uptake ($\mu mol\ g^{-1}$)	Oxygen atom site density ($10^{18}\ m^{-2}$)	Dispersion O/V
Fresh 5VAl	175	315	2.2	66.8
Fresh 7.5VAl	171	378	2.7	53.5
Fresh 10VAl	145	552	4.6	58.4

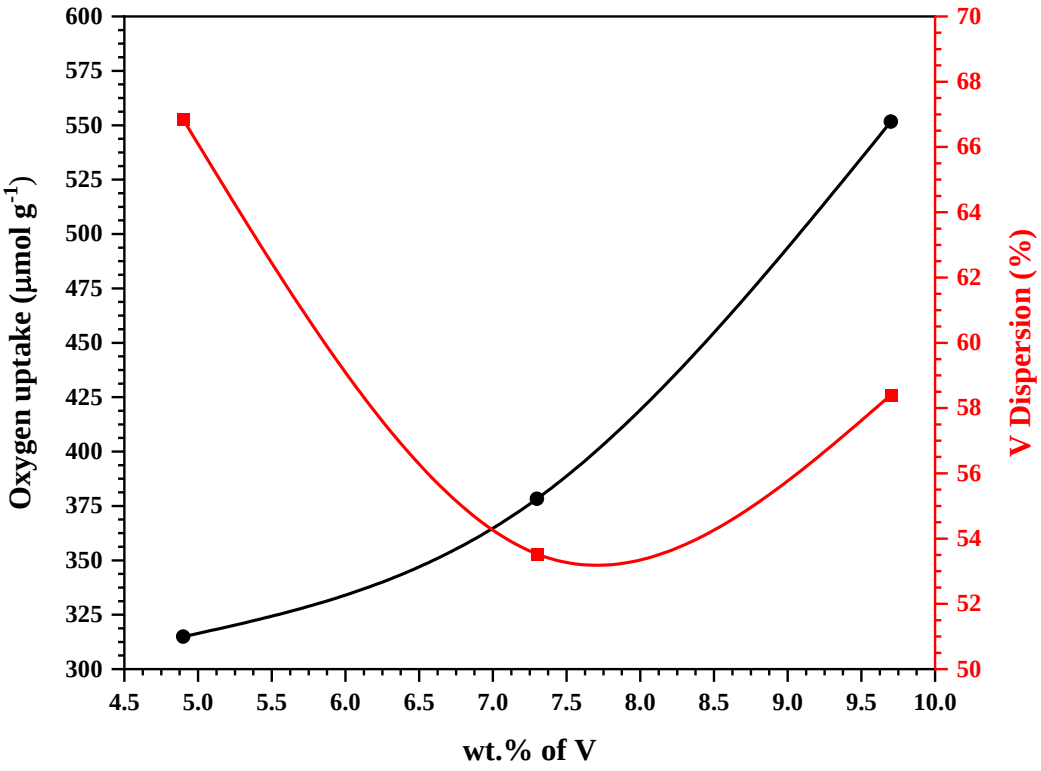

Figure 22: Oxygen uptake and dispersion of fresh VAl plotted as a function of V wt. %

4.1.5 Raman Spectroscopy

Raman spectra obtained for the γ-Al_2O_3 support and fresh VAl catalysts are presented in Figure 23.

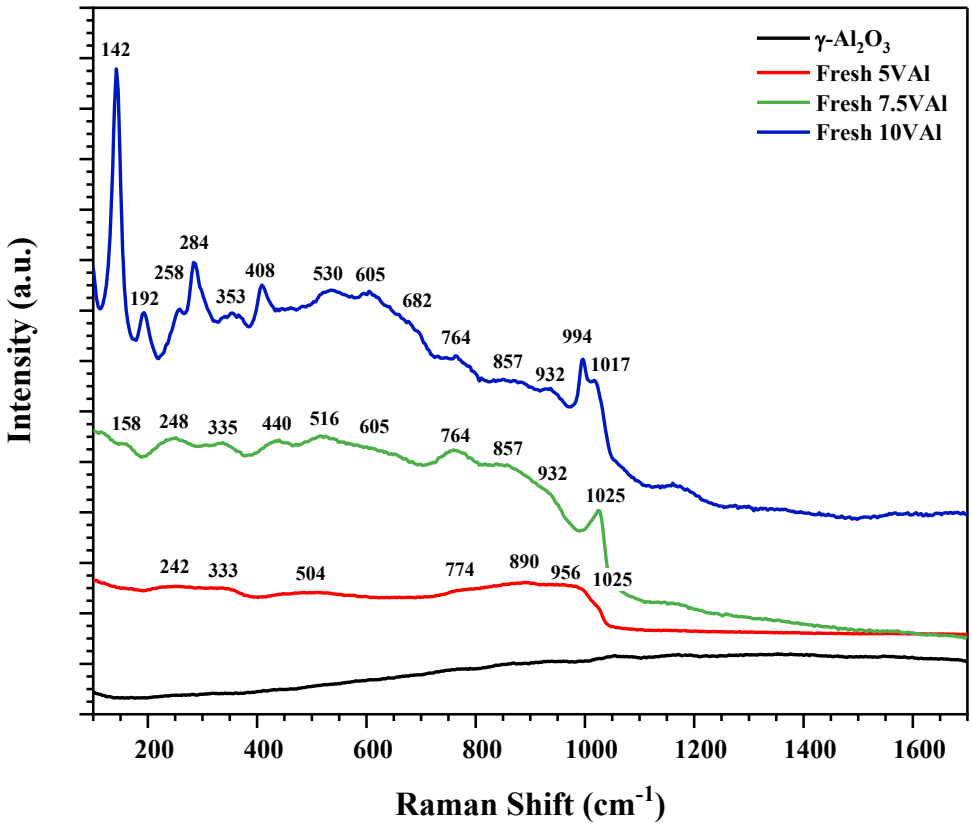

Figure 23: Raman spectra of γ-Al_2O_3 and fresh VAl catalysts

Pre-reaction Raman reveals that the γ-Al_2O_3 support does not exhibit any Raman features in the 100-1700 cm^{-1} region. Therefore, all Raman bands present in the spectra of fresh VAl catalysts are assigned to vanadium oxide vibrations. A notable difference is observed between the spectra of fresh VAl catalysts, which suggests that the structure of vanadia species is strongly influenced by the vanadium loading.

Raman spectra obtained for both fresh 5 and 7.5VAl catalysts display a band at ~1025 cm^{-1} which corresponds to the symmetric vibration of terminal mono-oxo vanadyl (V=O) bond in monovanadate VO_4 species. In the spectra obtained for the fresh 10VAl catalyst, this band shifts to ~1017 cm^{-1}, which corresponds to the same symmetric vibration of the V=O bond, this time for polyvanadate species. [95] As such, this shift from 1025 to 1017 cm^{-1} suggests an increase in polymerisation as the loading increases to 10 V wt.%.

Raman features at ~994, 682, 408, 284, 258, 192 and 142 cm^{-1} are also observed in the spectrum of fresh 10VAl which are characteristic of crystalline V_2O_5 species. [31, 96]

Lastly, there are features which indicate the presence of polyvanadate species in the Raman spectra of all fresh VAl catalysts with broad bands in the region of ~200-400, ~400-600 and ~600-956 cm^{-1}. These have previously been assigned in literature as the bending modes, symmetric and asymmetric stretching vibrations found in polymeric V-O-V linkages, respectively. [31, 45, 51, 97, 98]

4.1.6 XRD

XRD patterns obtained for the alumina support and fresh VAl catalyst samples are shown in Figure 24. The diffraction patterns are noisy, exhibiting broad peaks at 2θ = 37.1, 46.0 and 66.7° exclusive to the amorphous γ-Al_2O_3 support. The lack of sharp and intense crystalline diffraction peaks indicates that the vanadia species present in fresh VAl samples are highly dispersed on the support and do not exhibit any long-range ordering.

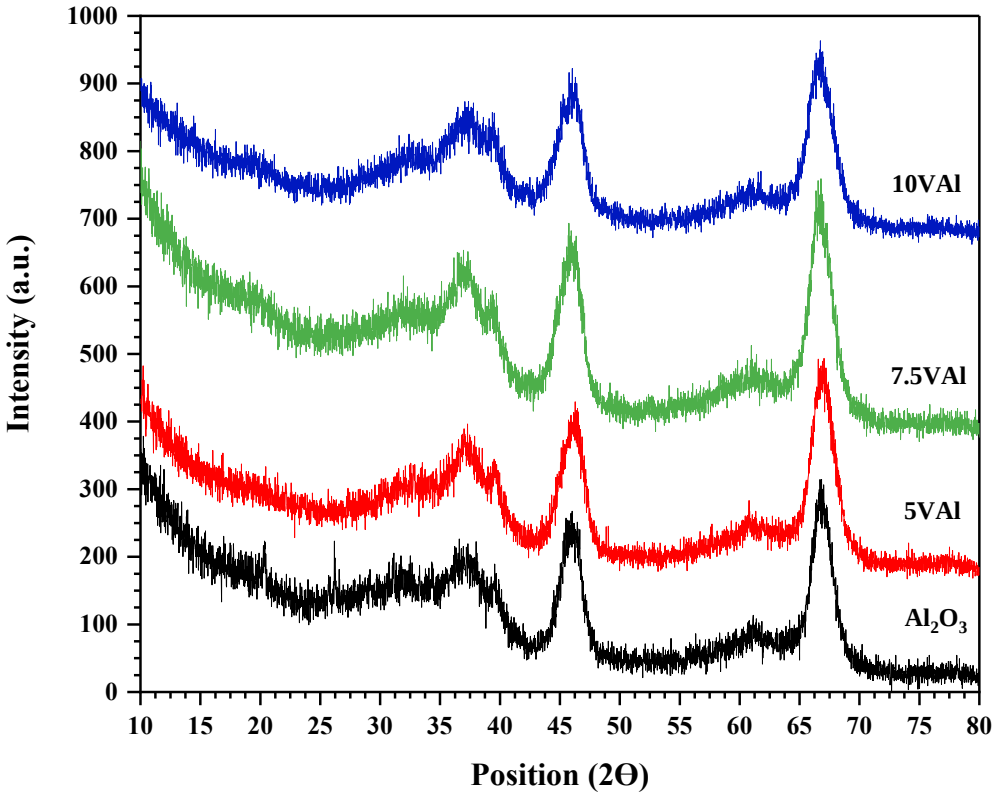

Figure 24: XRD patterns of γ-Al_2O_3 and fresh VAl catalysts

4.2 Thermodynamic Analysis

Thermodynamic analysis was conducted to investigate the feasibility of chemical reactions which may occur within CL-PODH cycling tests performed over vanadium oxide catalysts. The second law of thermodynamics principally determines the spontaneity of a reaction and whether it will proceed preferentially in the forward or reverse direction. The law is mathematically expressed in Equations 18 and 19 and is based around the entropy of a system.

Equation 18: The Second Law of Thermodynamics

$$\Delta S = \frac{\Delta Q}{T}$$

Equation 19: The Second Law of Thermodynamics

$$\Delta S_{universe} = \Delta S_{system} + \Delta S_{surroundings}$$

Where ΔS is the change in entropy, ΔQ is the heat transferred within the system and T is the temperature.

At constant temperature and pressure, Equation 18 can be rearranged to define a new thermodynamic quantity known as the Gibbs free energy, mathematically expressed in Equation 20.

Equation 20: Gibbs Free Energy

$$\Delta G = \Delta H - T\Delta S$$

Where ΔG is the change in Gibbs free energy, ΔH is the change in enthalpy, T is the temperature and ΔS is the change in entropy.

The change in Gibbs free energy of a chemical reaction can be quantified by subtracting the Gibbs free energy of the reactants from the products, where the sign of the resulting value relates to reaction spontaneity as follows:

- When $\Delta G > 0$, the process is not spontaneous in the forward direction and will proceed reversibly to form more reactants.

- When $\Delta G = 0$, the system is in equilibrium where the concentration of reactants and products are constant.

- When $\Delta G < 0$, the process is spontaneous in the forward direction and will favour the formation of products.

The basic thermodynamic data of reactants and products, V_2O_5, V_2O_4, V_2O_3, CO, CO_2, graphitic carbon, propane, propene, ethane, ethene, methane, H_2O, H_2, O_2 and N_2O were obtained. [99-102] and used to calculate the change in Gibbs free energy of chemical reactions which proceed in PDH and catalyst regeneration steps including any possible side reactions that may occur. The resulting Gibbs free energies of each reaction were plotted as a function of temperature, where a negative value indicates that the reaction is spontaneous and therefore thermodynamically feasible.

4.2.1 Propane Dehydrogenation Step

The chemical equations of reactions which may proceed during the PDH step are listed in Table 13. Reactions (1-6) are the stoichiometric equations of propane oxidising to propene, CO, CO_2 and H_2O by utilising the lattice oxygen sites within the vanadium oxide catalyst. Reactions (7-10) are the equations of the desired propene product re-adsorbing onto lattice oxygen sites and combusting to CO, CO_2 and H_2O.

Table 13: Chemical equations for reactions occurring during the PDH step of CL-PODH redox cycles utilising VAl catalysts

Reaction	Chemical Equation	Reaction No.
PDH over V_2O_5 and V_2O_4 sites	$C_3H_8\,(g) + V_2O_5\,(s) \rightarrow V_2O_4\,(s) + C_3H_6\,(g) + H_2O\,(g)$	(1)
	$C_3H_8\,(g) + 10V_2O_5\,(s) \rightarrow 10V_2O_4\,(s) + 3CO_2\,(g) + 4H_2O\,(g)$	(2)
	$C_3H_8\,(g) + 7V_2O_5\,(s) \rightarrow 7V_2O_4\,(s) + 3CO\,(g) + 4H_2O\,(g)$	(3)
	$C_3H_8\,(g) + V_2O_4\,(s) \rightarrow V_2O_3\,(s) + C_3H_6\,(g) + H_2O\,(g)$	(4)
	$C_3H_8\,(g) + 10V_2O_4\,(s) \rightarrow 10V_2O_3\,(s) + 3CO_2\,(g) + 4H_2O\,(g)$	(5)
	$C_3H_8\,(g) + 7V_2O_4\,(s) \rightarrow 7V_2O_3\,(s) + 3CO\,(g) + 4H_2O\,(g)$	(6)
	$C_3H_6\,(g) + 9V_2O_5\,(s) \rightarrow 9V_2O_4\,(s) + 3CO_2\,(g) + 3H_2O\,(g)$	(7)
	$C_3H_6\,(g) + 6V_2O_5\,(s) \rightarrow 6V_2O_4\,(s) + 3CO\,(g) + 3H_2O\,(g)$	(8)
	$C_3H_6\,(g) + 9V_2O_4\,(s) \rightarrow 9V_2O_3\,(s) + 3CO_2\,(g) + 3H_2O\,(g)$	(9)
	$C_3H_6\,(g) + 6V_2O_4\,(s) \rightarrow 6V_2O_3\,(s) + 3CO\,(g) + 3H_2O\,(g)$	(10)

Gibbs free energy plots of reactions (1-10) are displayed in Figures 25 and 26. Overall, the oxidation of both propane (Fig. 7) and propene (Fig. 8) utilising V_2O_5 and resulting V_2O_4 sites display negative values at 773 K and are therefore spontaneous and thermodynamically feasible at our reaction conditions. Ultimately, however, the production of CO and CO_2 during the oxidation of propane display lower Gibbs free energies than the production of the desired product propene and water and are consequently more favourable.

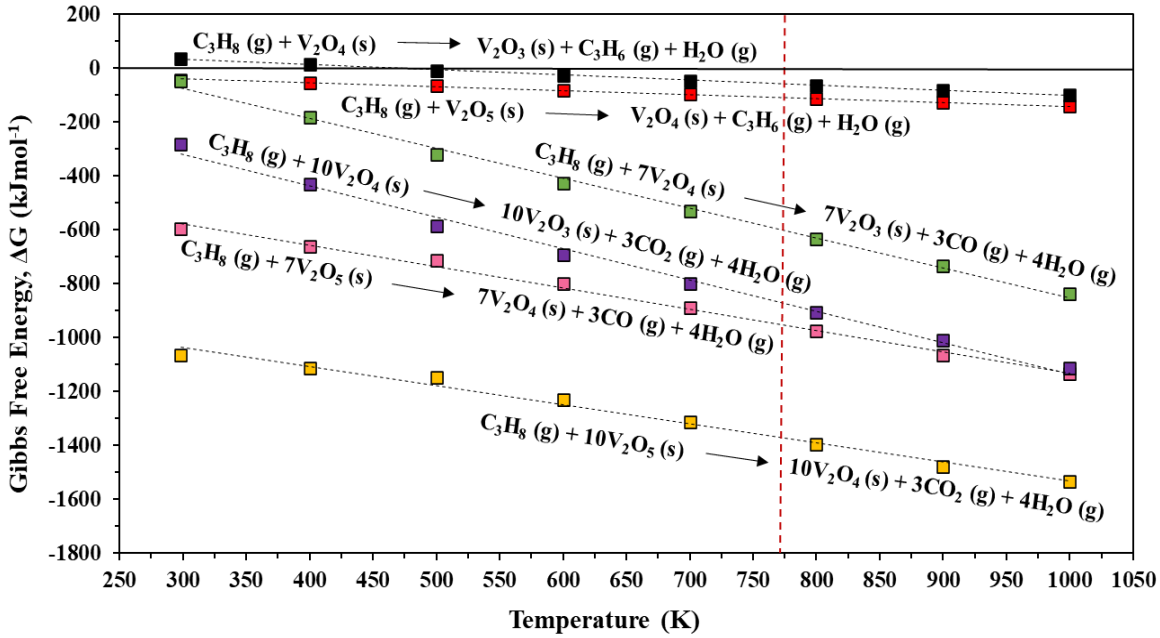

Figure 25: Gibbs free energies of reactions (1-6) plotted as a function of temperature

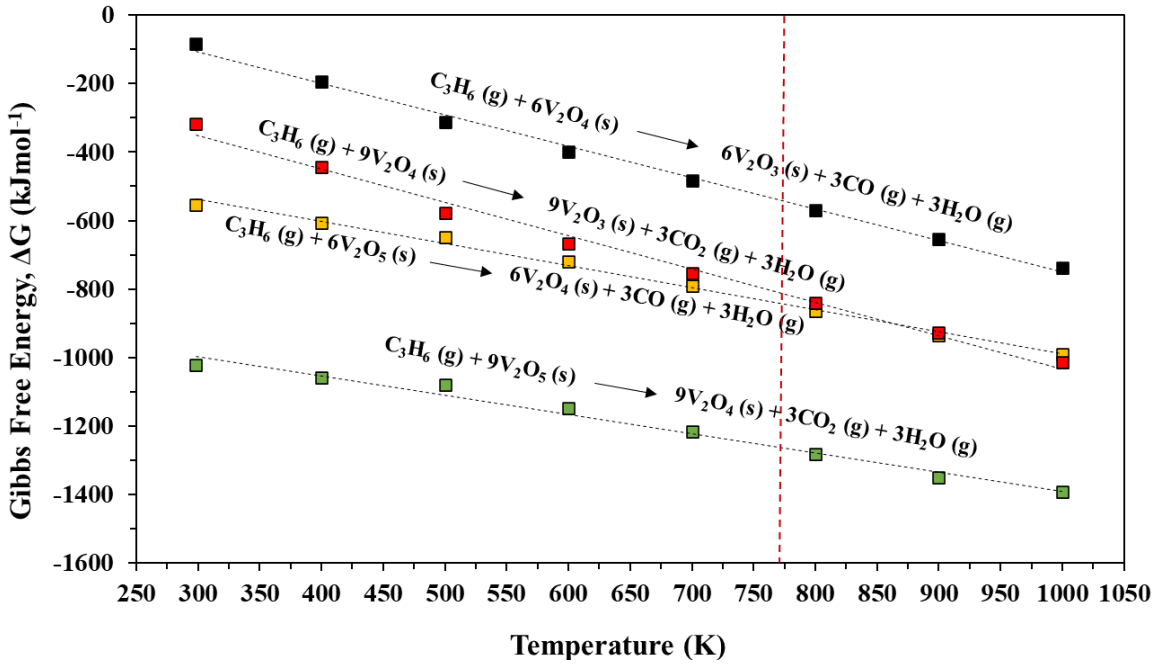

Figure 26: Gibbs free energies of reactions (7-10) plotted as a function of temperature

4.2.2 Regeneration Step

The reactions which may occur during the catalyst regeneration step using O_2, N_2O and CO_2 oxidants are tabulated in Table 14. Reactions (11) and (12) are the stoichiometric equations relating to the reoxidation of resulting V_2O_3 and V_2O_4 sites utilising O_2 as the oxidant. Reactions (13-16) are those regenerated with N_2O and CO_2 oxidants.

Table 14: Chemical equations for reactions occurring during the regeneration step of CL-PODH redox cycles utilising VAl catalysts

Reaction	Chemical Equation	Reaction No.
Catalyst Regeneration (Oxidant – O_2)	$2V_2O_4\,(s) + O_2\,(g) \rightarrow 2V_2O_5\,(s)$	(11)
	$2V_2O_3\,(s) + O_2\,(g) \rightarrow 2V_2O_4\,(s)$	(12)
Catalyst Regeneration (Oxidant – N_2O)	$V_2O_4\,(s) + N_2O\,(g) \rightarrow V_2O_5\,(s) + N_2\,(g)$	(13)
	$V_2O_3\,(s) + N_2O\,(g) \rightarrow V_2O_4\,(s) + N_2\,(g)$	(14)
Catalyst Regeneration (Oxidant – CO_2)	$V_2O_4\,(s) + CO_2\,(g) \rightarrow V_2O_5\,(s) + CO\,(g)$	(15)
	$V_2O_3\,(s) + CO_2\,(g) \rightarrow V_2O_4\,(s) + CO\,(g)$	(16)

The Gibbs free energy plot of reactions (11-16) is displayed in Figure 27. Overall, the reoxidation of resulting V_2O_4 and V_2O_3 sites with O_2 and N_2O oxidants display negative Gibbs free energy values at 773 K. On the other hand, the reoxidation with CO_2 displays large positive values, indicating that the reactions are not thermodynamically feasible and will occur in the reverse direction. The non-spontaneity of CO_2 re-oxidising the resulting V_2O_3 and V_2O_4 sites is attributed to the inherent inertness of the CO_2 molecule which comprises a large Gibbs energy of formation of -395 kJ mol^{-1}.

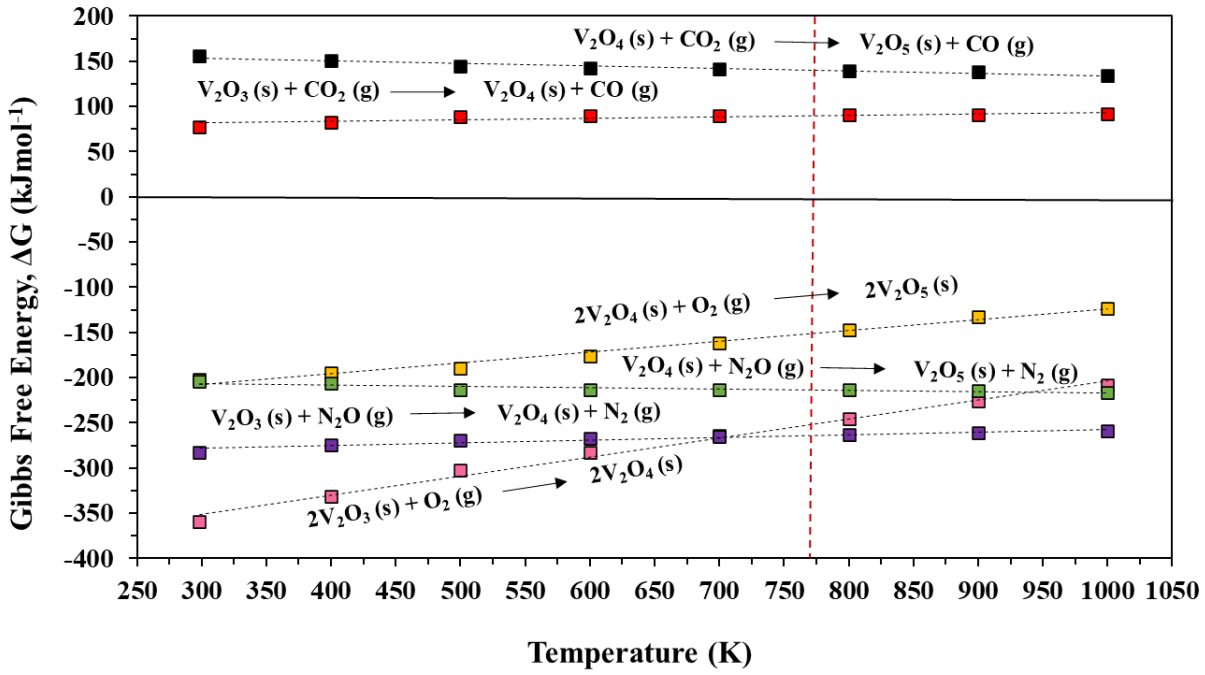

Figure 27: Gibbs free energies of reactions (11-16) plotted as a function of temperature

4.2.3 Direct PDH & Side Reactions

In addition to the reactions already discussed, a number of side reactions may proceed during the PDH step of CL-PODH redox cycles. The stoichiometric equations of these reactions are tabulated in Table 15 and include the direct dehydrogenation of propane (17), cracking reactions (18-23), dry/steam reforming reactions (24-28) and the reverse water gas shift (RWGS) reaction (29).

Table 15: Chemical equations for side reactions which may occur during the PDH step of CL-PODH redox cycles

Reaction	Chemical Equation	Reaction No.
Direct PDH & Side Reactions	$C_3H_8\,(g) \rightleftharpoons C_3H_6\,(g) + H_2\,(g)$	(17)
	$C_3H_8\,(g) \rightarrow CH_4\,(g) + C_2H_4\,(g)$	(18)
	$C_2H_4\,(g) + H_2\,(g) \rightleftharpoons C_2H_6\,(g)$	(19)
	$C_3H_8\,(g) \rightarrow C\,(s) + 2CH_4\,(g)$	(20)
	$C_3H_8\,(g) \rightarrow 3C\,(s) + 4H_2\,(g)$	(21)
	$C_2H_6\,(g) \rightarrow 2C\,(s) + 3H_2\,(g)$	(22)
	$CH_4\,(g) \rightarrow C\,(s) + 2H_2\,(g)$	(23)
	$CH_4\,(g) + H_2O\,(g) \rightarrow CO\,(g) + 3H_2\,(g)$	(24)
	$CH_4\,(g) + 2H_2O\,(g) \rightarrow CO_2\,(g) + 4H_2\,(g)$	(25)
	$C_2H_6\,(g) + 2H_2O\,(g) \rightarrow 2CO\,(g) + 5H_2\,(g)$	(26)
	$CH_4\,(g) + CO_2\,(g) \rightleftharpoons 2CO\,(g) + 2H_2\,(g)$	(27)
	$C_2H_6\,(g) + 2CO_2\,(g) \rightarrow 4CO\,(g) + 3H_2\,(g)$	(28)
	$CO_2\,(g) + H_2\,(g) \rightleftharpoons CO\,(g) + H_2O\,(g)$	(29)

The Gibbs free energy plot of reactions (17-23) is presented in Figure 28.

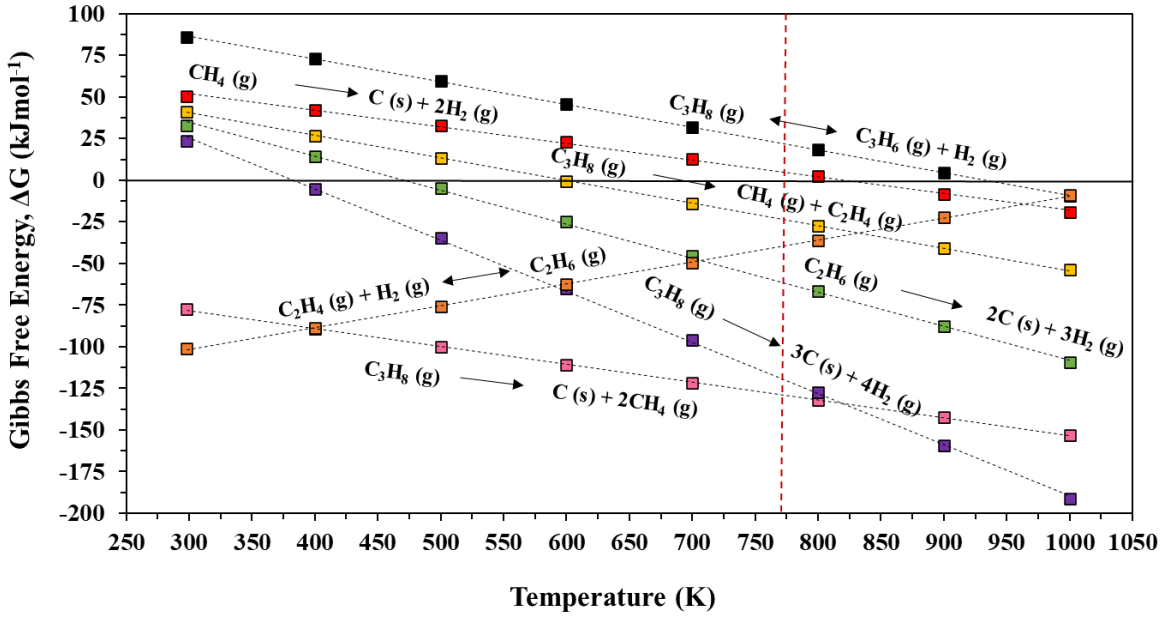

Figure 28: Gibbs free energies of reactions (17-23) plotted as a function of temperature

The direct dehydrogenation of propane (PDH) displays a positive value at 773 K in the Gibbs free energy plot and is therefore described as not spontaneous. However, the Gibbs free energy value of the PDH reaction remains small enough (<50 kJ mol^{-1}) that equilibrium and kinetic factors may come into effect, whereby propene formation occurs despite the reaction being thermodynamically non-spontaneous.

Reaction (18) details the cracking reaction of propane to both methane and ethene products and reaction (19) is the subsequent hydrogenation of the ethene product. At 773 K, both reactions possess negative Gibbs free energy values and are therefore thermodynamically feasible. Lastly, reactions (20-23) involve the formation of coke from propane, ethane and methane. At 773 K, coke formation from both propane and ethane reactants are thermodynamically feasible and are highly favourable reactions since they exhibit the lowest Gibbs free energies out of the possible competing side reactions listed.

The Gibbs free energy plot of reactions (24-29) is presented in Figure 29.

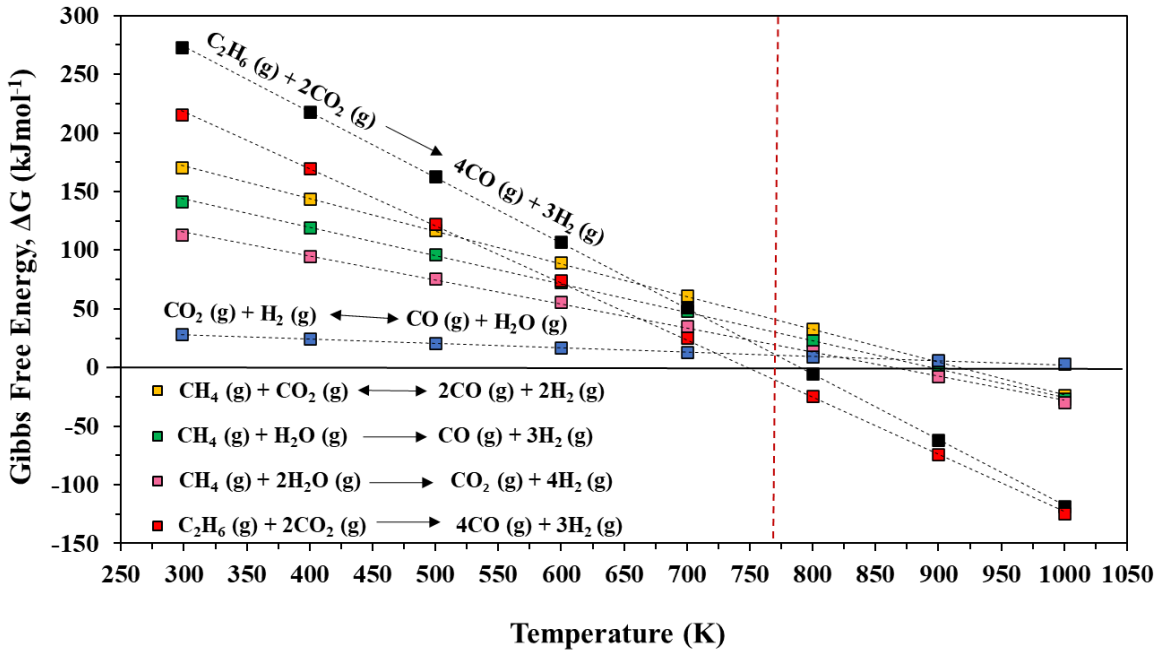

Figure 29: Gibbs free energies of reactions (24-29) plotted as a function of temperature

Reactions (24-26) relate to the steam reforming of methane (SRM) and ethane (SRE), which exhibit positive Gibbs free energies at 773 K and are therefore non-spontaneous reactions. Reactions (27) and (28) relate to the dry reforming of methane (DRM) and ethane (DRE) and whilst DRM displays a positive Gibbs free energy at 773 K, DRE exhibits a negative value and is thermodynamically feasible at these temperature conditions. Lastly, reaction (29) represents the RWGS reaction where carbon dioxide reacts with hydrogen to form carbon monoxide and water. Figure 29 shows that the RWGS reaction displays a positive Gibbs free energy value at 773 K. This value decreases progressively towards zero as the temperature increases, suggesting that RWGS will become thermodynamically feasible at temperatures exceeding 1000 K.

4.2.4 Removal of Carbon Laydown

Since coke formation during CL-PODH redox cycles is thermodynamically feasible, it was also of interest to investigate the feasibility of its removal via the lattice oxygen sites of V_2O_5, and V_2O_4 species and O_2, N_2O and CO_2 oxidants. The chemical equations of such reactions are presented in Table 16 where reactions (30-32) relate to the combustion of carbon using the catalyst lattice oxygen sites and reactions (33-35) relate to the combustion with O_2, N_2O and CO_2 oxidants used in the catalyst regeneration step.

Table 16: Chemical equations for reactions relating to the removal of carbon laydown

Reaction	Chemical Equation	Reaction No.
Removal of carbon laydown	$C\,(s) + V_2O_5\,(s) \rightleftharpoons V_2O_4\,(s) + CO\,(g)$	(30)
	$C\,(s) + V_2O_5\,(s) \rightleftharpoons V_2O_3\,(s) + CO_2\,(g)$	(31)
	$C\,(s) + V_2O_4\,(s) \rightleftharpoons V_2O_3\,(s) + CO\,(g)$	(32)
	$C\,(s) + O_2\,(g) \rightleftharpoons CO_2\,(g)$	(33)
	$C\,(s) + N_2O\,(g) \rightleftharpoons CO\,(g) + N_2\,(g)$	(34)
	$C\,(s) + CO_2\,(g) \rightleftharpoons 2CO\,(g)$	(35)

The Gibbs free energy plot of reactions (30-35) is displayed in Figure 30. At 773 K, the combustion of carbonaceous deposits with V_2O_5, V_2O_4 and V_2O_3 species display negative Gibbs free energy values. The removal of coke with O_2 and N_2O oxidants also display negative values whilst the reaction using CO_2 displays a positive Gibbs free energy, indicating that the removal with CO_2 is not thermodynamically feasible.

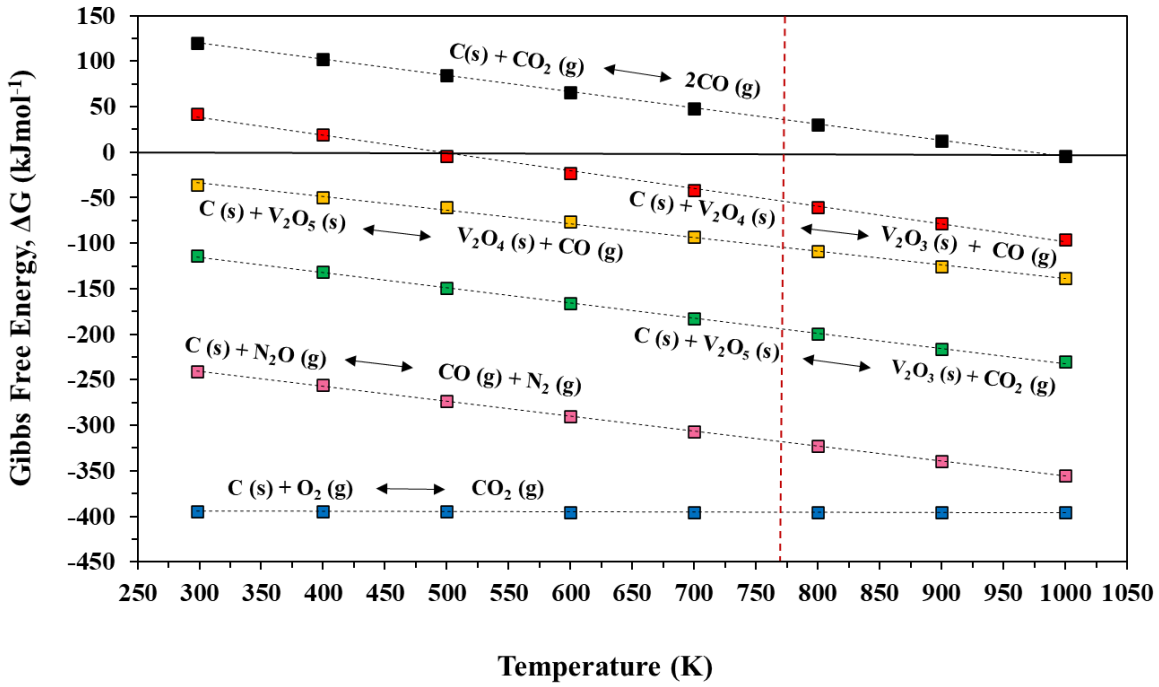

Figure 30: Gibbs free energies of reactions (30-35) plotted as a function of temperature

4.3 Reactivity Tests

This section details the results obtained from CL-PODH redox cycling tests using the fresh 5, 7.5 and 10VAl catalysts and O_2, N_2O and CO_2 oxidants as described in Section 3.3.3.

4.3.1 CL-PODH Redox Cycles with O_2

Results from CL-PODH redox cycling tests performed over the fresh 5, 7.5 and 10VAl catalysts using O_2 as the oxidant in the regeneration step are presented here. Reaction profiles detailing propane conversions and propene selectivities and yields are shown in Figures 31-33, which compare the catalyst activity and selectivity to the olefin product as a function of vanadium loading. The selectivity and resulting yield to the undesired CO_2 product has also been investigated and are presented in Figures 34 and 35.

It should be noted that the data presented is the instantaneous performance obtained at the end of the 30 min PDH step of each corresponding redox cycle.

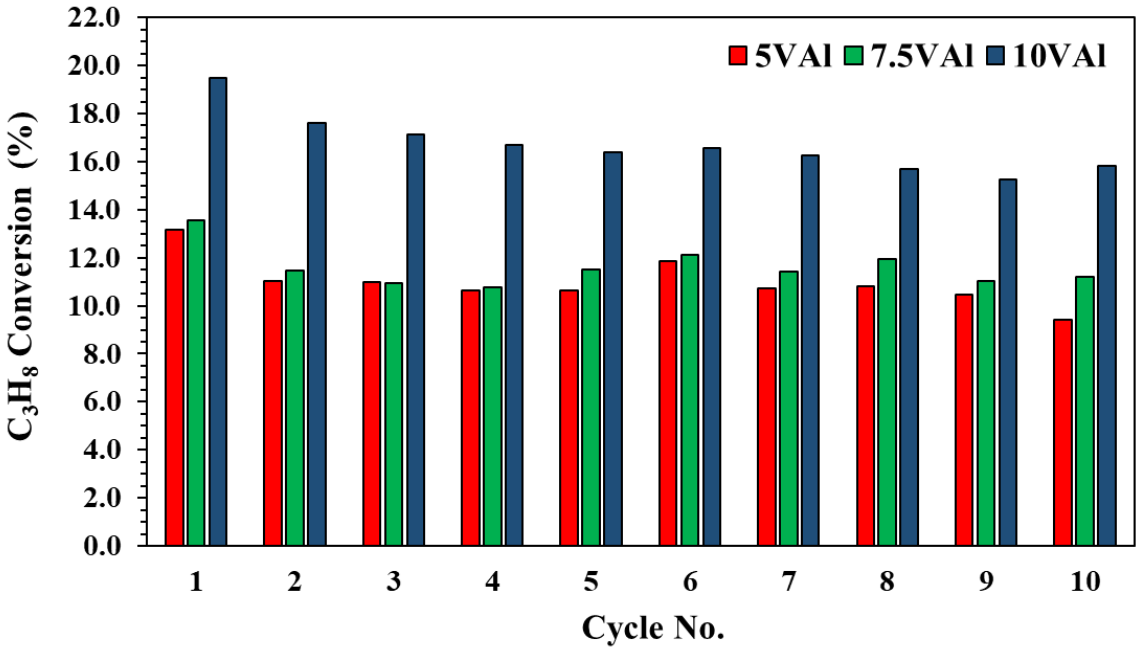

Figure 31: Instantaneous C_3H_8 conversions using 5, 7.5 and 10VAl catalysts, O_2 oxidant, 773 K, 1 atm

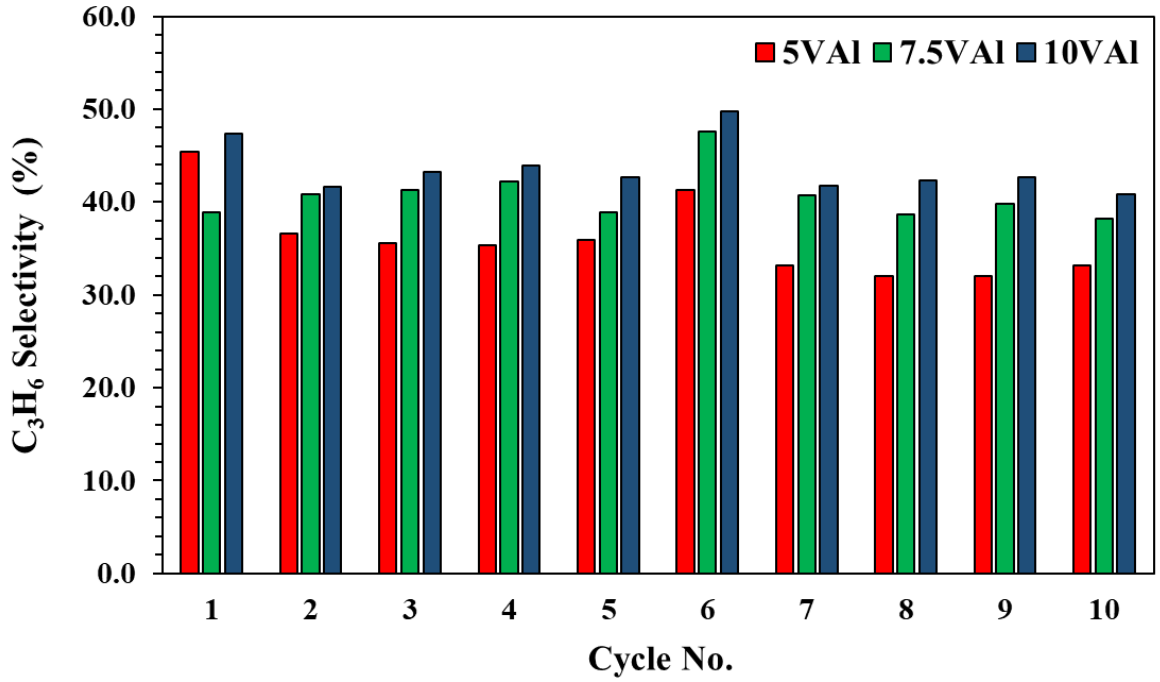

Figure 32: Instantaneous C_3H_6 selectivities using 5, 7.5 and 10VAl catalysts, O_2 oxidant, 773 K, 1 atm

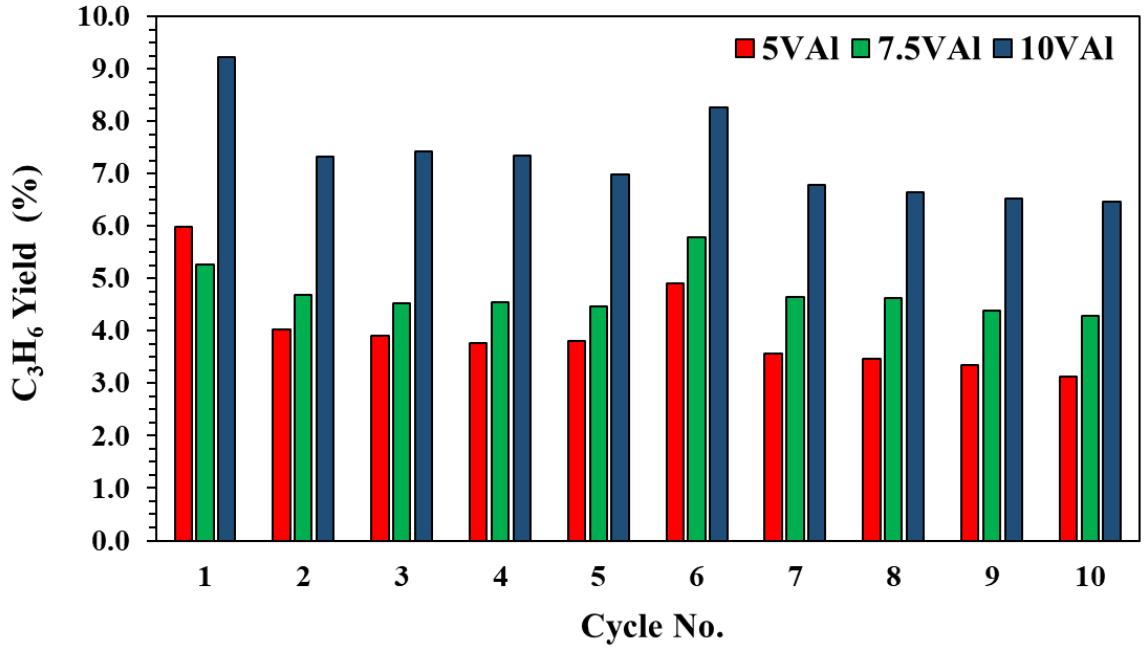

Figure 33: Instantaneous C_3H_6 yields obtained using 5, 7.5 and 10VAl catalysts, O_2 oxidant, 773 K, 1 atm

It is evident from Figures 31-33 that CL-PODH redox cycling tests performed over the 10VAl catalyst generate the most promising results in this series.

Propane conversions in tests using the 5 and 7.5VAl catalyst reached ~13.2 and 13.6 % at the end of the 1st PDH step, which decreased significantly to ~11.0 % during the PDH step of cycles 2 to 5. Both catalysts demonstrated a slight enhancement in activity during the PDH step of cycle 6, which is performed after holding the catalyst overnight under argon, before decreasing again during the PDH step of cycles 7 to 10. When utilising the 10VAl catalyst, propane conversion reached ~19.5 % at the end of the 1st PDH step. Notable catalyst deactivation is observed during the PDH step of subsequent cycles, with conversions reaching ~15.8 % in the PDH step of cycle 10.

Furthermore, propene selectivity reaches ~47.4 % by the end of the 1st PDH step when using the 10VAl catalyst. A subsequent decay is observed during the PDH step of cycle 2, resulting in a decrease in propene yield from ~9.2 to ~7.3 %. Propene selectivities and yields remain comparable in cycles 2 to 5 with an enhancement again observed in the PDH step of cycle 6. Both propene selectivity and yield decrease during the PDH step of cycle 7 before remaining relatively stable during subsequent cycles. A similar trend is observed in the tests using the 5 and 7.5VAl catalyst, indicating that vanadium oxide catalysts are relatively stable for propene production with no significant deactivation as CL-PODH redox cycles proceed.

Figures 34 and 35 present CO_2 selectivities and resulting yields obtained at the end of each 30 min PDH step. Notably, the instantaneous production of the undesired CO_2 product at the end of each PDH step is significantly lower in comparison to propene formation.

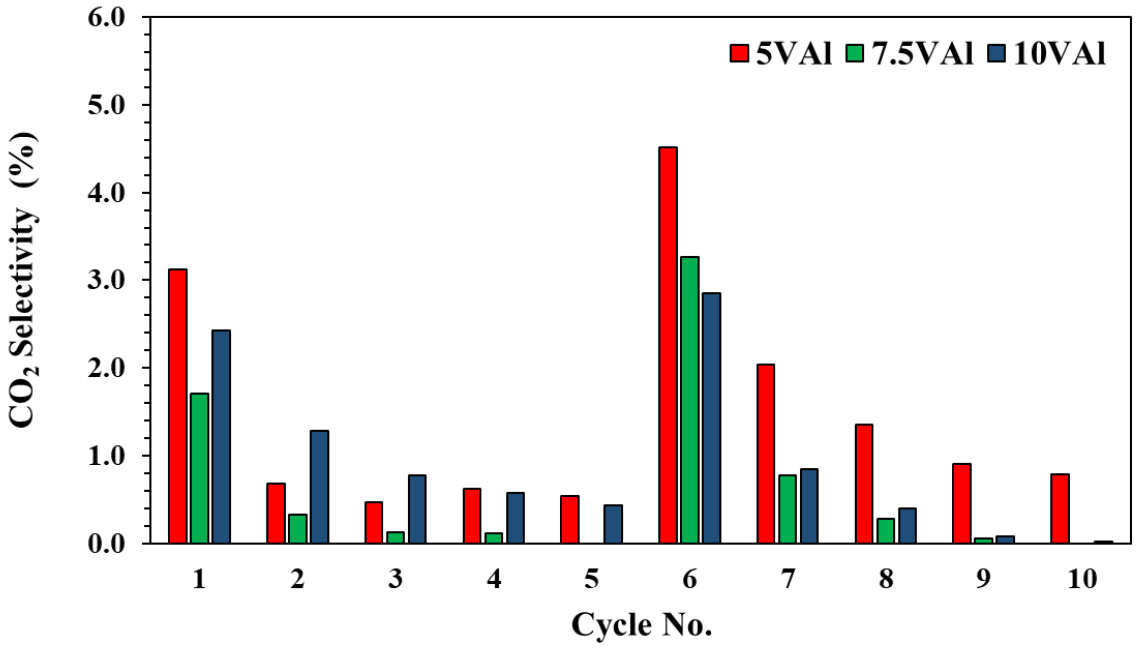

Figure 34: Instantaneous CO_2 selectivities obtained using 5, 7.5 and 10VAl catalysts, 773 K, 1 atm

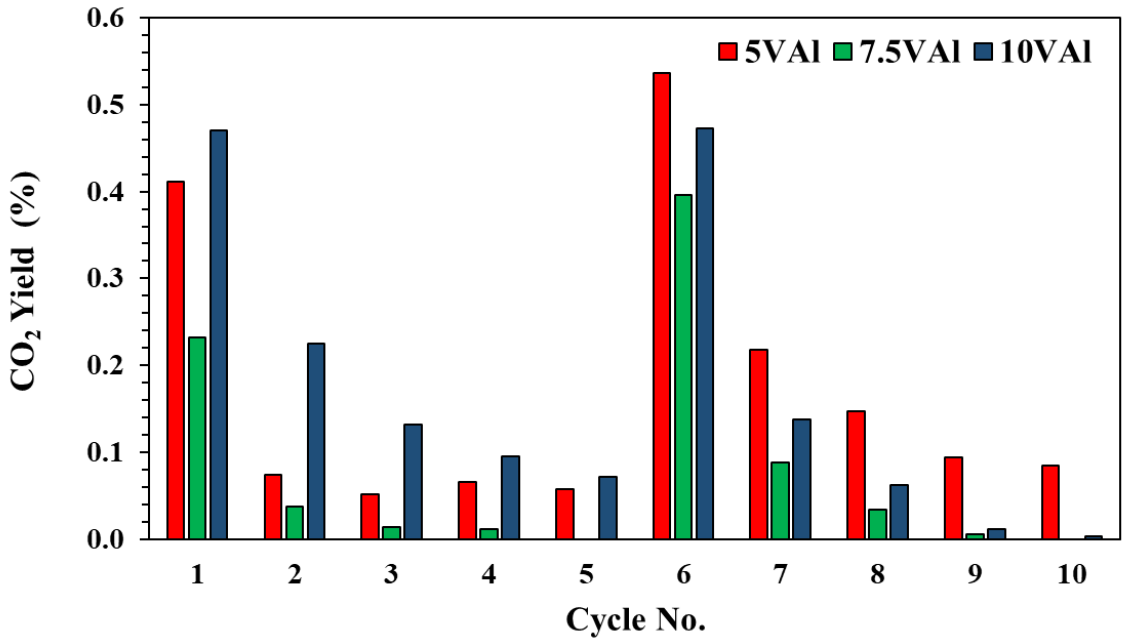

Figure 35: Instantaneous CO_2 yields obtained using 5, 7.5 and 10VAl catalysts, 773 K, 1 atm

It is apparent that initial CO_2 yields are highest in the test performed over the 10VAl catalyst. During this reaction, CO_2 yields progressively decrease throughout cycles 2 to 5. An enhancement is observed again in the PDH step of cycle 6 before they diminish as the cycles proceed.

The 5VAl catalyst exhibits a higher selectivity to CO_2 in comparison to the 7.5VAl catalyst, which results in higher CO_2 yields despite the increased activity of the 7.5VAl catalyst. Furthermore, the trend in CO_2 selectivity and yield obtained by the 5 and 7.5VAl catalysts are similar to those achieved when using the 10VAl catalyst. Both the selectivity and resulting yield decrease as the cycles proceed, with the exception to the data obtained during the PDH step of cycle 6 where an improvement is observed.

Reaction profiles detailing the data obtained from the entire 30 min PDH step over the 10VAl catalyst are presented in Figures 36-38. Since the PDH step of cycles 2 to 5 are relatively comparable, the data presented is exclusively from the PDH step of cycle 1 versus cycle 2. Figures 36 and 37 are propane conversion, propene and CO_2 selectivity plots and Figure 38 presents the resulting propene and CO_2 yield.

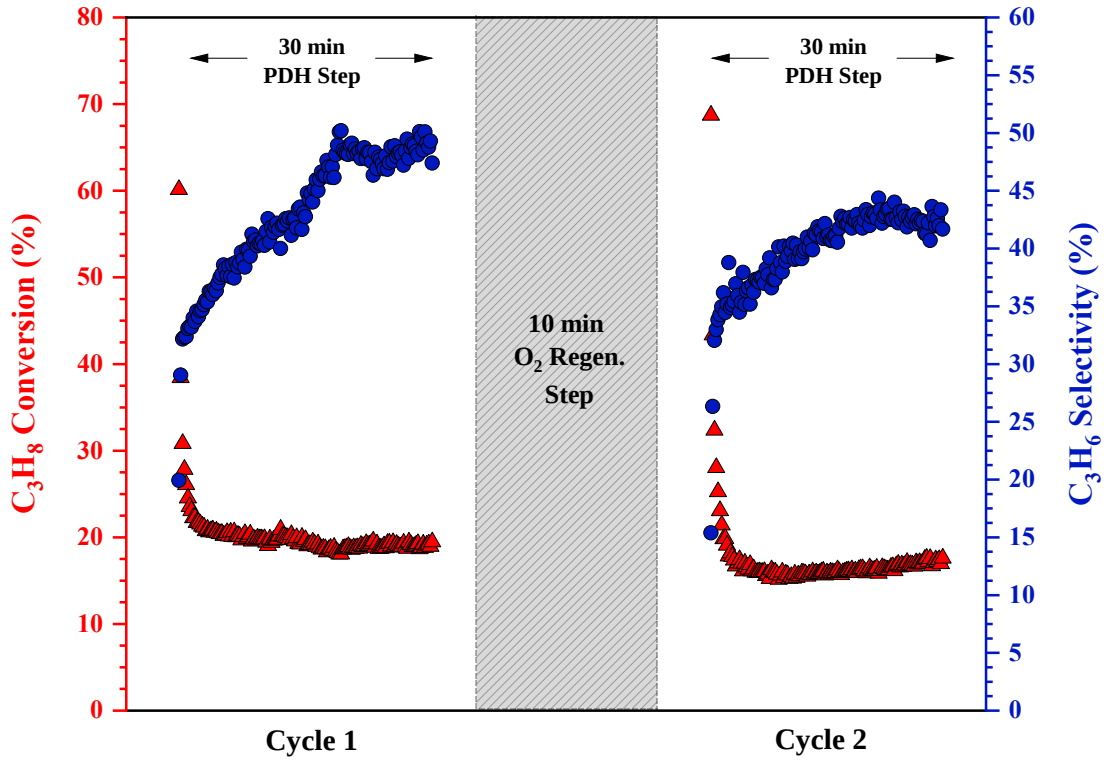

Figure 36: Reaction profile of C_3H_8 conversion and C_3H_6 selectivity during the PDH step of cycle 1 versus cycle 2: 10VAl, O_2 oxidant, 773 K, 1 atm

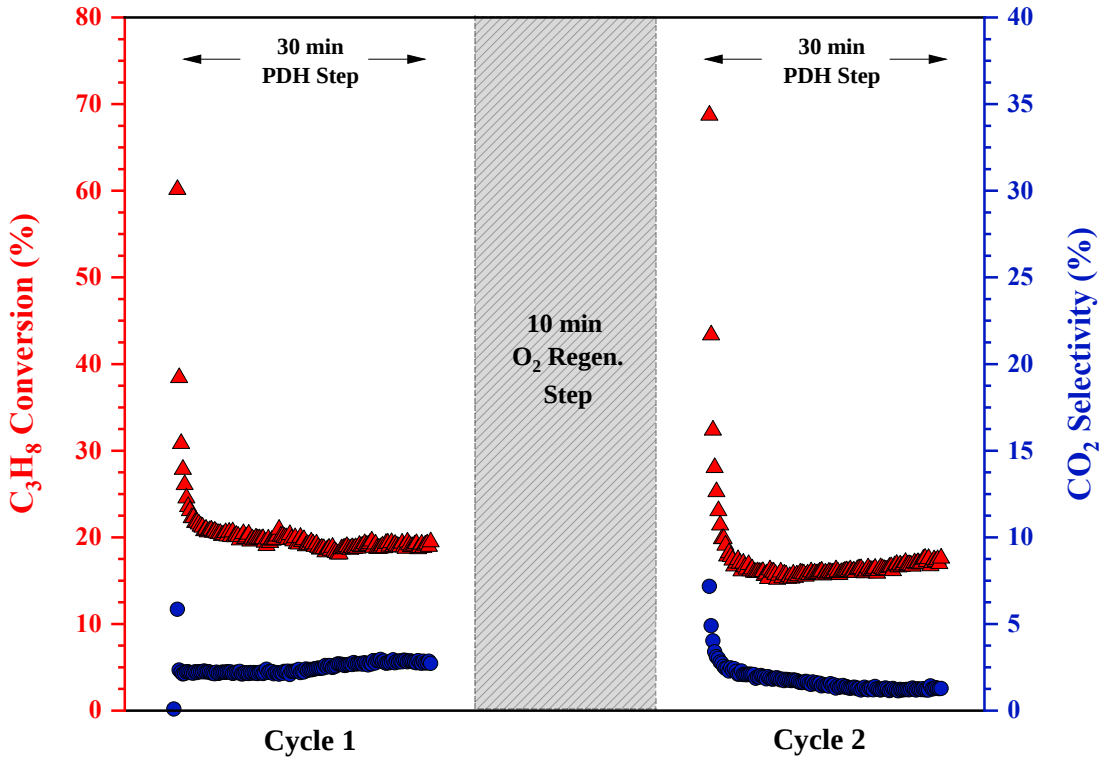

Figure 37: Reaction profile of C_3H_8 conversion and CO_2 selectivity during the PDH step of cycle 1 versus cycle 2: 10VAl, O_2 oxidant, 773 K, 1 atm

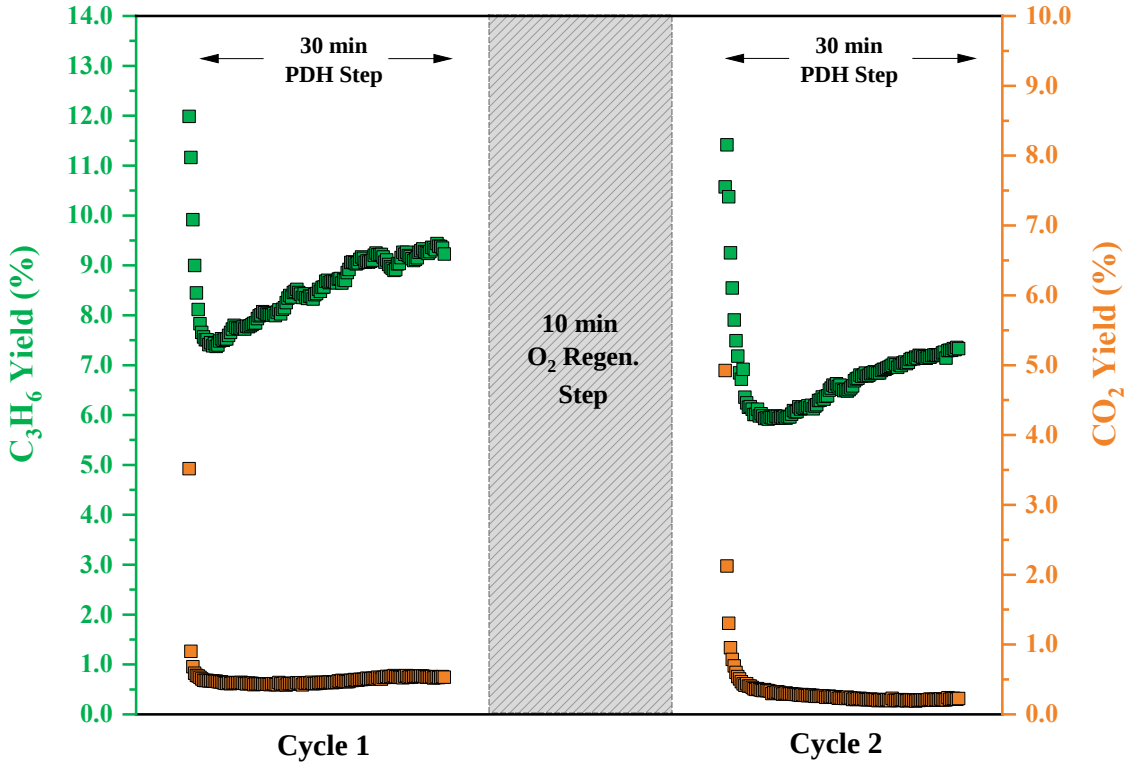

Figure 38: Reaction profile of C_3H_6 and CO_2 yields during the PDH step of cycle 1 versus cycle 2: 10VAl, O_2 oxidant, 773 K, 1 atm

Notably, a decrease in propene yield is observed in the PDH step of cycle 2, a result of the decay in propene selectivity from 47.4 to 41.7 % at similar propane conversions. Furthermore, it is apparent from the reaction profiles that different reactivity regions exist throughout the PDH step. In Figure 38, propene and CO_2 yields are maximised within the first ~1.5 min of switching on the propane feed in both cycles 1 and 2. Propene yields begin to decrease as the propane conversion drops off significantly until ~6.0 min into the PDH step. As the reaction proceeds beyond this point, propane conversions reach steady state, where propene yields rise and an increase in selectivity is observed. CO_2 yields also decrease, however, the selectivity to CO_2 remains low and, in contrast with propene, the resulting yield is not replenished.

Propane conversions, propene/CO_2 selectivities and the resulting propene/CO_2 yields achieved at these different regions in CL-PODH redox cycles 1 and 2 are summarised in Table 17 and Table 18.

Table 17: Summary of C_3H_8 conversions, C_3H_6 and CO_2 selectivities and yields obtained at the different reaction regions during the PDH step of cycle 1: 10VAl, O_2 oxidant, 773 K, 1 atm

Time into PDH Step (min)	C_3H_8 Conversion (%)	C_3H_6 Selectivity (%)	C_3H_6 Yield (%)	CO_2 Selectivity (%)	CO_2 Yield (%)
1.5	60.1	19.9	12.0	5.8	3.5
6	21.7	34.1	7.4	2.2	0.5
30	19.5	47.4	9.8	2.7	0.5

Table 18: Summary of C_3H_8 conversions and C_3H_6 and CO_2 selectivities and yields obtained at the different reaction regions during the PDH step of cycle 2: 10VAl, O_2 oxidant, 773 K, 1 atm

Time into PDH Step (min)	C_3H_8 Conversion (%)	C_3H_6 Selectivity (%)	C_3H_6 Yield (%)	CO_2 Selectivity (%)	CO_2 Yield (%)
1.5	68.7	16.5	11.4	7.1	4.9
6	16.4	36.2	5.9	2.0	0.3
30	17.6	41.7	7.3	1.3	0.2

An improvement in productivity is observed once again in the PDH step of cycle 6 after holding the catalysts overnight under a continuous flow of argon. To gain a better insight, reaction profiles detailing the data obtained from the entire 30 min PDH step of cycle 5 versus cycle 6 have been compared. Figures 39 and 40 show propane conversion, propene and CO_2 selectivity plots and Figure 41 shows resulting propene and CO_2 yields.

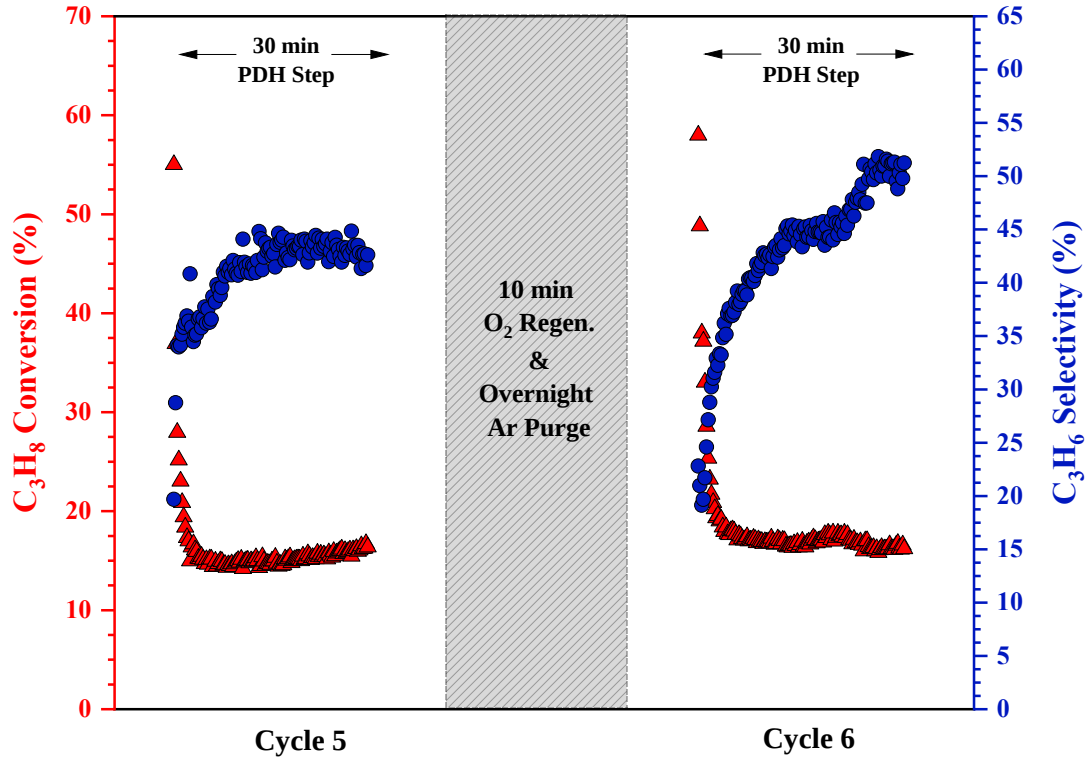

Figure 39: Reaction profile of C_3H_8 conversion and C_3H_6 selectivity during the PDH step of cycle 5 versus cycle 6: 10VAl, O_2 oxidant, 773 K, 1 atm

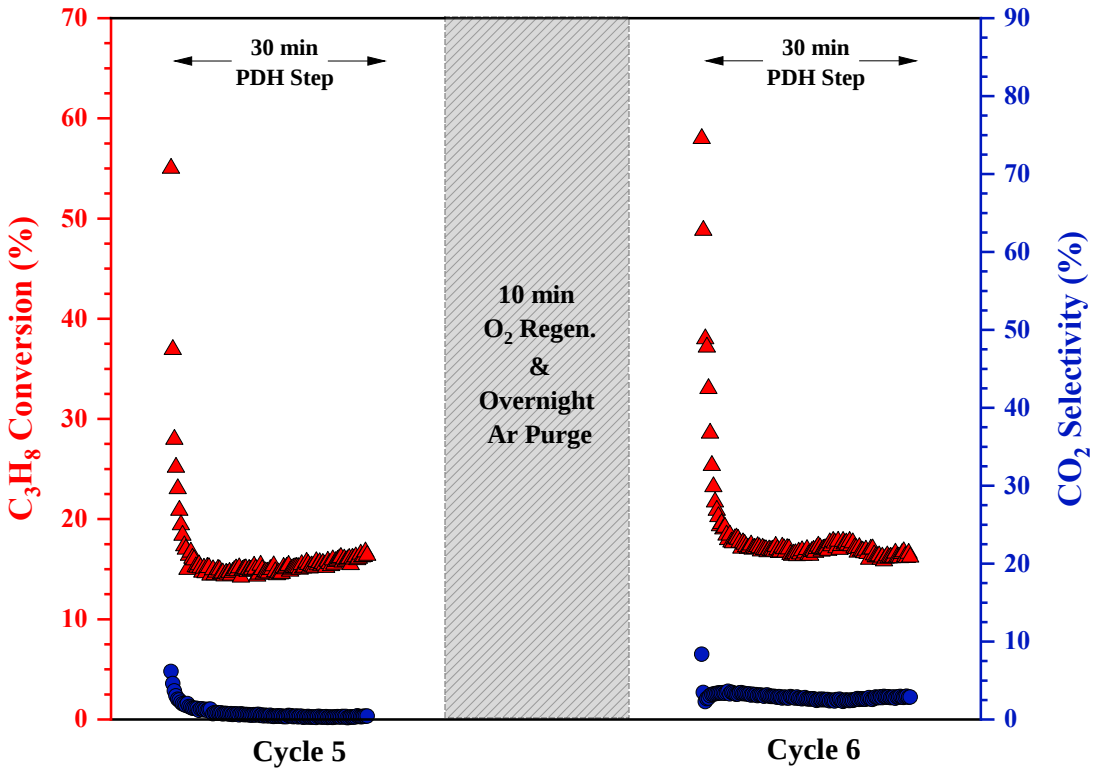

Figure 40: Reaction profile of C_3H_8 conversion and CO_2 selectivity during the PDH step of cycle 5 versus cycle 6: 10VAl, O_2 oxidant, 773 K, 1 atm

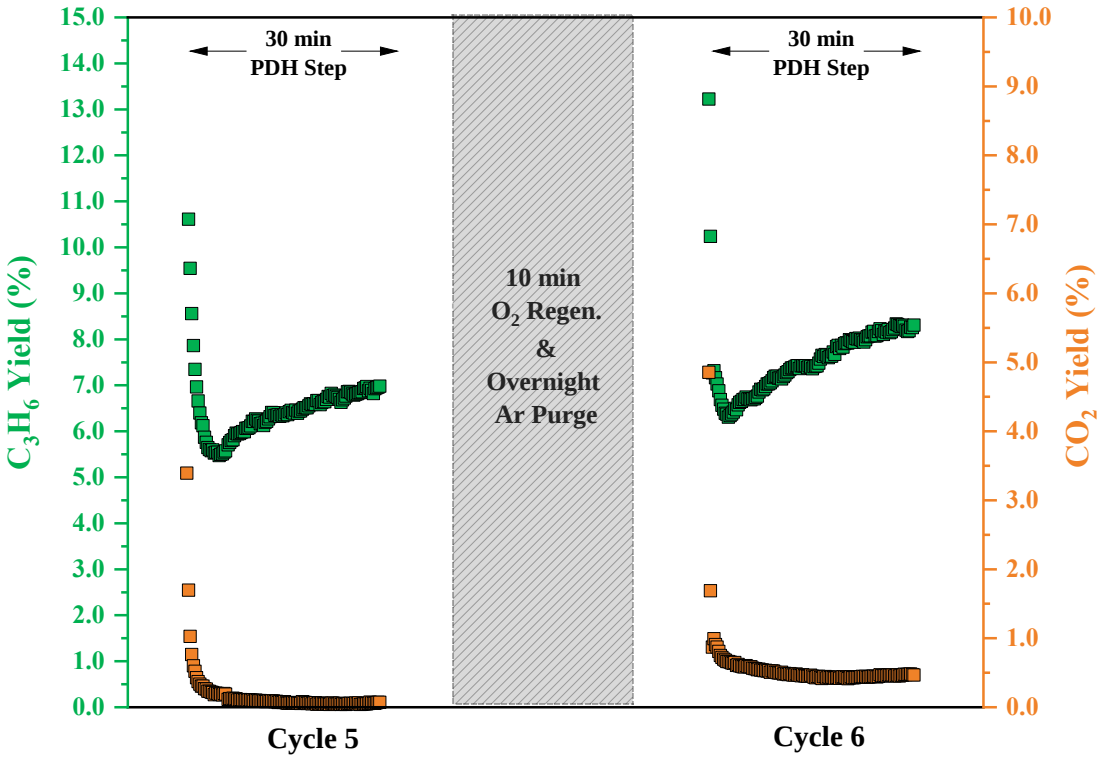

Figure 41: Reaction profile of C_3H_6 and CO_2 yields during the PDH step of cycle 5 versus cycle 6: 10VAl, O_2 oxidant, 773 K, 1 atm

A similar trend is observed in the PDH step of cycles 5 and 6 regarding the different reactivity regions throughout. Notably, the maximum propene and CO_2 yields achieved within the first ~1.5 min are highest in the PDH step of cycle 6. Propane conversions stabilise as the reaction proceeds and propene yields begin to increase resulting from an enhanced propene selectivity. Comparison of both cycles shows the selectivity to both propene and CO_2 is further enhanced in the PDH step of cycle 6. Ultimately, higher propene and CO_2 yields are achieved, increasing from ~7.0 and 0.1 % to ~8.3 and 0.5 %, respectively.

Propane conversions, propene/CO_2 selectivities and the resulting propene/CO_2 yields achieved at these different reactivity regions in CL-PODH redox cycles 5 and 6 are summarised in Table 19 and Table 20.

Table 19: Summary of C_3H_8 conversions and C_3H_6 and CO_2 selectivities and yields obtained at the different reaction regions during the PDH step of cycle 5: 10VAl, O_2 oxidant, 773 K, 1 atm

Time into PDH Step (min)	C_3H_8 Conversion (%)	C_3H_6 Selectivity (%)	C_3H_6 Yield (%)	CO_2 Selectivity (%)	CO_2 Yield (%)
1.5	55.0	19.7	10.8	6.1	3.4
6	15.1	36.2	5.5	1.2	0.2
30	16.4	42.6	7.0	0.4	0.1

Table 20: Summary of C_3H_8 conversions and C_3H_6 and CO_2 selectivities and yields obtained at the different reaction regions during the PDH step of cycle 6: 10VAl, O_2 oxidant, 773 K, 1 atm

Time into PDH Step (min)	C_3H_8 Conversion (%)	C_3H_6 Selectivity (%)	C_3H_6 Yield (%)	CO_2 Selectivity (%)	CO_2 Yield (%)
1.5	58.0	22.8	13.2	8.4	4.9
6	19.5	32.3	6.3	3.4	0.7
30	16.2	51.2	8.3	2.9	0.5

4.3.2 Long Duration PDH Test over the 10VAl Catalyst

The extent of catalyst deactivation with increasing time on stream (TOS) was investigated by performing a long duration 3 h PDH test over the 10VAl catalyst at 773 K. Significant deactivation is observed, where the conversion of propane reaches ~19.8 % after 75 min, decreasing to ~13.8 % after 180 min TOS.

The results are presented in Figure 42, which also displays the selectivity and resulting yield of the olefin product propene. Since the relationship between propane conversion and selectivity towards propene is inverse, propene selectivity increases with TOS as the conversion of propane decreases. As a result, propene yields remain relatively stable throughout, reaching ~9.1 % by the end of the long duration 3 h PDH test.

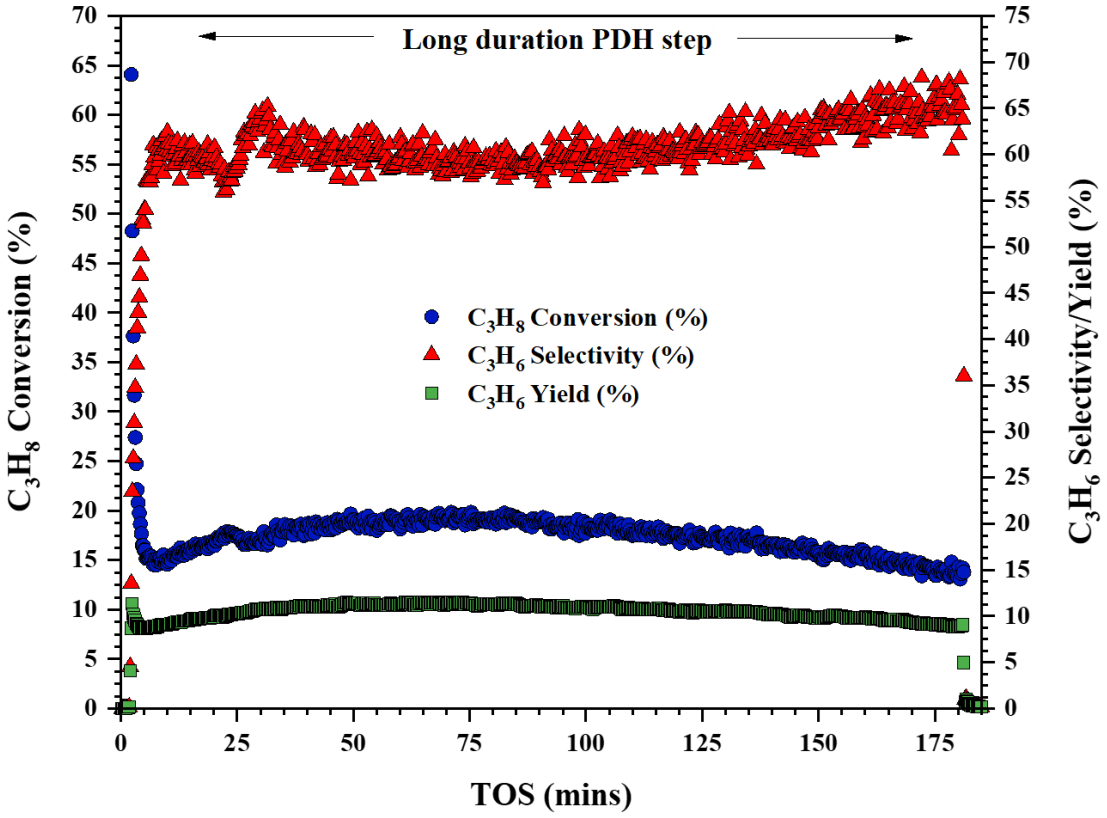

Figure 42: Reaction profile of the long duration 3 h PDH test: 10VAl, 773 K, 1 atm

4.3.3 CL-PODH Redox Cycles with Alternative Oxidants

The instantaneous performance obtained from the CL-PODH redox cycles using the 10VAl catalyst and alternative oxidants (N_2O and CO_2) in the catalyst regeneration step are presented here. Reaction profiles detailing propane conversions and propene selectivities and yields are shown in Figures 43-45, which compare the catalyst activity and selectivity towards the olefin product, as a function of varying oxidant. The selectivity and resulting yield of the undesired CO_2 product are shown in Figures 46 and 47.

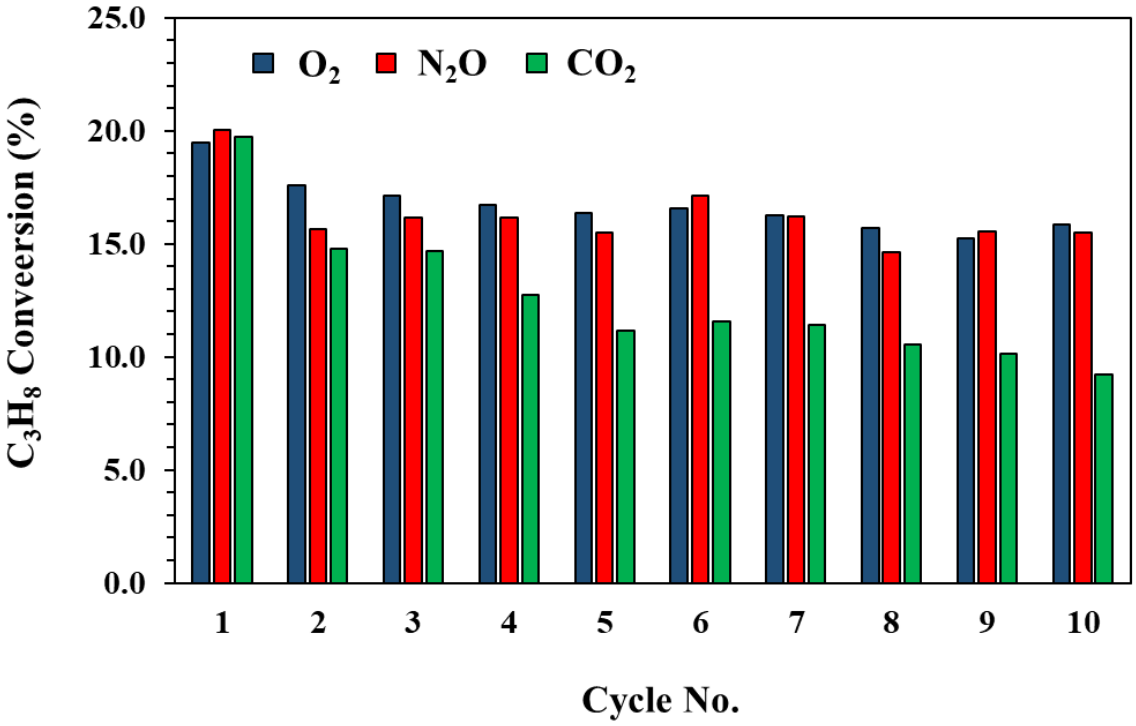

Figure 43: Instantaneous C_3H_8 conversions using the 10VAl catalyst and varying oxidants in the regeneration step, 773 K, 1 atm

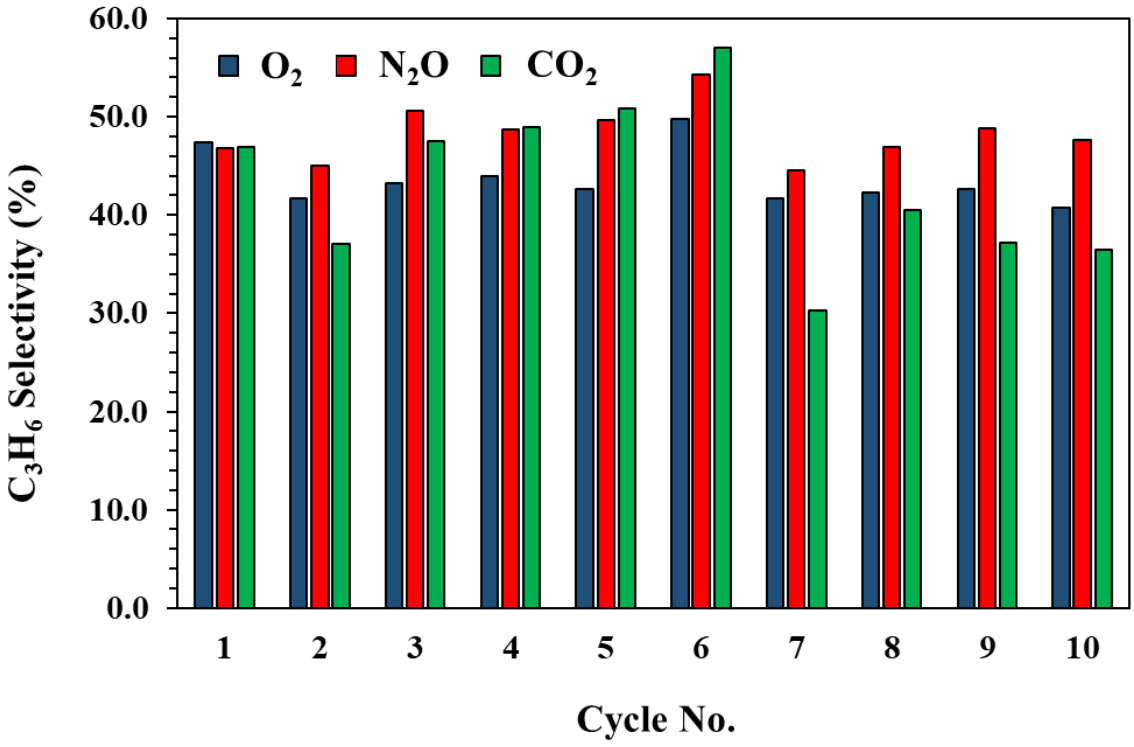

Figure 44: Instantaneous C_3H_6 selectivities using the 10VAl catalyst and varying oxidants in the regeneration step, 773 K, 1 atm

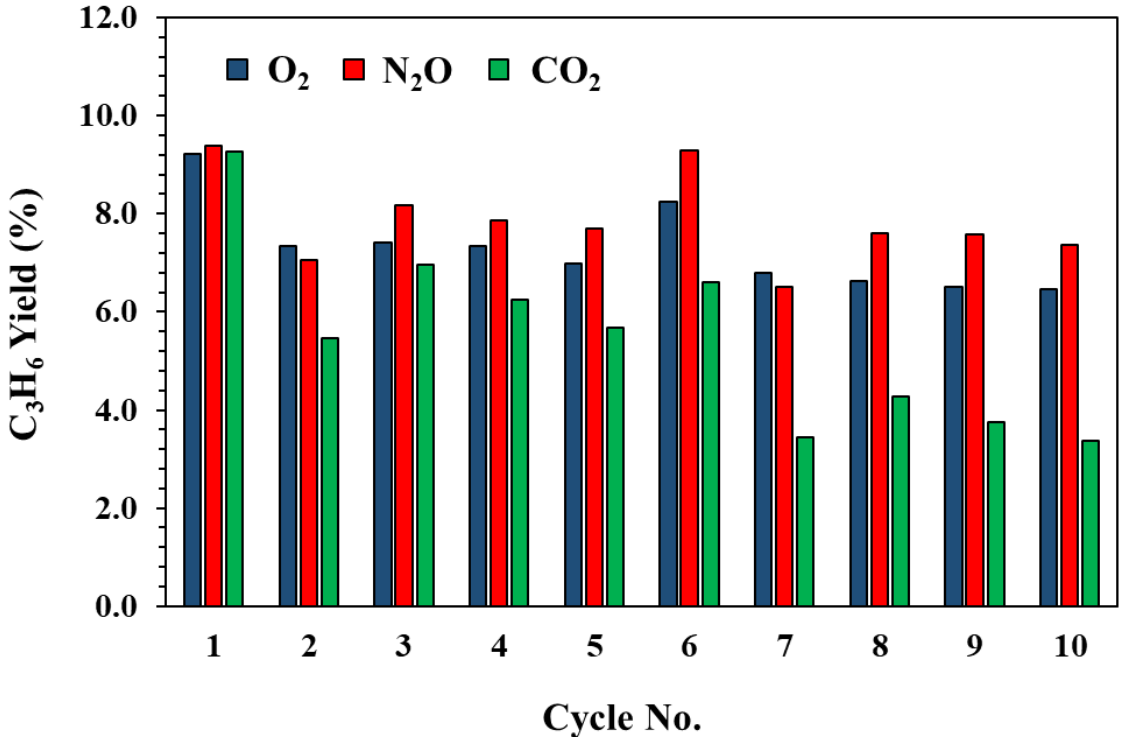

Figure 45: Instantaneous C_3H_6 yields using the 10VAl catalyst and varying oxidants in the regeneration step, 773 K, 1 atm

It is evident from Figures 43-45 that CL-PODH redox cycling tests using the 10VAl catalyst exhibit different catalyst activities when using N_2O and CO_2 oxidants in the regeneration step. On comparison, catalyst activity is highest in CL-PODH redox cycles N_2O as the oxidant, with propane conversions reaching ~15.5 % by the end of the 10^{th} PDH step. Overall, the activity trend is comparable to cycling tests which use O_2 as the oxidant, where propane conversions decrease in the PDH step of cycles 2 to 5. An enhancement in activity during the PDH step of cycle 6 is also observed, with propane conversions rising from ~15.5 to ~17.1 %, before decreasing in subsequent cycles.

Overall, propene selectivity remains highest throughout the CL-PODH redox cycles when using N_2O as the oxidant, resulting in a higher propene yield as the ten cycles proceed. By the end of the 10^{th} PDH step, the selectivity towards propene reaches ~47.6 %, resulting in a propene yield of ~7.4 %.

When using CO_2 as the oxidant however, a loss in catalyst activity is observed as propane conversions decay across the ten cycles. Propene selectivities remain low, resulting in propene yields which are substantially poorer than those observed when using O_2 and N_2O. By the end of the 10^{th} PDH step, propane conversion decreases to ~9.2 %. At this conversion, the selectivity to propene is ~36.5 % resulting in a propene yield of ~3.4 %.

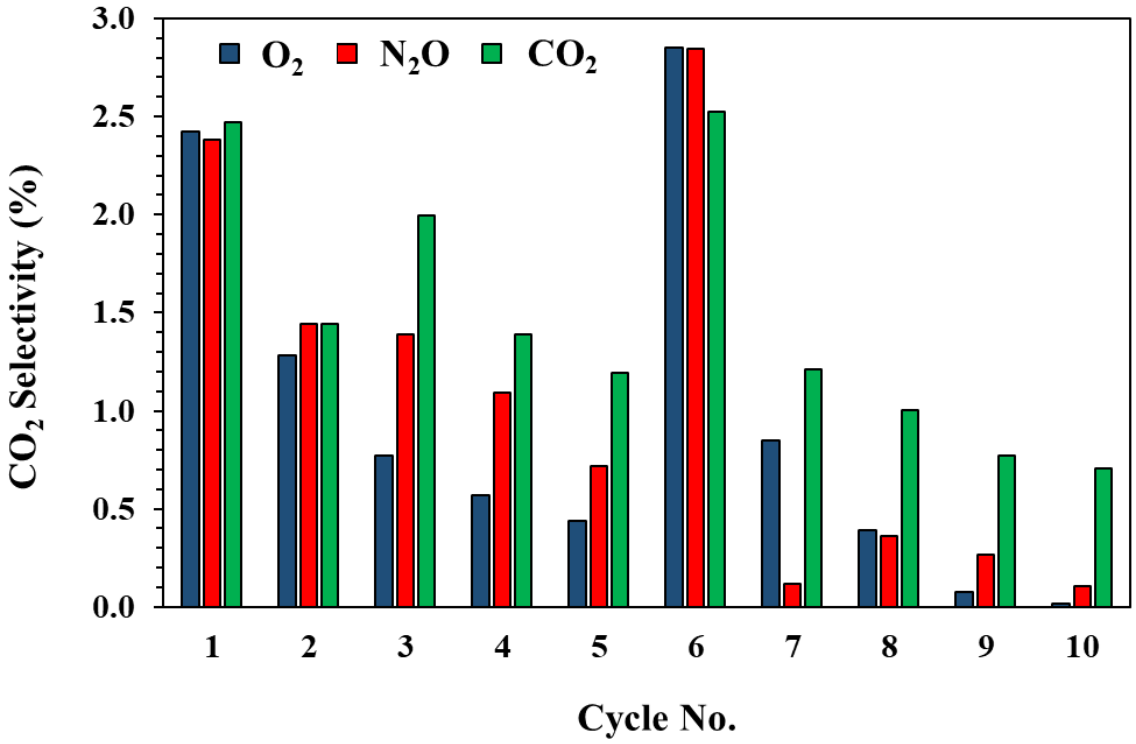

Figure 46: Instantaneous CO_2 selectivities using the 10VAl catalyst and varying oxidants in the regeneration step, 773 K, 1 atm

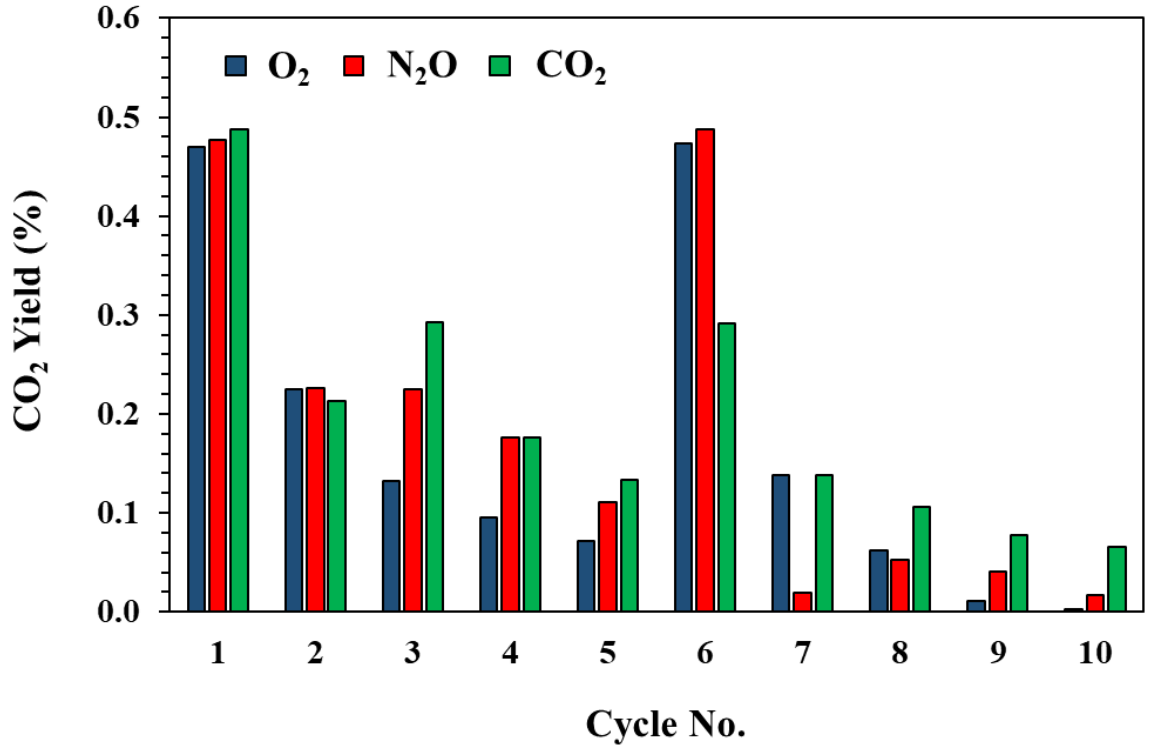

Figure 47: Instantaneous CO_2 yields using the 10VAl catalyst and varying oxidants in the regeneration step, 773 K, 1 atm

Figures 46 and 47 shows that the selectivity towards the undesired CO_2 product remains extremely low at the end of each PDH cycle with respect to the selectivity towards propene. Despite this, the trend in CO_2 selectivity and yield is analogous to those observed for propene.

Both the selectivity and yield of CO_2 decrease as the cycles proceed, with the exception of the PDH step of cycle 6 where an enhancement is observed. During the 6th PDH step, it is the CL-PODH redox cycles regenerated with N_2O which exhibit the highest selectivity towards CO_2. By the end of the 10th PDH step however, the selectivity and resulting CO_2 yield are highest in CL-PODH cycling tests which use CO_2 as the oxidant in the regeneration step.

Reaction profiles obtained during the PDH step of cycles 1 and 2, where alternative oxidants are used in the catalyst regeneration step, are also shown. Figure 48-50 show propane conversion and propene/CO_2 selectivity and yield profiles when using N_2O in the regeneration step. Figures 51-53 show the reaction profiles obtained when regenerating the catalyst with the CO_2 oxidant.

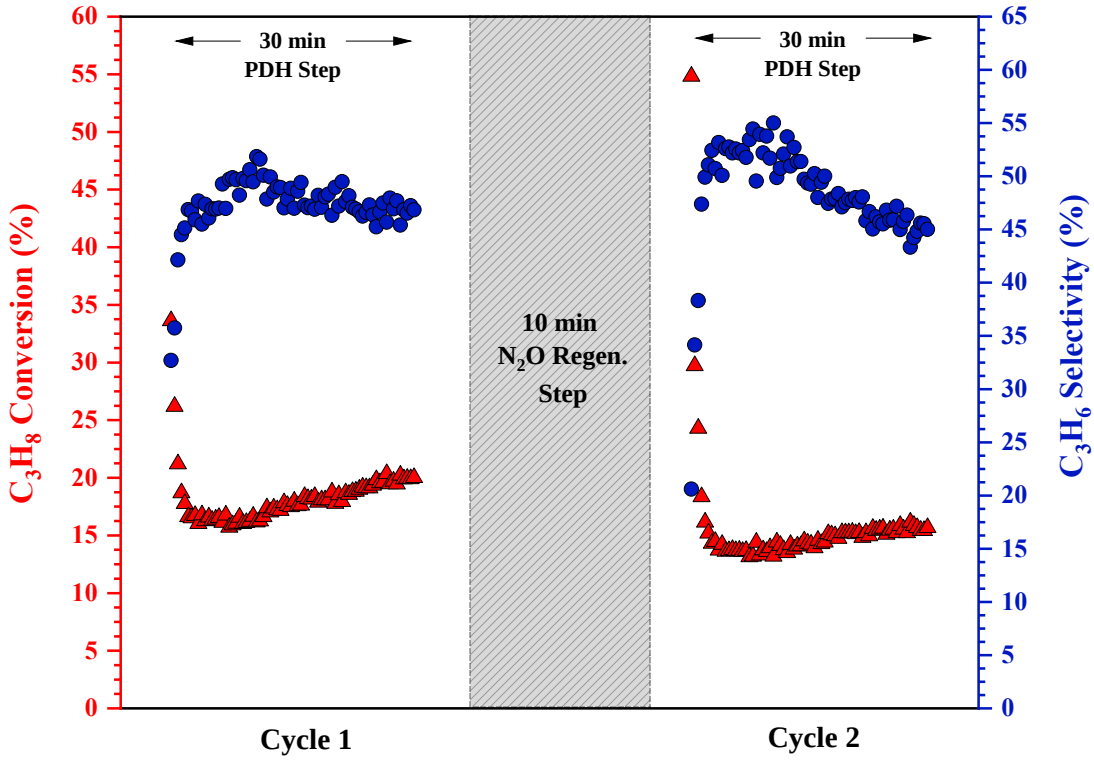

Figure 48: Reaction profile of C_3H_8 conversion and C_3H_6 selectivity during the PDH step of cycle 1 versus cycle 2: 10VAl, N_2O oxidant, 773 K, 1 atm

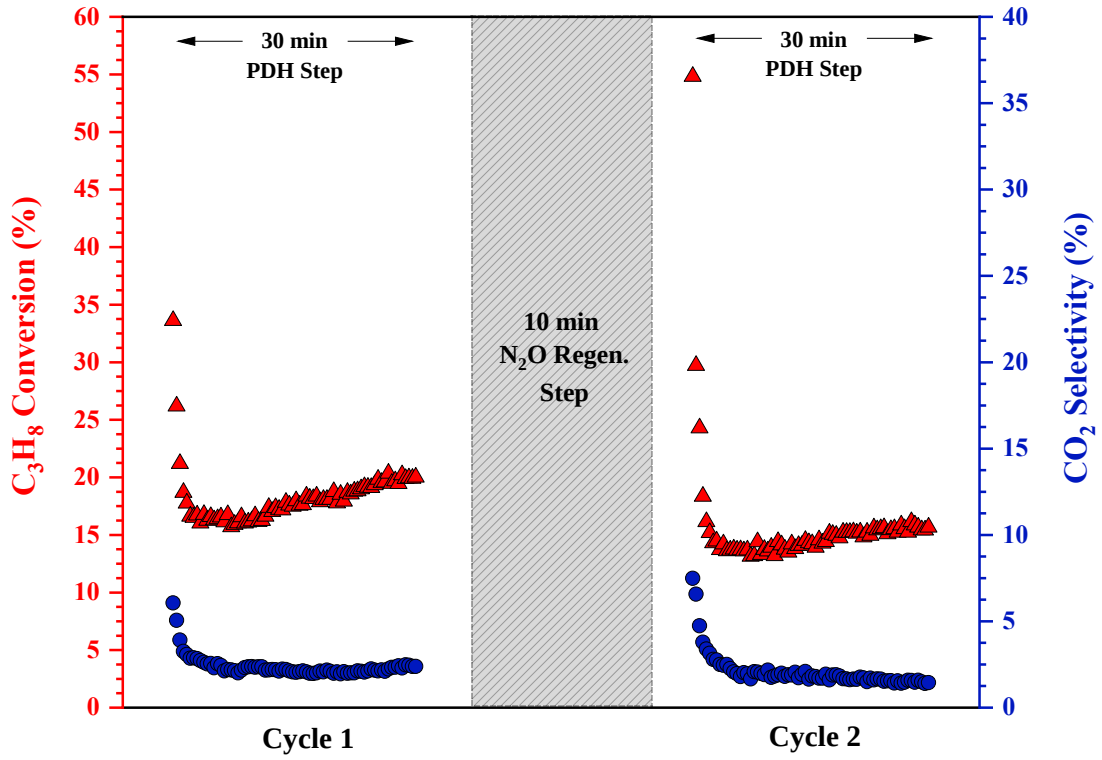

Figure 49: Reaction profile of C_3H_8 conversion and CO_2 selectivity during the PDH step of cycle 1 versus cycle 2: 10VAl, N_2O oxidant, 773 K, 1 atm

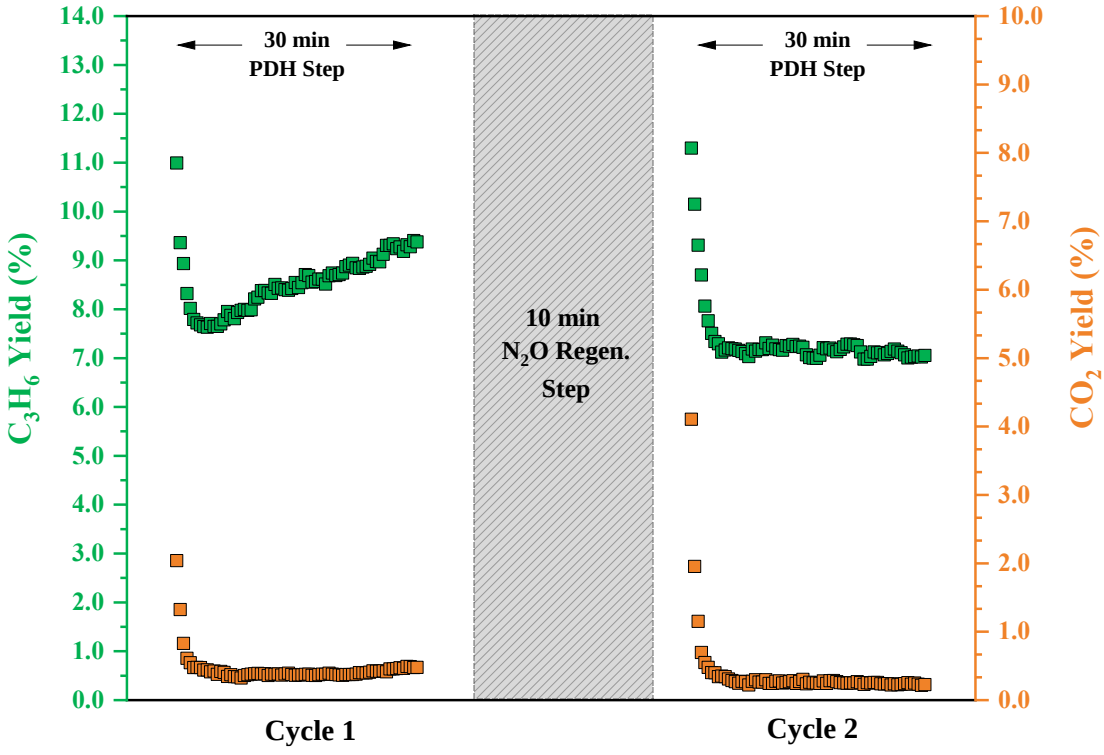

Figure 50: Reaction profile of C_3H_6 and CO_2 yields during the PDH step of cycle 1 versus cycle 2: 10VAl, N_2O oxidant, 773 K, 1 atm

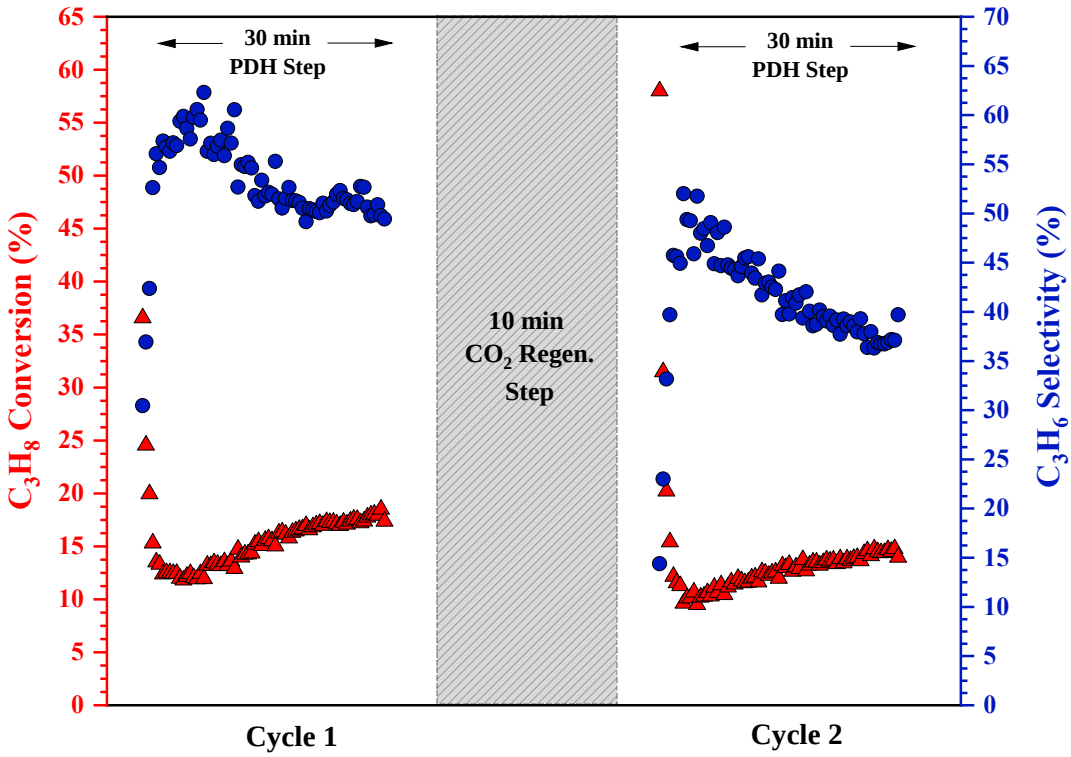

Figure 51: Reaction profile of C_3H_8 conversion and C_3H_6 selectivity during the PDH step of cycle 1 versus cycle 2: 10VAl, CO_2 oxidant, 773 K, 1 atm

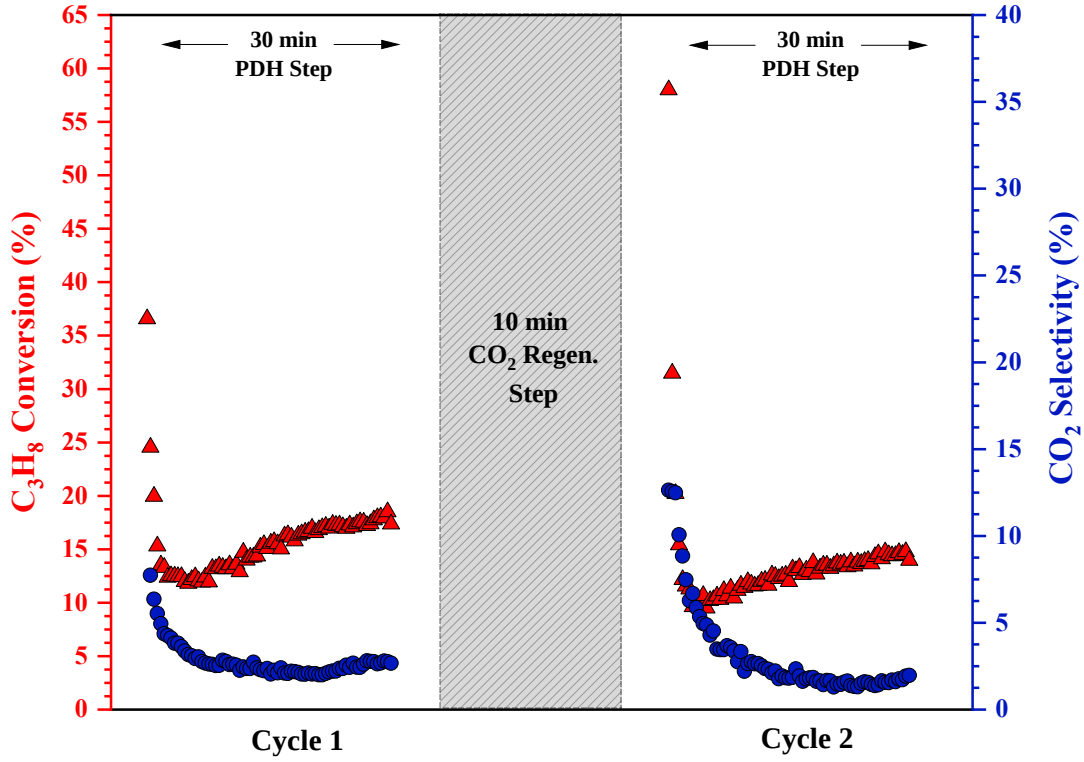

Figure 52: Reaction profile of C_3H_8 conversion and CO_2 selectivity during the PDH step of cycle 1 versus cycle 2: 10VAl, CO_2 oxidant, 773 K, 1 atm

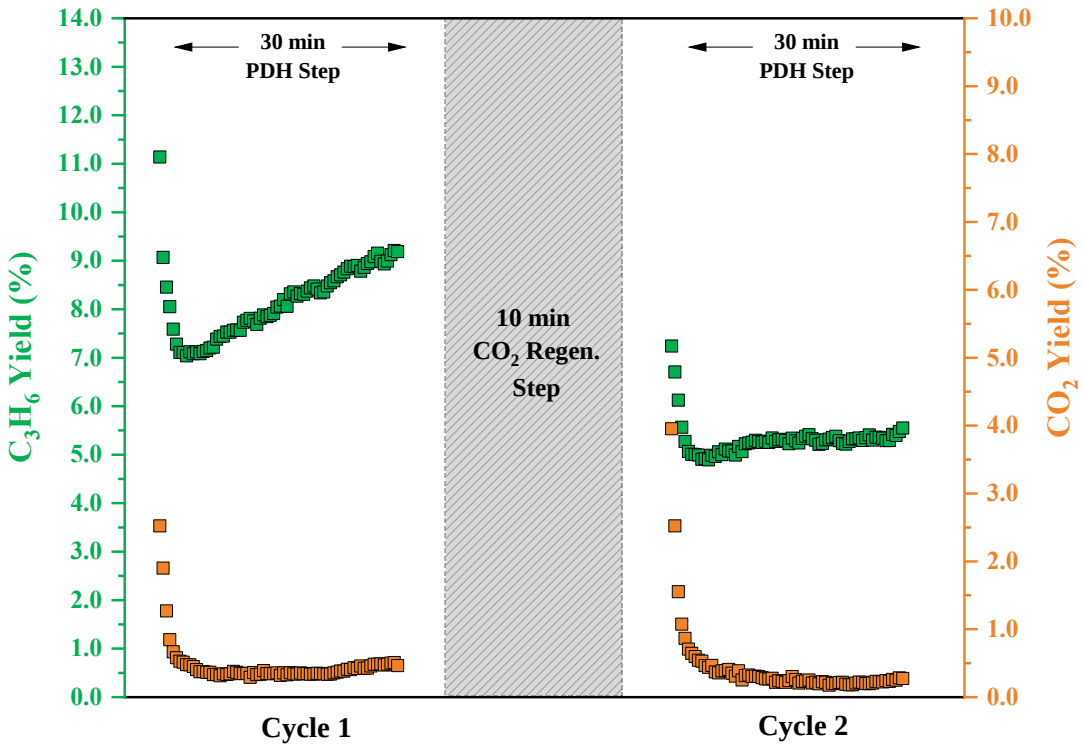

Figure 53: Reaction profile of C_3H_6 and CO_2 yields during the PDH step of cycle 1 versus cycle 2: 10VAl, CO_2 oxidant, 773 K, 1 atm

It is apparent from Figure 48-53 that different reactivity regions also exist when using alternative oxidants, N_2O and CO_2, to regenerate the catalyst. Similar to the CL-PODH redox cycles performed using the 10VAl catalyst and O_2 as the oxidant, propene and CO_2 yields are maximised within the first ~1.5 min of switching on the propane feed. Propene yields begin to decrease as the propane conversion drops off, ultimately reaching a minimum point ~6.0 min into reaction. Following this, propane conversion stabilises, whereas propene yields increase with increasing selectivity. CO_2 yields also decrease after ~1.5 min into the PDH test, however, they remain comparatively low with respect to propene.

For CL-PODH redox cycles regenerated with N_2O, a decrease in propene yield from ~9.4 to 7.1 % is observed on going from cycle 1 to cycle 2. This decay is attributed to a loss in catalyst activity where propane conversion decreases from ~ 20.0 to 15.6 % by the end of the 2nd PDH step. With regards to CL-PODH redox cycles where CO_2 is utilised as the oxidant, a decline in both catalyst activity and propene selectivity is observed on going from cycle 1 to cycle 2. Consequently, propene yields suffer significantly and diminish from 9.3 to 5.5 % by the end of 2nd PDH step.

Propane conversions, propene/CO_2 selectivities and resulting propene/CO_2 yields achieved at these different regions in CL-PODH redox cycles 1 and 2, regenerated with N_2O and CO_2, are summarised below in Tables 21-24.

Table 21: Summary of C_3H_8 conversions, C_3H_6 and CO_2 selectivities and yields obtained at the different reaction regions during the PDH step of cycle 1: 10VAl, N_2O oxidant, 773 K, 1 atm

Time into PDH Step (min)	C_3H_8 Conversion (%)	C_3H_6 Selectivity (%)	C_3H_6 Yield (%)	CO_2 Selectivity (%)	CO_2 Yield (%)
1.5	33.6	32.7	11.0	6.1	2.0
6	15.7	49.7	7.8	2.2	0.3
30	20.0	46.8	9.4	2.4	0.5

Table 22: Summary of C_3H_8 conversions and C_3H_6 and CO_2 selectivities and yields obtained at the different reaction regions during the PDH step of cycle 2: 10VAl, N_2O oxidant, 773 K, 1 atm

Time into PDH Step (min)	C_3H_8 Conversion (%)	C_3H_6 Selectivity (%)	C_3H_6 Yield (%)	CO_2 Selectivity (%)	CO_2 Yield (%)
1.5	54.8	20.6	11.3	7.4	4.1
6	13.1	53.4	7.0	1.7	0.2
30	15.6	45.0	7.1	1.4	0.2

Table 23: Summary of C_3H_8 conversions, C_3H_6 and CO_2 selectivities and yields obtained at the different reaction regions during the PDH step of cycle 1: 10VAl, CO_2 oxidant, 773 K, 1 atm

Time into PDH Step (min)	C_3H_8 Conversion (%)	C_3H_6 Selectivity (%)	C_3H_6 Yield (%)	CO_2 Selectivity (%)	CO_2 Yield (%)
1.5	36.6	30.45	11.1	6.9	2.5
6	11.8	59.9	7.1	3.2	0.4
30	18.8	49.4	9.3	2.7	0.5

Table 24: Summary of C_3H_8 conversions and C_3H_6 and CO_2 selectivities and yields obtained at the different reaction regions during the PDH step of cycle 2: 10VAl, CO_2 oxidant, 773 K, 1 atm

Time into PDH Step (min)	C_3H_8 Conversion (%)	C_3H_6 Selectivity (%)	C_3H_6 Yield (%)	CO_2 Selectivity (%)	CO_2 Yield (%)
1.5	58.0	14.4	8.3	12.6	7.3
6	9.5	51.8	4.9	4.9	0.5
30	14.0	39.7	5.5	2.0	0.3

An improvement in productivity is also observed in the PDH step of cycle 6 after regenerating with the alternative oxidants and holding the catalysts overnight under a continous flow of argon. For clarity, the reaction profiles obtained from the entire PDH step of cycle 5 versus cycle 6 have been compared. Figures 54-56 show propane conversion and propene/CO_2 selectivity and yield profiles when using N_2O in the regeneration step. Figure 57-59 are those obtained when regenerating the catalyst with CO_2.

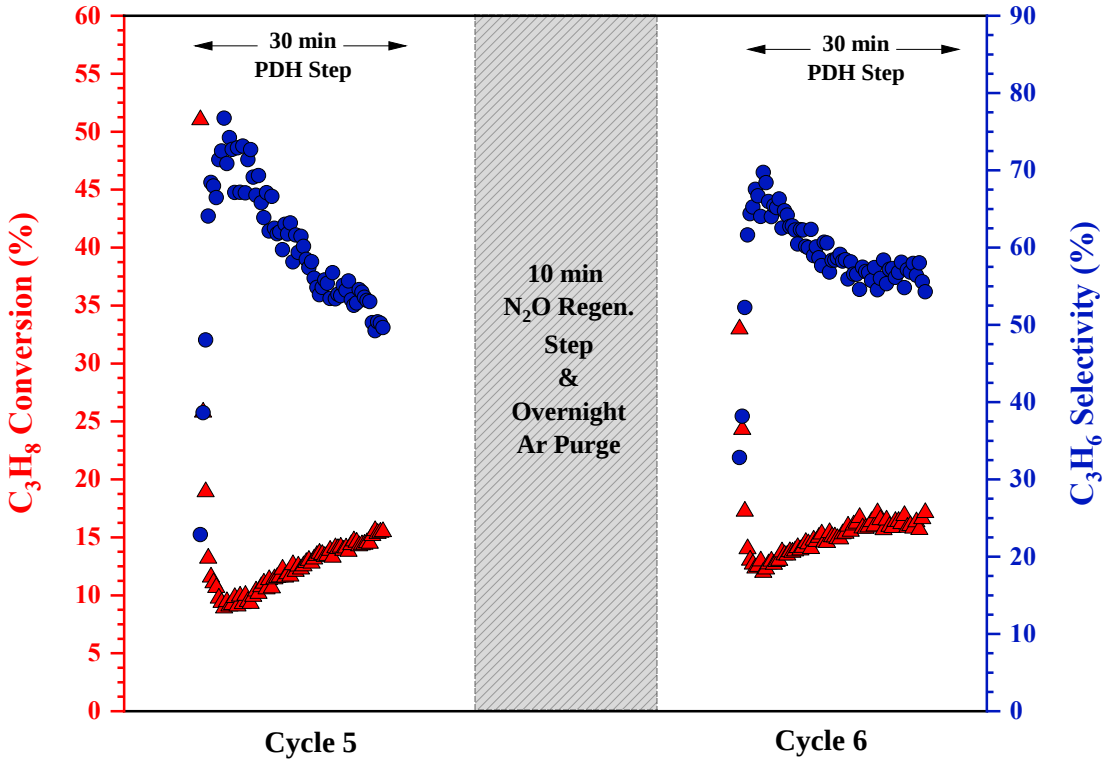

Figure 54: Reaction profile of C_3H_8 conversion and C_3H_6 selectivity during the PDH step of cycle 5 versus cycle 6: 10VAl, N_2O oxidant, 773 K, 1 atm

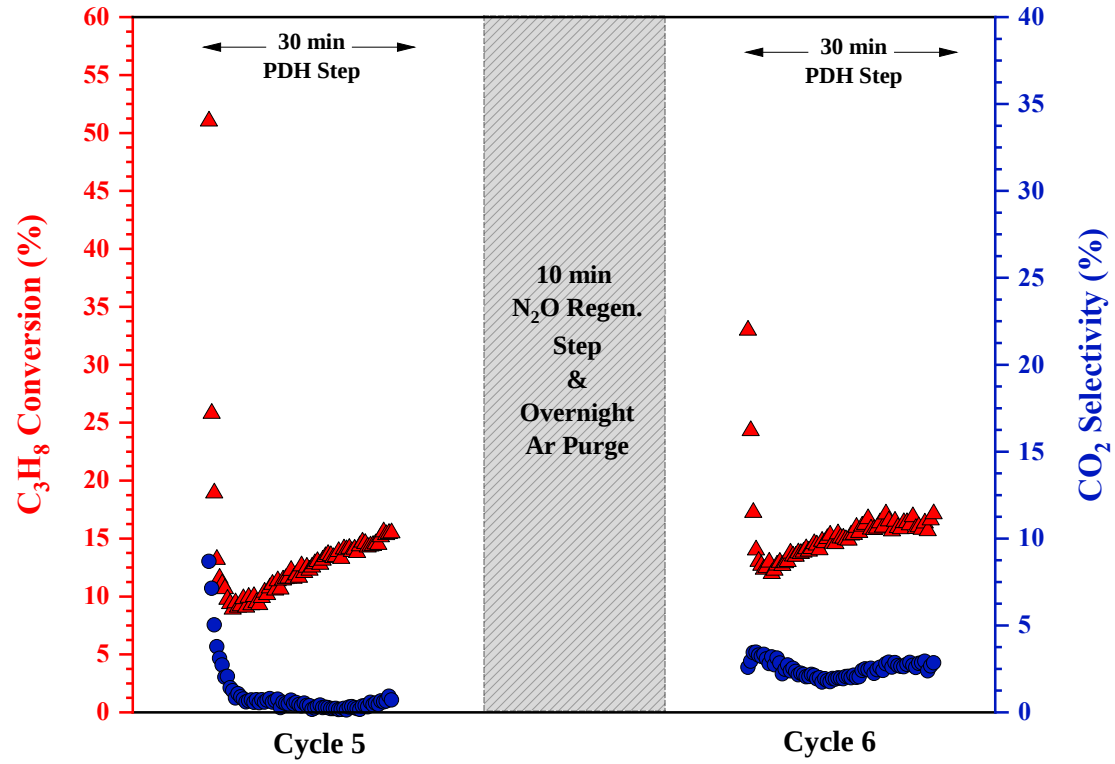

Figure 55: Reaction profile of C_3H_8 conversion and CO_2 selectivity during the PDH step of cycle 5 versus cycle 6: 10VAl, N_2O oxidant, 773 K, 1 atm

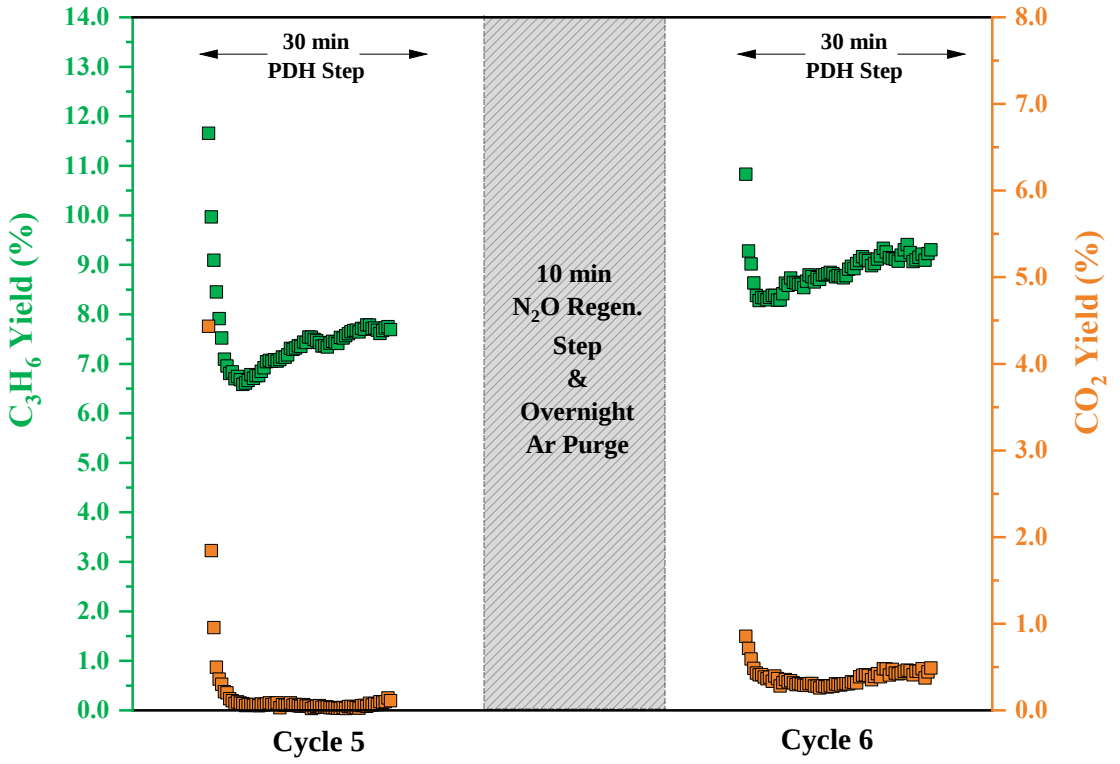

Figure 56: Reaction profile of C_3H_6 and CO_2 yields during the PDH step of cycle 5 versus cycle 6: 10VAl, N_2O oxidant, 773 K, 1 atm

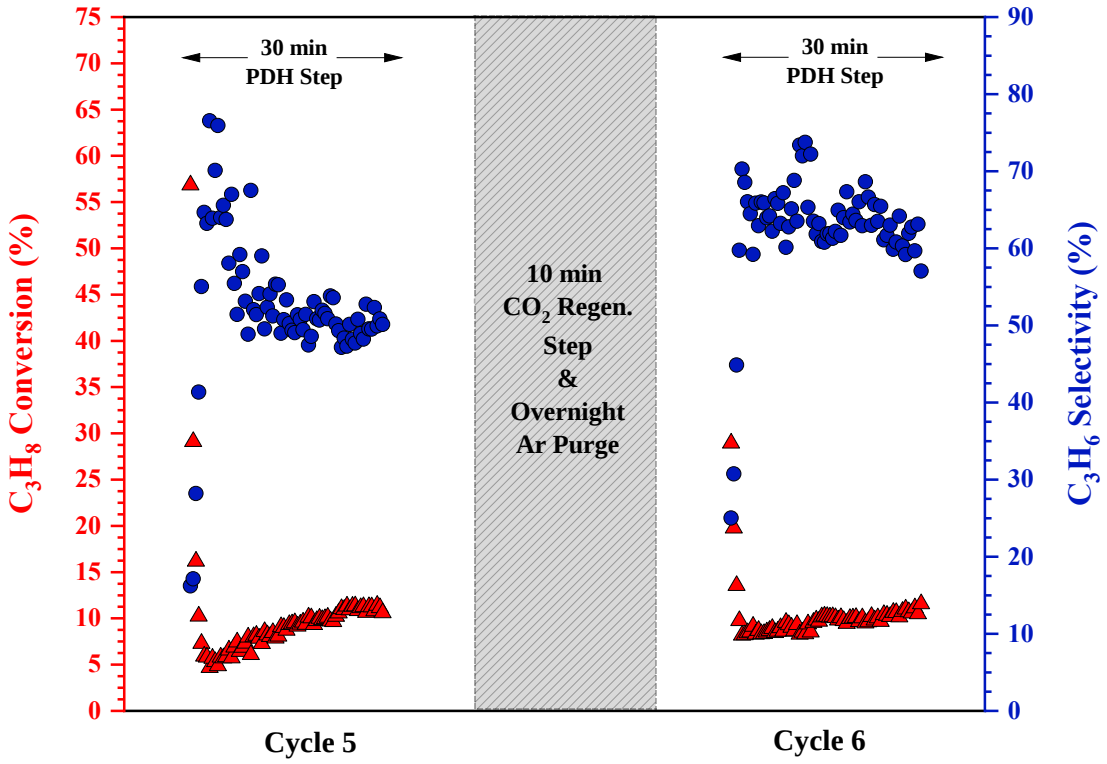

Figure 57: Reaction profile of C_3H_8 conversion and C_3H_6 selectivity during the PDH step of cycle 5 versus cycle 6: 10VAl, CO_2 oxidant, 773 K, 1 atm

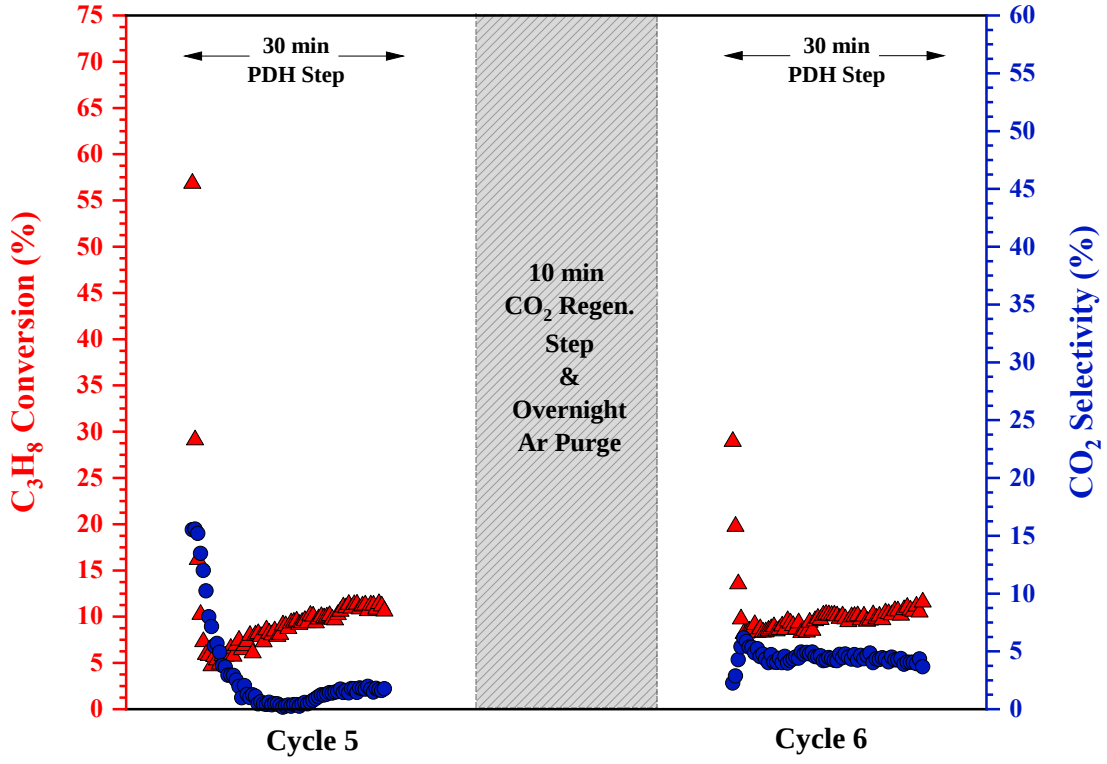

Figure 58: Reaction profile of C_3H_8 conversion and CO_2 selectivity during the PDH step of cycle 5 versus cycle 6: 10VAl, CO_2 oxidant, 773 K, 1 atm

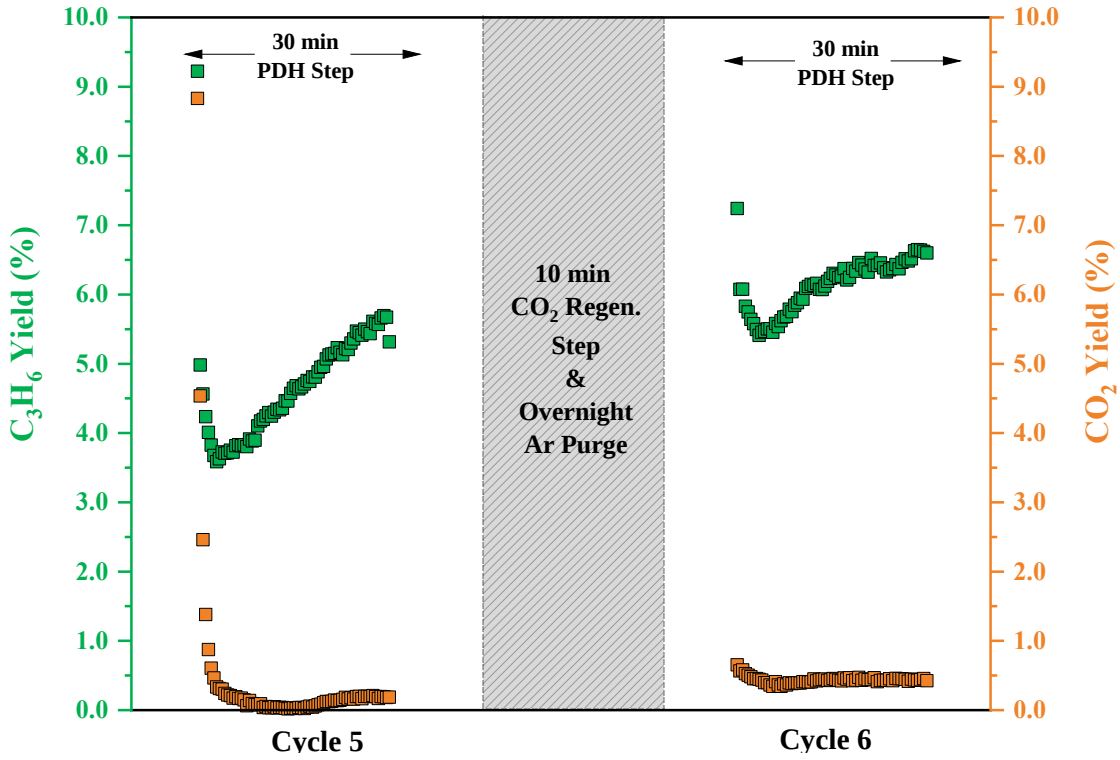

Figure 59: Reaction profile of C_3H_6 and CO_2 yields during the PDH step of cycle 5 versus cycle 6: 10VAl, CO_2 oxidant, 773 K, 1 atm

Different reactivity regions are also observed in the PDH step of cycles 5 and 6 when using the alternative oxidants in the regeneration step. As observed in the cycling test which utilises O_2 in the regeneration step, the maximum propene and CO_2 yields achieved within the first ~1.5 min are highest in the PDH step of cycle 6 when both N_2O and CO_2 oxidants have been used. Propane conversions stabilise as the reaction proceeds, where enhanced propene yields are observed resulting from increased propene selectivity.

Comparison of both cycles shows the selectivity to both propene and CO_2 is further enhanced by the end of the 6th PDH step. Overall, higher propene and CO_2 yields are achieved in comparison to those obtained in cycle 5. Propene and CO_2 yields increase from ~7.7 and 0.1 % to ~9.3 and 0.5 %, respectively, when regenerating with N_2O. When regenerating with CO_2, propene and CO_2 yields are also enhanced, increasing from ~5.6 and 0.2 % to ~6.6 and 0.4 %, respectively.

Propane conversions, propene/CO_2 selectivities and resulting propene/CO_2 yields achieved at these different regions in CL-PODH redox cycles 5 and 6, regenerated with N_2O and CO_2, are summarised below in Tables 25-28.

Table 25: Summary of C_3H_8 conversions, C_3H_6 and CO_2 selectivities and yields obtained at the different reaction regions during the PDH step of cycle 5: 10VAl, N_2O oxidant, 773 K, 1 atm

Time into PDH Step (min)	C_3H_8 Conversion (%)	C_3H_6 Selectivity (%)	C_3H_6 Yield (%)	CO_2 Selectivity (%)	CO_2 Yield (%)
1.5	51.0	22.8	11.7	8.7	4.4
6	8.9	76.7	6.9	1.2	0.1
30	15.5	49.6	7.7	0.7	0.1

Table 26: Summary of C_3H_8 conversions and C_3H_6 and CO_2 selectivities and yields obtained at the different reaction regions during the PDH step of cycle 6: 10VAl, N_2O oxidant, 773 K, 1 atm

Time into PDH Step (min)	C_3H_8 Conversion (%)	C_3H_6 Selectivity (%)	C_3H_6 Yield (%)	CO_2 Selectivity (%)	CO_2 Yield (%)
1.5	33.0	32.8	10.8	2.6	0.9
6	12.0	69.8	8.3	3.2	0.4
30	17.1	54.3	9.3	2.8	0.5

Table 27: Summary of C_3H_8 conversions, C_3H_6 and CO_2 selectivities and yields obtained at the different reaction regions during the PDH step of cycle 5: 10VAl, CO_2 oxidant, 773 K, 1 atm

Time into PDH Step (min)	C_3H_8 Conversion (%)	C_3H_6 Selectivity (%)	C_3H_6 Yield (%)	CO_2 Selectivity (%)	CO_2 Yield (%)
1.5	36.9	16.2	6.0	15.5	5.7
6	4.7	76.6	3.6	7.1	0.3
30	11.3	50.1	5.6	1.8	0.2

Table 28: Summary of C_3H_8 conversions and C_3H_6 and CO_2 selectivities and yields obtained at the different reaction regions during the PDH step of cycle 6: 10VAl, CO_2 oxidant, 773 K, 1 atm

Time into PDH Step (min)	C_3H_8 Conversion (%)	C_3H_6 Selectivity (%)	C_3H_6 Yield (%)	CO_2 Selectivity (%)	CO_2 Yield (%)
1.5	28.9	25.0	7.2	2.3	0.7
6	8.3	65.8	5.5	5.2	0.4
30	11.6	57.0	6.6	3.7	0.4

4.3.4 Propane Pulsing Tests

Since propene and CO_2 yields are maximised within the first ~1.5 min of the PDH cycle, it was of paramount importance to investigate the initial reactivity of the 10VAl catalyst and gain a clearer understanding on the reaction chemistry taking place. This was achieved by performing a series of propane pulsing tests, where a sequence of 20 propane pulses were directed over the sample at various stages, before resuming the continuous flow CL-PODH reaction.

In order to investigate any variations after the O_2 catalyst regeneration step and overnight argon purge, propane pulsing tests were performed at the initial stage of the 1^{st}, 2^{nd}, and 6^{th} PDH step. Reaction profiles detailing the data obtained from the propane pulsing test at the initial stage of the 1^{st} PDH cycle are presented in Figure 60-62. Figures 60 and 61 are propane conversion, propene and CO_2 selectivity plots and Figure 62 presents the resulting propene and CO_2 yield.

From Figure 60, it can be seen that full conversion of propane occurs during the initial 8 propane pulses whereupon, a rapid drop in conversion is observed in subsequent injections, falling to ~ 40 % by pulse number 15. Thereafter, the decline in conversion slows, reaching ~30% by the 20th propane pulse. As would be expected from the inverse selectivity-conversion relationship, the selectivity profile for propene shows a clear correlation with that of the propane conversion. In marked contrast to this, the selectivity profile for CO_2, as presented in Figure 61, shows an immediate selectivity to CO_2 of ~20 %, declining gradually to negligible levels by pulse number 12. The resulting yield profiles, shown in Figure 62, behave accordingly: an initial CO_2 yield of ~19.7 % decreases steadily to near zero by pulse 15, with propene formation beginning from pulse 10, and a maximum yield of ~18.1 % is achieved by reaction end.

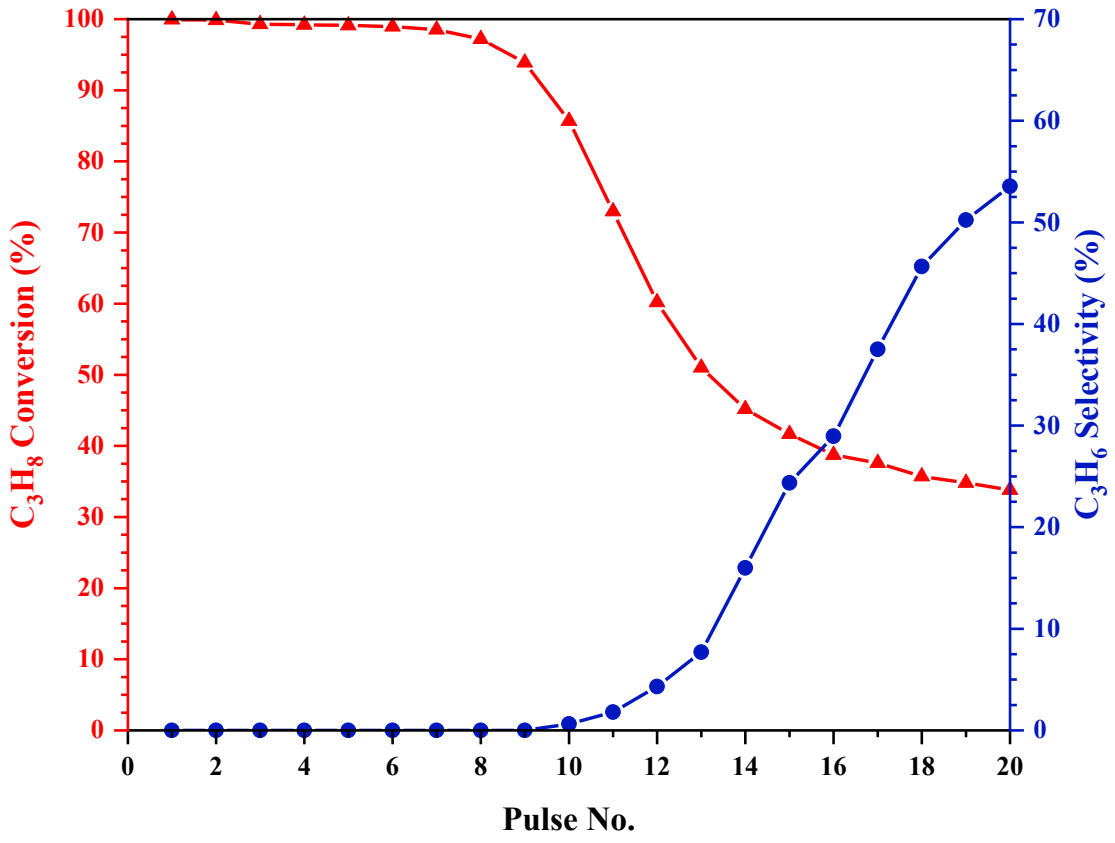

Figure 60: Reaction profile of C_3H_8 conversion and C_3H_6 selectivity during the propane pulsing test performed at the initial stage of the 1st PDH step: 10VAl, 773 K, 1 atm

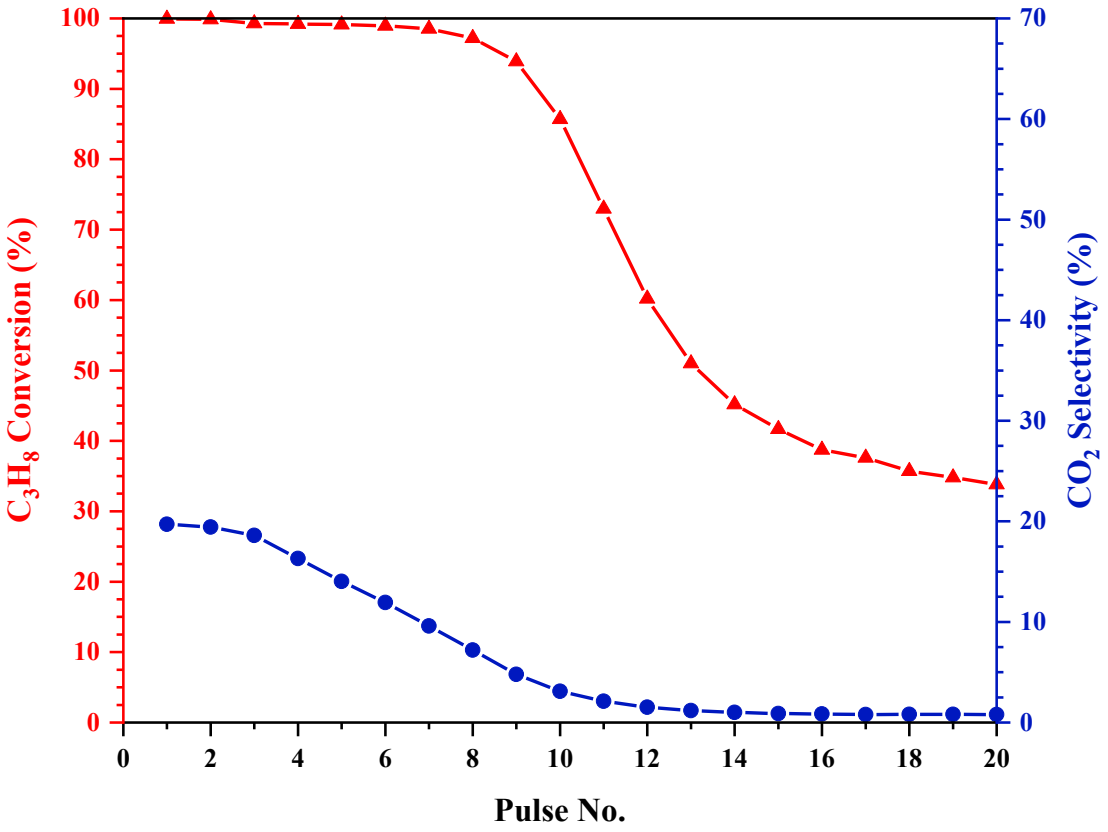

Figure 61: Reaction profile of C_3H_8 conversion and CO_2 selectivity during the propane pulsing test performed at the initial stage of the 1st PDH step: 10VAl, 773 K, 1 atm

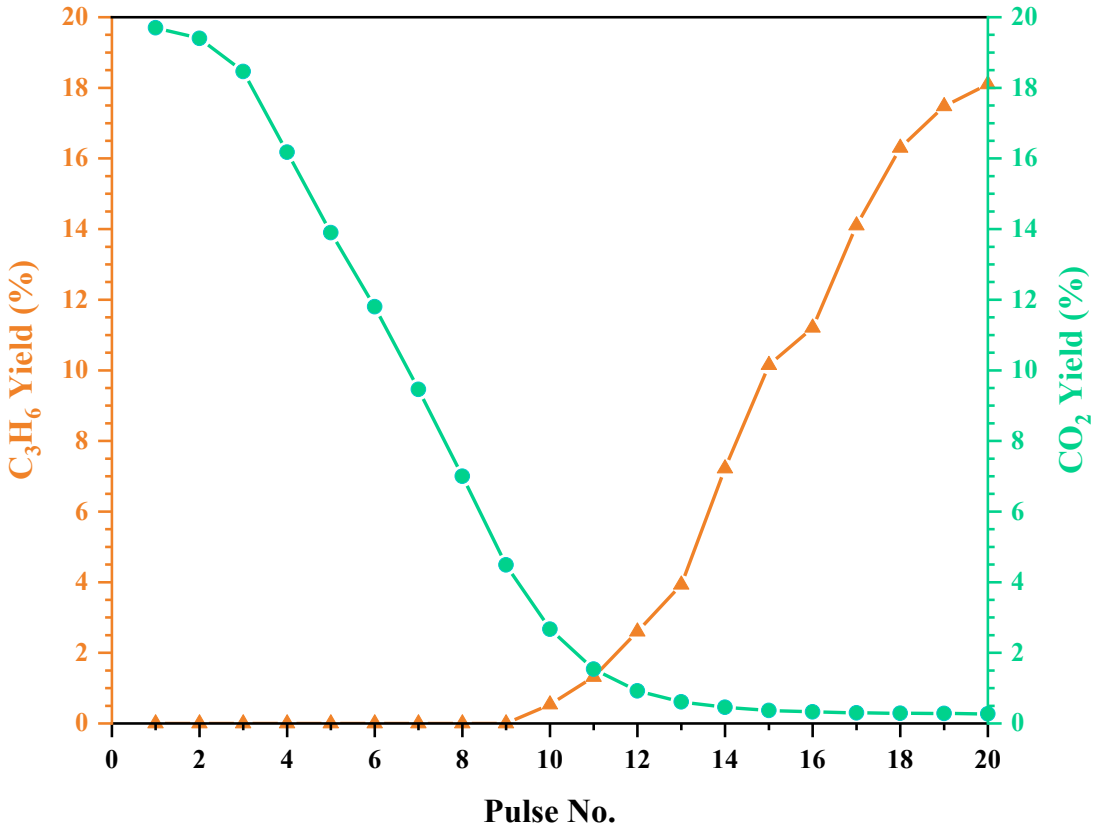

Figure 62: Reaction profile of C_3H_6 and CO_2 yields during the propane pulsing test performed at the initial stage of the 1st PDH step: 10VAl, 773 K, 1 atm

Reaction profiles detailing the data obtained from the propane pulsing test at the initial stage of the 2nd PDH cycle are presented in Figures 63-65. Figures 63 and 64 are propane conversion, propene and CO_2 selectivity plots and Figure 65 presents the resulting propene and CO_2 yield. Notably, conversion, selectivity and yield profiles obtained from the propane pulsing test during the 2nd PDH step are analogous to those obtained during the 1st cycle.

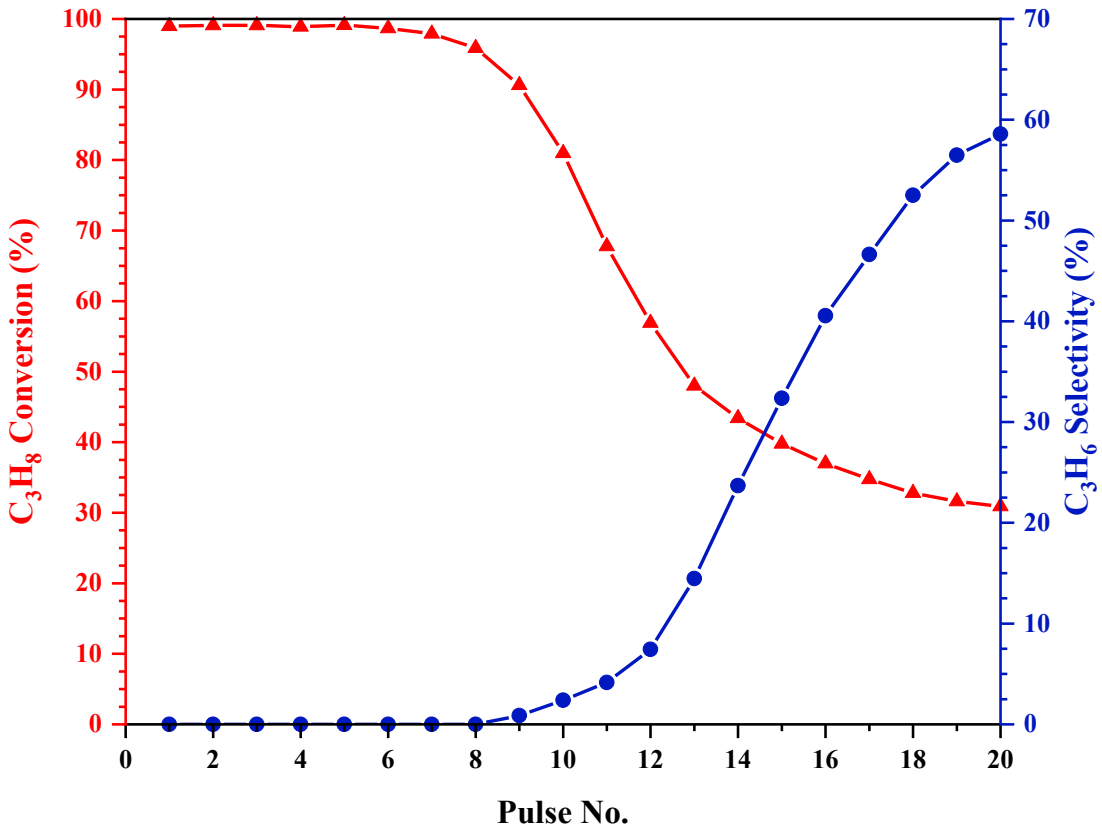

Figure 63: Reaction profile of C_3H_8 conversion and C_3H_6 selectivity during the propane pulsing test performed at the initial stage of the 2nd PDH step: 10VAl, O_2 oxidant, 773 K, 1 atm

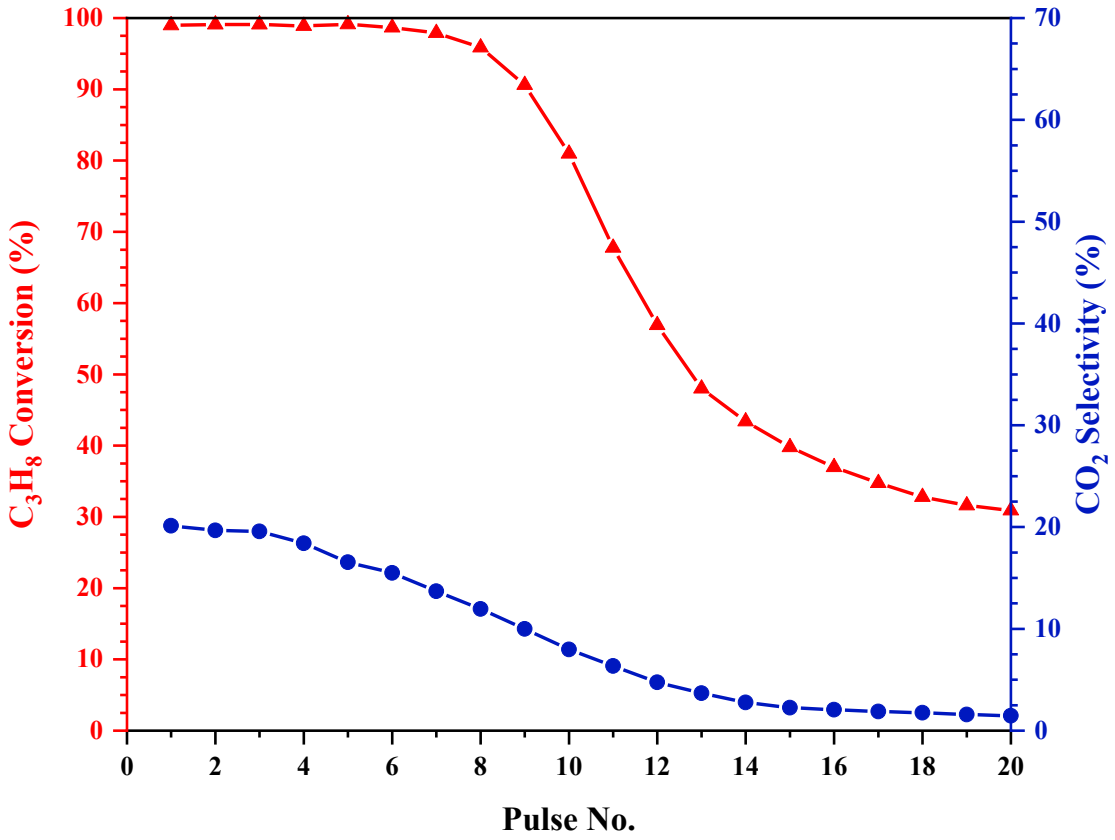

Figure 64: Reaction profile of C_3H_8 conversion and CO_2 selectivity during the propane pulsing test performed at the initial stage of the 2nd PDH step: 10VAl, O_2 oxidant, 773 K, 1 atm

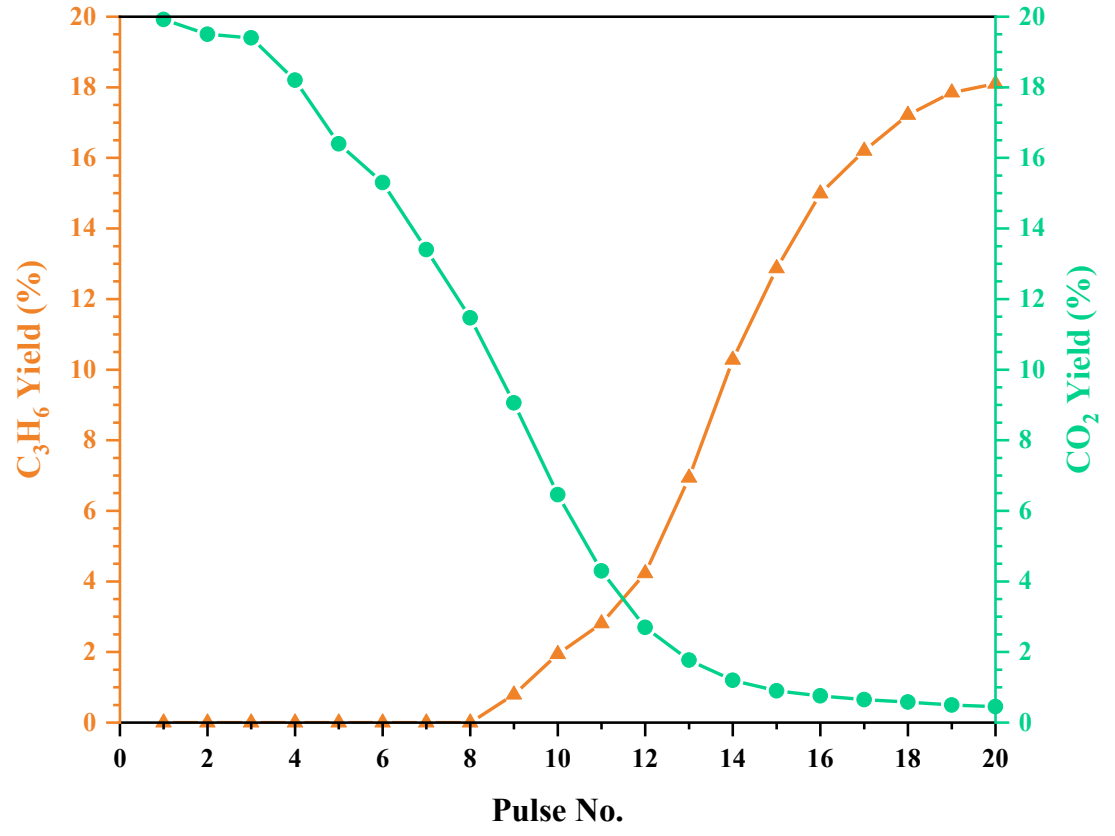

Figure 65: Reaction profile of C_3H_6 and CO_2 yields during the propane pulsing test performed at the initial stage of the 2nd PDH step: 10VAl, O_2 oxidant, 773 K, 1 atm

Reaction profiles detailing the data obtained from the propane pulsing test at the initial stage of the 6th PDH cycle are presented in Figure 66-68. Figure 66 and 67 are propane conversion, propene and CO_2 selectivity plots and Figure 68 presents the resulting propene and CO_2 yield. As discussed, this propane pulsing test was performed immediately after holding the catalysts overnight under a constant flow of argon.

A clear disparity in propane conversions is observed with respect to those obtained from pulsing tests performed in the 1st and 2nd PDH step. As seen in Figure 66, propane conversion exhibits an exponential decay, dropping from ~83.7 % to ~ 33.0 % by the 12th propane pulse whereafter, it remains relatively stable until reaction completion. Similarly, the inverse selectivity-conversion relationship comes into play as the selectivity to propene rises as propane conversion falls. Contrary to this, the selectivity profile for CO_2, as presented in Figure 67, is significantly lower during initial propane injections, where an immediate selectivity to CO_2 of ~2.3 % is observed, declining to negligible levels thereafter. The resulting yield profiles, shown in Figure 68, behave accordingly: an initial CO_2 yield of ~1.9 % decreases to nominal quantities by pulse number 3, where propene formation occurs immediately, reaching a maximum yield of ~20.1 % by reaction end.

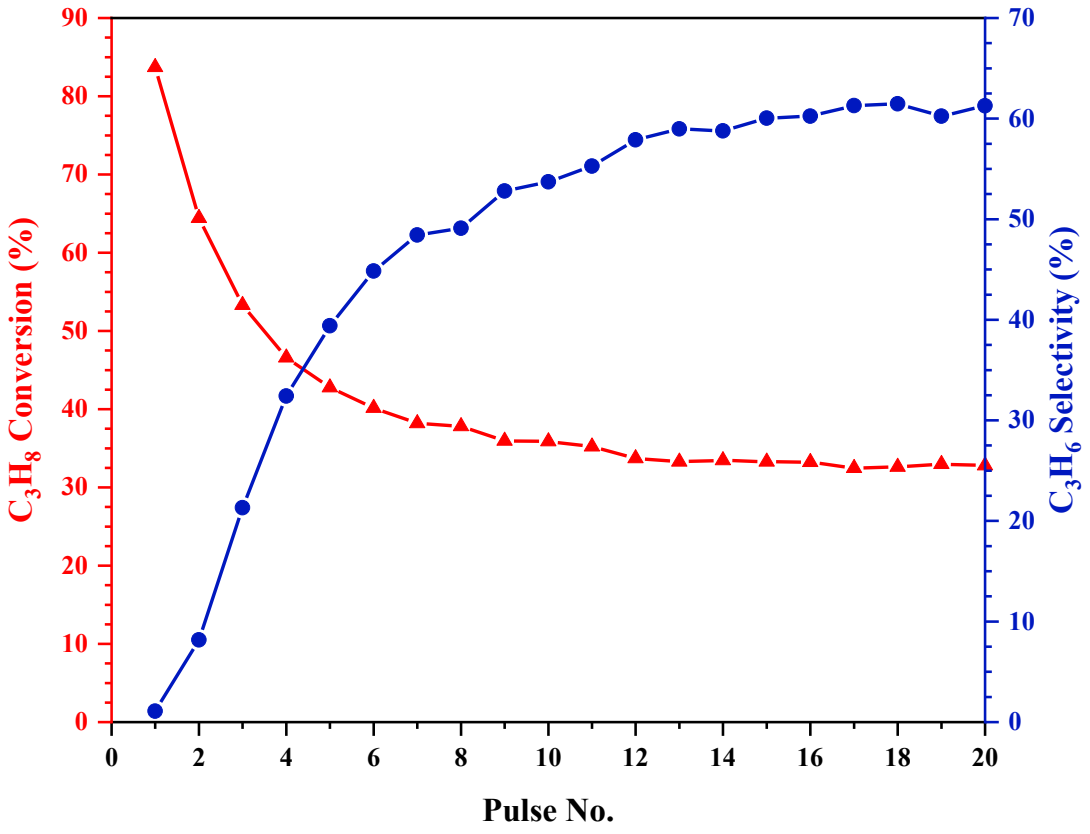

Figure 66: Reaction profile of C_3H_8 conversion and C_3H_6 selectivity during the propane pulsing test performed at the initial stage of the 6th PDH step: 10VAl, O_2 oxidant, 773 K, 1 atm

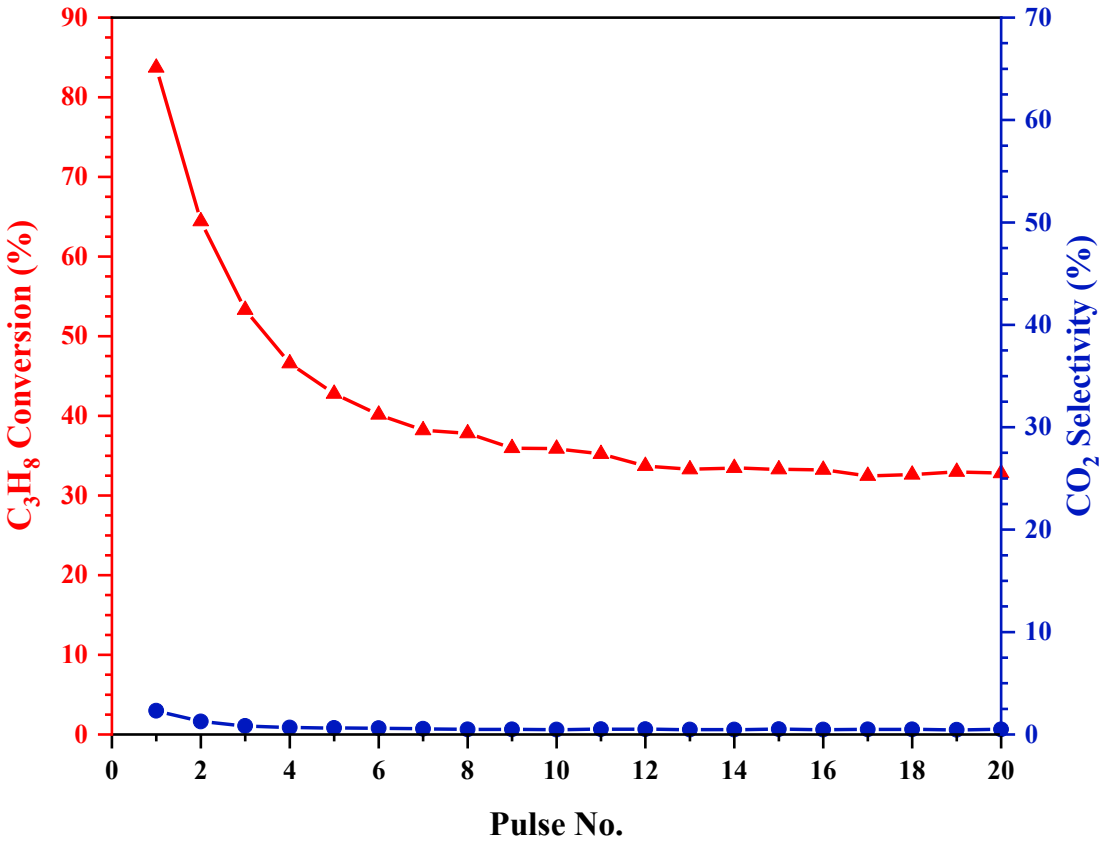

Figure 67: Reaction profile of C_3H_8 conversion and CO_2 selectivity during the propane pulsing test performed at the initial stage of the 6th PDH step: 10VAl, O_2 oxidant, 773 K, 1 atm

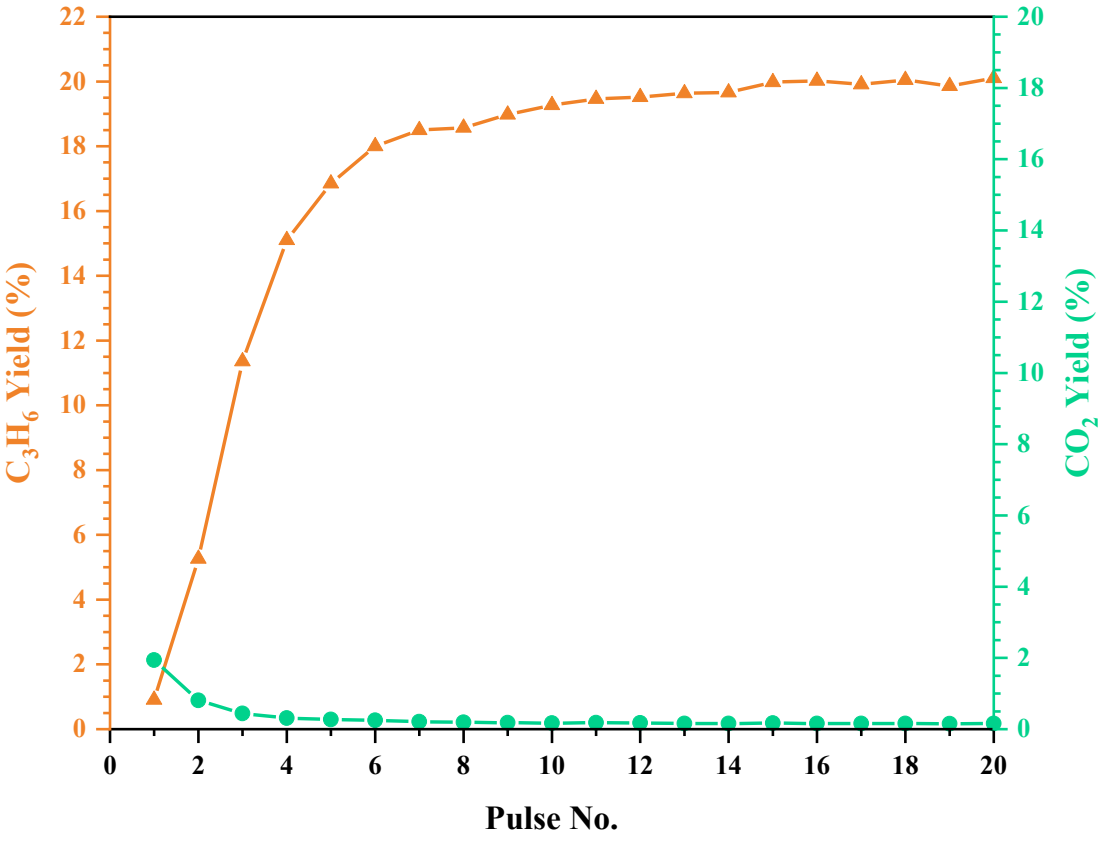

Figure 68: Reaction profile of C_3H_6 and CO_2 yields during the propane pulsing test performed at the initial stage of the 6th PDH step: 10VAl, O_2 oxidant, 773 K, 1 atm

In order to investigate the reaction chemistry when utilising N_2O as the oxidant in the catalyst regeneration step, propane pulsing tests were performed at the initial stage of the 2nd and 6th PDH step of CL-PODH-N_2O cycles.

Reaction profiles detailing the pulse data obtained from the 2nd PDH step, in cycles utilising N_2O, are presented in Figures 69-71. Figures 69 and 70 are propane conversion, propene and CO_2 selectivity plots and Figure 71 presents the resulting propene and CO_2 yield. It appears from Figure 69 that the trend in propane conversion versus propene/CO_2 selectivity is comparable to the pulse data obtained after regenerating with O_2. Propane converts fully during the first 6 propane pulses, followed by a rapid drop in conversion in subsequent injections, falling to ~30 % by the 20th propane pulse. As anticipated, propene selectivity is inversely related to the propane conversion. The selectivity profile for CO_2 presented in Figure 70, shows an initial selectivity towards CO_2 of ~20 %, which gradually declines to insignificant levels by the 15th pulse. The resulting yield profiles (Figure 71) behave accordingly: an initial CO_2 yield of ~19.9 % decreases steadily to negligible quantities, where propene formation begins from pulse number 9, reaching a maximum yield of ~18.1 % by the end of the test.

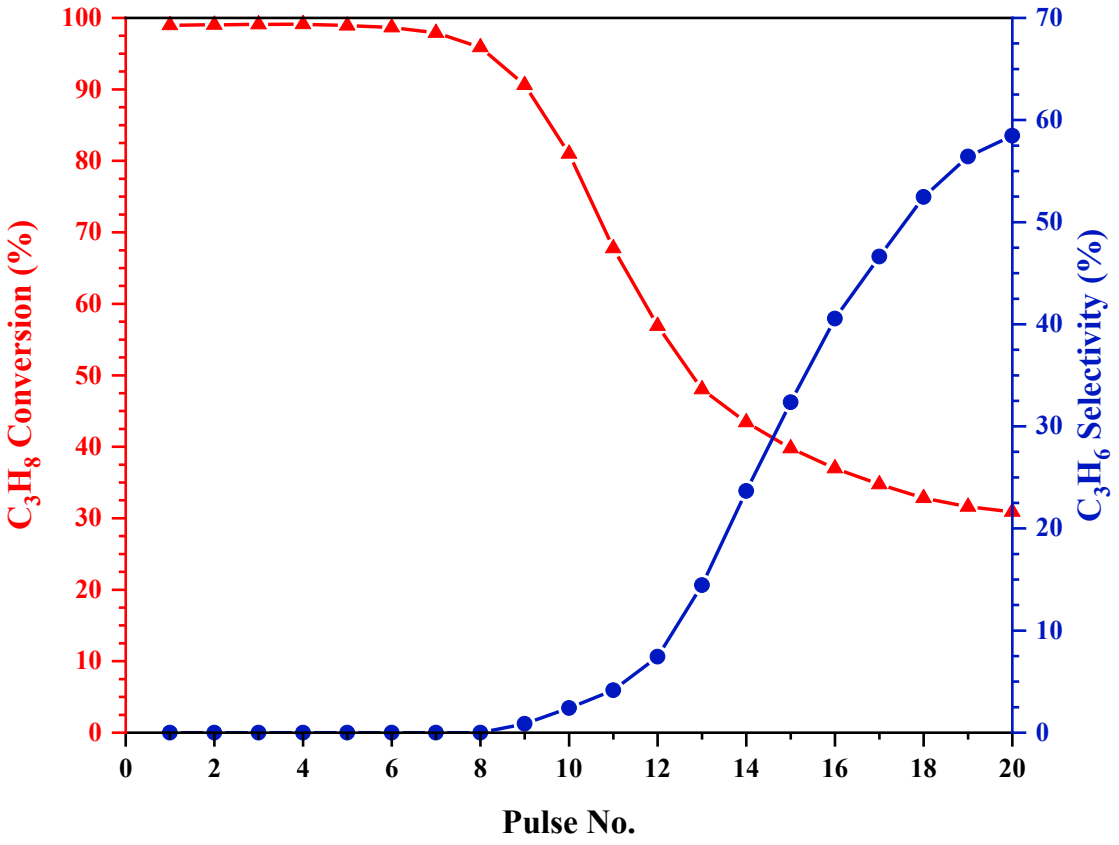

Figure 69: Reaction profile of C_3H_8 conversion and C_3H_6 selectivity during the propane pulsing test performed at the initial stage of the 2nd PDH step: 10VAl, N_2O oxidant, 773 K, 1 atm

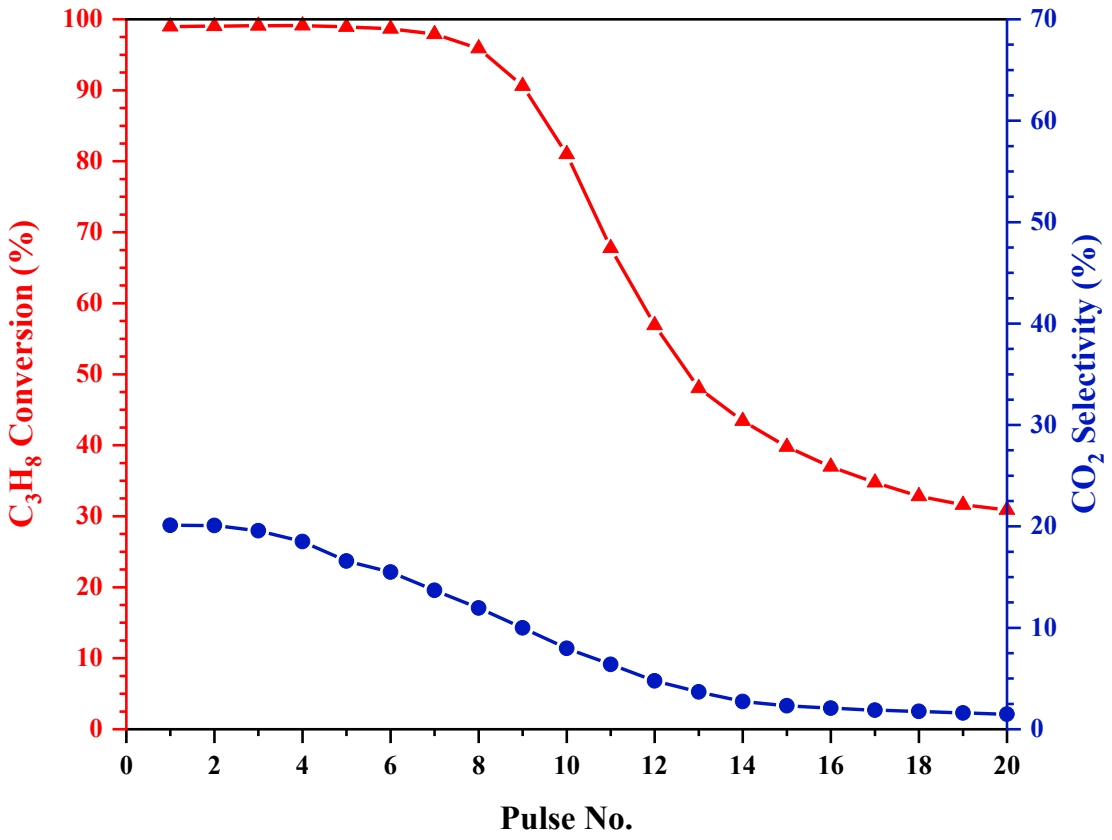

Figure 70: Reaction profile of C_3H_8 conversion and CO_2 selectivity during the propane pulsing test performed at the initial stage of the 2nd PDH step: 10VAl, N_2O oxidant, 773 K, 1 atm

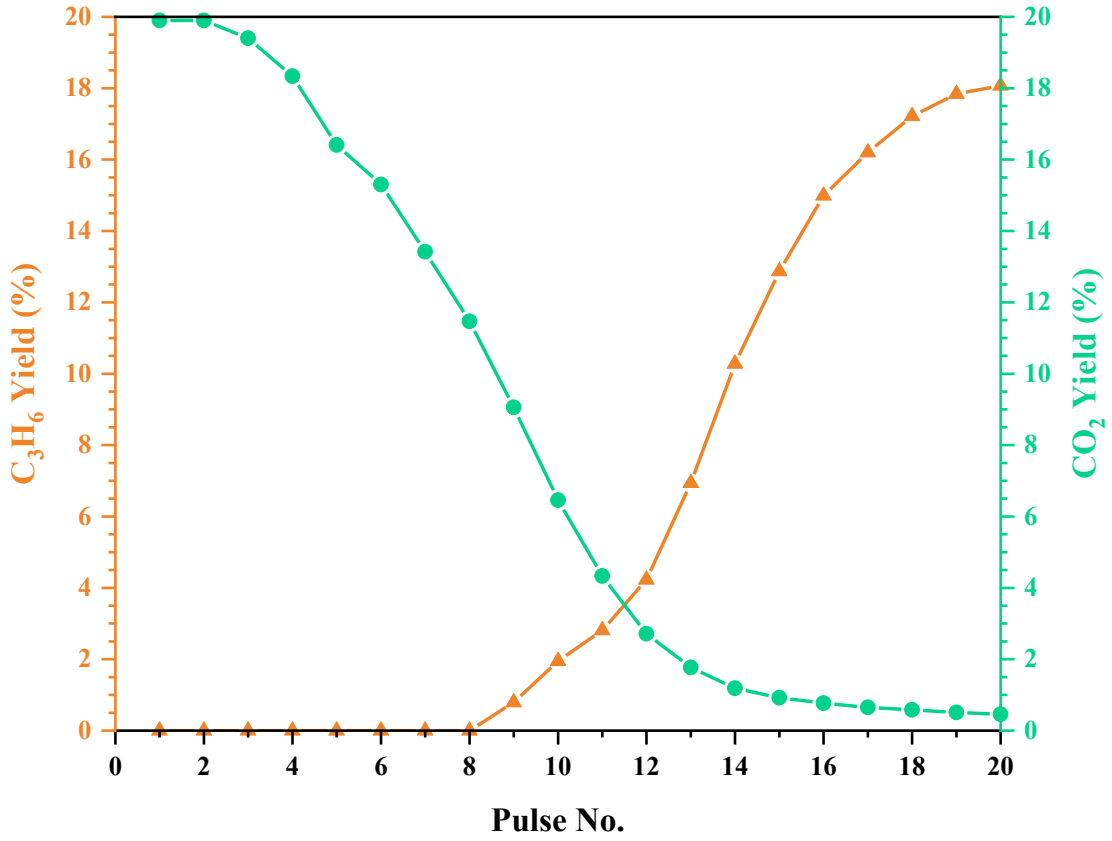

Figure 71: Reaction profile of C_3H_6 and CO_2 yields during the propane pulsing test performed at the initial stage of the 2nd PDH step: 10VAl, N_2O oxidant, 773 K, 1 atm

Reaction profiles detailing the pulsing data obtained from the 6th PDH step in cycles utilising N_2O, are presented in Figures 72-74. Figures 72 and 73 are propane conversion, propene and CO_2 selectivity plots and Figure 74 presents the resulting propene and CO_2 yield.

A notable change in the propane conversion is found in comparison to those obtained during the 2nd PDH step of CL-PODH redox cycles utilising N_2O. This change was also observed in the data obtained when employing O_2 as the oxidant. From Figure 72 below, propane conversion decays rapidly, dropping from ~67.1 % to 33.0 % by the 12th propane pulse whereafter, it remains relatively stable until reaction completion. Likewise, the inverse relationship between propane conversion and propene selectivity is apparent, where a decline in propane conversion occurs with a rise in selectivity towards propene. Figure 73 displays the selectivity profile for CO_2, where the selectivity towards CO_2 remains significantly low throughout the entirety of the pulsing test. An initial CO_2 selectivity of ~0.7 % is observed, declining to negligible levels in consecutive pulses. The resulting yield profiles, shown in Figure 74 behave accordingly: CO_2 yields remain insignificant throughout the test, where propene production forms instantly and is inherently favoured, where a maximum yield of ~20.1 % is achieved by the end of the test.

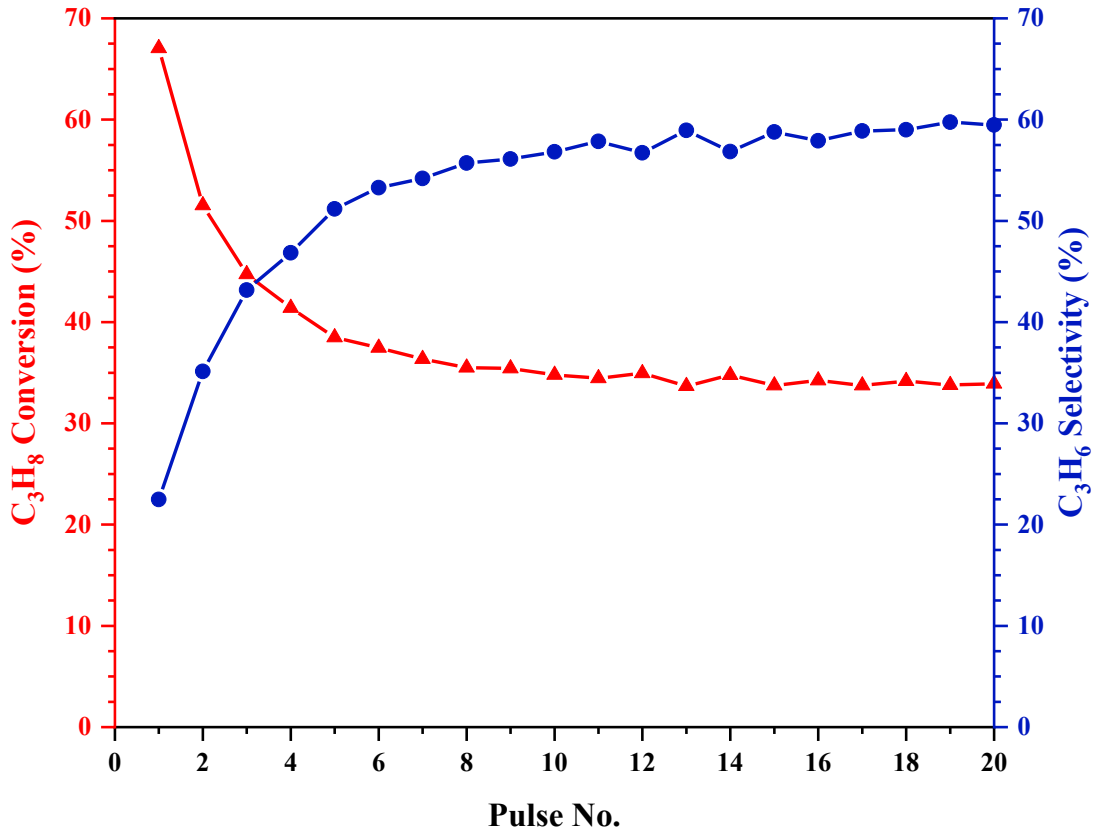

Figure 72: Reaction profile of C_3H_8 conversion and C_3H_6 selectivity during the propane pulsing test performed at the initial stage of the 6th PDH step: 10VAl, N_2O oxidant, 773 K, 1 atm

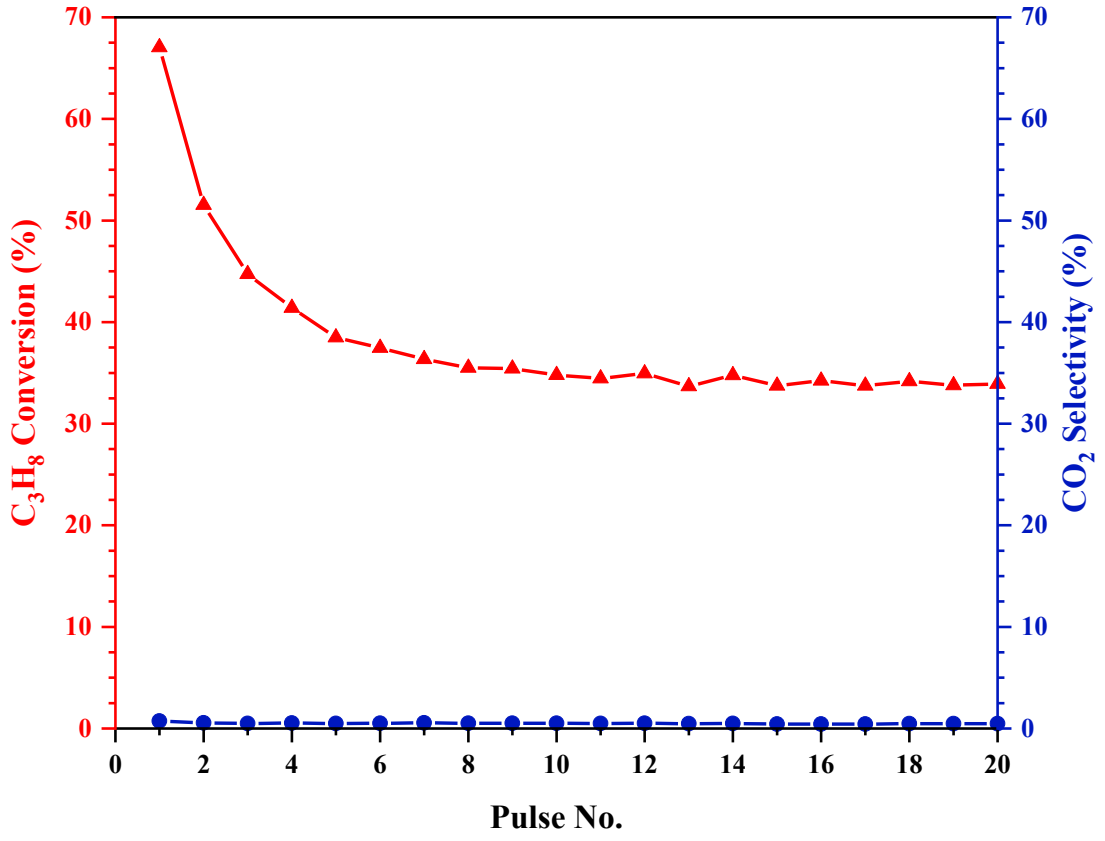

Figure 73: Reaction profile of C_3H_8 conversion and CO_2 selectivity during the propane pulsing test performed at the initial stage of the 6th PDH step: 10VAl, N_2O oxidant, 773 K, 1 atm

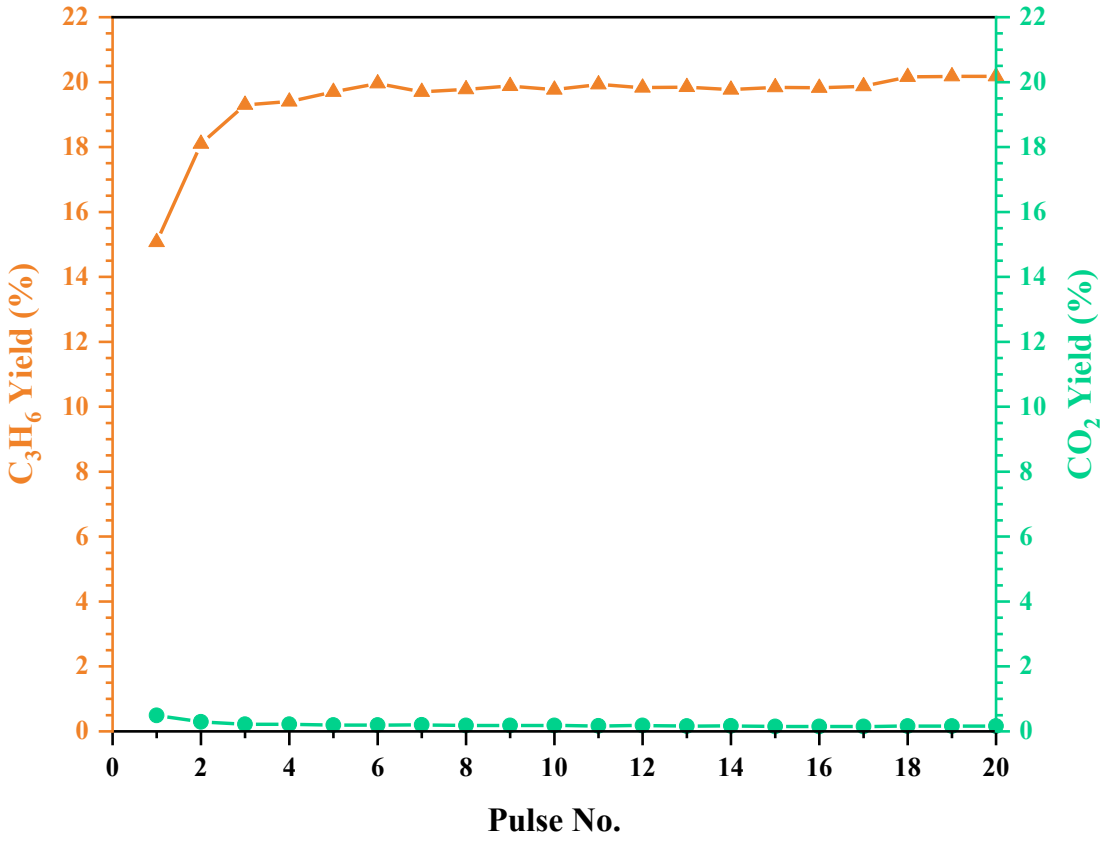

Figure 74: Reaction profile of C_3H_6 and CO_2 yields during the propane pulsing test performed at the initial stage of the 6th PDH step: 10VAl, N_2O oxidant, 773 K, 1 atm

4.4 Post-Reaction Characterisation

This section details the post-reaction characterisation results of various spent VAl catalyst samples by BET, Raman, XRD, TGA-TPO and XPS.

4.4.1 VAl Catalysts, CL-PODH Cycling Tests, O_2 Oxidant

4.4.1.1 BET Surface Area Determination

Table 29 summarises the BET results obtained for spent 5, 7.5 and 10VAl catalysts, analysed upon completion of CL-PODH redox cycling tests using O_2 as the oxidant.

Table 29: Surface area, pore volume and average pore diameter of spent 5, 7.5 and 10VAl catalysts from CL-PODH redox cycles utilising O_2 as the oxidant

Sample	S_{BET} ($m^2\ g^{-1}$)	V_{pore} ($cm^3\ g^{-1}$)	Avg. pore diameter (Å)
Fresh 5VAl	175	0.64	48
Spent 5VAl 10 Cycles, 773 K, O_2	178	0.66	48
Fresh 7.5VAl	171	0.62	48
Spent 7.5VAl 10 Cycles, 773 K, O_2	145	0.54	54
Fresh 10VAl	145	0.55	43
Spent 10VAl 10 Cycles, 773 K, O_2	129	0.51	62

Post-reaction results obtained by BET analysis for the 5VAl catalyst are comparable to those obtained for the fresh sample. However, a profound loss in both the surface area and pore volume of spent 7.5 and 10VAl catalysts was found. This observation is indicative of either pore blockage from coke deposits or the sintering of the catalyst surface which may occur due to the elevated reaction temperatures. [103]

4.4.1.2 Raman Spectroscopy

Raman spectra obtained for spent VAl catalysts from CL-PODH redox cycling tests utilising O_2 as the oxidant are presented below in Figure 75.

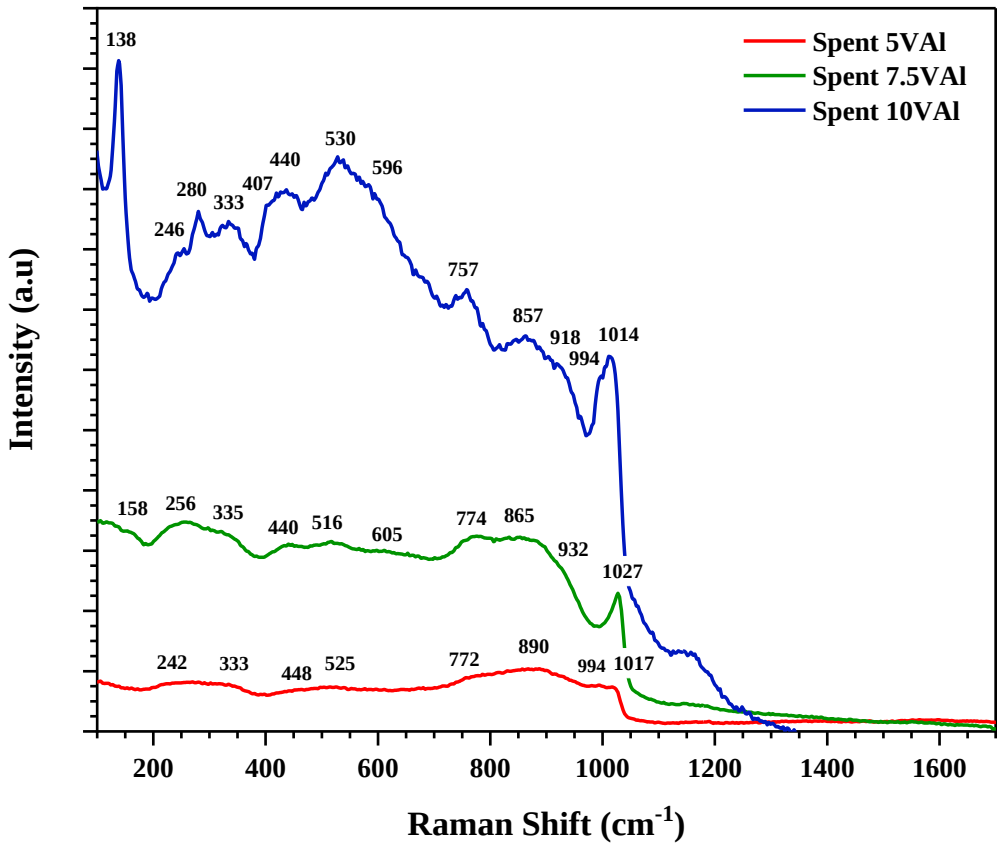

Figure 75: Raman spectra spent VAl catalysts from CL-PODH redox cycles utilising O_2 as the oxidant

Raman bands at ~1017 and 1014 cm^{-1}, which relate to the symmetric vibration of the V=O bond in polyvanadate species, are present in the spectra for spent 5 and 10VAl catalysts. This band shifts to 1027 cm^{-1} in the post-reaction Raman of the 7.5VAl catalyst, which is associated with V=O bond in monovanadates, as observed in the spectrum of the fresh 7.5VAl sample. Raman features attributed to crystalline V_2O_5 are present at ~994, 407, 280, 246, and 138 cm^{-1} in the spectrum associated with the 10VAl catalyst [31, 96], whilst broad Raman bands which indicate the presence of polyvanadate species are present in the spectra for all spent VAl samples. As discussed previously, broad bands in the region of ~200-400, ~400-600 and ~600-956 cm^{-1} have previously been assigned to the bending modes, symmetric stretching and asymmetric stretching vibrations found in polymeric V-O-V linkages. [31, 45, 51, 97, 98]

Post-reaction Raman spectra for 10VAl catalyst also reveal the formation of a broad shouldering band at ~918 cm^{-1}, which has been established in literature as the vibration

correlating to V-O-Al linkages. [68]. Notably, this feature was not present in the Raman spectra of fresh VAl samples.

4.4.1.3 XRD

XRD patterns of spent VAl catalysts are presented in Figure 76. The diffraction patterns are indistinguishable to those obtained for the fresh VAl samples, which exhibiting broad peaks characteristic of the amorphous γ-Al_2O_3 support at 2θ = 37.1, 46.0 and 66.7°. The absence of sharp peaks relating to crystalline V_2O_5 implies that the vanadia species present in spent VAl samples is highly dispersed on the surface.

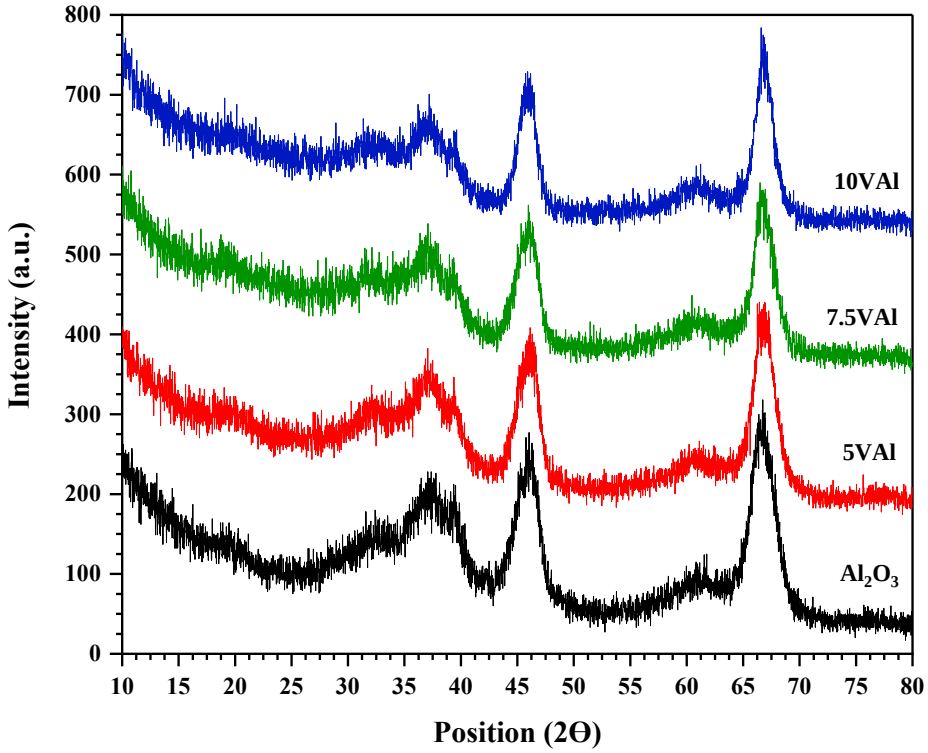

Figure 76: XRD patterns of γ-Al_2O_3 and spent VAl catalysts from CL-PODH redox cycles utilising O_2 as the oxidant

4.4.1.4 TGA-TPO

TGA-TPO measurements were conducted to investigate the extent of carbon laydown on spent VAl catalyst samples. Figures 77-85 present post-reaction TPO and MS profiles, following the ion current produced from m/z 18 and m/z 44 for H_2O and CO_2 evolution.

Table 30 shows the overall weight loss at the temperature range (465 – 887 K) associated with CO_2 evolution observed in the MS data. Unfortunately, water evolution occurs simultaneously at these temperatures, thus achieving accurate weight loss data exclusive to carbon deposits is not possible and the values obtained are relative estimations.

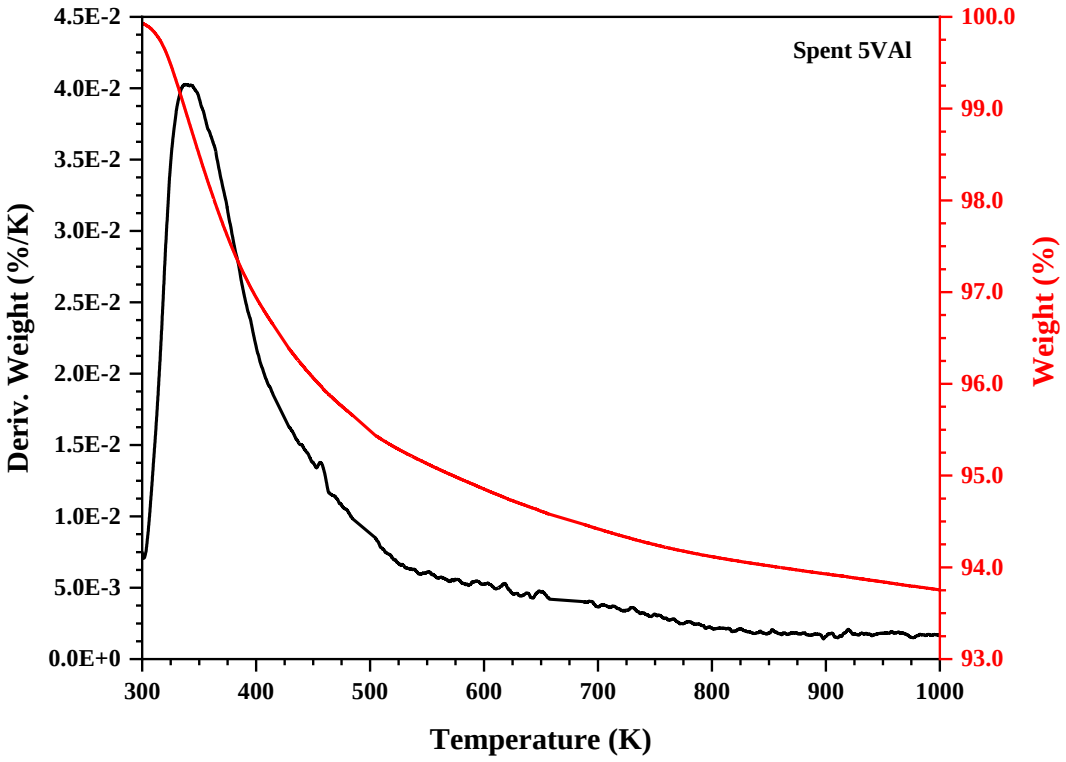

Figure 77: TPO weight loss profile of the spent 5VAl catalyst, CL-PODH redox cycling test, O_2 oxidant, 773 K

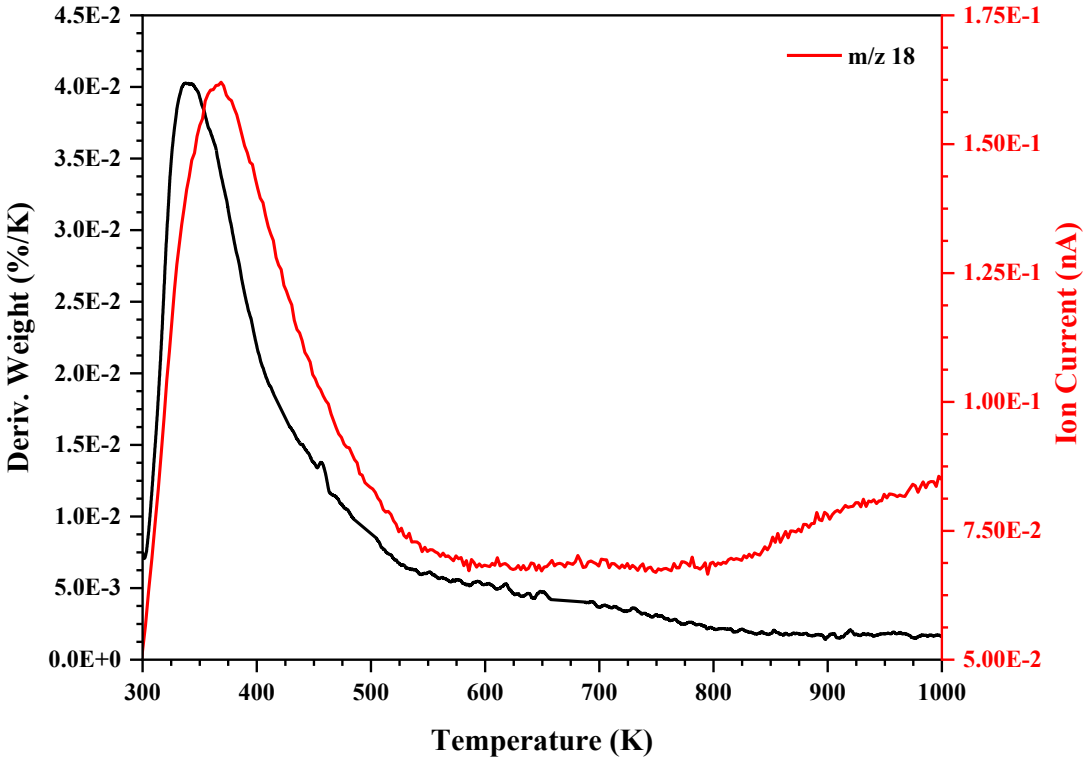

Figure 78: TPO-MS profile of the spent 5VAl catalyst, m/z = 18

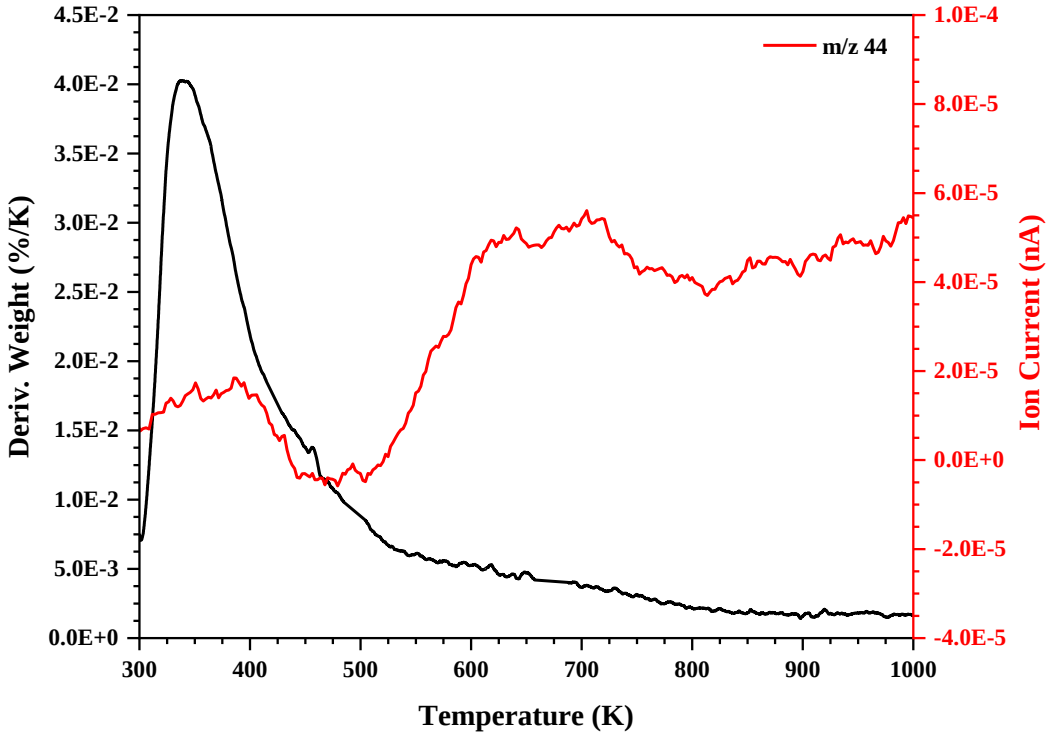

Figure 79: TPO-MS profile of the spent 5VAl catalyst, m/z = 44

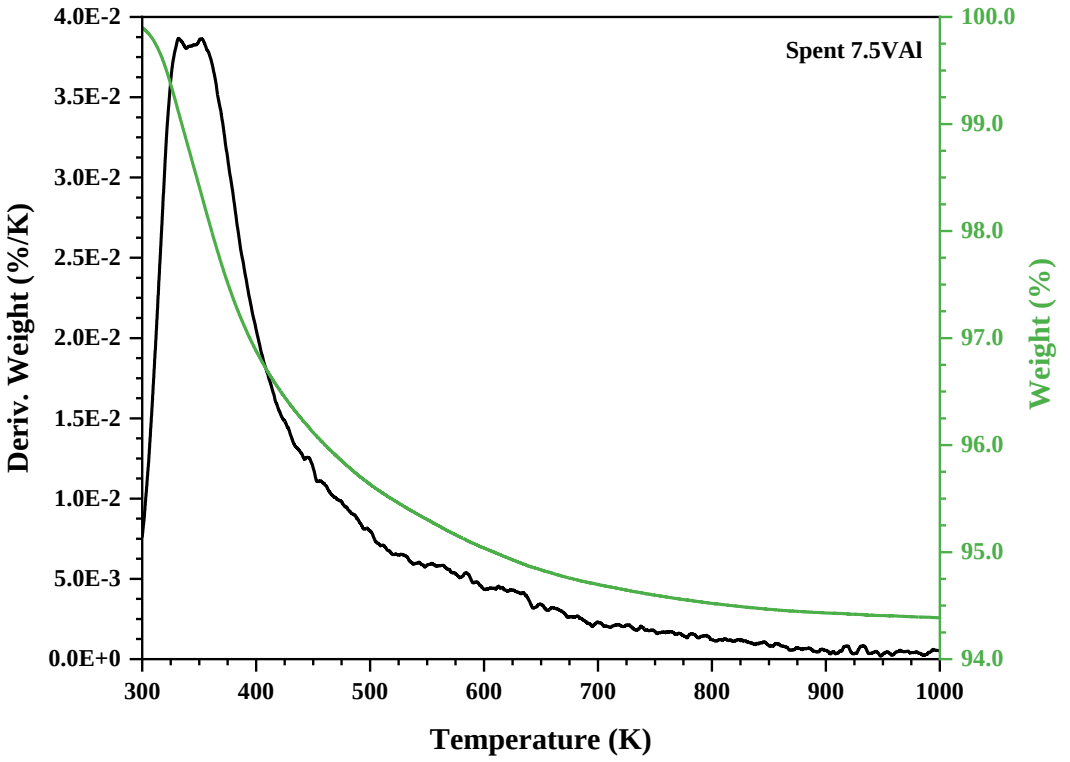

Figure 80: TPO weight loss profile of the spent 7.5VAl catalyst, CL-PODH redox cycling test, O_2 oxidant, 773 K

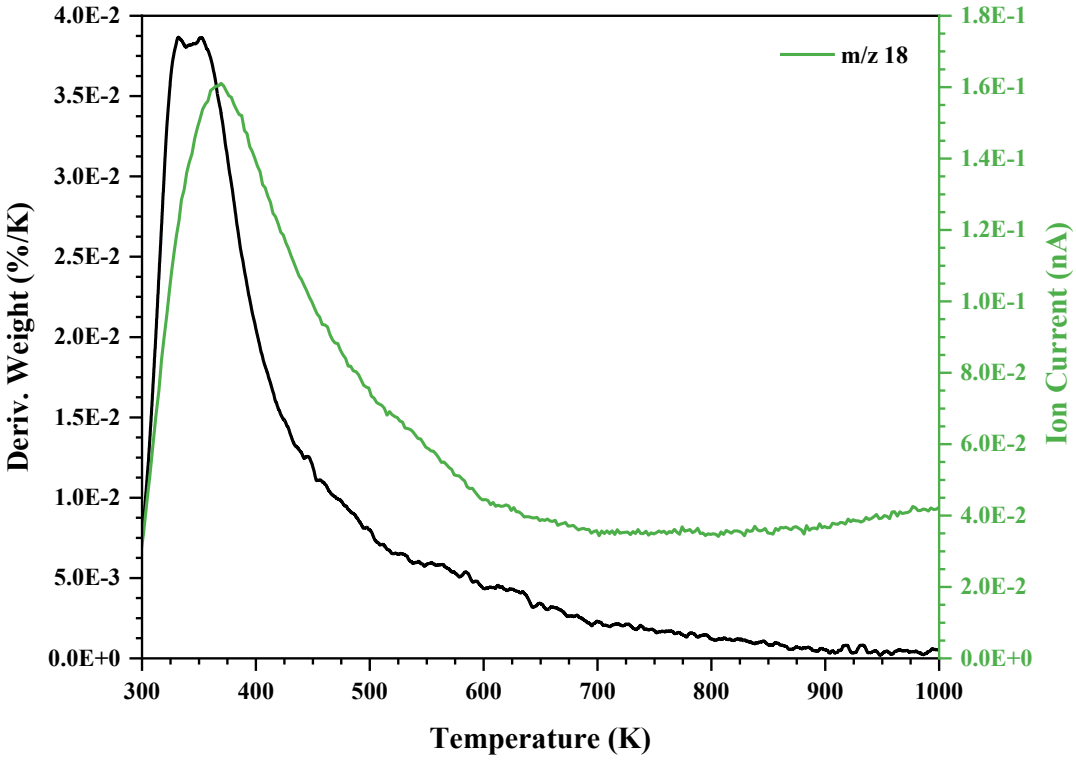

Figure 81: TPO-MS profile of the spent 7.5VAl catalyst, m/z = 18

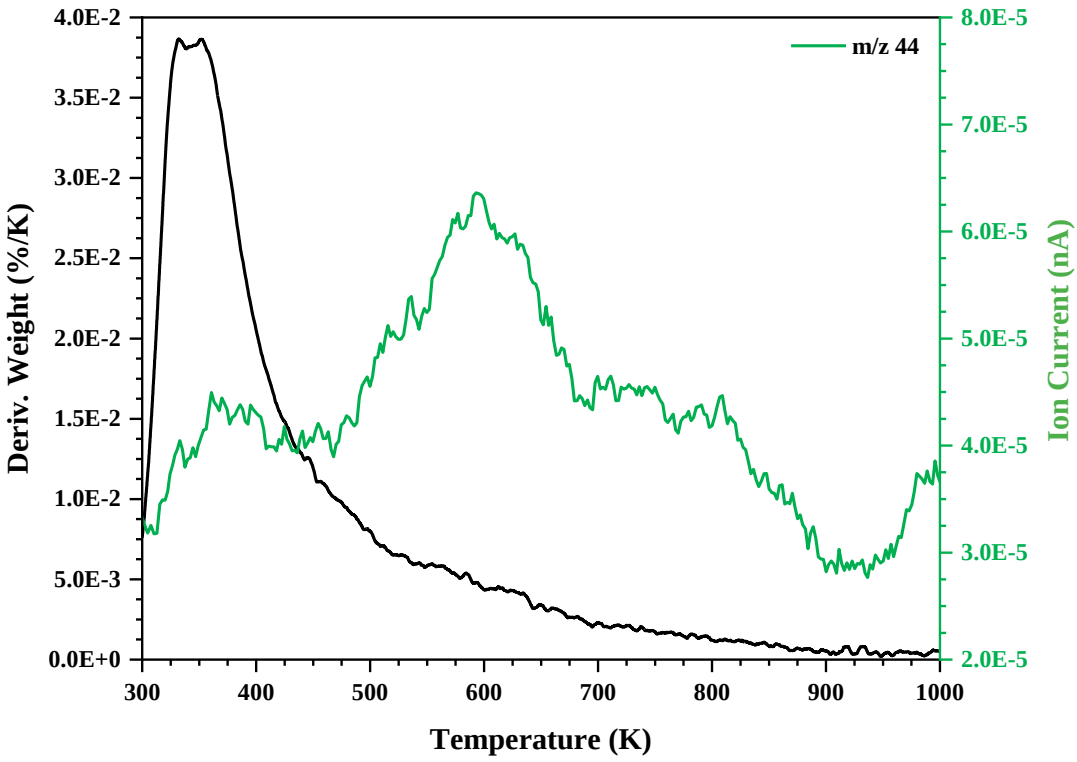

Figure 82: TPO-MS profile of the spent 7.5VAl catalyst, m/z = 44

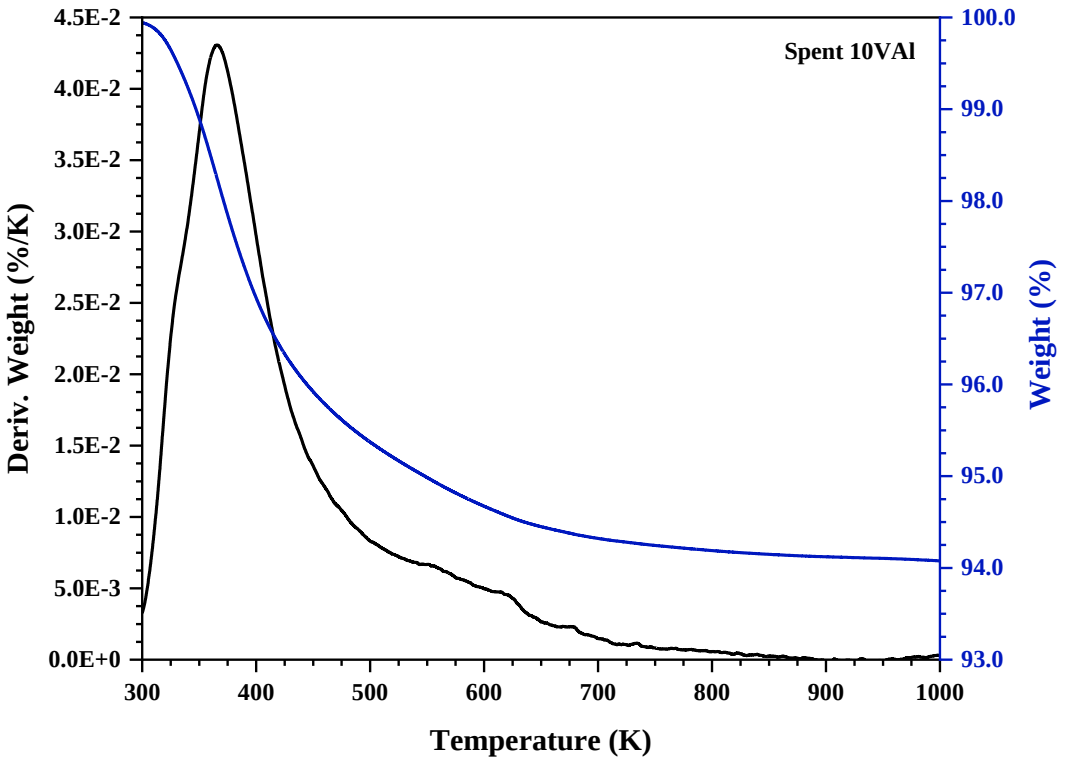

Figure 83: TPO weight loss profile of the spent 10VAl catalyst, CL-PODH redox cycling test, O_2 oxidant, 773 K

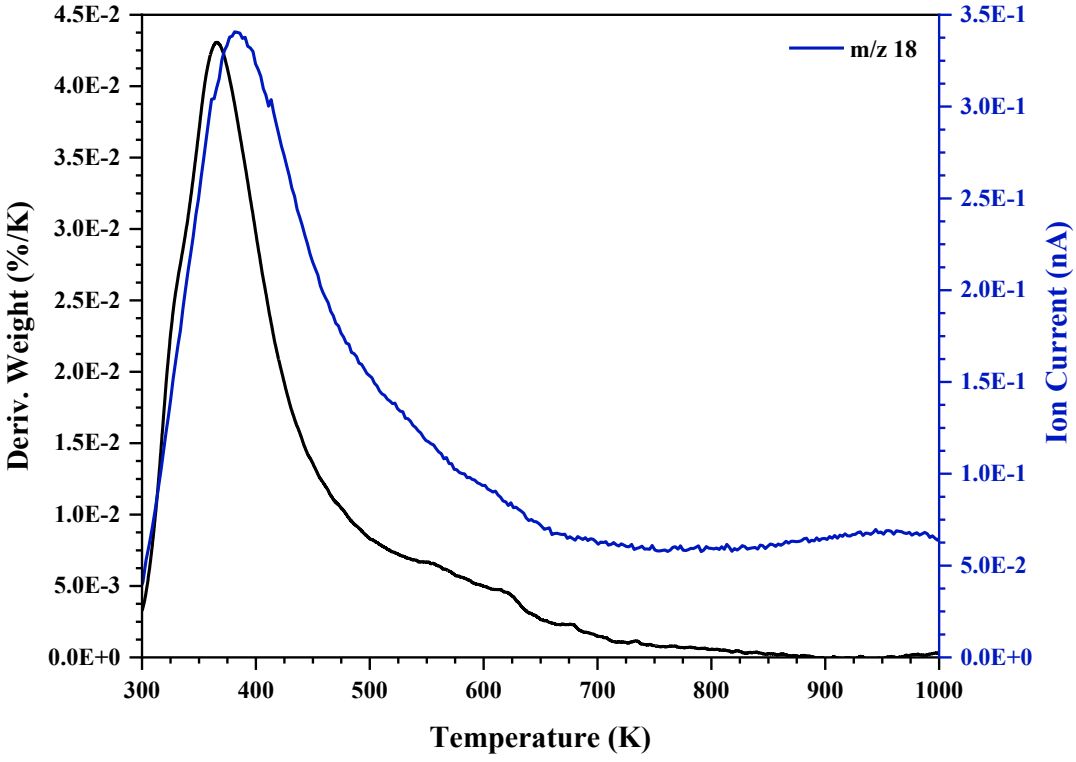

Figure 84: TPO-MS profile of the spent 10VAl catalyst, m/z = 18

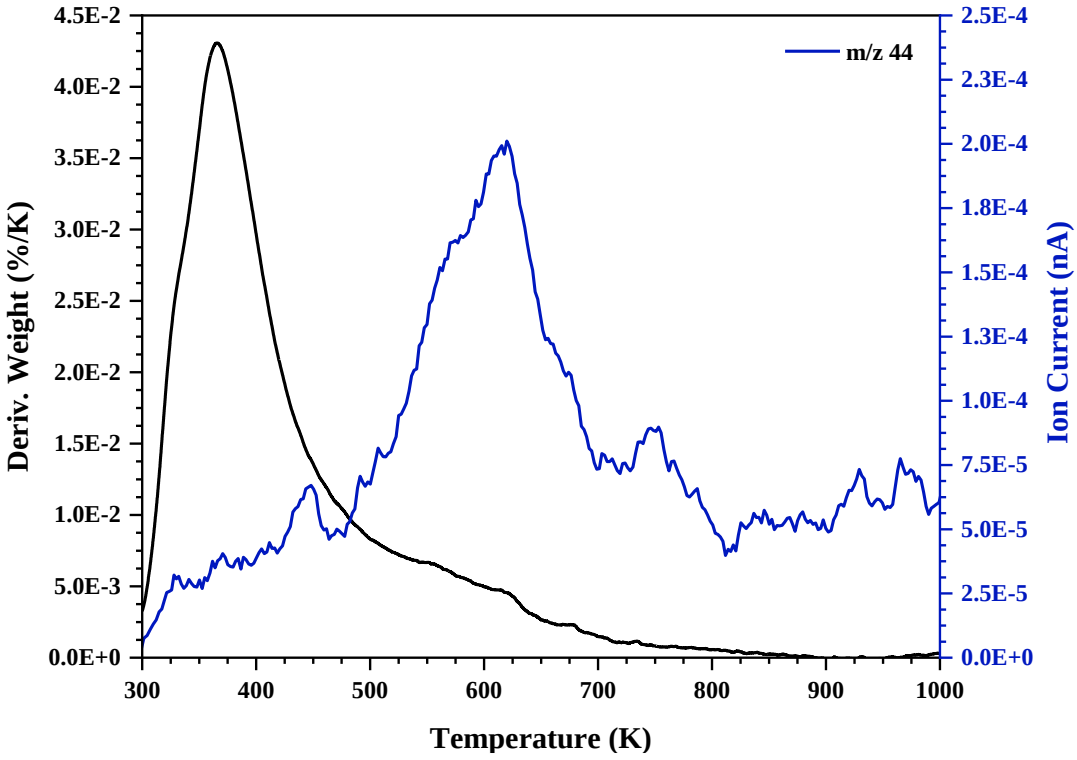

Figure 85: TPO-MS profile of the spent 10VAl catalyst, m/z 44

Table 30: Weight loss at temperatures associated with CO_2 evolution, 465-887 K

Sample	Weight Loss (%)
Spent 5VAl 10 Cycles, 773 K, O_2	1.9
Spent 7.5VAl 10 Cycles, 773 K, O_2	1.5
Spent 10VAl 10 Cycles, 773 K, O_2	1.6

Since water and CO_2 evolution occurs simultaneously, we cannot distinguish between the two or draw any tangible conclusions regarding the extent of carbon laydown. Although the ion current of m/z 44 is comparatively weak to m/z 18, its presence in the mass spectral data suggests that, despite performing a catalyst regeneration step, carbon laydown is present on all three spent VAl catalyst samples. The evolution of CO_2 is more marked in the mass spectral plot for the spent 10VAl catalyst; however, the weight loss is highest in the 5VAl catalyst sample which may be as a result of a greater loss of water.

4.4.2 10VAl Catalyst: Long Duration PDH Test

4.4.2.1 BET Surface Area Determination

Table 31 summarises the BET results obtained for the spent 10VAl catalyst sample from the long duration 3 h PDH test. A loss in the surface area and pore volume is observed with respect to the fresh 10VAl catalyst, again implying either catalyst sintering or the blockage of pores from carbonaceous deposits. [103]

Table 31: Surface area, pore volume and average pore diameter of the spent 10VAl catalyst removed after the long duration 3 h PDH step, 773 K

Sample	S_{BET} ($m^2\ g^{-1}$)	V_{pore} ($cm^3\ g^{-1}$)	Avg. pore diameter (Å)
Fresh 10VAl	145	0.55	43
Spent 10VAl 3 h PDH, 773 K	124	0.43	48

4.4.2.2 Raman Spectroscopy

Raman spectra for the post-reaction 10VAl catalyst from the long duration 3 h PDH test is presented in Figure 86.

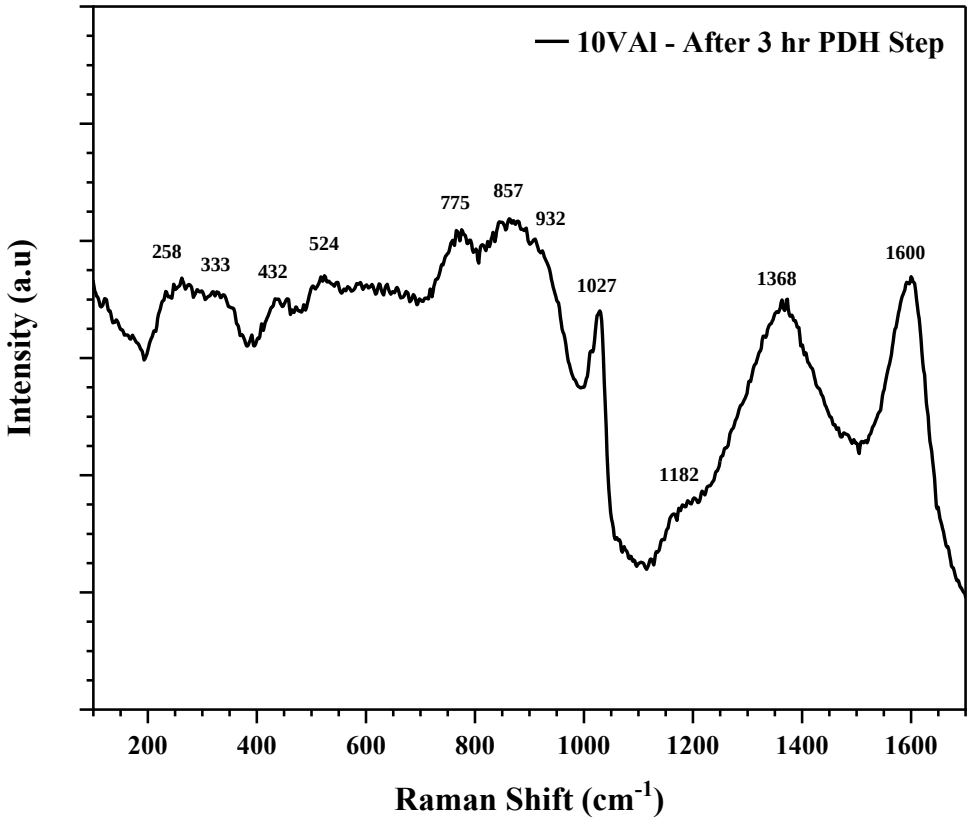

Figure 86: Raman spectra for spent 10VAl catalyst sample: 3 h PDH step, 773 K

Post-reaction Raman provides evidence of significant coke formation with the presence of G (~1600 cm^{-1}) and D (~1368 cm^{-1}) bands even after catalyst regeneration, in addition to a shoulder at ~1182 cm^{-1}.[104] Notably, Raman bands which relate to crystalline V_2O_5 are now essentially non-existent, with the spectra exhibiting bands at ~1027 and 259-932 cm^{-1}, assigned exclusively to monomeric and polymeric vanadia species as previously discussed.

4.4.2.3 XRD

The XRD pattern of the post 3 h PDH step sample, is identical to the spent 10VAl sample in Figure 76. The diffraction pattern remains noisy with broad peaks at 2θ = 37.1, 46.0 and 66.7°, which are characteristic only of the amorphous γ-Al_2O_3 support.

4.4.2.4 TGA-TPO

A post-reaction TPO measurement was performed to investigate the extent of carbon deposition. Figures 87-89 present post-reaction TPO and MS profiles, following the ion current produced by m/z 18 and m/z 44. The MS data reveals that the temperature associated with CO_2 evolution is 486 to 860 K and the weight loss associated with carbon is approximately 2.5 %.

Measured water in the mass spectral data is nominal indicating that this weight loss arises mainly from CO_2 evolution which occurs from the burn-off of carbonaceous deposits.

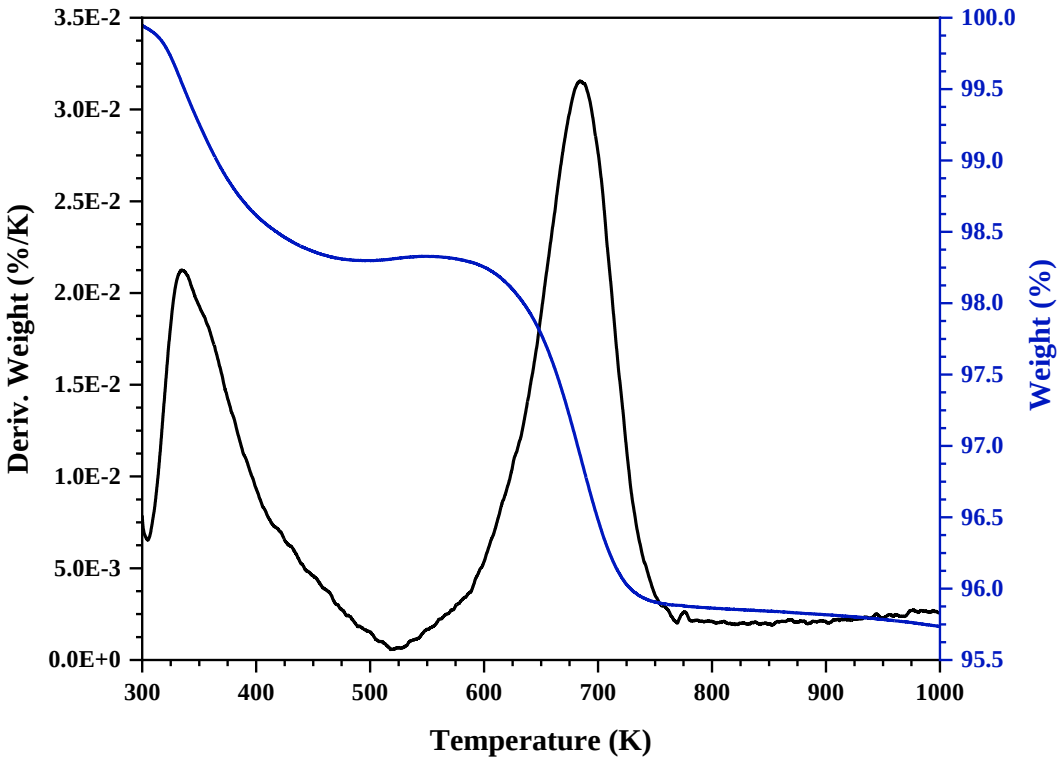

Figure 87: TPO weight loss profile of the spent 10VAl catalyst, 3 h PDH step

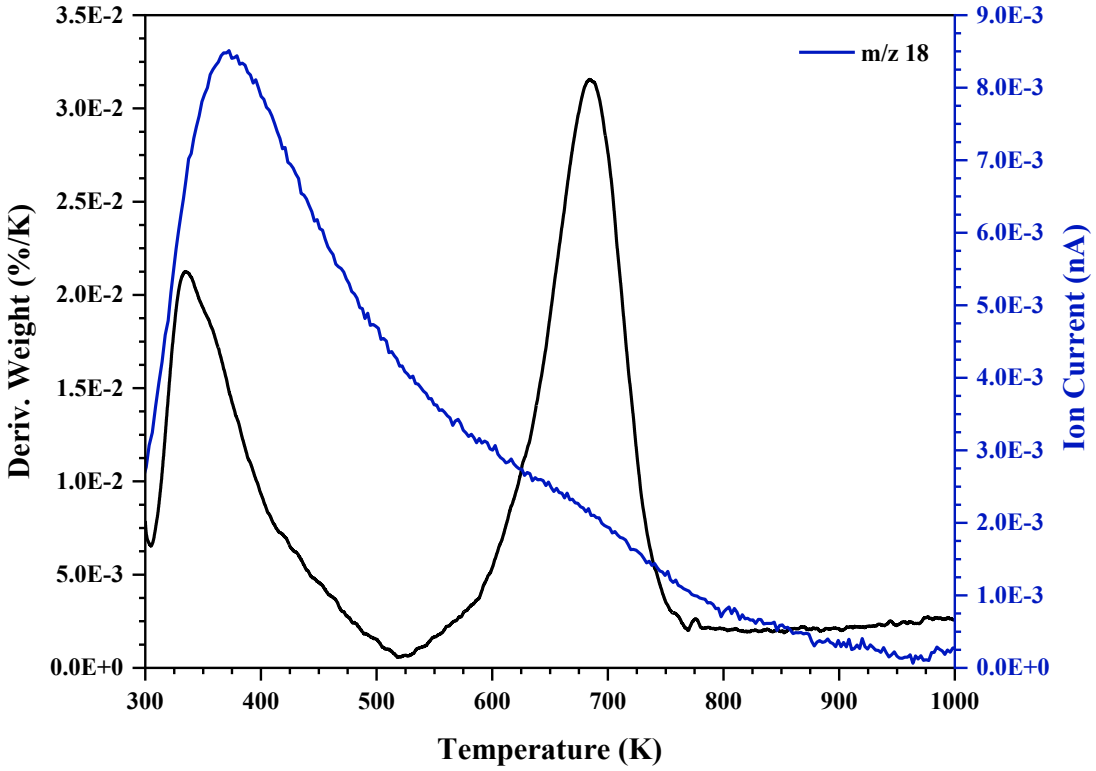

Figure 88: TPO-MS profile of the spent 10VAl catalyst, 3 h PDH step, m/z = 18

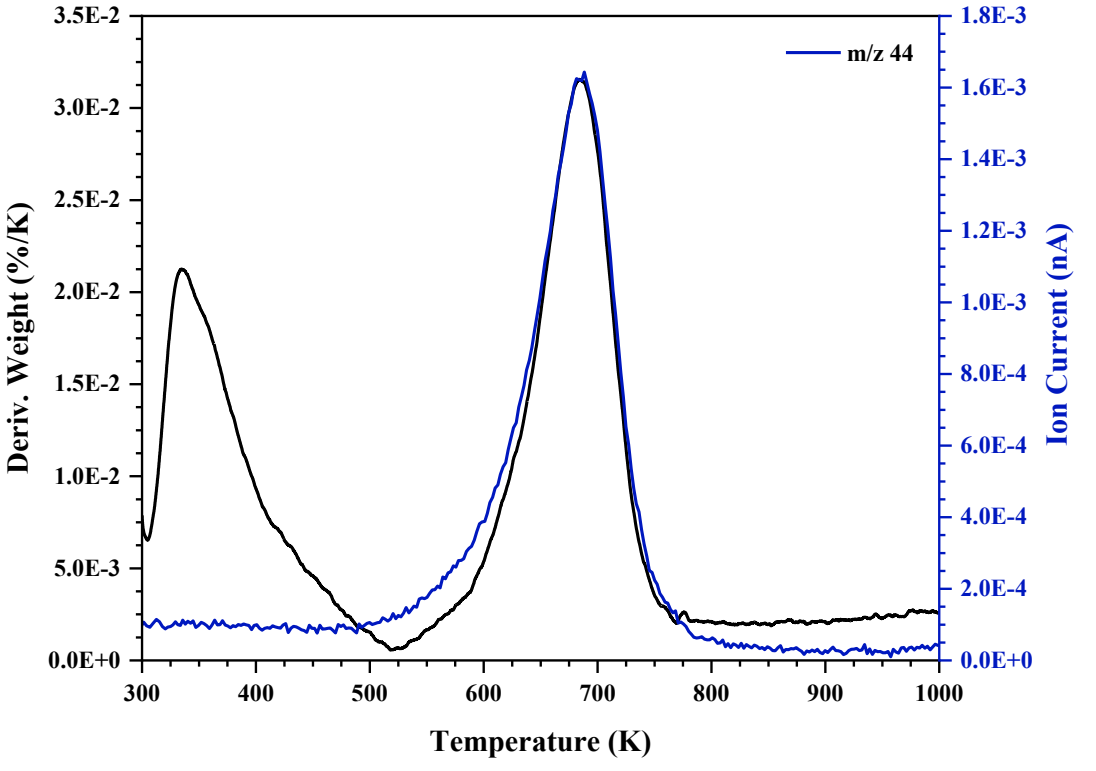

Figure 89: TPO-MS profile of the spent 10VAl catalyst, 3 h PDH step, m/z = 44

4.4.3 10VAl Catalyst: CL-PODH Cycling Tests, N_2O and CO_2 Oxidants

4.4.3.1 BET Surface Area Determination

Table 32 summarises the BET results obtained for post-reaction 10VAl catalyst samples from CL-PODH redox cycling tests utilising N_2O and CO_2 oxidants in the catalyst regeneration step.

Table 32: Surface area, pore volume and average pore diameter of spent 10VAl catalyst samples from CL-PODH redox cycles utilising N_2O and CO_2 oxidants

Sample	S_{BET} ($m^2\ g^{-1}$)	V_{pore} ($cm^3\ g^{-1}$)	Avg. pore diameter (Å)
Fresh 10VAl	145	0.55	43
Spent 10VAl 10 Cycles, 773 K, N_2O	137	0.49	54
Spent 10VAl 10 Cycles, 773 K, CO_2	120	0.49	61

On comparing with the fresh 10VAl sample, a loss in both surface area and pore volume is observed. This again suggests the presence of either catalyst sintering, or pore blockage due to coke formation, despite regeneration steps with N_2O and CO_2 being carried out. [103] The loss is most profound in the catalyst using CO_2 in the cycling test, which also displays a significant increase in the average pore diameter.

4.4.3.2 Raman Spectroscopy

Raman spectra obtained for spent 10VAl catalysts from CL-PODH redox cycling tests utilising N_2O and CO_2 oxidants are presented below in Figure 90.

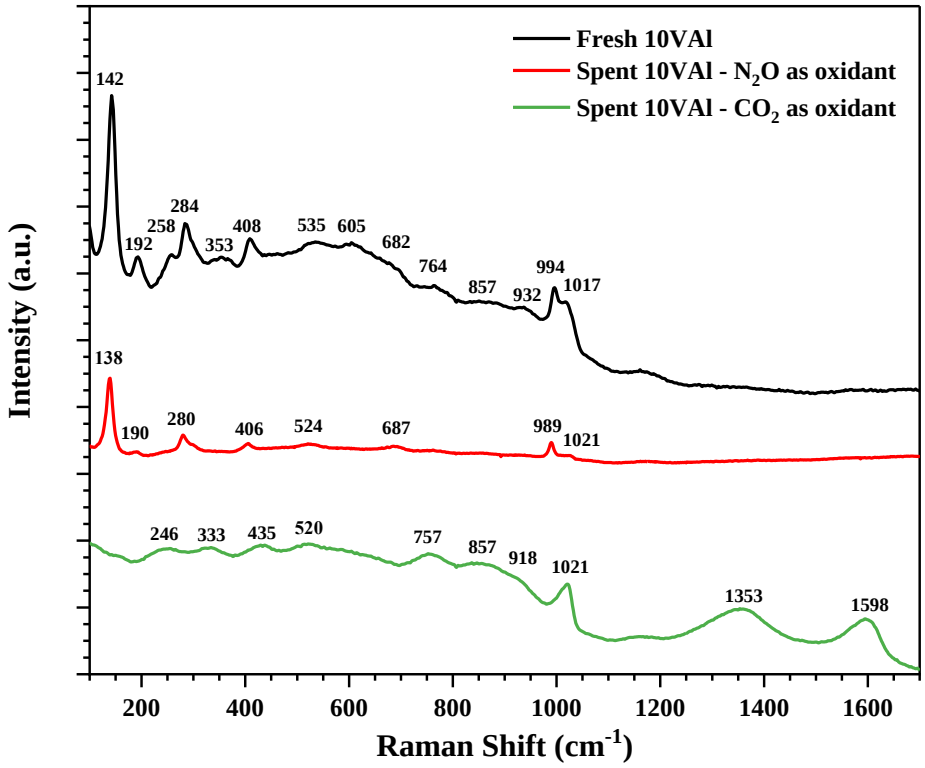

Figure 90: Raman spectra for spent 10VAl catalysts from CL-PODH redox cycles utilising N_2O and CO_2 oxidants

Post-reaction Raman of the sample analysed after CL-PODH redox cycles using N_2O proposes that the catalyst is completely re-oxidised back to crystalline V_2O_5-like species. This is apparent from the loss of broad features in the ~200-956 cm^{-1} region relating to bridging polyvanadate species and the reduction in the relative instensity of the 1021cm^{-1} band, relating to isolated monovanadates.

Post-reaction Raman of the sample analysed after redox cycles using CO_2 however, changes significantly with respect to the fresh 10VAl sample. Raman features relating to vanadium oxide species are masked with the formation of two broad bands at ~1598 and 1353 cm^{-1}, characteristic of the G and D bands present in coke. [104]

4.4.3.3 XRD

The XRD patterns of spent 10VAl samples removed after CL-PODH redox cycling tests utilising N_2O and CO_2 oxidants are identical to the pattern obtained for the fresh 10VAl sample. The diffraction pattern remains noisy with broad peaks at $2\theta = 37.1$, 46.0 and 66.7°, which are characteristic only of the γ-Al_2O_3 support.

4.4.3.4 TGA-TPO

Post-reaction TPO measurements were also conducted to investigate the extent of carbon laydown after CL-PODH redox cycling tests utilising N_2O and CO_2 oxidants.

Figure 91 presents the resulting TPO derivative weight profile and Table 33 summarises the total weight loss at temperatures associated with CO_2 evolution. It should be noted that MS data was not obtained for these measurements. Consequently, the temperature range established for CO_2 evolution in the mass spectral data in Section 4.4.1.4 was used to estimate the weight loss here.

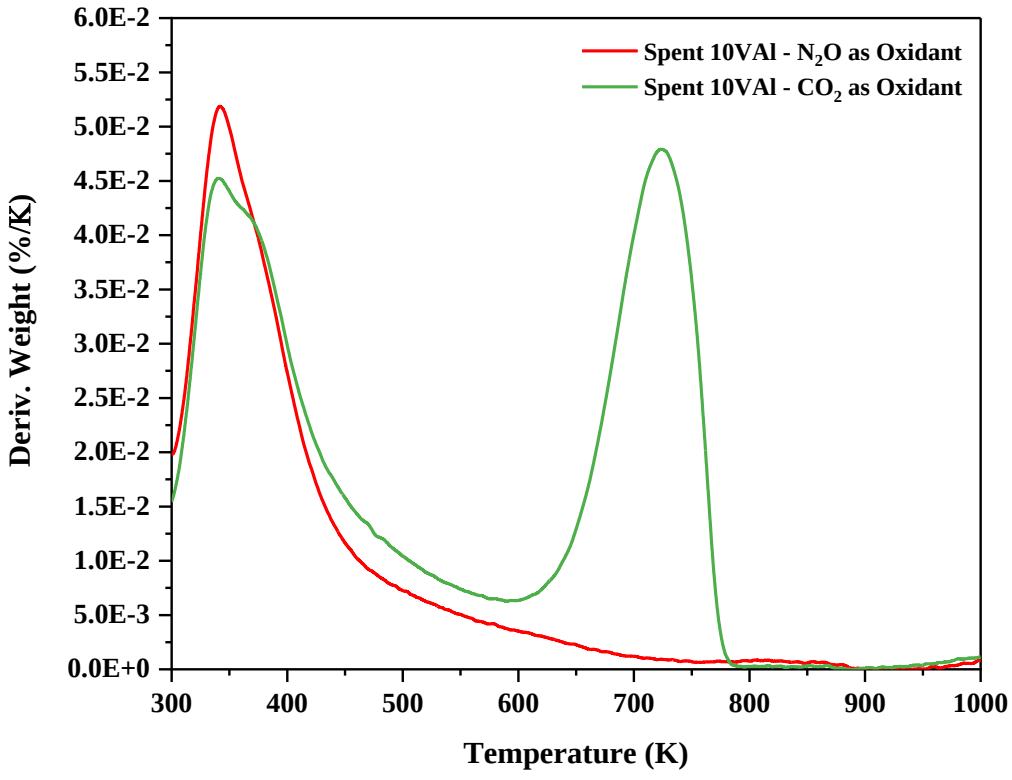

Figure 91: TPO weight loss profile of the spent 10VAl catalyst, CL-PODH redox cycling test, N_2O and CO_2 oxidant, 773 K

Table 33: Weight loss at temperatures associated with CO_2 evolution, 465-887 K

Sample	Weight Loss (%)
Spent 10VAl 10 Cycles, 773 K, N_2O	1.2
Spent 10VAl 10 Cycles, 773 K, CO_2	5.6

The calculated weight loss varies considerably between samples which use N_2O and CO_2 oxidants in the catalyst regeneration step. Since water and CO_2 evolution may occur simultaneously, a conclusive determination regarding the extent of carbon laydown cannot be made for the sample removed after CL-PODH redox cycles using N_2O. Where CO_2 is used as the oxidant however, the weight loss associated with CO_2 evolution is significant, occurring at distinctively higher temperatures than those observed for H_2O evolution. In this case, the overall weight loss was >5 %, implying that the extent of carbon laydown is substantial when using CO_2 as the oxidant.

4.4.4 10VAl Catalyst: Characterised at Various Stages of the CL-PODH Redox Cycling Test

Since the 10VAl catalyst generates the most promising results within the varying vanadium loading series, additional post-characterisation tests were performed to analyse this catalyst at various stages throughout the CL-PODH cycling tests.

4.4.4.1 BET Surface Area Determination

BET results for spent 10VAl catalyst samples, removed and characterised at various stages are detailed in Table 34.

Table 34: Surface area, pore volume and average pore diameter of spent 10VAl catalyst samples, CL-PODH redox cycles, O_2 oxidant, 773 K

Sample	S_{BET} ($m^2\ g^{-1}$)	V_{pore} ($cm^3\ g^{-1}$)	Avg. pore diameter (Å)
Fresh 10VAl	145	0.55	43
Spent 10VAl After 1st PDH Step	119	0.46	43
Spent 10VAl After 1st O_2 Regen Step	132	0.49	48
Spent 10VAl After 5th PDH Step	126	0.49	48
Spent 10VAl After 5th O_2 Regen Step	132	0.48	48
Spent 10VAl After Overnight Ar Purge	134	0.52	53
Spent 10VAl After 6th PDH Step	124	0.52	53
Spent 10VAl After 10th PDH Step	120	0.48	53
Spent 10VAl After 10th O_2 Regen Step	129	0.51	62

A significant loss in the surface area and pore volume is observed for the sample removed after the 1st PDH step, indicating the formation of coke on the catalyst. Upon re-oxidising the catalyst with O_2 in the subsequent catalyst regeneration step however, an increase in both the surface area and pore volume is observed. This trend is reflected throughout the subsequent PDH and catalyst regeneration steps in cycles 5 and 10. A further increase in the surface area, pore volume and average pore diameter is observed for the catalyst sample removed after the overnight argon purge. However, the surface area decreases once more in the catalyst sample removed after the subsequent 6th PDH step.

4.4.4.2 Raman Spectroscopy

Figures 92 and 93 present Raman spectra for spent 10VAl catalyst samples removed at the various stages, labelled accordingly.

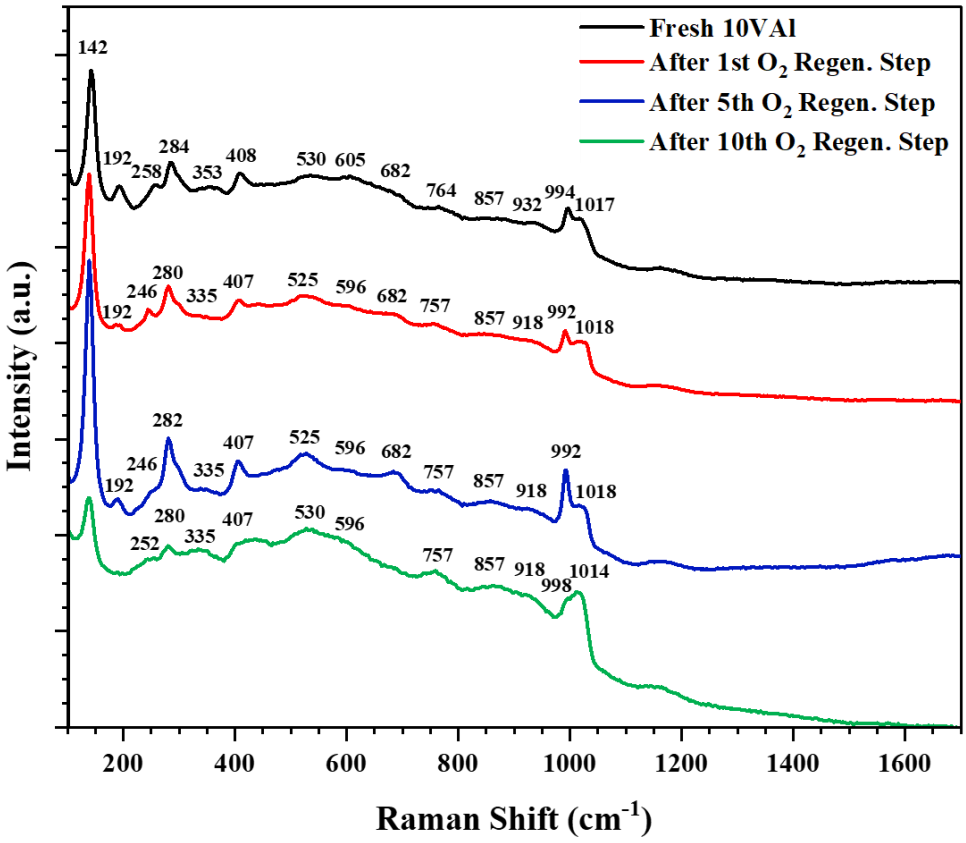

Figure 92: Raman spectra for spent 10VAl catalyst samples removed after catalyst regeneration steps

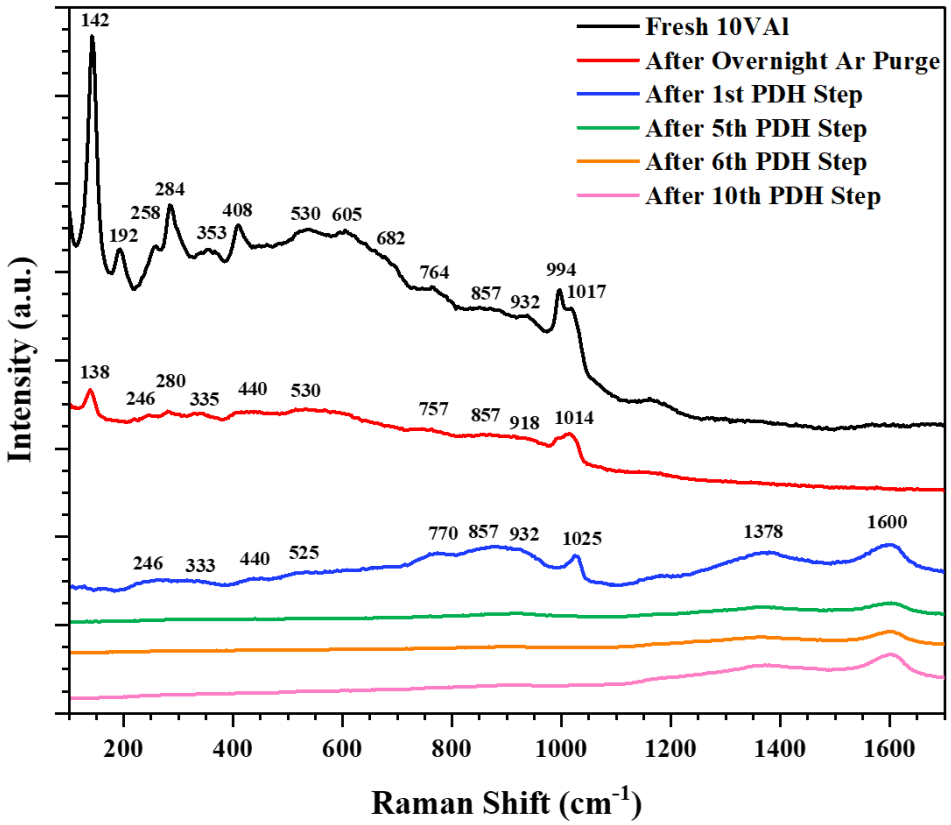

Figure 93: Raman spectra for spent 10VAl catalyst samples removed after overnight Ar purge and PDH steps

Post-reaction Raman of catalyst samples, removed after the 1st and 5th catalyst regeneration step, display minimal changes and remain comparable to the spectra obtained for the fresh 10VAl sample. Slight changes in the spectra are observed in the Raman of the sample removed after the 10th catalyst regeneration step, however, bands relating to crystalline V_2O_5 become less pronounced. The sharp, prominent ~994 cm^{-1} band shifts to ~998 cm^{-1} and decreases in intensity with respect to the ~1014 cm^{-1} band.

Broad Raman bands at ~1600 and 1378 cm^{-1}, attributed to coke formation, are present in the spectra of samples removed after the PDH steps. Furthermore, Raman features relating to monomeric and polymeric vanadia species diminish as the PDH steps proceed. The spectra for the catalyst removed after the overnight argon purge also changes considerably, where Raman bands relating to crystalline V_2O_5 species become less prominent than those observed for the sample removed after the 5th O_2 regeneration step.

4.4.4.3 XRD

XRD patterns of 10VAl catalyst samples removed at the various stages remain identical to the spent 10VAl sample in Figure 76. Diffraction patterns remain noisy with broad peaks at $2\theta = 37.1$, 46.0 and 66.7°, which are characteristic only of the γ-Al_2O_3 support.

4.4.4.4 TGA-TPO

Post-reaction TPO measurements were also performed on 10VAl catalyst samples to investigate the extent of carbon deposition at various stages of the CL-PODH redox cycling test. Figures 94 and 95 present the resulting TPO derivative weight profiles and Table 35 summarises the total weight loss at temperatures associated with CO_2 evolution. MS data was not obtained for the spent 10VAl catalysts removed at the different stages. As such, the temperature range established for CO_2 evolution in the mass spectral data in Section 4.4.1.4 was used to estimate the weight loss here.

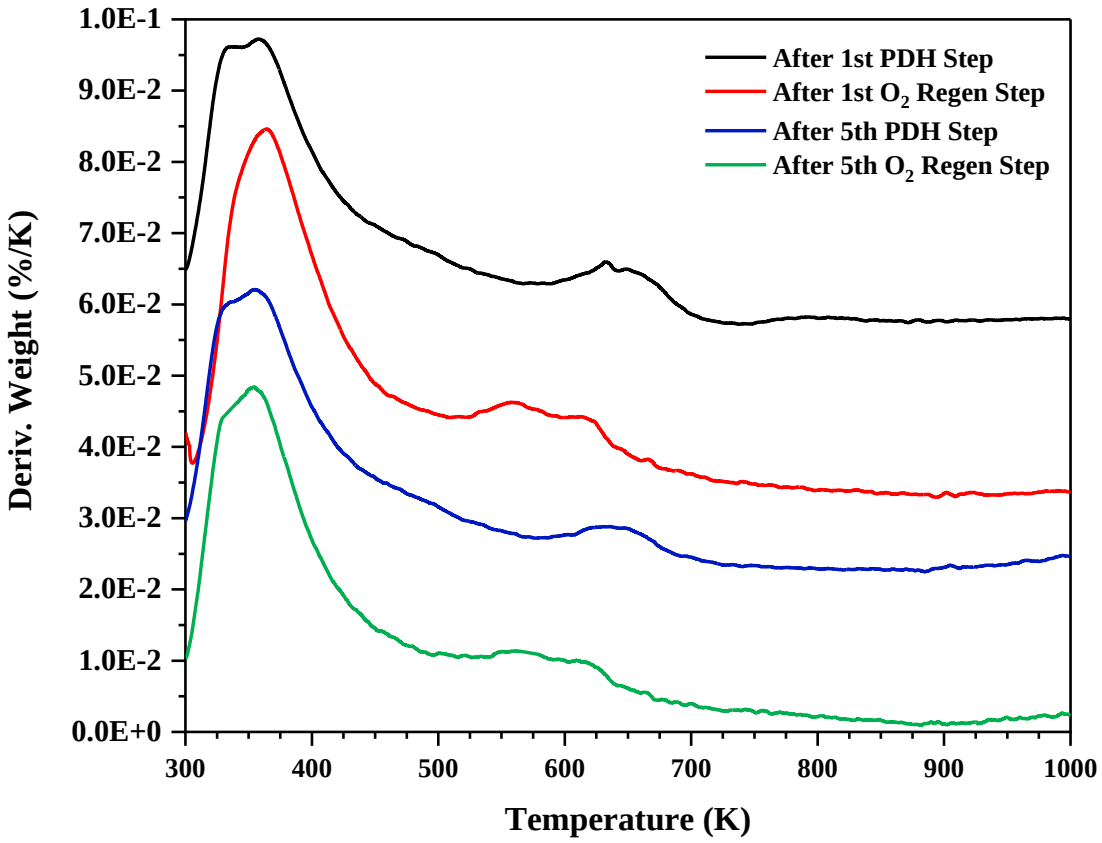

Figure 94: TPO derivative weight profile of spent 10VAl catalyst samples

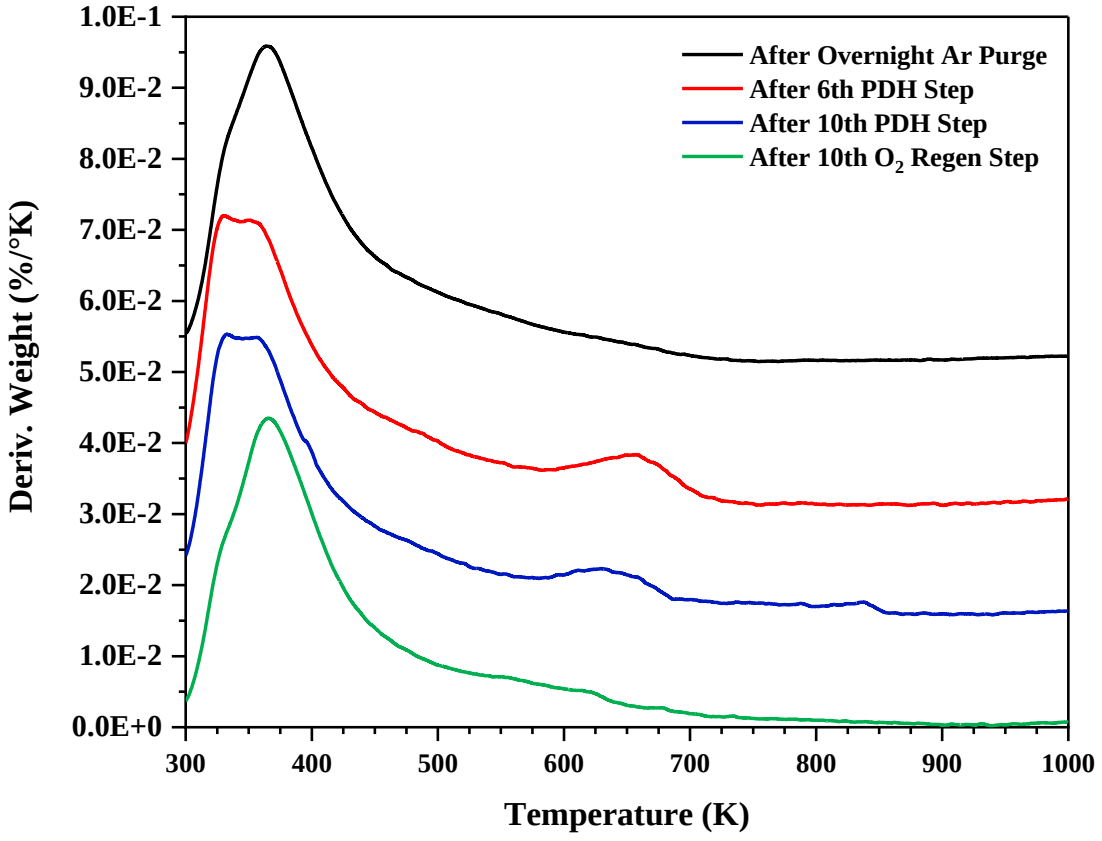

Figure 95: TPO derivative weight profile of spent 10VAl catalyst samples

Table 35: Weight loss at temperatures associated with CO_2 evolution, 465-887 K

Sample	Weight Loss (%)
Spent 10VAl After 1st PDH Step	1.92
Spent 10VAl After 1st O_2 Regen Step	1.69
Spent 10VAl After 5th PDH Step	1.74
Spent 10VAl After 5th O_2 Regen Step	1.11
Spent 10VAl After Overnight Ar Purge	0.54
Spent 10VAl After 6th PDH Step	1.77
Spent 10VAl After 10th PDH Step	1.85
Spent 10VAl After 10th O_2 Regen Step	1.60

At the temperature range tested, the percentage weight loss is highest for catalysts removed after performing the PDH steps. A decrease in the weight loss is observed in samples removed after subsequent catalyst regeneration steps, suggesting that some of the carbon laydown formed from the PDH reaction is successfully removed. The weight loss observed in the catalyst removed after the overnight argon purge decreases further, indicating additional carbon laydown is removed even after the 5th O_2 regeneration step has been performed.

4.4.4.5 XPS

XPS was performed on spent 10VAl samples removed at various stages of CL-PODH redox cycling tests. Results from the XPS measurements are presented in Figure 96 and Table 36, which compare the resulting atomic concentrations of surface V^{4+} and V^{5+} species at the various stages throughout the CL-PODH redox cycles.

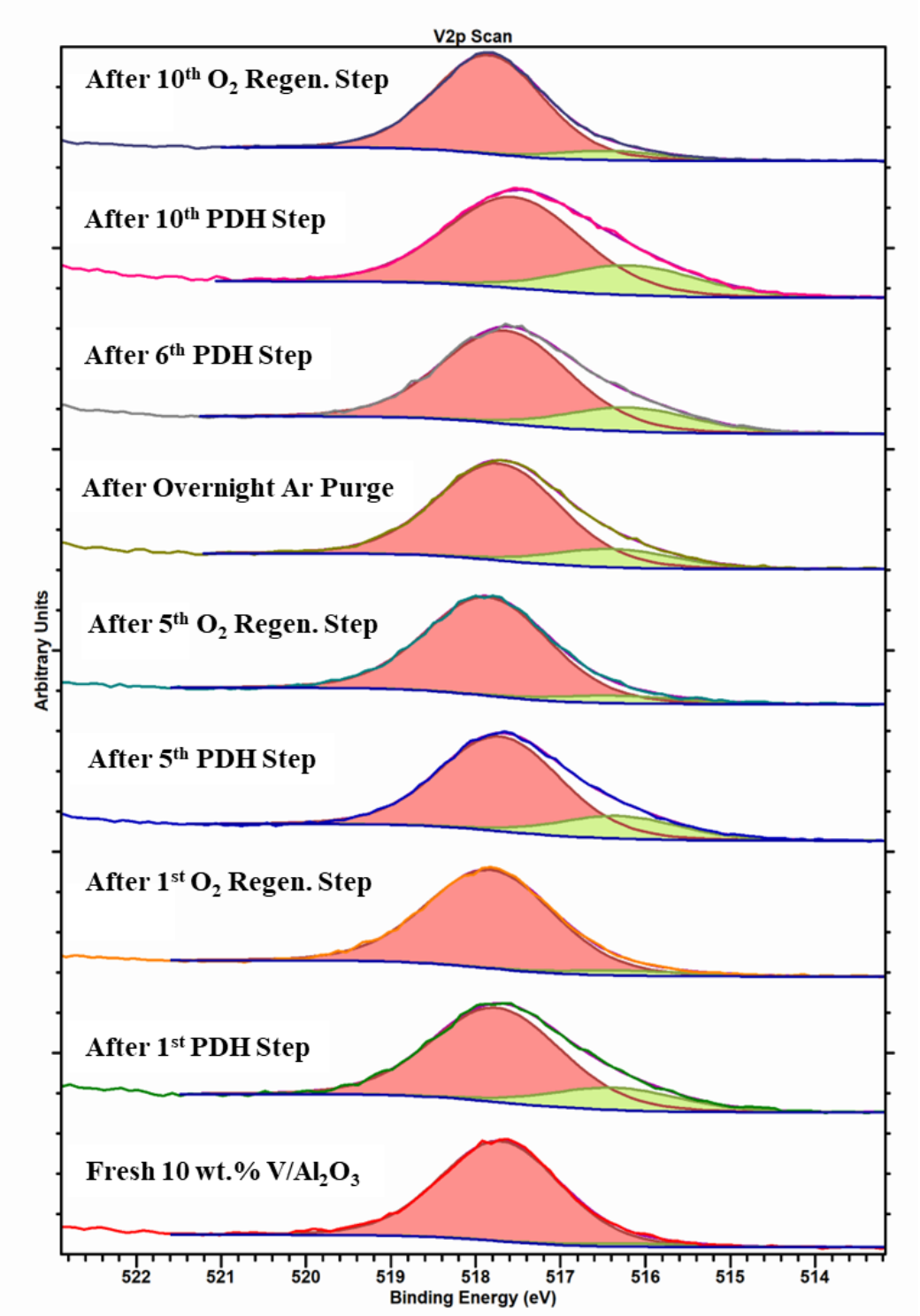

Figure 96: XPS spectra of fresh and spent 10VAl catalyst samples, $V2p^{3/2}$ where pink represents V^{5+} species and green represents V^{4+} species

Table 36: Summary of XPS results detailing the atomic % concentration of surface V^{5+} and V^{4+} species in fresh and spent 10VAl samples

Sample	% Conc. V $2p^{3/2}$ (V^{5+})	% Conc. V $2p^{3/2}$ (V^{4+})	Ratio of V^{5+}/V^{4+}
Fresh 10VAl	**3.04**	**0.10**	**30.4**
Spent 10VAl After 1st PDH Step	**2.52**	**0.60**	**4.2**
Spent 10VAl After 1st O_2 Regen Step	**3.18**	**0.16**	**19.9**
Spent 10VAl After 5th PDH Step	**2.47**	**0.59**	**4.2**
Spent 10VAl After 5th O_2 Regen Step	**3.10**	**0.22**	**14.1**
Spent 10VAl After Overnight Ar Purge	**2.61**	**0.50**	**5.2**
Spent 10VAl After 6th PDH Step	**2.20**	**0.56**	**3.9**
Spent 10VAl After 10th PDH Step	**2.40**	**0.78**	**3.1**
Spent 10VAl After 10th O_2 Regen Step	**3.19**	**0.30**	**10.6**

The ratio has been taken between the atomic concentrations of V^{5+}/V^{4+}, where smaller values indicate higher levels of surface V^{4+} species, which implies that the catalyst is in a more reduced state. The XPS spectra and V^{5+}/V^{4+} ratios of the fresh 10VAl catalyst indicate that V^{5+} species are prevalent on the surface. A considerable increase in surface V^{4+} species is observed after performing the PDH steps, where the V^{5+}/V^{4+} ratio decreases from 30.4 to 4.2 and 3.9. After each corresponding catalyst regeneration step, the presence of surface V^{5+} species increases. However, the ratio exhibits an overall decrease as the CL-PODH redox cycles proceed, suggesting that the catalyst is never fully regenerated back to its original state, despite the reoxidation of the catalyst surface. Another interesting observation is the V^{5+}/V^{4+} ratio in the sample removed after the overnight argon purge, where an increase in surface V^{4+} species is observed as the ratio decreases further from 14.1 to 5.3.

XPS measurements were also performed on spent 10VAl samples removed at various stages of the CL-PODH redox cycling test utilising N_2O as the oxidant. The resulting atomic concentrations of surface V^{4+} and V^{5+} species at the various stages are presented in Figure 97 and Table 37.

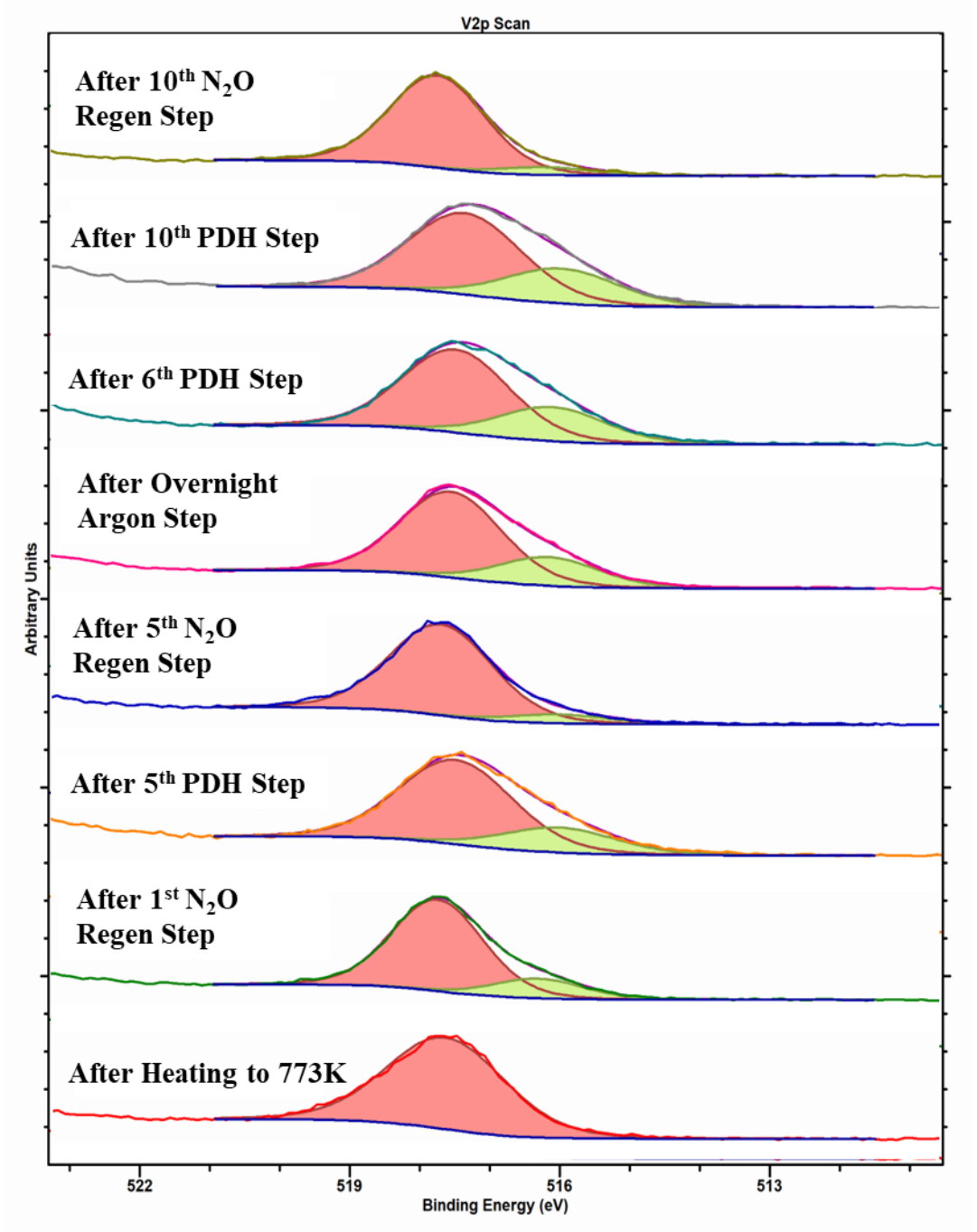

Figure 97: XPS spectra of fresh and spent 10VAl catalyst samples, $V2p^{3/2}$ where pink represents V^{5+} species and green represents V^{4+} species

Table 37: Summary of XPS results detailing the atomic % concentration of surface V^{5+} and V^{4+} species in fresh and spent 10VAl samples

Sample	% Conc. V $2p^{3/2}$ (V^{5+})	% Conc. V $2p^{3/2}$ (V^{4+})	Ratio of V^{5+}/V^{4+}
Spent 10VAl After Heating to 773K	**3.64**	**0.00**	***a***
Spent 10VAl After 1st N_2O Regen Step	**3.78**	**0.80**	**4.7**
Spent 10VAl After 5th PDH Step	**2.72**	**0.81**	**3.4**
Spent 10VAl After 5th N_2O Regen Step	**3.71**	**0.36**	**10.3**
Spent 10VAl After Overnight Ar Purge	**3.33**	**1.11**	**3.0**
Spent 10VAl After 6th PDH Step	**2.56**	**1.05**	**2.4**
Spent 10VAl After 10th PDH Step	**2.66**	**1.14**	**2.3**
Spent 10VAl After 10th N_2O Regen Step	**3.84**	**0.32**	**12.0**

[a] V^{4+} ions were not observed on the surface of the sample removed after heating to 773 K

XPS measurements reveal an even higher increase in surface V^{4+} species after the 5th and 6th PDH step than 10VAl samples where O_2 was utilised as the oxidant. Upon further comparison, the regeneration of V^{5+} sites after corresponding catalyst regeneration steps are also not as significant, owing to the fact that N_2O is a milder oxidant. The presence of surface V^{5+} actually increases as CL-PODH redox cycles proceed, which indicates that that the re-oxidation of catalyst sites is favoured with increasing TOS. Lastly, the V^{5+}/V^{4+} ratio decreases once more in the sample removed after the overnight argon purge from 10.3 to 3.0, indicating that, despite being held under an inert atmosphere, there are more surface V^{4+} species present.

4.4.5 10VAl Catalyst: Investigating the Colour Gradient of the Bed

When removing the spent 10VAl catalyst from redox cycling tests utilising O_2 as the oxidant, we observe a profile along the catalyst bed with a colour gradient (Figure 98). The catalyst bed was separated into three sections, denoted A, B and C, to represent the top, middle and bottom of the bed. The samples were subsequently analysed with Raman and TGA-TPO measurements to investigate the variation in vanadium oxide species and extent of carbon laydown within these distinct regions.

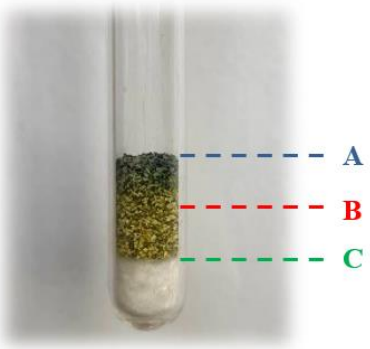

Figure 98: Spent 10VAl catalyst bed, O_2 oxidant, 773 K, 1 atm

4.4.5.1 Raman Spectroscopy

Raman spectra of the distinct regions which exist along the spent 10VAl catalyst bed are presented in Figure 99.

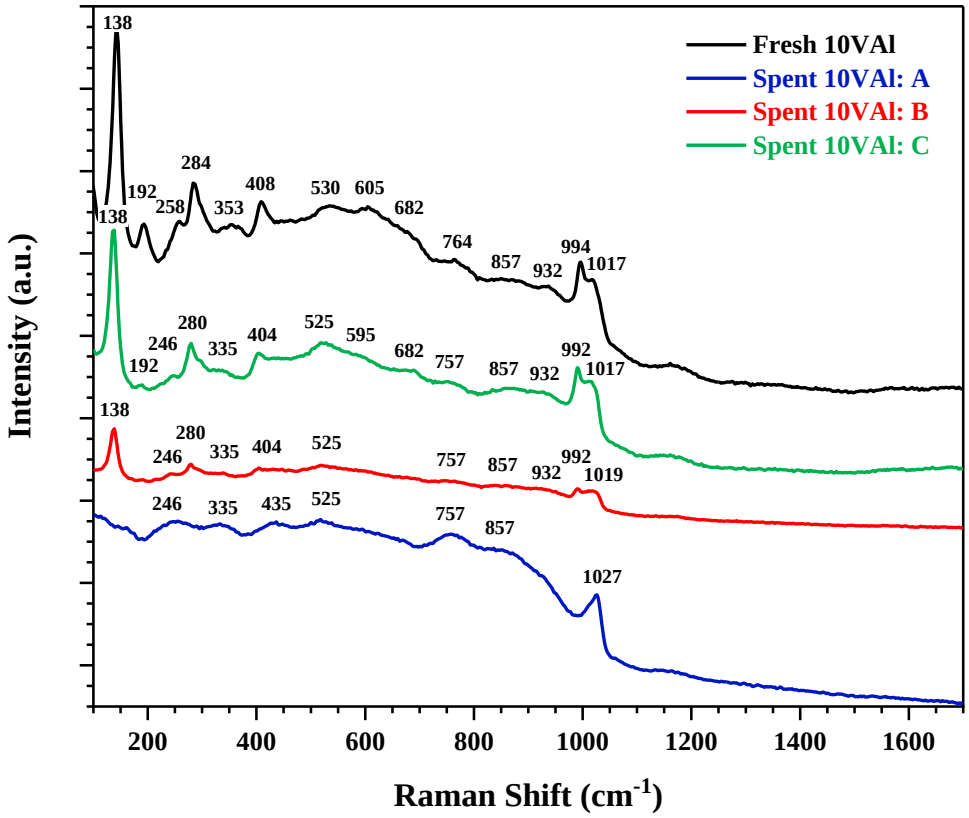

Figure 99: Raman spectra of samples A, B and C, which relate to the top, middle and bottom of the catalyst bed

A clear disparity is observed in the Raman spectra of samples taken along the catalyst bed. The spectra of the sample taken from the bottom of the bed (C) exhibits similar Raman features to those observed in the fresh 10VAl catalyst. The spectra of the sample taken from the middle of the bed (B) is also comparable, however, the bands have become less prominent.

The sample removed from the top of the catalyst bed (A) is visibly darker in colour and it is this sample which exhibits the greatest change. Sharp Raman features which correlate to crystalline V_2O_5 species are no longer present, with remaining bands exclusively assigned to monomeric and polymeric vanadia species. Remarkably, both G and D bands resulting from coke formation are absent, therefore any carbon laydown that may be present along the spent 10VAl catalyst bed was undetected by the Raman measurement.

4.4.5.2 TGA-TPO

Since there was no evidence of carbon laydown from Raman spectroscopy, TPO measurements were performed to investigate the extent of carbon deposition along the catalyst bed. Figures 100-102 present the derivative weight profiles, and Table 38 details the total weight loss at temperatures associated with CO_2 evolution. Mass spectral data was not obtained in these measurements, thus the temperature range associated with CO_2 evolution in Section 4.4.1.4 was again used to estimate the weight loss.

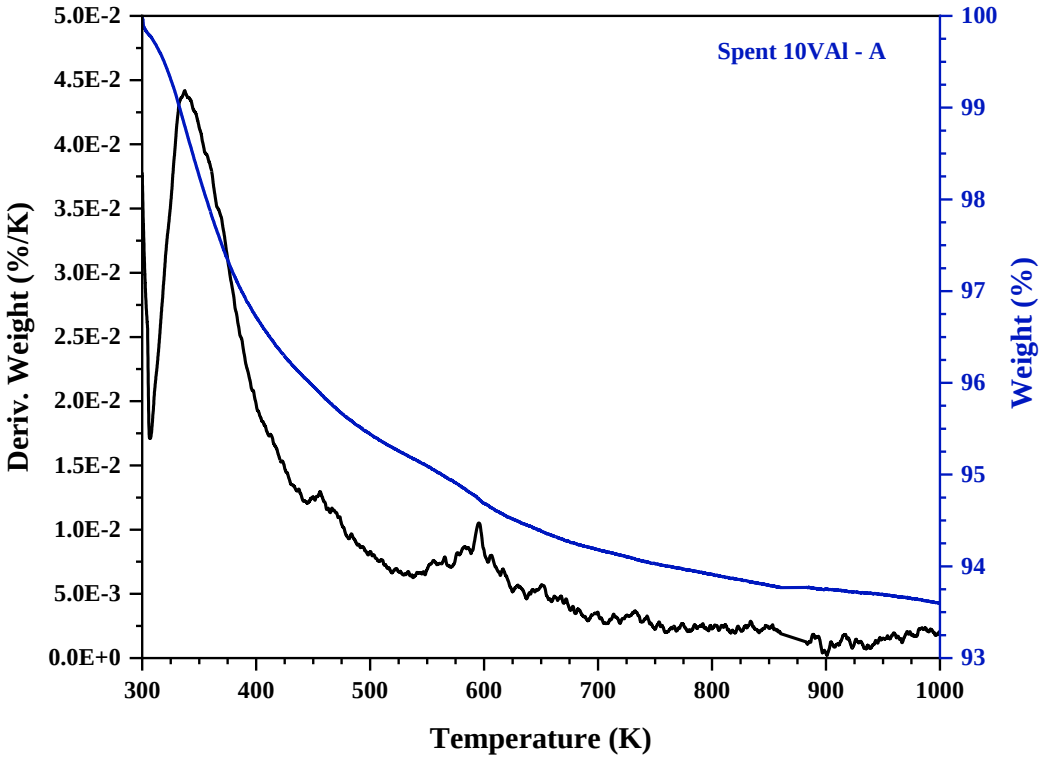

Figure 100: TPO weight loss profile of sample A, top of the catalyst bed

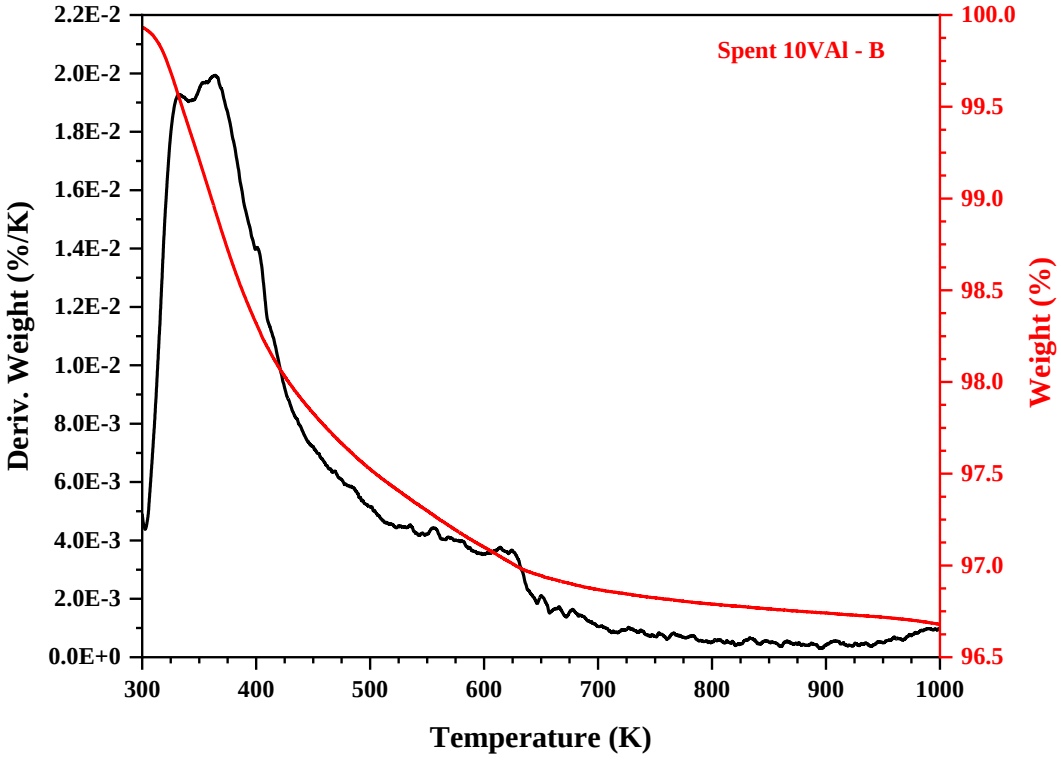

Figure 101: TPO weight loss profile of sample B, middle of the catalyst bed

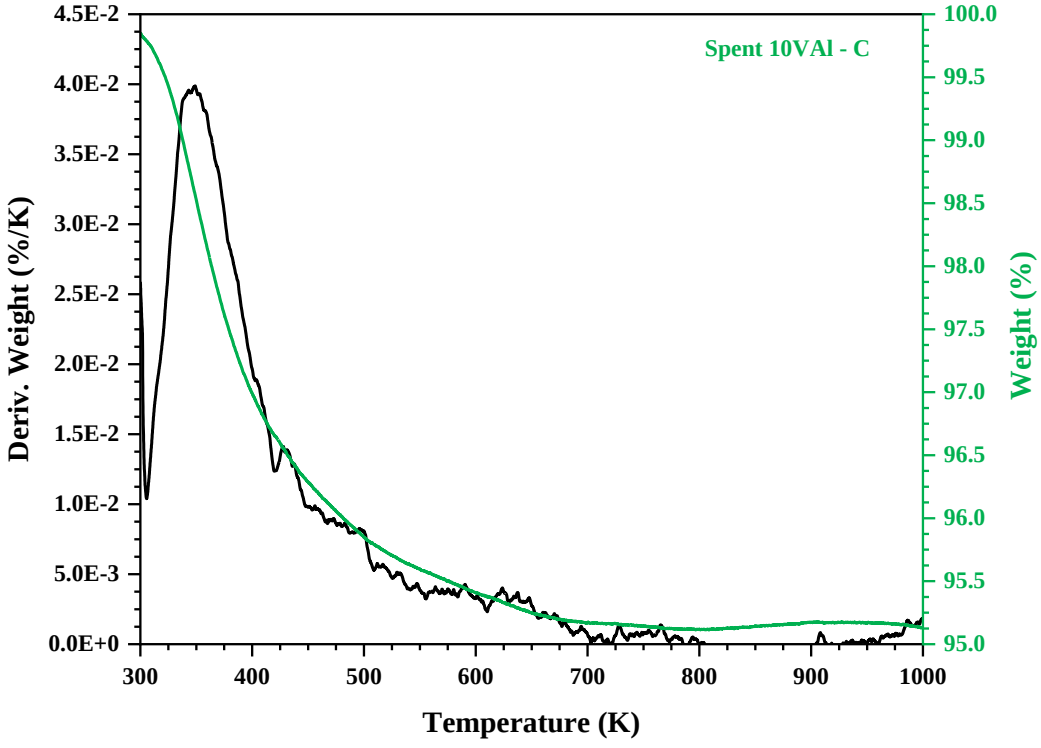

Figure 102: TPO weight loss profile of sample C, bottom of the catalyst bed

Table 38: Weight loss at temperatures associated with CO_2 evolution, 465-887 K

Sample	Weight Loss (%)
Spent 10VAl – Sample A (Top) 10 Cycles, 773 K, O_2	1.9
Spent 10VAl – Sample B (Middle) 10 Cycles, 773 K, O_2	1.0
Spent 10VAl – Sample (Bottom) 10 Cycles, 773 K, O_2	1.0

When compared, it is apparent that a variation in the percentage weight loss of samples along the catalyst bed exists. Specifically, the weight loss observed in the sample removed from the top of the catalyst bed is ~1.9 %, which is almost double the weight loss recorded in samples taken from the middle and the bottom of the bed. Since both water and CO_2 evolution may occur within the temperature range evaluated, only relative comparisons can be made between the samples when investigating the extent of carbon laydown. As a result, the weight loss results provide only an indication that there are higher levels of carbon deposition at the top of the catalyst bed.

5 Molybdenum Oxide

5.1 Pre-Reaction Characterisation

This section details the characterisation results of the 9.4MoAl catalyst, performed prior to the CL-PODH redox cycling test. The characterisation techniques include ICP-OES, BET, H_2-TPR, O_2 chemisorption, Raman spectroscopy and XRD.

5.1.1 ICP-OES

ICP-OES was performed to determine the molybdenum content in the fresh 9.4MoAl catalyst. The molybdenum loading that was achieved via the incipient wetness impregnation technique was 9.3 wt.%, indicating that the catalyst preparation had been performed successfully.

5.1.2 BET Surface Area Determination

Adsorption-desorption isotherms for the γ-Al_2O_3 support and 9.4MoAl are presented in Figure 103. Similar to the VAl catalyst series, the isotherm obeys the Type IV model with the characteristic H1-Type hysteresis loop.

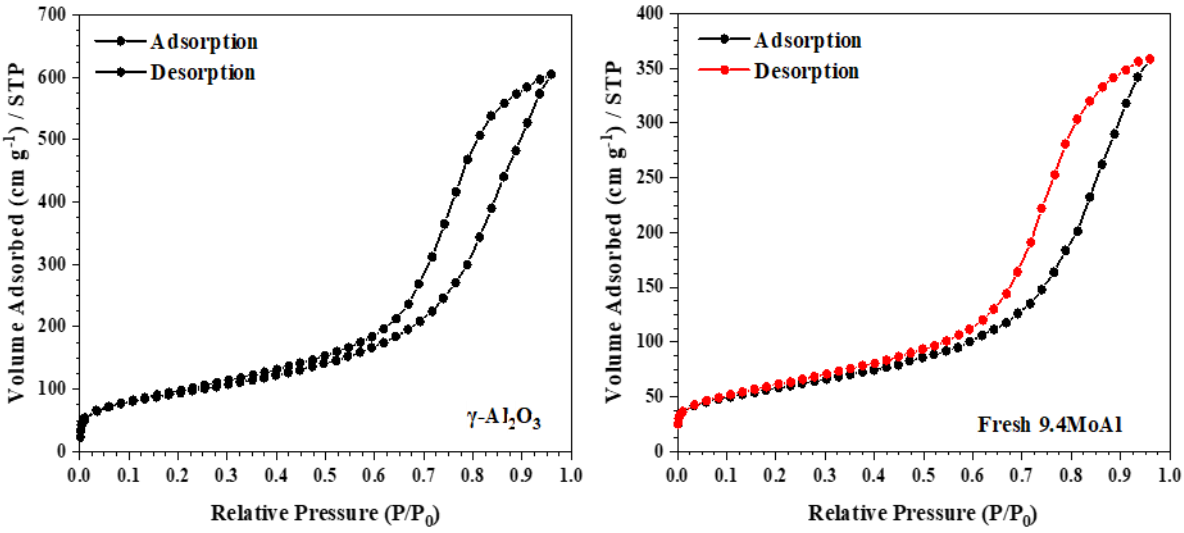

Figure 103: N_2 adsorption-desorption isotherm of the fresh 9.4MoAl catalyst

Table 39 details the surface area, pore volume and average pore diameter of the γ-Al_2O_3 support and fresh 9.4MoAl catalyst. The surface area of γ-Al_2O_3 was 258 $m^2 g^{-1}$, which decreased upon loading with the molybdenum precursor and calcination at 823 K for 12 h.

Table 39: Surface area, pore volume and average pore diameter of the γ-Al_2O_3 support and 9.4MoAl

Sample	S_{BET} ($m^2 g^{-1}$)	V_{pore} ($cm^3 g^{-1}$)	Avg. pore diameter (Å)	Surface Density (Mo nm^{-2})
γ-Al_2O_3	258	0.93	54	-
Fresh 9.4MoAl	155	0.55	48	3.8

The molybdenum surface density of 9.4MoAl is also presented, which was calculated using the molybdenum loading and BET surface area of the 9.4MoAl catalyst, as described in Equation 21.

Equation 21: Molybdenum Surface Density Calculation

$$Molybdenum\ Surface\ Density = \frac{(\frac{Mo\ wt.\%}{100}) \times N_A}{M_W \times S_{BET} \times 10^{18}}$$

Whereby,

- N_A is Avogadro's constant (6.02×10^{23} mol^{-1}),
- M_w is the molar weight of molybdenum (95.95 g mol^{-1})
- S_{BET} ($m^2 g^{-1}$) is the specific surface area of the catalysts

5.1.3 H_2-TPR

H_2-TPR measurements were employed to provide insight into the reducibility of the molybdena species present in the fresh 9.4MoAl catalyst. The resulting H_2-TPR profile and corresponding peak maxima are presented in Figure 104 and Table 40, which reveals two distinct reduction events between 500-900 K.

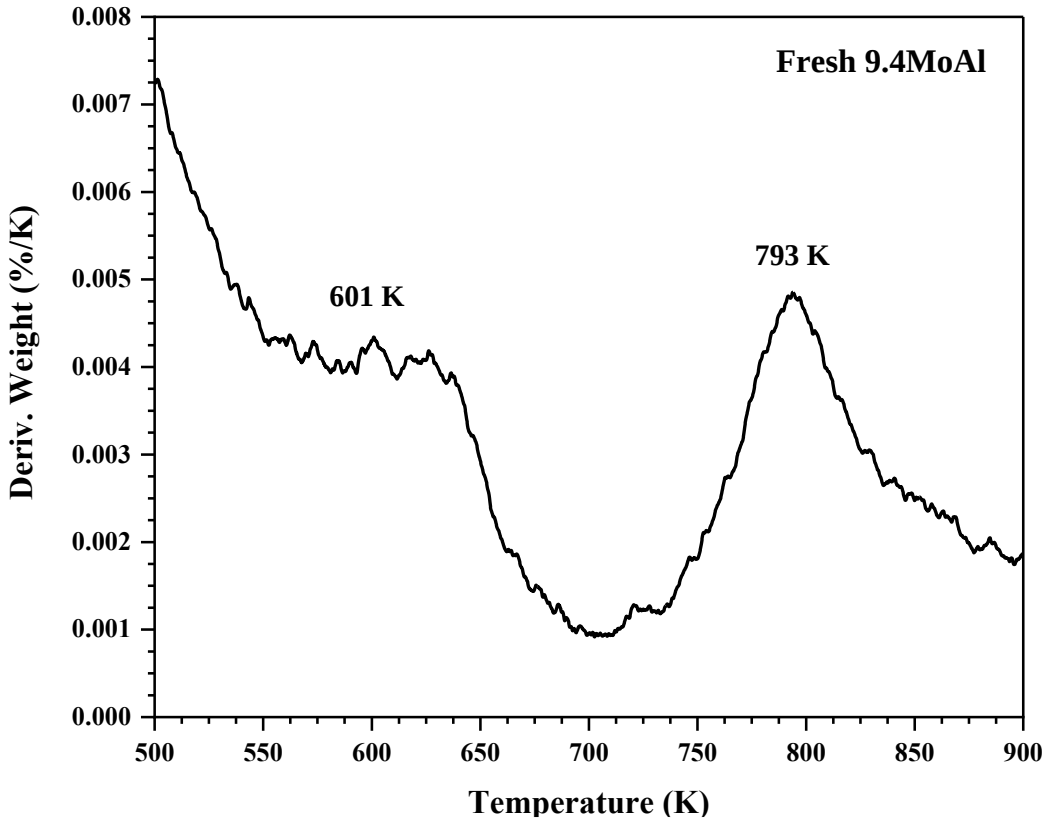

Figure 104: H_2-TPR profile of the fresh 9.4MoAl catalyst

Table 40: H_2-TPR data summarising T_{max} of reduction peaks in the fresh 9.4MoAl catalyst

Sample	T_{max} (K)	
	A	B
Fresh 9.4MoAl	601	793

It is well established in literature that the reduction of MoO_3 is a two-step process: an initial reduction to MoO_2 with a subsequent, further reduction to the Mo metal. The reduction of MoO_3 to MoO_2 is reported to occur between 723 K and 923 K, therefore, the higher temperature reduction event observed in the H_2-TPR profile of 9.4MoAl is ascribed to reduction of MoO_3 species. [105] The total weight loss at 700-900 K was determined, with results showing that approximately one oxygen atom was lost per one molybdenum atom, which concurs with the proposal that the higher temperature reduction event is due to the reduction of MoO_3 to MoO_2.

Chary *et al.* propose that octahedral polymolybdate species, found in catalysts comprising moderate molybdenum loadings, are much more easily reducible than both isolated tetrahedral molybdena and MoO_3 species; reducing at lower temperatures of 673-693 K in comparison to 1073-1270 K. [106, 107] Therefore, the lower temperature reduction peak observed at 601 K is assigned to the reduction of octahedral polymolybdate species. [107]

5.1.4 Oxygen Chemisorption

Oxygen chemisorption was performed on the reduced 9.4MoAl catalyst as described in Section 3.3.2. The cumulative oxygen uptake is plotted as a function of the pulse number in Figure 105, which shows a cumulative oxygen uptake of 9.4MoAl to be 221 µmol g^{-1}.

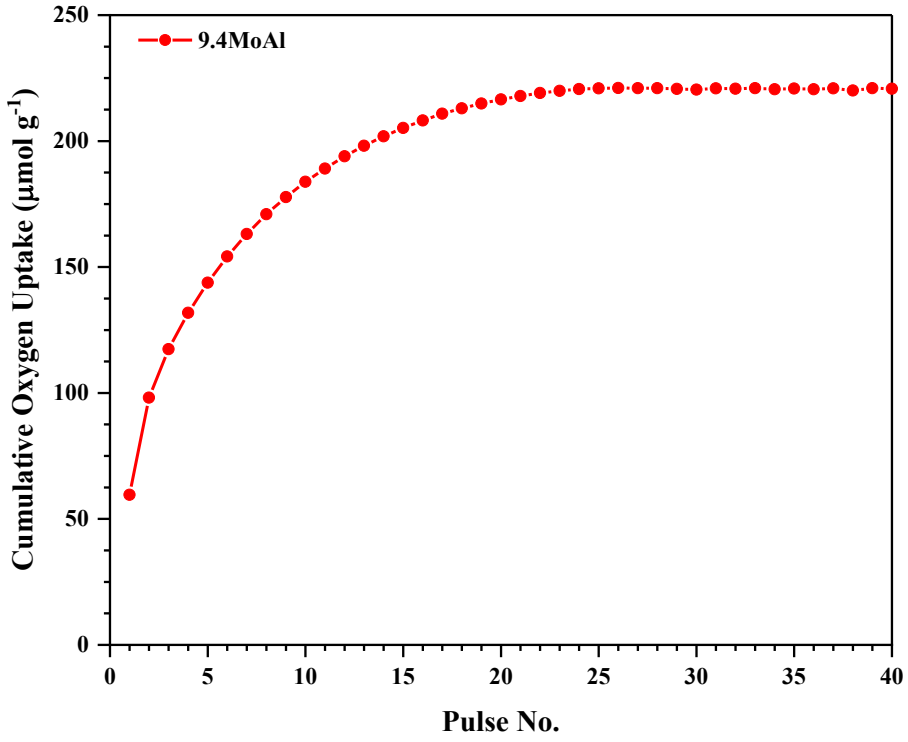

Figure 105: Cumulative oxygen uptake of fresh 9.4MoAl

The resulting oxygen uptake capacity allows us to obtain the oxygen atom site density and metal dispersion of the fresh 9.4MoAl catalyst. The oxygen atom site density was calculated as the ratio of oxygen atoms to the specific BET surface area, and the dispersion was determined by taking the ratio of adsorbed oxygen to total molybdenum atoms, assuming $O_{ads}/Mo_{atoms} = 1$. The results are summarised in Table 41.

Table 41: Oxygen uptake, atom site density and dispersion of fresh 9.4MoAl calculated from oxygen chemisorption measurements

Sample	S_{BET} ($m^2\ g^{-1}$)	Oxygen uptake (µmol g^{-1})	Oxygen atom site density (O nm^{-2})	Dispersion O/Mo
Fresh 9.4MoAl	154	221	1.7	45.1

5.1.5 Raman Spectroscopy

Raman spectra obtained for the γ-Al_2O_3 support versus the fresh 9.4MoAl catalyst is presented in Figure 106.

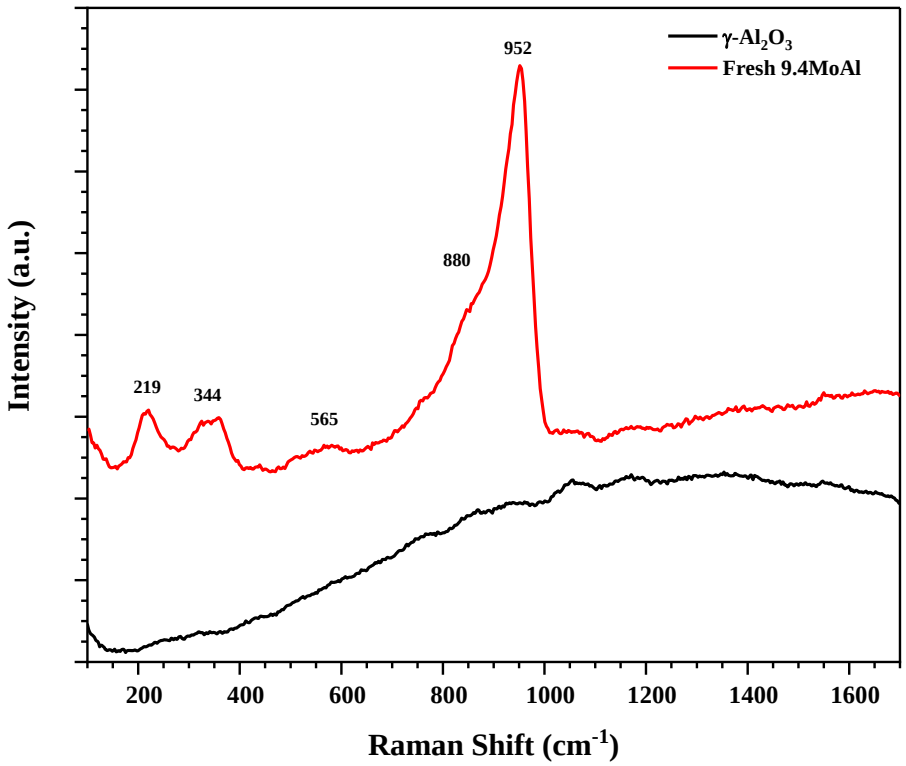

Figure 106: Raman spectra of γ-Al_2O_3 and the fresh 9.4MoAl catalyst

Since the spectrum of the γ-Al_2O_3 support does not exhibit any characteristic features in the ~100-1700 cm^{-1} region, all Raman bands observed in the spectrum of the fresh 9.4MoAl catalyst are ascribed to molybdenum oxide vibrations. A thorough literature search reveals that Raman shifts observed at ~952 and 344 cm^{-1} are characteristic of the symmetric stretch and the bending mode of molybdenyl bonds (Mo=O) present within octahedral polymolybdate species, respectively. [108-111] Furthermore, polymeric molybdenum oxide species are further characterised by the shouldering band at ~880 cm^{-1} and broad bands at ~565 and 219 cm^{-1}, which are assigned to the asymmetric stretch, the symmetric stretch and deformation mode of bridging Mo-O-Mo bonds, respectively. [108, 111]

5.1.6 XRD

The XRD pattern obtained for the fresh 9.4MoAl catalyst is shown in Figure 107. Similar to the VAl catalyst series, the diffraction pattern of 9.4MoAl exhibits peaks relating exclusively to the amorphous alumina support, indicating that the molybdena species present in 9.4MoAl is highly dispersed and does not exhibit long range ordering.

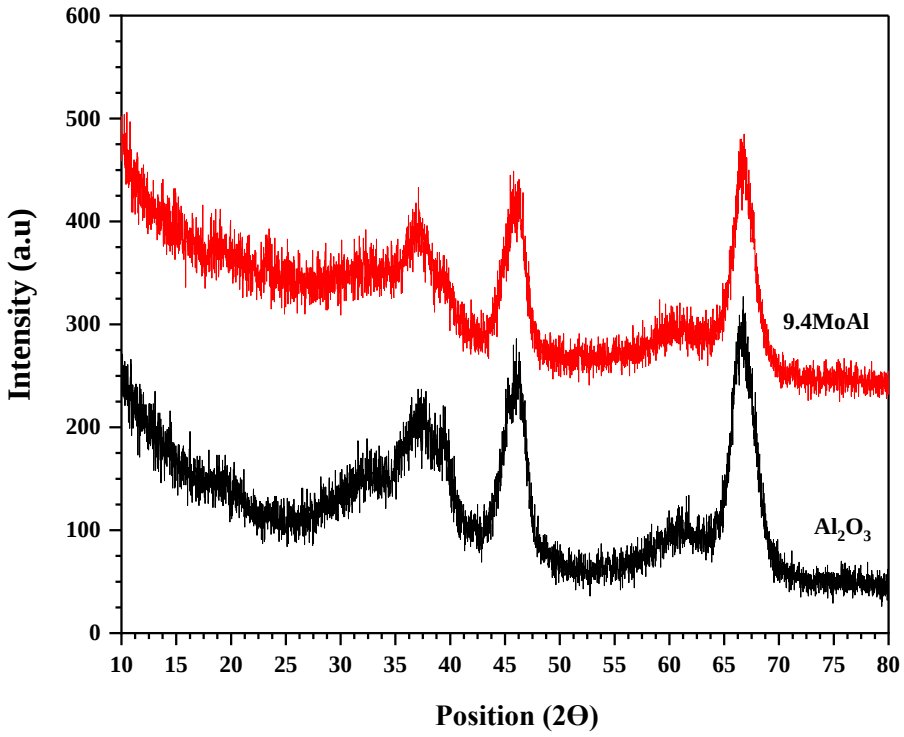

Figure 107: XRD patterns of γ-Al_2O_3 and the fresh 9.4MoAl catalyst

5.2 Thermodynamic Analysis

Thermodynamic analysis was carried out to investigate the feasibility of chemical reactions that occur when performing CL-PODH redox cycles over molybdenum oxide catalysts. Any possible side reactions which may occur are described previously in Section 4.2.3.

The basic thermodynamic data of reactants and products, MoO_3, MoO_2, CO, CO_2, graphitic carbon, propane, propene, O_2 and H_2O were obtained [99-102] and used to calculate the change in Gibbs free energy of chemical reactions which occur during the CL-PODH cycling test. The resulting Gibbs free energies of each reaction were plotted as a function of temperature, where a negative value indicates that the reaction is thermodynamically feasible.

5.2.1 Propane Dehydrogenation Step

The chemical equations of reactions which may proceed during the PDH step are listed in Table 42. Reactions (36-38) are the stoichiometric equations of propane oxidising to propene, CO, CO_2 and H_2O by utilising the lattice oxygen sites of molybdenum oxide species. Reactions (39) and (40) are the stoichiometric equations of the desired propene product subsequently re-adsorbing onto lattice oxygen sites and combusting further to CO, CO_2 and H_2O.

Table 42: Chemical equations for reactions occurring during the PDH step of CL-PODH redox cycles utilising 9.4MoAl

Reaction	Chemical Equation	Reaction No.
PDH over MoO_3 sites	$C_3H_8\,(g) + MoO_3\,(s) \rightarrow MoO_2\,(s) + C_3H_6\,(g) + H_2O\,(g)$	(36)
	$C_3H_8\,(g) + 10MoO_3\,(s) \rightarrow 10MoO_2\,(s) + 3CO_2\,(g) + 4H_2O\,(g)$	(37)
	$C_3H_8\,(g) + 7MoO_3\,(s) \rightarrow 7MoO_2\,(s) + 3CO\,(g) + 4H_2O\,(g)$	(38)
	$C_3H_6\,(g) + 9MoO_3\,(s) \rightarrow 9MoO_2\,(s) + 3CO_2\,(g) + 3H_2O\,(g)$	(39)
	$C_3H_6\,(g) + 6MoO_3\,(s) \rightarrow 6MoO_2\,(s) + 3CO\,(g) + 3H_2O\,(g)$	(40)

The Gibbs free energy plot of reactions (36-40) are displayed in Figure 108. Overall, the oxidation of both propane and propene utilising MoO_3 display negative values at 773 K, therefore, they are spontaneous and thermodynamically feasible at our reaction conditions. Notably, the production of CO and CO_2 during the oxidation of propane and propene display lower Gibbs free energies than the production of the desired product propene and are consequently more favourable.

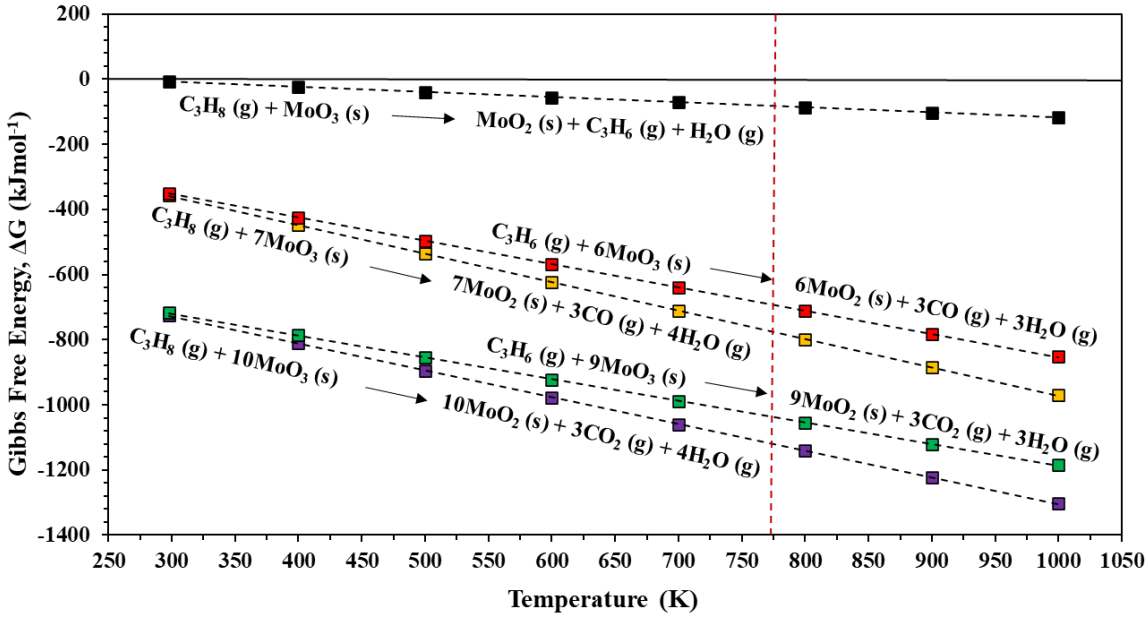

Figure 108: Gibbs free energies of reactions (36-40) plotted as a function of temperature

5.2.2 Regeneration Step & Removal of Carbon Laydown

Reactions which may transpire during the catalyst regeneration step in CL-PODH redox cycling tests utilising the 9.4MoAl catalyst and O_2, N_2O and CO_2 oxidants are tabulated in Table 43. Reaction (41) is the stoichiometric equation relating to the reoxidation of resulting MoO_2 sites utilising O_2 as the oxidant, whilst reactions (42) and (43) are those regenerated with N_2O and CO_2 oxidants.

Section 4.2.3 details any possible side reactions that may occur during the CL-PODH redox cycles, where chemical reactions resulting in coke formation exhibit negative Gibbs free energies. As a result, it was also of interest to investigate the possibility of carbon laydown removal via the lattice oxygen sites of MoO_3 species. The chemical equations of such reactions are also presented in Table 43, labelled as reaction (44) and (45).

Table 43: Chemical equations for reactions occurring during the regeneration step of CL-PODH redox cycles utilising 9.4MoAl

Reaction	Chemical Equation	Reaction No.
Catalyst Regeneration (Oxidant – O_2)	$2MoO_2\,(s) + O_2\,(g) \rightarrow 2MoO_3\,(s)$	(41)
Catalyst Regeneration (Oxidant – N_2O)	$MoO_2\,(s) + N_2O\,(g) \rightarrow MoO_3\,(s) + N_2\,(g)$	(42)
Catalyst Regeneration (Oxidant – CO_2)	$MoO_2\,(s) + CO_2\,(g) \rightarrow MoO_3\,(s) + CO\,(g)$	(43)
Removal of carbon laydown	$C\,(s) + MoO_3\,(s) \rightleftharpoons MoO_2\,(s) + CO\,(g)$	(44)
	$C\,(s) + 2MoO_3\,(s) \rightleftharpoons 2MoO_2\,(s) + CO_2\,(g)$	(45)

The Gibbs free energy plot of reactions (41-45) is displayed in Figure 109. Overall, the re-oxidation of resulting MoO_2 species with O_2 and N_2O oxidants display negative Gibbs free energy values at 773 K. The reoxidation with CO_2, however, exhibits a large positive value due to the inherent inertness of CO_2, indicating that the reaction is not thermodynamically feasible and will proceed in the reverse direction. Reactions (44) and (45), associated with the combustion of carbon laydown to CO and CO_2, also exhibit negative Gibbs free energies, which implies that carbon removal using the lattice oxygen sites of MoO_3 catalysts is thermodynamically feasible.

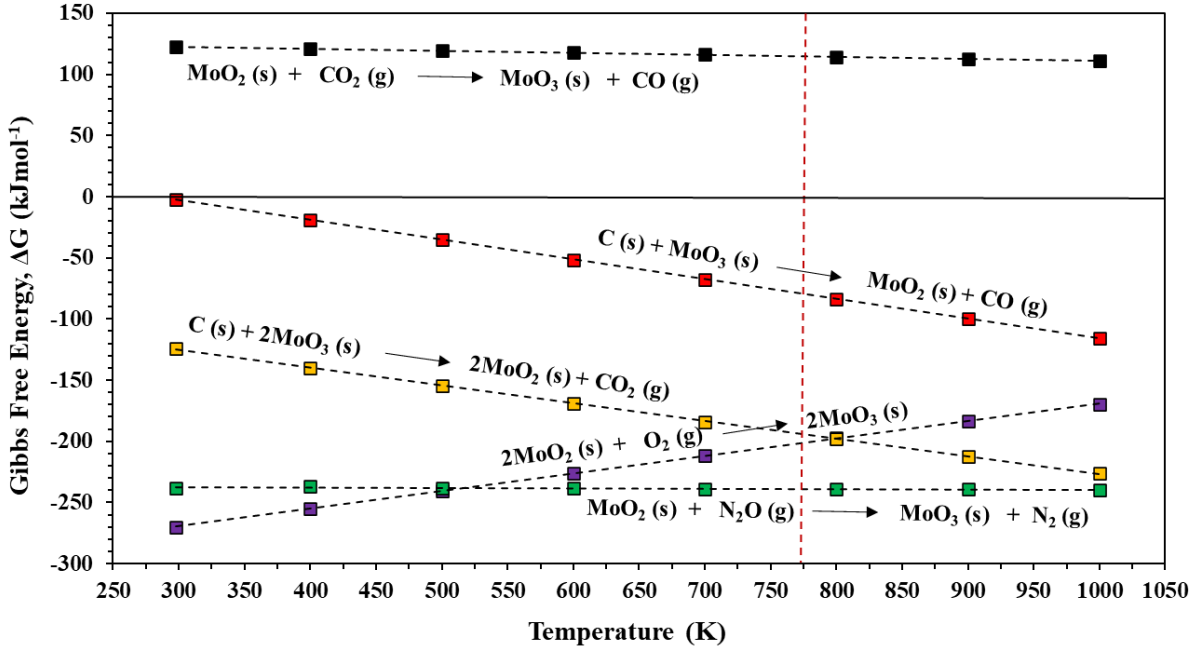

Figure 109: Gibbs free energies of reactions (41-45) plotted as a function of temperature

5.3 Reactivity Tests

This section details the results obtained from the CL-PODH redox cycling test performed using the fresh 9.4MoAl catalyst, as described in Section 3.3.3.

5.3.1 CL-PODH Redox Cycles with O_2

Results from the CL-PODH redox cycling test performed over the fresh 9.4MoAl catalyst, using O_2 as the oxidant in the regeneration step, are presented here. The reaction profile detailing the conversion of propane and selectivity to propene and CO_2 products is shown in Figure 110. Furthermore, the resulting yields of the desired olefin product and CO_2 are presented in Figure 111.

The data presented is the instantaneous performance obtained at the end of the 30 min PDH step of each corresponding redox cycle.

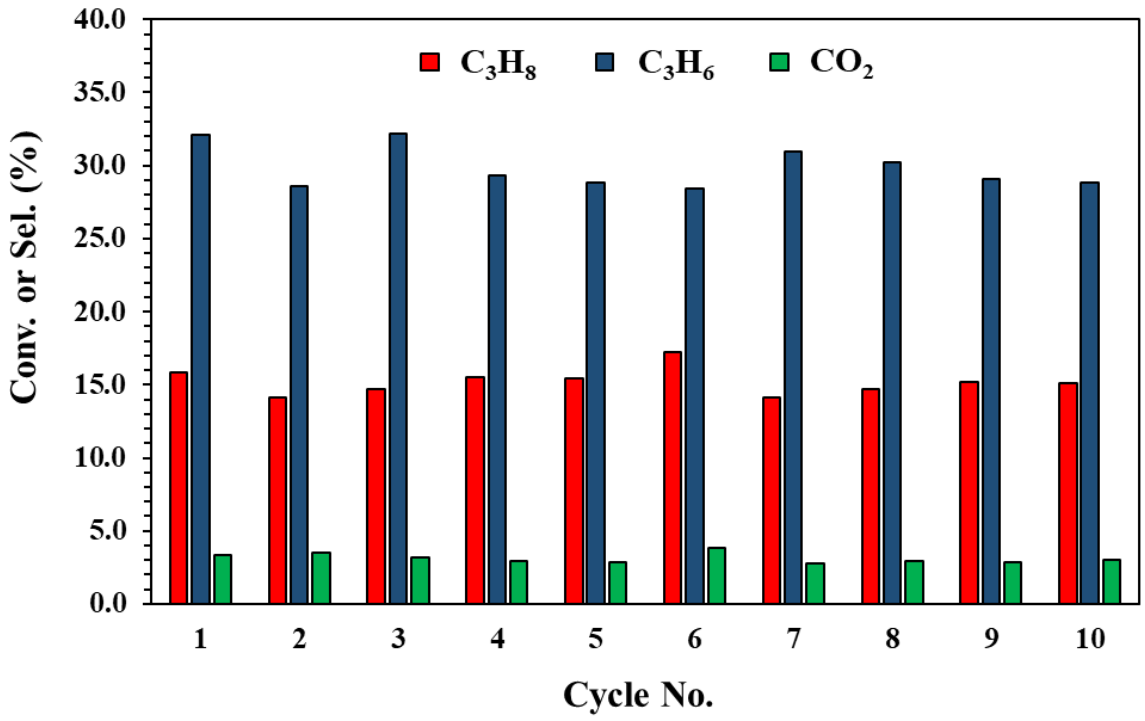

Figure 110: Instantaneous C_3H_8 conversions and C_3H_6/CO_2 selectivities using the 9.4MoAl catalyst, 773 K, 1 atm

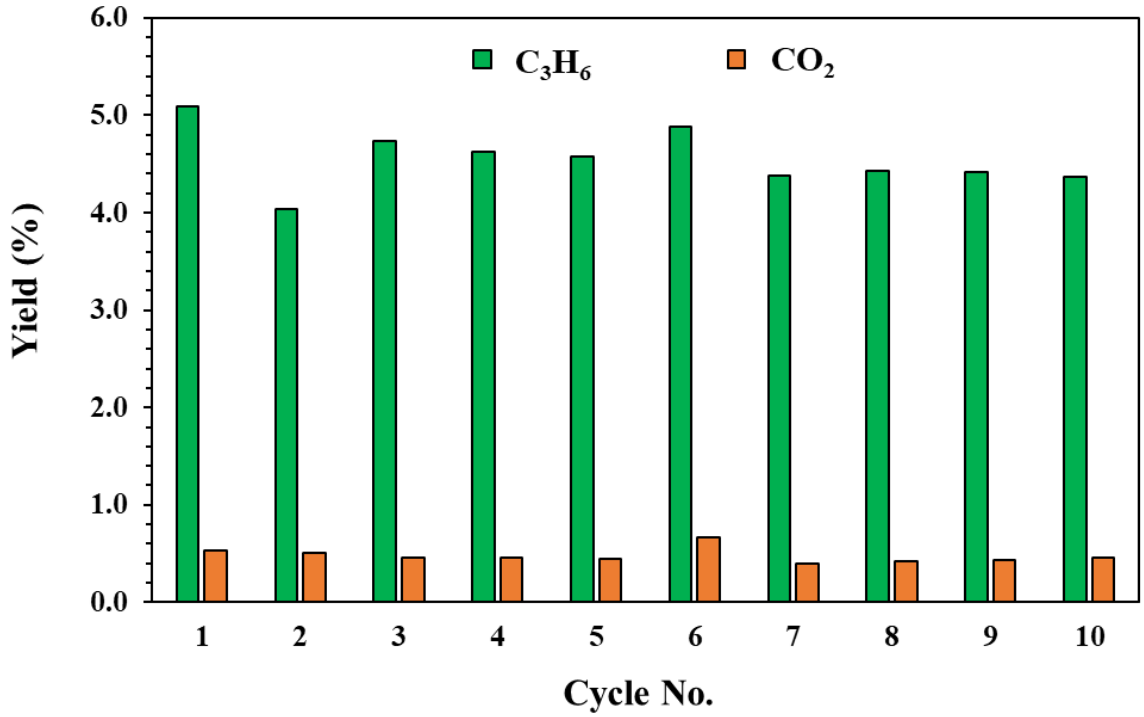

Figure 111: Instantaneous C_3H_6 and CO_2 yields using the 9.4MoAl catalyst, 773 K, 1 atm

Significantly, propane conversions in the CL-PODH redox cycling test utilising 9.4MoAl are comparatively lower than those obtained in tests performed over the 10VAl catalyst.

Propane conversions using the 9.4MoAl catalyst reached ~15.9 % at the end of the 1st PDH step, which decreased marginally to ~14-15 % in the PDH step of cycles 2 to 5. The 9.4MoAl catalyst demonstrated an enhancement in activity during the PDH step of cycle 6, which was performed after the overnight argon purge, before decreasing again during the PDH step of cycles 7 to 10.

Furthermore, the selectivity to propene is low when using the 9.4MoAl catalyst, reaching ~32.1 % by the end of the 1st PDH step. A subsequent decay is observed during the PDH step of cycle 2, resulting in a decrease in propene yield from ~5.1 to ~4.0 %. Propene yields remain comparable in cycles 2 to 5 with an enhancement again observed in the PDH step of cycle 6 due to an increase in catalyst activity. Both propene selectivity and yield decay during the PDH step of cycle 7, before remaining relatively stable during successive cycles, indicating that no significant catalyst deactivation had occurred.

It should be noted, however, that CO_2 selectivities remain significantly lower than those observed for propene. The selectivity to CO_2 reaches ~3.3 % by the end of the 1st PDH step, which increases nominally to ~3.5 % in the PDH step of cycle 2 before decaying in cycles 3-5 to ~3.0 %. An enhancement in CO_2 selectivity is observed in the PDH step of cycle 6, which similarly decays throughout successive CL-PODH redox cycles 7-10. As a result, the overall CO_2 yield that was obtained displays a similar trend throughout.

Reaction profiles displaying the activity trend over the entire 30 min PDH step, using the 9.4MoAl catalyst, are presented in Figures 112-114. It should be noted that the data presented relates exclusively to the PDH step of cycle 1 versus cycle 2. Figures 112 and 113 convey propane conversion and propene and CO_2 selectivity plots and Figure 114 presents the resulting propene and CO_2 yield.

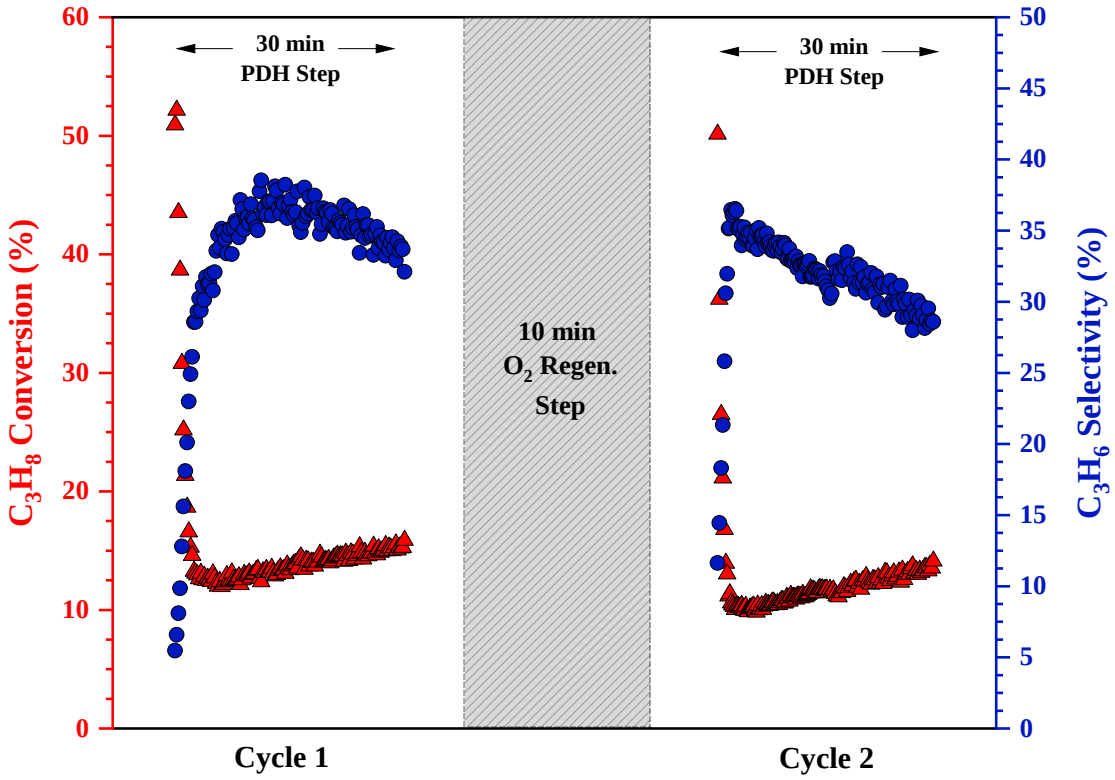

Figure 112: Reaction profile of C_3H_8 conversion and C_3H_6 selectivity during the PDH step of cycle 1 versus cycle 2: 9.4MoAl, O_2 oxidant, 773 K, 1 atm

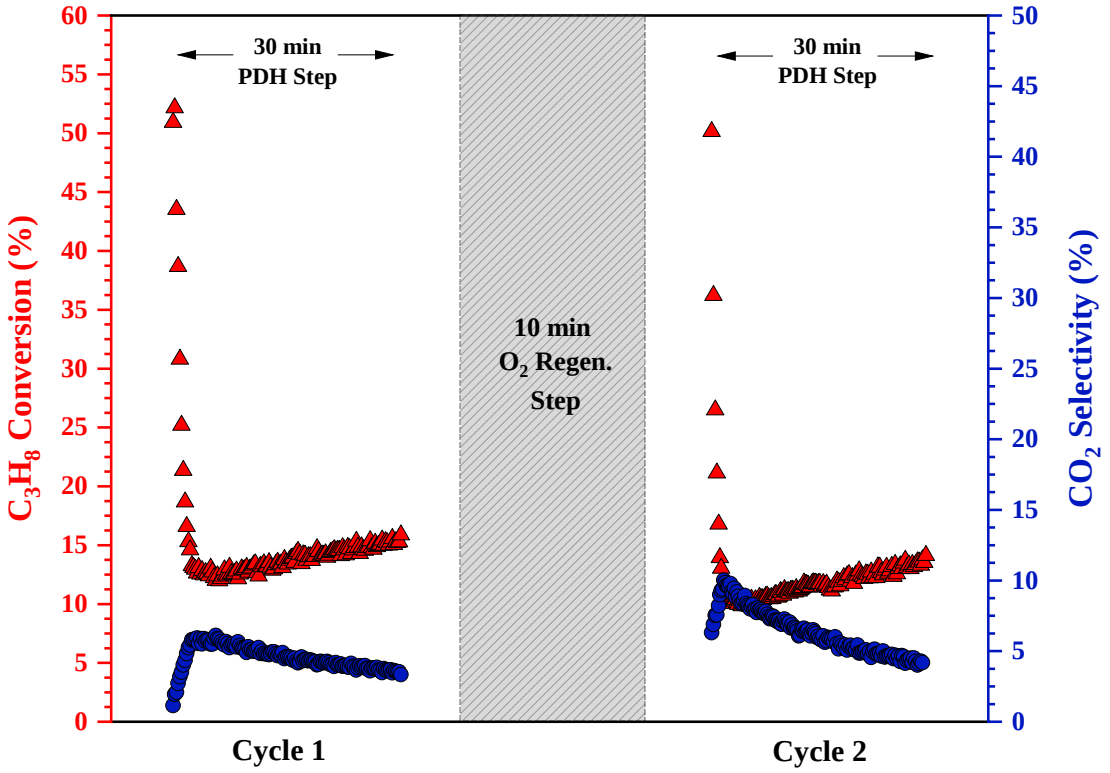

Figure 113: Reaction profile of C_3H_8 conversion and CO_2 selectivity during the PDH step of cycle 1 versus cycle 2: 9.4MoAl, O_2 oxidant, 773 K, 1 atm

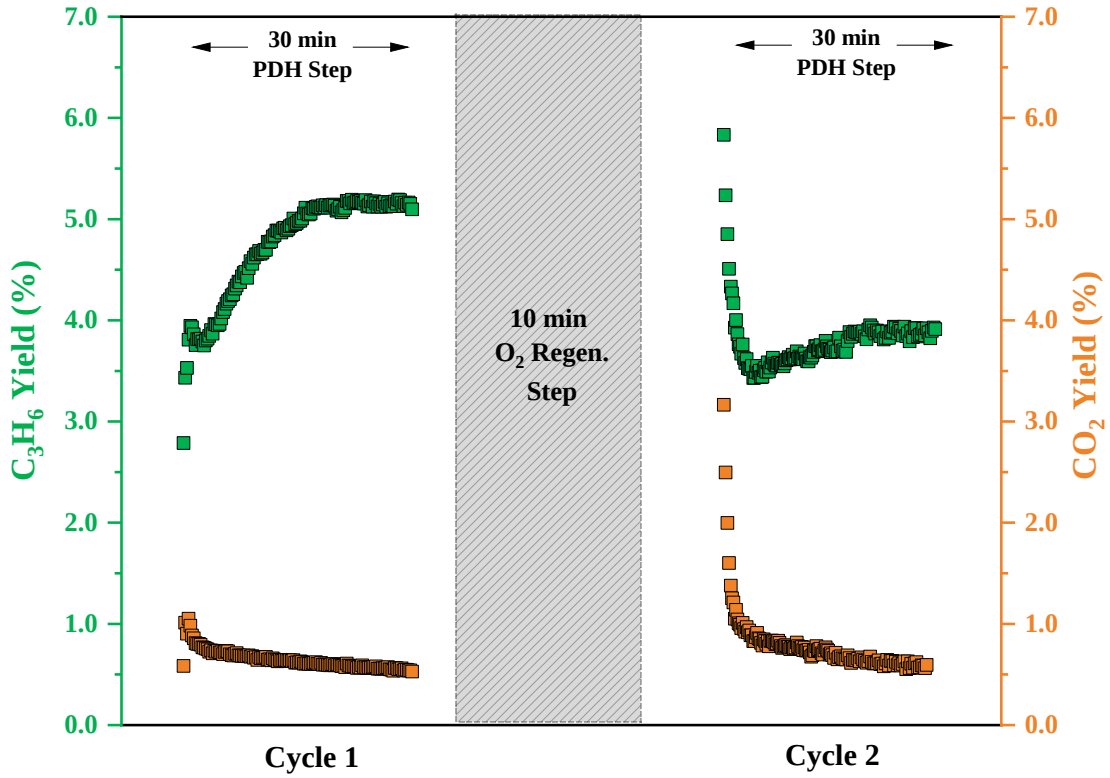

Figure 114: Reaction profile of C_3H_6 and CO_2 yields during the PDH step of cycle 1 versus cycle 2: 9.4MoAl, O_2 oxidant, 773 K, 1 atm

Reaction profiles obtained with the 9.4MoAl catalyst display different reactivity zones throughout the 30 min PDH step. Interestingly, propene and CO_2 yields do not reach a maximum value within the first ~1.5 min of cycle 1. However, propene and CO_2 yields reach this maximum point in the PDH step of cycle 2. In this case, propene yields decrease as propane conversion drops off significantly until ~6.0 min into the reaction. As the reaction progresses, propene selectivities decrease in conjunction with increasing propane conversions, resulting in relatively stable propene yields. A similar trend is observed with respect to CO_2 selectivities; however, the decay is far more substantial than observed in the case with propene, thus the overall CO_2 yield decreases despite an increase in catalyst activity.

Propane conversions, propene/CO_2 selectivities and the resulting propene/CO_2 yields achieved ~1.5, 6 and 30 min into the PDH step of cycles 1 and 2 are summarised in Table 44 and Table 45.

Table 44: Summary of C_3H_8 conversions, C_3H_6 and CO_2 selectivities and yields obtained at the different reaction regions during the PDH step of cycle 1: 9.4MoAl, O_2 oxidant, 773 K, 1 atm

Time into PDH Step (min)	C_3H_8 Conversion (%)	C_3H_6 Selectivity (%)	C_3H_6 Yield (%)	CO_2 Selectivity (%)	CO_2 Yield (%)
1.5	30.8	12.8	3.9	3.2	1.0
6	13.1	28.6	3.7	5.8	0.8
30	15.9	32.1	5.1	3.3	0.5

Table 45: Summary of C_3H_8 conversions and C_3H_6 and CO_2 selectivities and yields obtained at the different reaction regions during the PDH step of cycle 2: 9.4MoAl, O_2 oxidant, 773 K, 1 atm

Time into PDH Step (min)	C_3H_8 Conversion (%)	C_3H_6 Selectivity (%)	C_3H_6 Yield (%)	CO_2 Selectivity (%)	CO_2 Yield (%)
1.5	50.1	11.6	5.8	6.3	3.2
6	9.9	34.5	3.4	8.1	0.8
30	14.1	28.6	4.0	4.2	0.6

An enhancement in catalyst activity is observed in the PDH step of cycle 6 after holding the 9.4MoAl catalyst overnight under argon. To obtain a clearer understanding, reaction profiles detailing the data from the entire 30 min PDH step of cycle 5 versus cycle 6 have been compared. Figures 115 and 116 detail propane conversion and propene and CO_2 selectivity plots and Figure 117 shows the resulting propene and CO_2 yields.

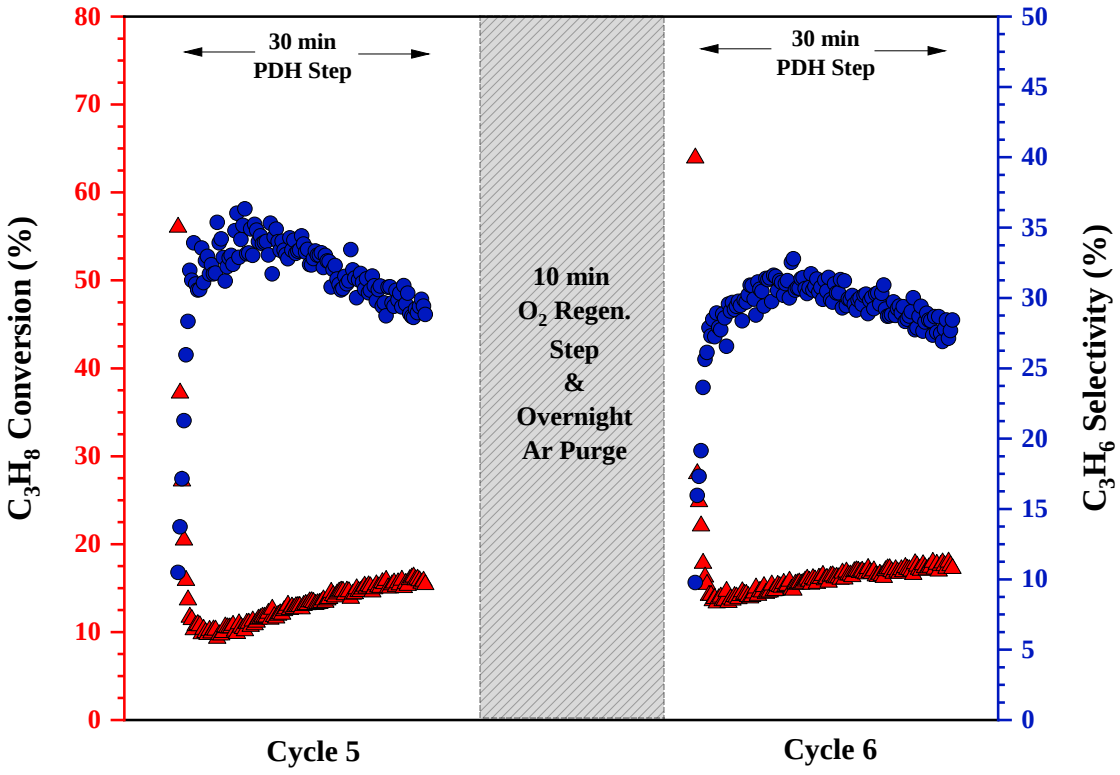

Figure 115: Reaction profile of C_3H_8 conversion and C_3H_6 selectivity during the PDH step of cycle 5 versus cycle 6: 9.4MoAl, O_2 oxidant, 773 K, 1 atm

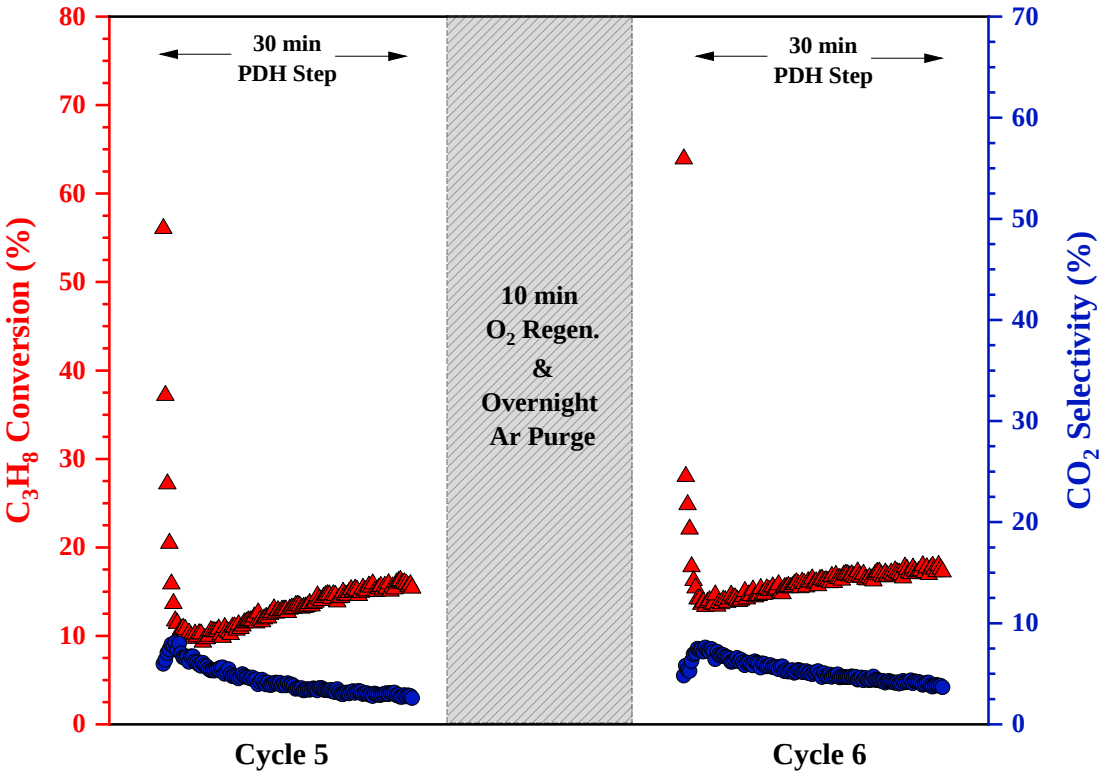

Figure 116: Reaction profile of C_3H_8 conversion and CO_2 selectivity during the PDH step of cycle 5 versus cycle 6: 9.4MoAl, O_2 oxidant, 773 K, 1 atm

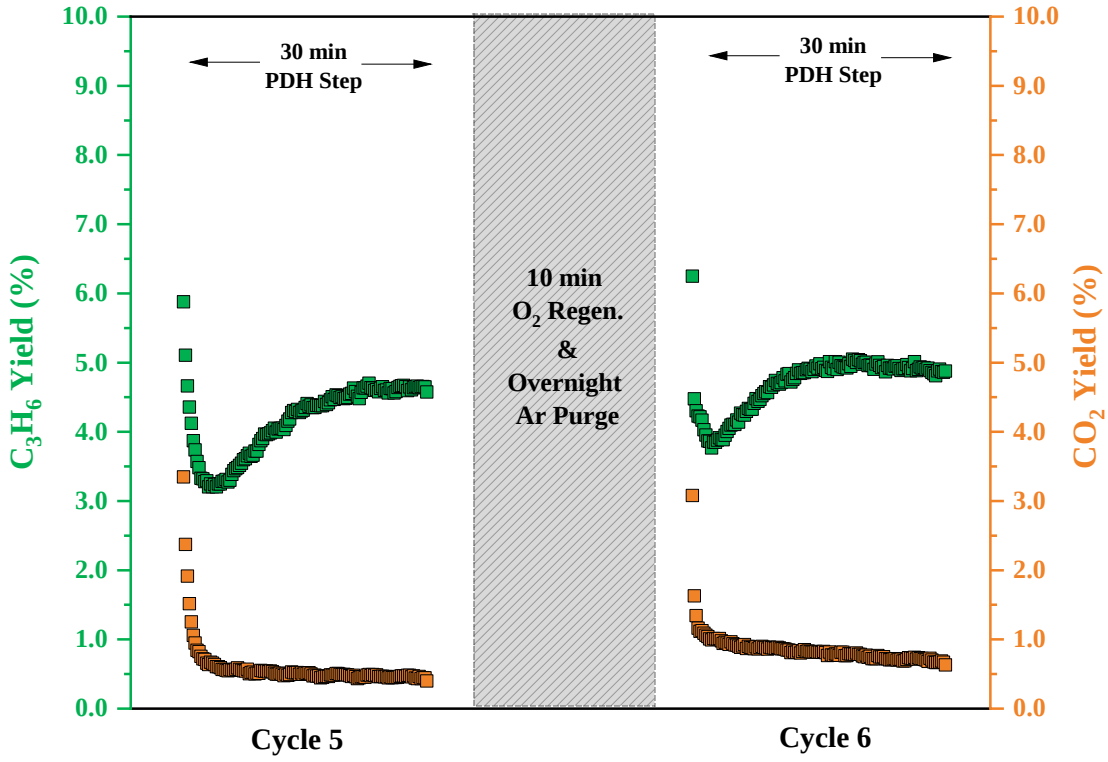

Figure 117: Reaction profile of C_3H_6 and CO_2 yields during the PDH step of cycle 5 versus cycle 6: 9.4MoAl, O_2 oxidant, 773 K, 1 atm

The PDH step of cycles 5 and 6 exhibit a similar trend, displaying different reactivity regions throughout the reaction. Comparably, propene and CO_2 yields are maximised within the first ~1.5 min. As the reaction proceeds, propene selectivities decrease with an increase in propane conversions, resulting in relatively stable propene yields by the end of reaction. Propene and CO_2 selectivities remain relatively comparable, however, an enhancement in catalyst activity ultimately achieves higher propene and CO_2 yields, which increase from ~4.6 and 0.4 % to ~5.9 and 0.7 %, respectively. Propane conversions, propene/CO_2 selectivities and the resulting propene/CO_2 yields achieved at these different reactivity regions in CL-PODH redox cycles 5 and 6 are summarised in Table 46 and Table 47.

Table 46: Summary of C_3H_8 conversions, C_3H_6 and CO_2 selectivities and yields obtained at the different reaction regions during the PDH step of cycle 5: 9.4MoAl, O_2 oxidant, 773 K, 1 atm

Time into PDH Step (min)	C_3H_8 Conversion (%)	C_3H_6 Selectivity (%)	C_3H_6 Yield (%)	CO_2 Selectivity (%)	CO_2 Yield (%)
1.5	56.0	10.5	5.9	6.0	3.3
6	9.9	32.4	3.2	6.1	0.6
30	15.4	28.8	4.6	2.8	0.4

Table 47: Summary of C_3H_8 conversions and C_3H_6 and CO_2 selectivities and yields obtained at the different reaction regions during the PDH step of cycle 6: 9.4MoAl, O_2 oxidant, 773 K, 1 atm

Time into PDH Step (min)	C_3H_8 Conversion (%)	C_3H_6 Selectivity (%)	C_3H_6 Yield (%)	CO_2 Selectivity (%)	CO_2 Yield (%)
1.5	64.0	9.8	6.2	4.8	3.1
6	13.8	27.2	3.8	7.2	1.0
30	17.2	28.4	4.9	3.8	0.7

5.4 Post-Reaction Characterisation

This section details the post-reaction characterisation results of the spent 9.4MoAl catalyst by BET, Raman, XRD and TGA-TPO.

5.4.1 BET Surface Area Determination

Table 48 summarises the BET results comparing the surface area, pore volume and average pore diameter of spent 9.4MoAl to those obtained for the fresh sample.

Table 48: Surface area, pore volume and average pore diameter of spent of the 9.4MoAl catalyst from CL-PODH redox cycles utilising O_2 as the oxidant

Sample	S_{BET} ($m^2\ g^{-1}$)	V_{pore} ($cm^3\ g^{-1}$)	Avg. pore diameter (Å)
Fresh 9.4MoAl	155	0.55	48
Spent 9.4MoAl 10 Cycles, 773 K, O_2	139	0.52	54

The post-reaction results obtained by BET analysis reveal a loss in surface area and pore volume, in conjunction with an increase in the mean pore diameter. A similar trend was observed in the BET analysis of spent VAl catalyst samples, which suggests the potential formation of coke despite employing a catalyst regeneration step.

5.4.2 Raman Spectroscopy

The post-reaction Raman spectrum obtained for the spent 9.4MoAl catalyst is presented below in Figure 118.

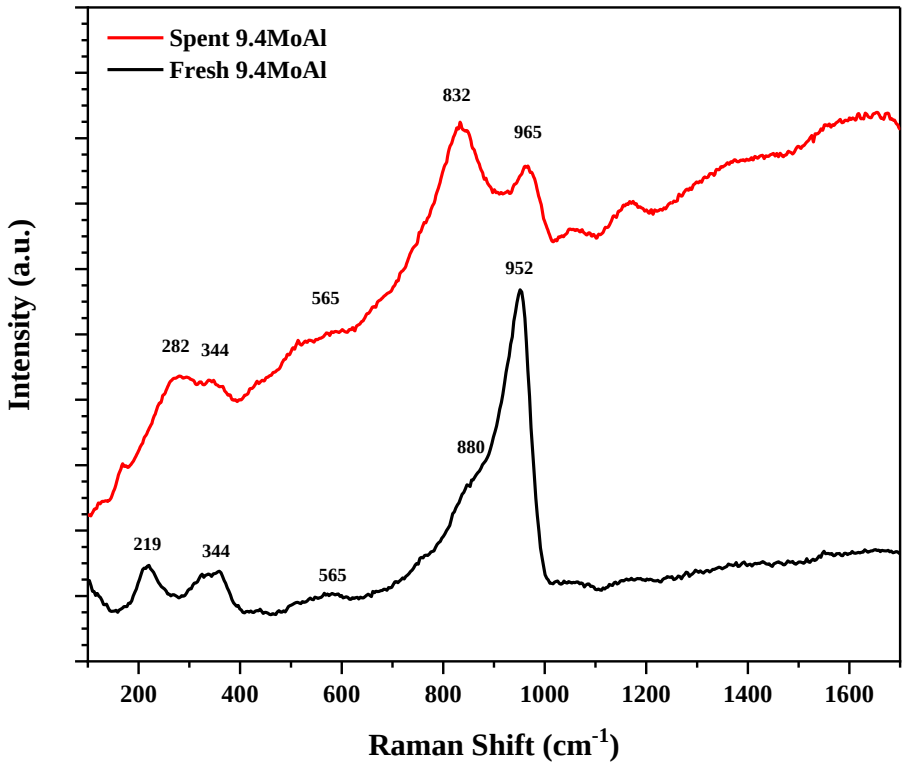

Figure 118: Raman spectra of spent 9.4MoAl from CL-PODH redox cycles utilising O_2 as the oxidant

Notable changes are observed in the Raman spectrum of spent 9.4MoAl when compared to that of the fresh sample. The sharp feature observed at ~952 cm^{-1}, previously assigned to the symmetric stretch of the molybdenyl bond of octahedral polymeric molybdena species, shifts to ~965 cm^{-1} and is significantly less prominent in the post-reaction Raman spectrum. [108]

Another clear disparity is the formation of the Raman band at ~832 cm^{-1}, which does not appear in the pre-reaction spectrum. A thorough literature search reveals that this feature may be characteristic of the stretching frequency of Mo=O in tetrahedrally coordinated surface molybdena domains, which comprise two terminal Mo=O bonds and two bridging Mo-O-Al bonds. [112] Furthermore, Raman features at ~565 and 344 cm^{-1}, present in the pre-reaction spectrum and assigned respectively as the bending mode of Mo=O and the symmetric stretch and bridging Mo-O-Mo bonds in polymeric molybdena species, remain present for the spent 9.4MoAl catalyst.

5.4.3 XRD

The XRD pattern obtained for the spent 9.4MoAl catalyst is presented in Figure 119. Similar to the fresh catalyst sample, the diffraction pattern is identical to that of γ-Al_2O_3, with reflections at 37.1, 46.0 and 66.7° correlating exclusively to the amorphous support material. The lack of intense diffraction peaks relating to crystalline MoO_3, indicates that the molybdenum oxide domains present in the post-reaction sample remain highly dispersed on the surface.

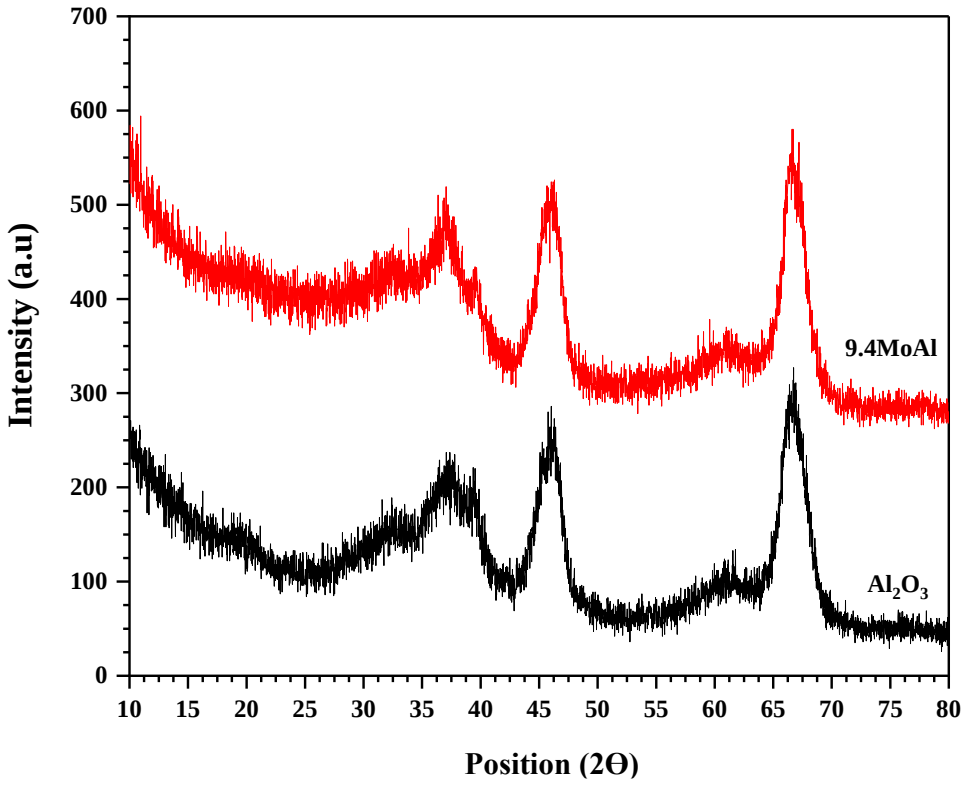

Figure 119: XRD patterns of spent 9.4MoAl from CL-PODH redox cycles utilising O_2 as the oxidant

5.4.4 TGA-TPO

A TGA-TPO measurement was employed to investigate the presence of carbonaceous deposits on the spent 9.4MoAl catalyst after performing ten CL-PODH redox cycles.

Figure 120 shows the post-reaction TPO weight loss profile, which displays the weight loss percentage obtained between 300-1000 K. The weight loss observed in the TPO profile results predominantly from H_2O evolution at lower temperatures. There were no combustion events observed at higher temperatures >500 K, which are typically associated with CO_2 evolution. This indicates that carbonaceous deposits were not present in the spent 9.4MoAl catalyst after performing the final catalyst regeneration step in CL-PODH redox cycling tests, utilising O_2 as the oxidant.

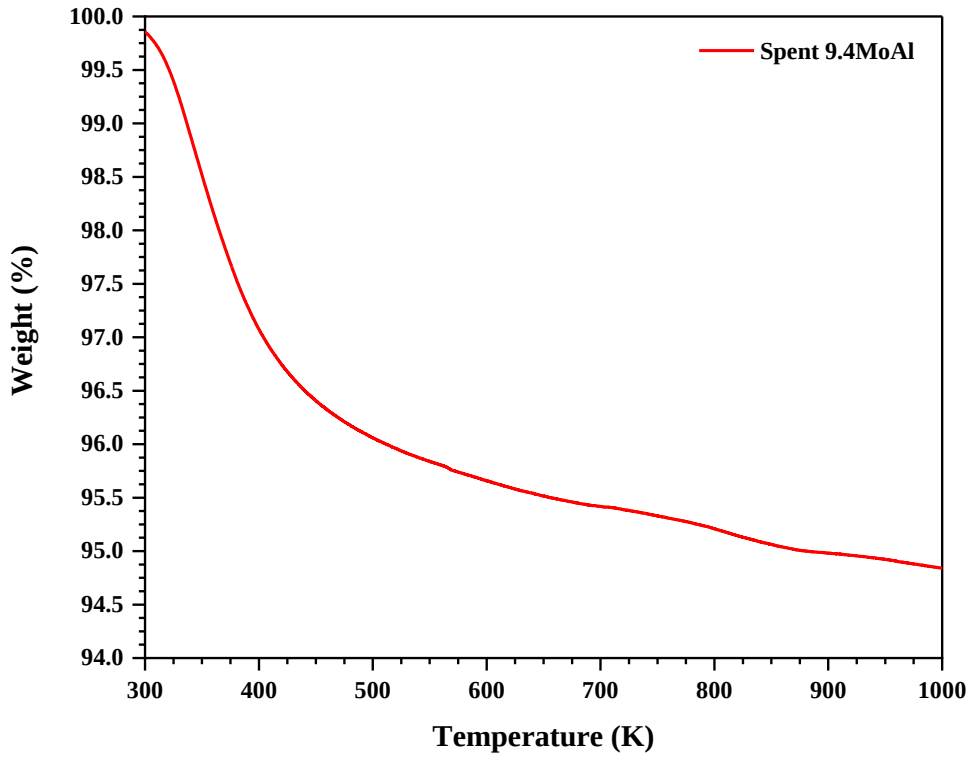

Figure 120: TPO weight loss profile of the spent 9.4MoAl catalyst, CL-PODH redox cycling test, O_2 oxidant, 773 K

6 Mixed Vanadium-Molybdenum Oxide

6.1 Pre-Reaction Characterisation

This section details the characterisation results of fresh VMoAl catalysts, conducted prior to CL-PODH reactivity tests. The techniques that were performed on VMoAl samples include MP-AES, ICP-OES, BET, H_2-TPR, O_2 chemisorption, Raman spectroscopy and XRD.

6.1.1 MP-AES and ICP-OES

Both MP-AES and ICP-OES measurements were employed to determine the vanadium and molybdenum content in fresh VMoAl catalyst samples. The desired vanadium loading was fixed at 10.0 wt.% with varying molybdenum loadings from 3.2, 4.7 and 9.4 wt.%, representing V/Mo molar ratios of 6:1, 4:1 and 2:1. The results detailing the vanadium and molybdenum content achieved via the impregnation technique are summarised in Table 49.

Table 49: MP-AES and ICP-OES results of fresh VMoAl catalysts

Sample	V wt.%	Mo wt.%
Fresh 10V3.2MoAl	9.7	3.4
Fresh 10V4.7MoAl	9.7	4.5
Fresh 10V9.4MoAl	9.7	9.6

MP-AES results show that an average V wt.% of 9.7 was achieved in fresh VMoAl catalysts. Furthermore, molybdenum loadings of 3.4, 4.5 and 9.6 wt.% were achieved for 10V3.2MoAl, 10V4.7MoAl and 10V9.4MoAl, respectively, indicating that catalyst preparations were carried out successfully throughout the VMoAl catalyst series.

6.1.2 BET Surface Area Determination

BET adsorption-desorption isotherms for the γ-Al_2O_3 support and fresh VMoAl catalysts are presented in Figure 121, which show that the isotherms obey the Type IV model observed previously in fresh VAl and MoAl catalysts.

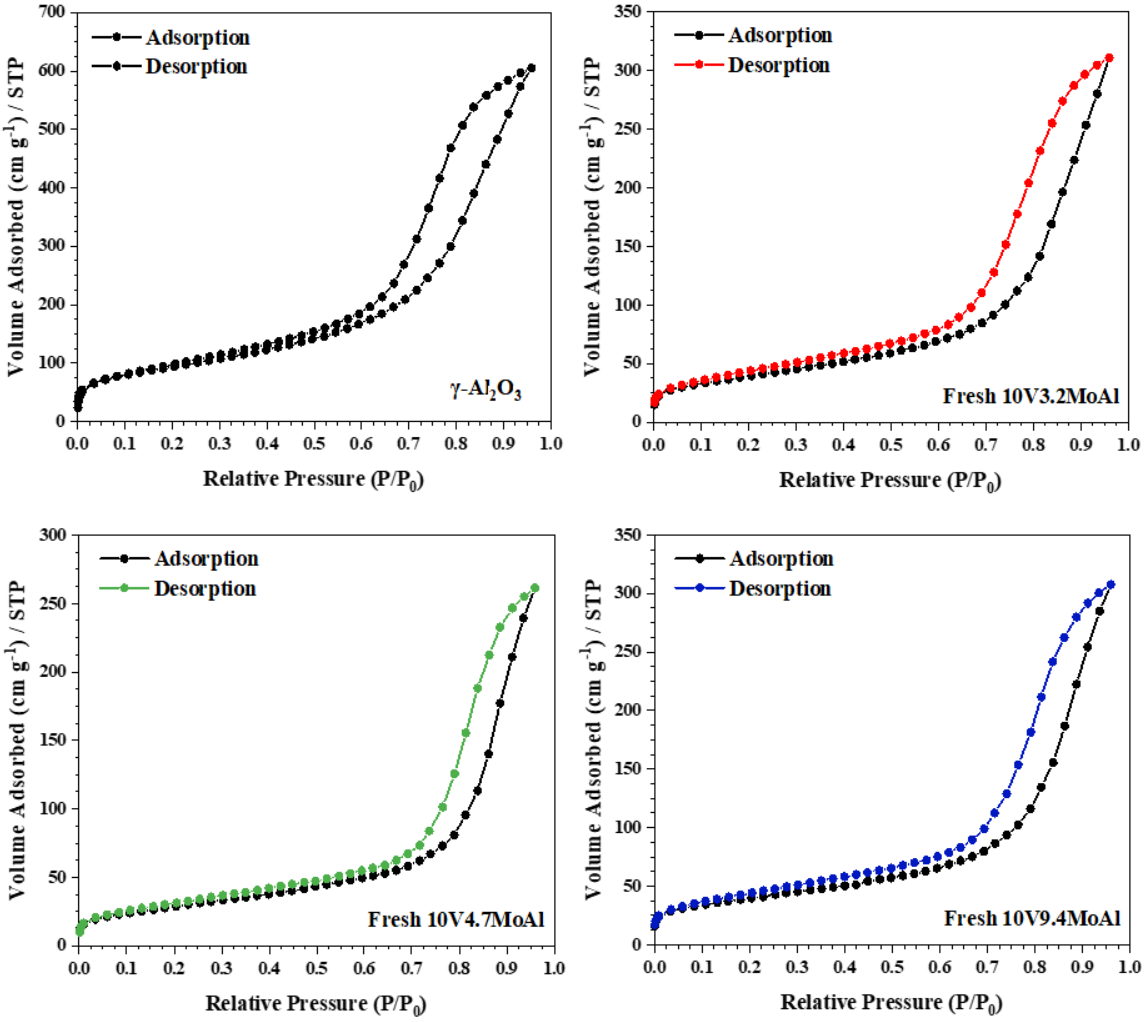

Figure 121: N_2 adsorption-desorption isotherms of fresh VMoAl catalysts

Table 50 displays the surface area, pore volume and average pore diameter of VMoAl samples. The surface area of the 10VAl catalyst was 145 $m^2 g^{-1}$, which decreased significantly to 117 $m^2 g^{-1}$ upon molybdenum incorporation in the 10V3.2MoAl sample. An increase in the average pore diameter is observed, which may be associated with the formation of crystalline MoO_3 species. Subsequent molybdenum incorporation yields lower surface areas and pore volumes, where the average pore diameter increases markedly from 61 to 84 Å. Vanadium and molybdenum surface densities are presented in Table 50, which were calculated as described in Equations 17 and 21.

Table 50: Surface area, pore volume and average pore diameter of fresh VMoAl catalysts

Sample	S_{BET} ($m^2 g^{-1}$)	V_{pore} ($cm^3 g^{-1}$)	Avg. pore diameter (Å)	Surface Density (Mo nm^{-2})	Surface Density (V nm^{-2})
Fresh 10VAl	145	0.55	43	-	7.9
Fresh 10V3.2MoAl	117	0.48	61	1.8	9.8
Fresh 10V4.7MoAl	85	0.40	71	3.3	13.5
Fresh 10V9.4MoAl	76	0.38	84	7.9	15.1

6.1.3 H_2-TPR

H_2-TPR measurements were performed to investigate the reducibility of both molybdena and vanadia sites as the molybdenum loading increased in fresh VMoAl catalysts. H_2-TPR profiles and corresponding peak maxima are presented in Figure 122 and Table 51, where two distinct reduction events above 500 K are observed.

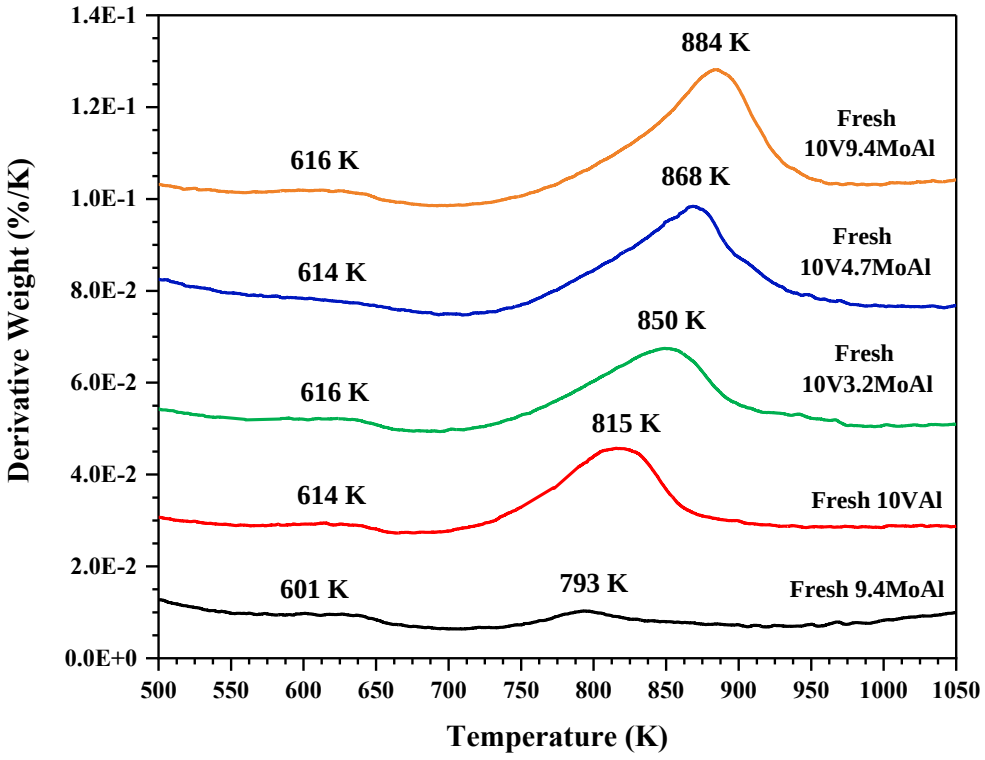

Figure 122: H_2-TPR profile of fresh VMoAl catalysts

Table 51: H_2-TPR data summarising T_{max} of reduction peaks in fresh VMoAl catalysts

Sample	T_{max} (K)	
	A	B
Fresh 10V3.2MoAl	616	850
Fresh 10V4.7MoAl	614	868
Fresh 10V9.4MoAl	616	884

Similar to the fresh 10VAl catalyst, VMoAl samples exhibit a lower temperature reduction peak, T_{max} = 614 and 616 K. This reduction event was previously ascribed to the reduction of amorphous monovanadate and polyvanadate surface species, which indicates their presence despite co-impregnating molybdena onto the catalyst support.

The second reduction event observed with the 10VAl catalyst occurs at 815 K, which shifts to higher temperatures in VMoAl samples of 850, 868 and 884 K. The formation of a shouldering reduction peak at ~800 K is also observed which is absent in the H_2-TPR profile of the 10VAl catalyst, indicating that it may arise from crystalline MoO_3 species or from a newly formed V-Mo-O mixed phase. The total weight loss associated with H_2O evolution at the higher temperature reduction event was determined and is tabulated in Table 52. The ratio of evolved oxygen to vanadium and molybdenum species in mixed VMoAl catalysts was approximately 0.8:1.0, which is less than the ratio observed in either of the VAl or MoAl catalyst series.

Table 52: Weight loss associated with H_2O evolution at the higher temperature reduction event in VMoAl catalysts

Sample	Weight Loss[a] (mg)	O moles (µmol)	V + Mo moles[b] (µmol)	O/(V+Mo) Ratio
Fresh 10V3.2MoAl	0.34	21.3	27.2	0.78
Fresh 10V4.7MoAl	0.32	20.0	23.3	0.85
Fresh 10V9.4MoAl	0.48	30.0	36.0	0.83

[a]Oxygen weight loss from H_2O evolution, [b]V+Mo moles present in the sample used for each TPR measurement.

6.1.4 Oxygen Chemisorption

Oxygen chemisorption measurements were performed on reduced VMoAl catalysts as described in Section 3.3.2. Figure 123 presents the cumulative oxygen uptake plotted as a function of pulse number.

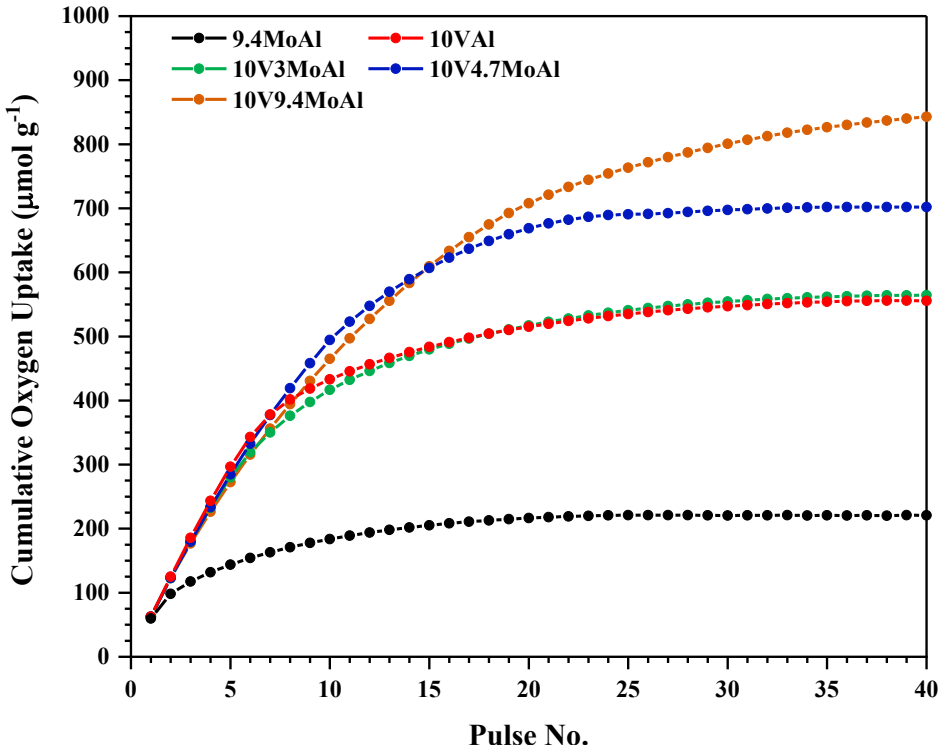

Figure 123: Cumulative oxygen uptake of fresh VMoAl catalysts

Figure 124 displays the trend in oxygen uptake as a function of increasing molybdenum loading. On comparison with the fresh 10VAl catalyst, only a slight increase in oxygen uptake is observed in the 10V3.2MoAl sample. Oxygen uptake becomes more significant with additional molybdenum loading, however, where 10V4.7MoAl and 10V9.4MoAl catalysts exhibit a systematic increase, reaching ~860 µmol g^{-1} for the 10V9.4MoAl sample. In previous chapters, the oxygen uptake was used to calculate the dispersion of vanadium and molybdenum metal in reduced VAl and MoAl samples. In the case of mixed vanadium and molybdenum catalyst systems however, an accurate metal dispersion cannot be obtained since it is possible that the molybdenum promoter may behave in an interactive manner, forming V-O-Mo domains.

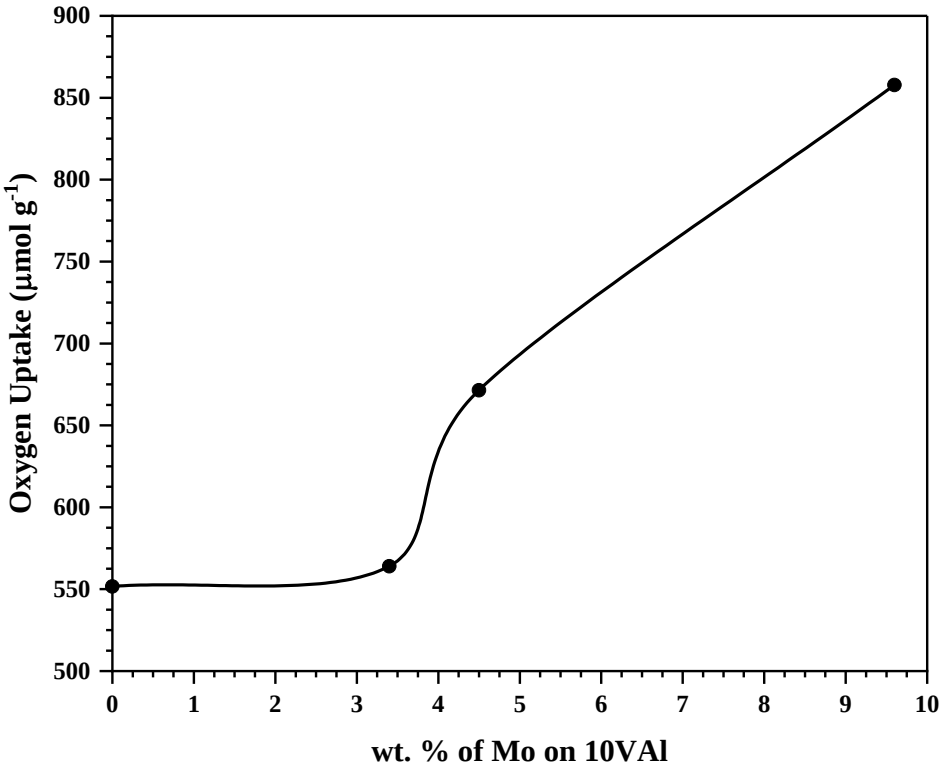

Figure 124: Oxygen uptake as a function of Mo wt.% incorporation on the 10VAl catalyst

6.1.5 Raman Spectroscopy

Raman spectra obtained for the fresh 10VAl catalyst versus VMoAl catalysts are presented in Figure 125.

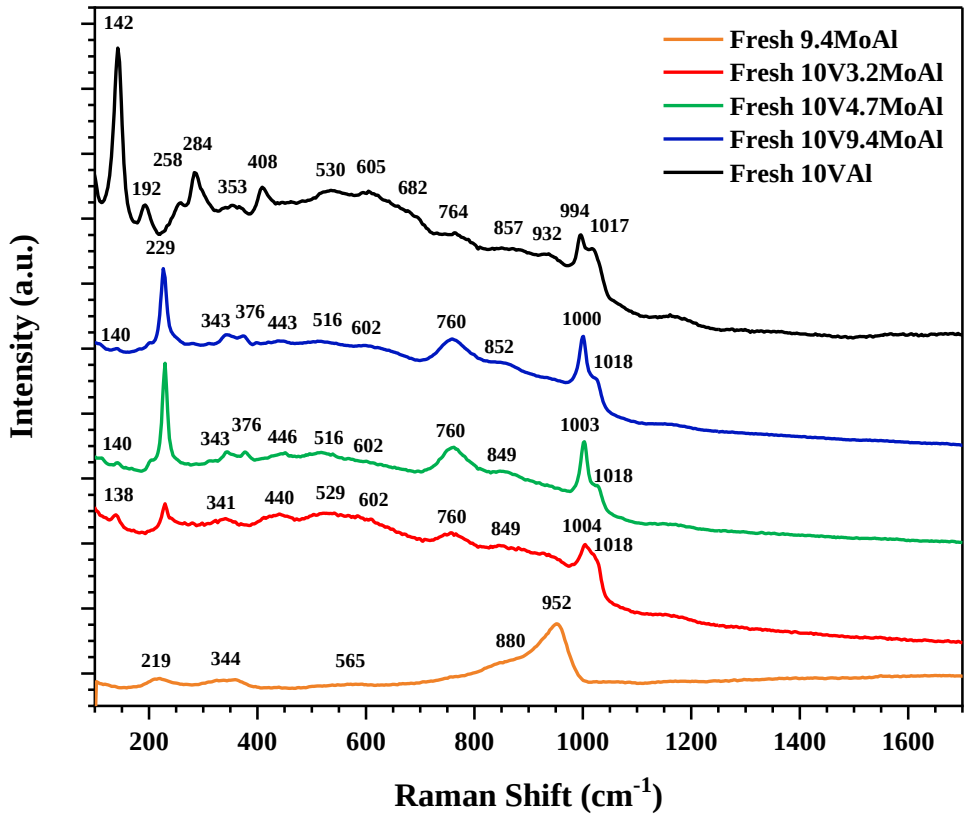

Figure 125: Raman spectra for fresh VMoAl catalysts

A significant difference is observed in the Raman spectra of VMoAl catalysts compared to that of the fresh 10VAl and 9.4MoAl samples. Most notably, the sharp and intense band at ~142 cm^{-1}, which is characteristic of crystalline V_2O_5 species, is absent in the Raman spectra of VMoAl samples. Raman shifts at ~994, 682, 408, 284, 258, and 192 cm^{-1} are also not observed, further indicating the absence of bulk V_2O_5 in the mixed vanadia and molybdena catalyst systems; however, the Raman band at ~1017 cm^{-1}, assigned to the V=O bond present in polyvanadate species, remains present in the Raman spectra of all fresh VMoAl catalyst samples.

In the spectra of the 10V3.2MoAl catalyst, a sharp band appears at ~1004 cm^{-1}, which shifts to 1000 cm^{-1} with increasing intensity as the molybdenum loading increases. This feature has previously been assigned in literature as the stretching frequency of the molybdenyl (Mo=O) bond present in surface monooxo molydena species. [64, 113, 114] Studies

performed by Chagas *et al.*, however, attribute the ~1000 cm^{-1} band to crystalline MoO_3 species in addition to bands at ~378 and 337 cm^{-1}. Raman features at ~376 and 343 cm^{-1} are also present in the pre-reaction Raman spectra of VMoAl samples, therefore, a conclusive assignment of the ~1004 cm^{-1} band cannot be made.

Lastly, a prominent band appears at ~229 cm^{-1} and 760 cm^{-1}, which become more pronounced with increasing molybdenum loading. A thorough literature search reveals that these features are proposed to arise from V-O-Mo stretches in mixed molybdovanadate species. [52, 65, 69, 115]

6.1.6 XRD

XRD patterns obtained for fresh VMoAl catalyst samples are shown in Figure 126. The pattern of 10V3.2MoAl exhibits peaks primarily characteristic of the amorphous γ-Al_2O_3 support, indicating that both vanadia and molybdena species are highly dispersed on the alumina surface. In comparison, the XRD patterns of 10V4.7MoAl and 10V9.4MoAl catalysts suggest the formation of crystalline V_2O_5, MoO_3 and a mixed oxide V_2MoO_8 phase. [65, 116-118]

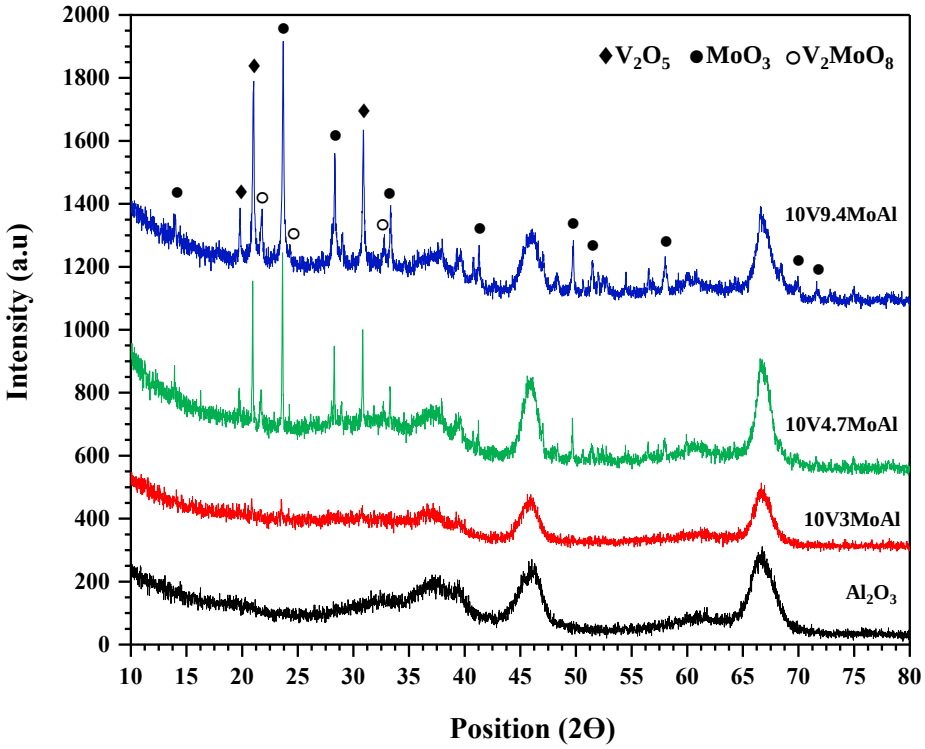

Figure 126: XRD patterns of γ-Al_2O_3 and fresh VMoAl catalysts

6.2 Reactivity Tests

This section details the results obtained from CL-PODH redox cycling tests using the fresh 10V3.2MoAl, 10V4.7MoAl and 10V9.4MoAl catalysts as described in Section 3.3.3.

6.2.1 CL-PODH Redox Cycles with O_2

Results from CL-PODH redox cycling tests performed over fresh VMoAl catalysts, using O_2 as the oxidant in the regeneration step, are presented here. Reaction profiles detailing propane conversions and propene selectivities and yields are presented in Figures 127-129, which compare the catalyst activity and selectivity to the olefin product as a function of increasing molybdenum loading. Additionally, the selectivity to the undesired CO_2 product and resulting yield has been investigated, which are detailed in reaction profiles presented in Figures 130 and 131.

The data presented is the instantaneous performance obtained at the end of the 30 min PDH step of each corresponding redox cycle.

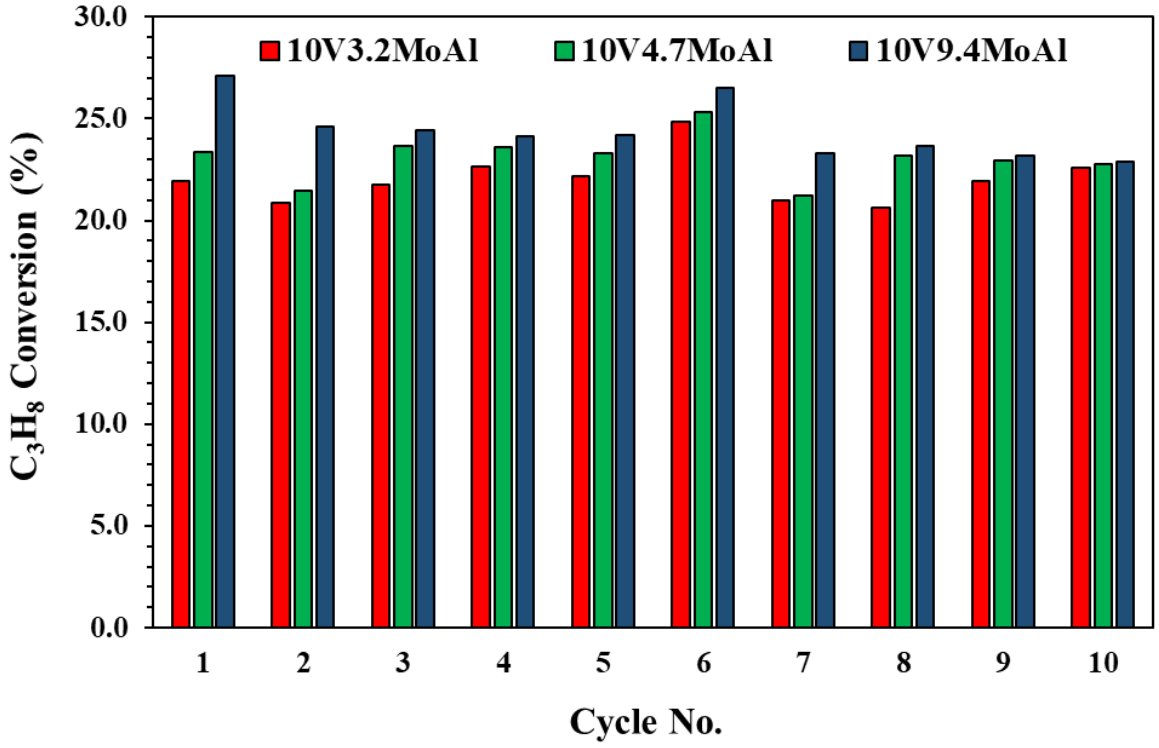

Figure 127: Instantaneous C_3H_8 conversions using 10V3.2MoAl, 10V4.7MoAl and 10V9.4MoAl catalysts, O_2 oxidant, 773 K, 1 atm

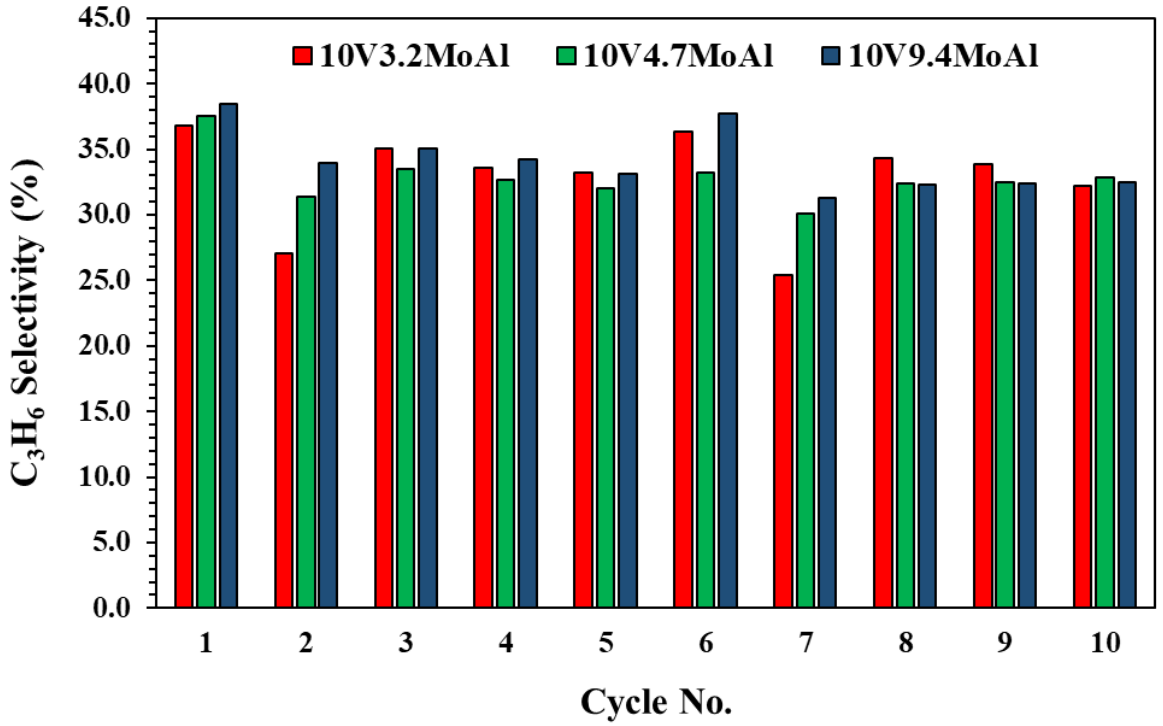

Figure 128: Instantaneous C_3H_6 selectivities using 10V3.2MoAl, 10V4.7MoAl and 10V9.4MoAl catalysts, O_2 oxidant, 773 K, 1 atm

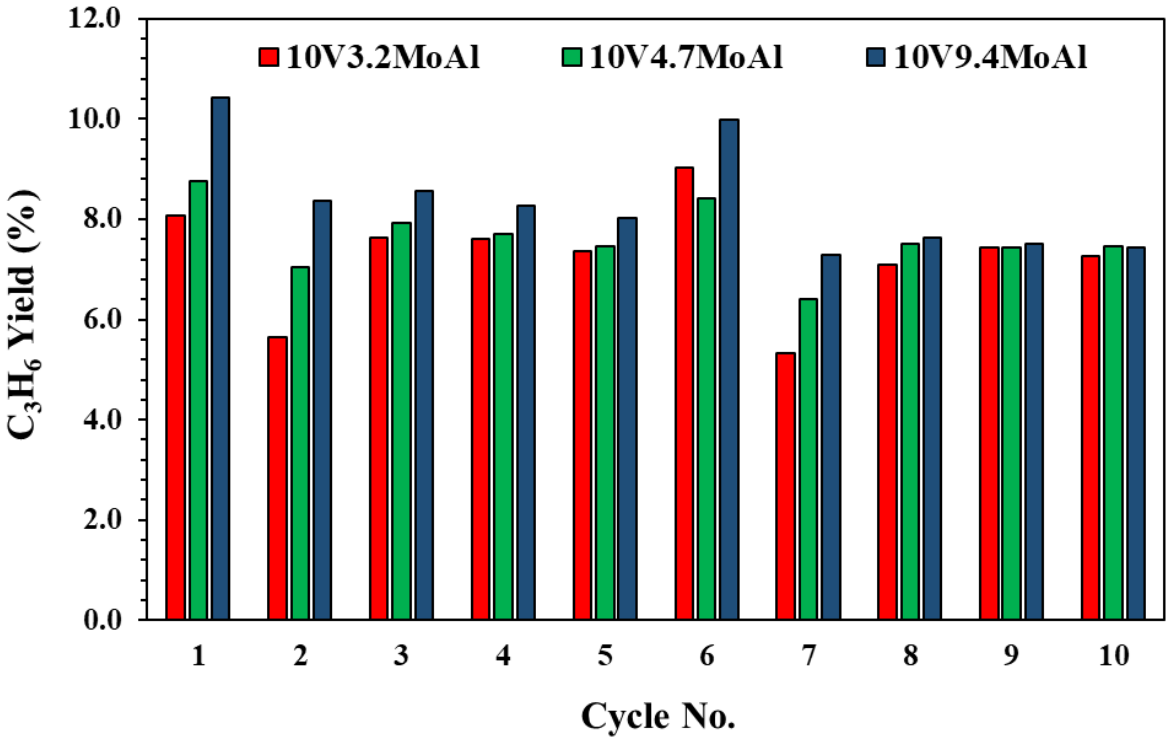

Figure 129: Instantaneous C_3H_6 yields using 10V3.2MoAl, 10V4.7MoAl and 10V9.4MoAl catalysts, O_2 oxidant, 773 K, 1 atm

Figures 127-129 reveal that CL-PODH redox cycling tests performed over the 10V9.4MoAl catalyst generate the most promising results within the VMoAl catalyst series.

Propane conversions obtained using 10V3.2MoAl and 10V4.7MoAl catalysts reach ~21.9 and 23.3 % by the end of the 1st PDH step, with no indication of catalyst deactivation during cycles 2 to 5. In both cases, an enhancement in activity is observed in the PDH step of cycle 6 followed by a decrease in cycles 7-10, affording propane conversions comparable to those obtained in cycles 2-5. The trend in propene selectivity is analogous in cycles 2 and 7, where a marked decrease is observed after the 1st and 6th PDH step. This decay occurs at similar propane conversions, thus resulting in an overall decrease in propene yield. Propene selectivity increases and remains relatively stable throughout cycles 3-5 and 8-10, indicating that the vanadia and molybdena sites which are selective towards the olefin product are regenerated as the CL-PODH redox cycles proceed.

When utilising the 10V9.4MoAl catalyst, a propane conversion of ~27.1 % is obtained by the end of the 1st PDH step. With the exception of the 6th PDH step, where an enhancement in activity is observed, catalyst deactivation occurs as propane conversion decreases to ~22.9 % in the PDH step of cycle 10. Overall, the 10V9.4MoAl catalyst exhibits a higher activity than the 10VAl sample, however, propene selectivities are notably lower. In the test using 10V9.4MoAl, propene yields decrease when going from cycle 1 to cycle 2 due to a decay in propene selectivity from ~38.5 to 34.0 %. An improvement in propene selectivity is observed in the PDH step of cycle 6, before it decreases and reaches steady state throughout cycles 7 to 10, where a propene yield of ~7.4 % is obtained by the end of cycle 10.

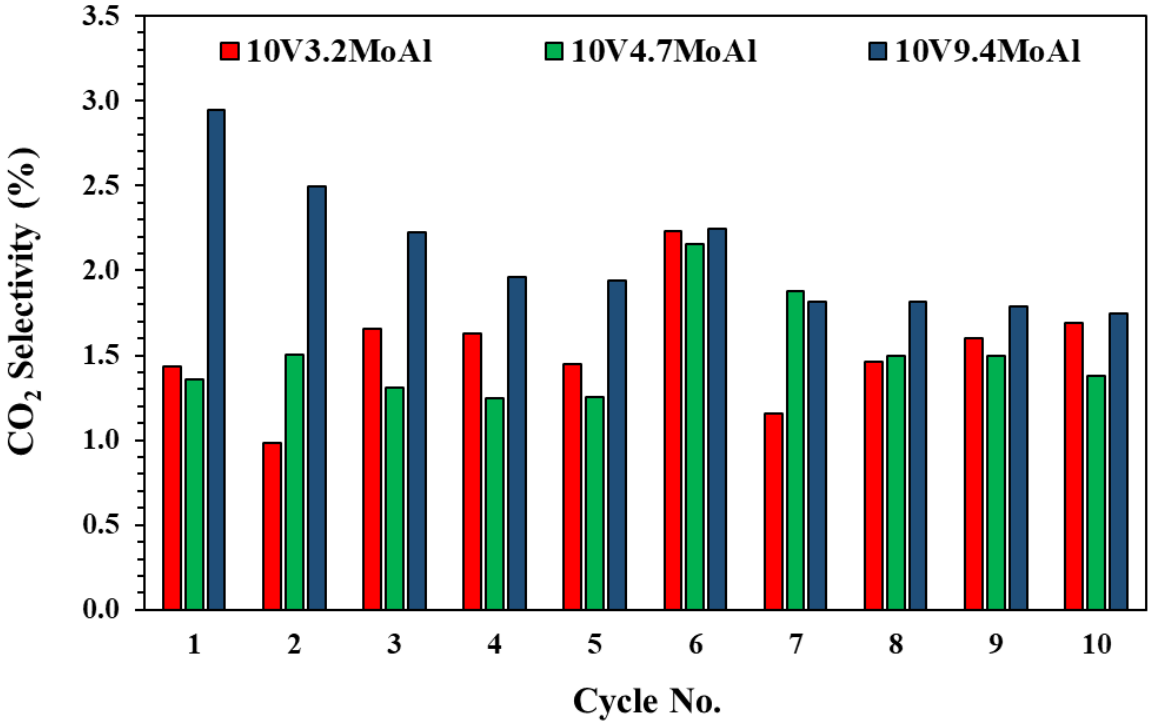

Figure 130: Instantaneous CO_2 selectivities using 10V3.2MoAl, 10V4.7MoAl and 10V9.4MoAl catalysts, O_2 oxidant, 773 K, 1 atm

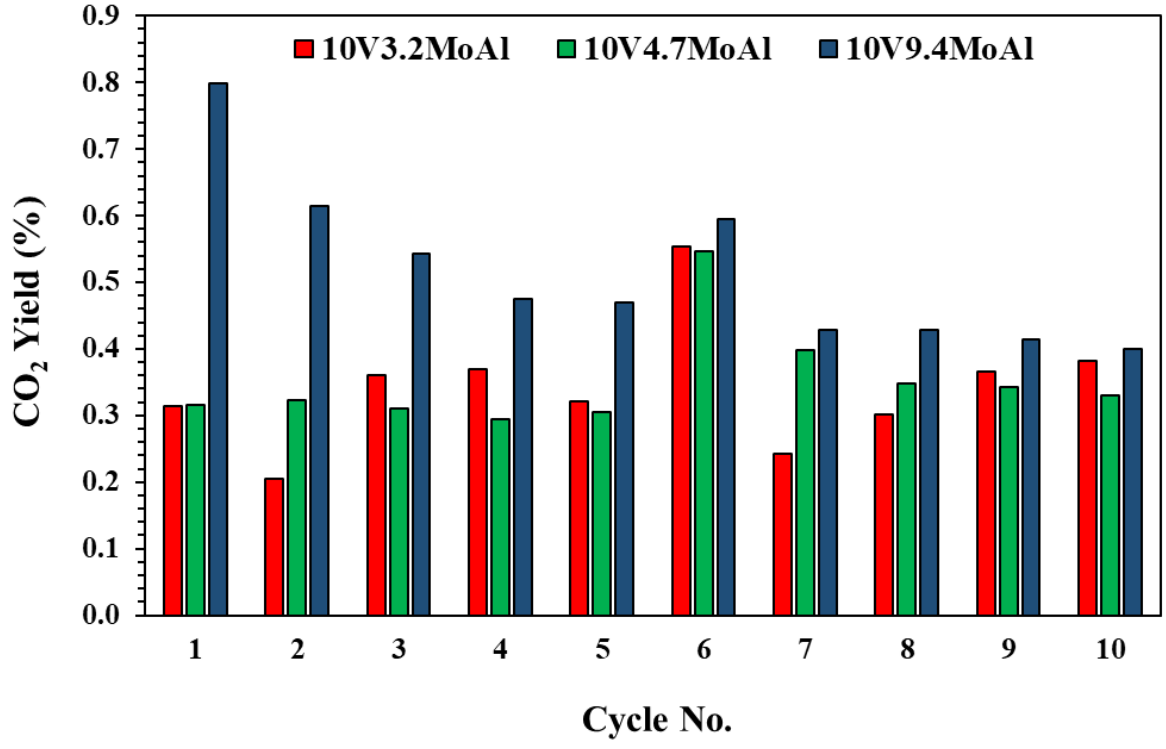

Figure 131: Instantaneous CO_2 yields using 10V3.2MoAl, 10V4.7MoAl and 10V9.4MoAl catalysts, O_2 oxidant, 773 K, 1 atm

Figures 130 and 131 present CO_2 selectivities and resulting yields obtained at the end of each 30 min PDH step. Notably, the instantaneous production of the undesired CO_2 product at the end of each PDH step is significantly lower in comparison to propene formation.

It is apparent that initial CO_2 yields are highest in the test performed over the 10V9.4MoAl catalyst. During this reaction, CO_2 yields decrease progressively throughout cycles 2 to 5. An enhancement is observed again in the PDH step of cycle 6 before they diminish as the remaining cycles proceed.

During the PDH step of cycles 2-5, the 10V3.2MoAl catalyst exhibits a higher selectivity to CO_2 in comparison to the 10V4.7MoAl catalyst. This results in higher CO_2 yields despite the increased activity of the latter. Furthermore, the trend in CO_2 selectivity and yield obtained by both catalysts are similar to those achieved when using the 10V9.4MoAl catalyst. Both the selectivity and resulting yield exhibit an overall decrease as the cycles progress, with the exception of those obtained during the PDH step of cycle 6 where an improvement is observed.

Reaction profiles detailing the data obtained from the entire 30 min PDH step utilising the 10V9.4MoAl catalyst are presented in Figures 132-134. The data presented is exclusively from the PDH step of cycle 1 versus cycle 2. Figures 132 and 133 are propane conversion, propene and CO_2 selectivity plots and Figure 134 presents the resulting propene and CO_2 yield.

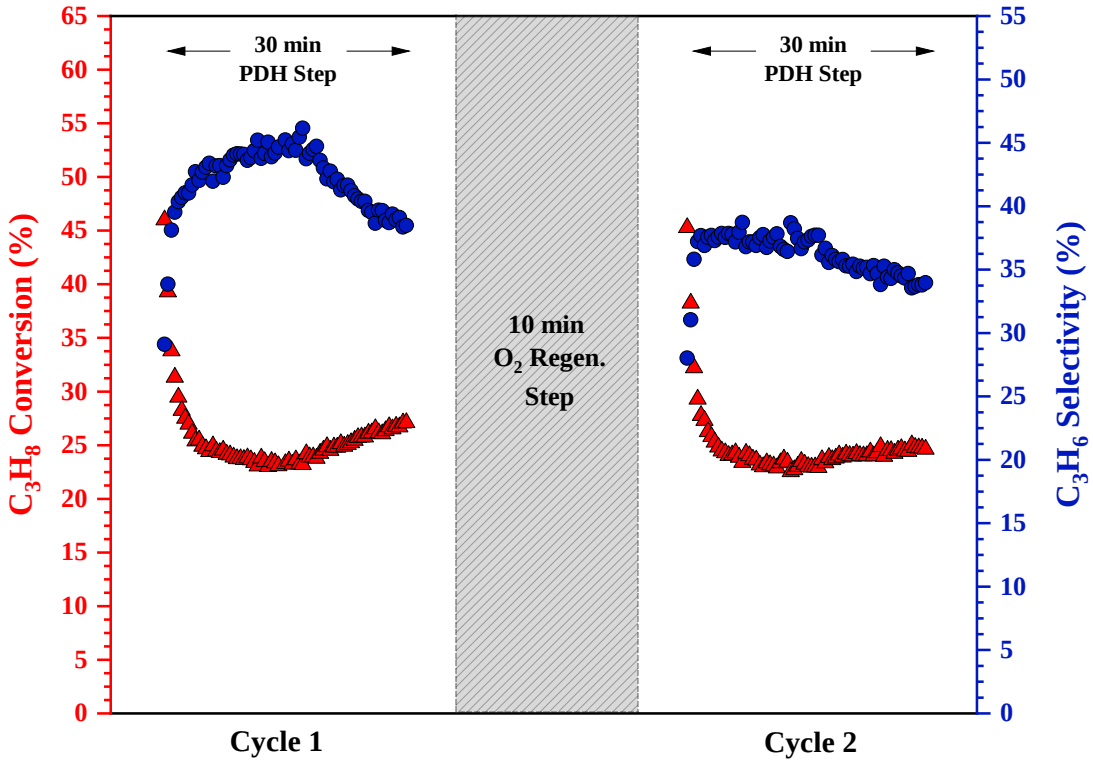

Figure 132: Reaction profile of C_3H_8 conversion and C_3H_6 selectivity during the PDH step of cycle 1 versus cycle 2: 10V9.4MoAl, O_2 oxidant, 773 K, 1 atm

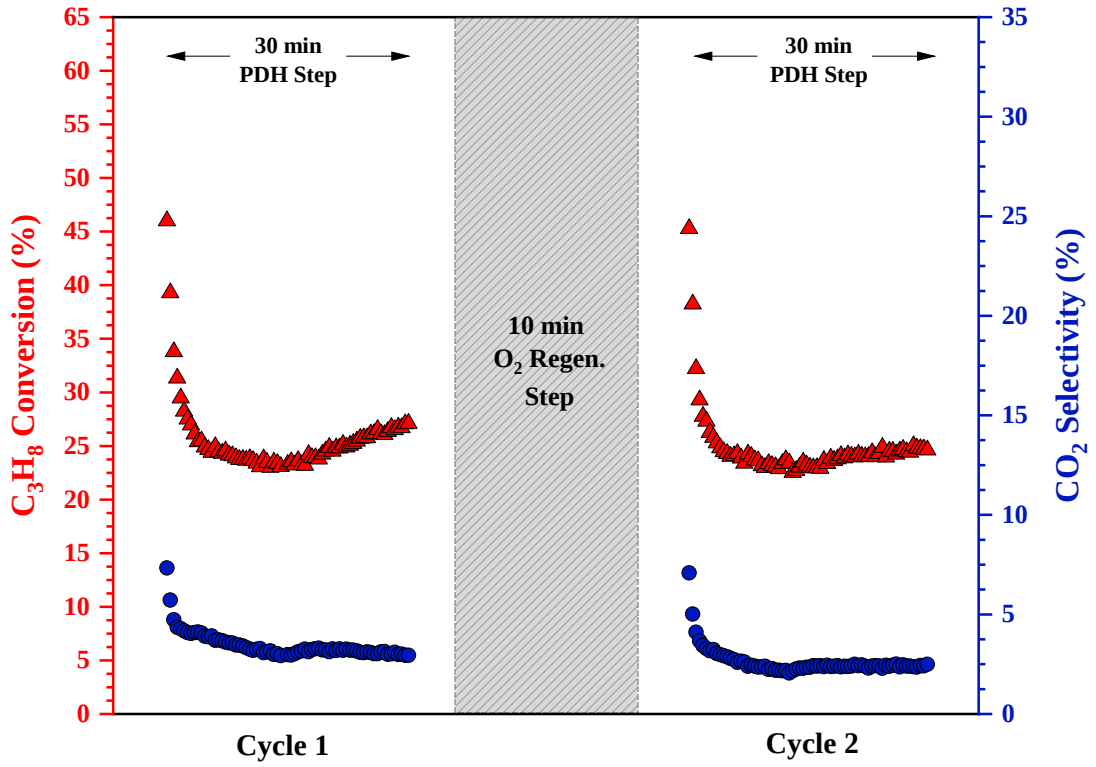

Figure 133: Reaction profile of C_3H_8 conversion and CO_2 selectivity during the PDH step of cycle 1 versus cycle 2: 10V9.4MoAl, O_2 oxidant, 773 K, 1 atm

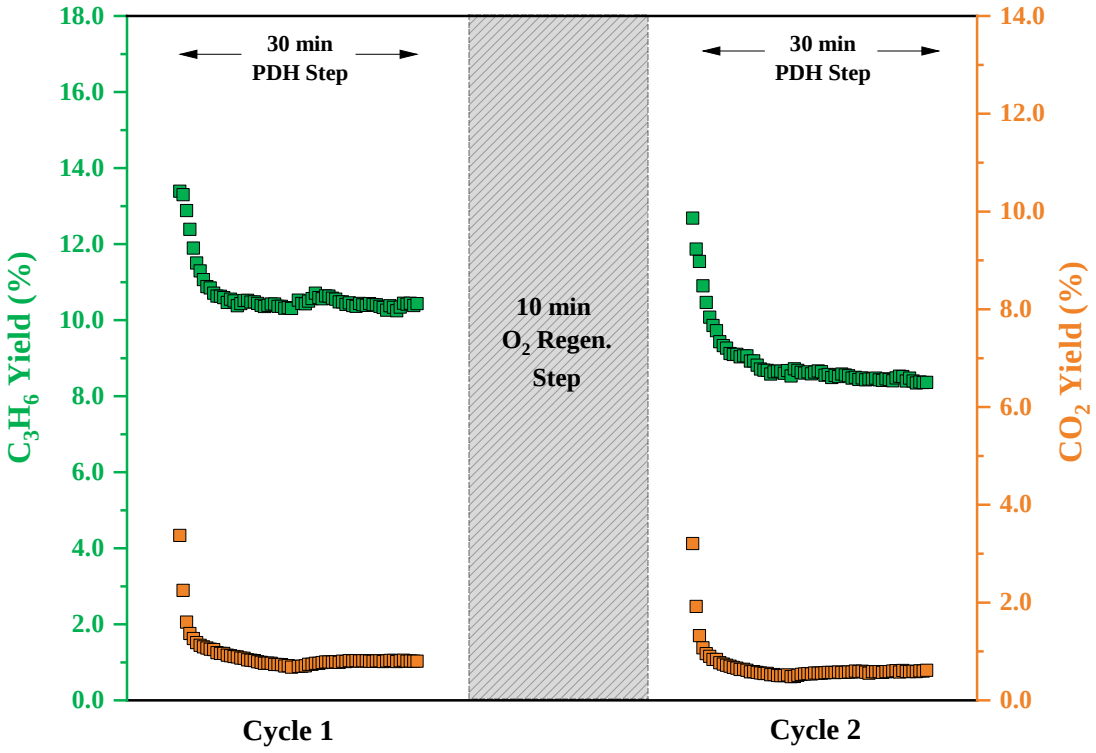

Figure 134: Reaction profile of C_3H_6 and CO_2 yields during the PDH step of cycle 1 versus cycle 2: 10V9.4MoAl, O_2 oxidant, 773 K, 1 atm

Similar to those of the 10VAl and 9.4MoAl catalyst, the reaction profiles exhibit different reactivity regions throughout the PDH step. Figure 134 reveals that propene and CO_2 yields are maximised within the first ~1.5 min of cycles 1 and 2, where propene yield decrease as propane conversion drops off. The continual decay in propene selectivity ultimately hampers the yield and does not exhibit a recovery, in contrast to that observed in PDH steps performed over the 10VAl catalyst. A similar trend is observed with respect to CO_2 yield, where selectivity to CO_2 remains low and the resulting yield declines as the PDH step proceeds.

Propane conversions, propene/CO_2 selectivities and the resulting propene/CO_2 yields achieved ~1.5, 6 and 30 min into the PDH step of cycles 1 and 2 are summarised in Table 53 and Table 54.

Table 53: Summary of C_3H_8 conversions, C_3H_6 and CO_2 selectivities and yields obtained at the different reaction regions during the PDH step of cycle 1: 10V9.4MoAl, O_2 oxidant, 773 K, 1 atm

Time into PDH Step (min)	C_3H_8 Conversion (%)	C_3H_6 Selectivity (%)	C_3H_6 Yield (%)	CO_2 Selectivity (%)	CO_2 Yield (%)
1.5	46.0	29.1	13.4	7.3	3.4
6	24.9	42.7	10.6	3.9	1.0
30	27.1	38.5	10.4	2.9	0.8

Table 54: Summary of C_3H_8 conversions and C_3H_6 and CO_2 selectivities and yields obtained at the different reaction regions during the PDH step of cycle 2: 10V9.4MoAl, O_2 oxidant, 773 K, 1 atm

Time into PDH Step (min)	C_3H_8 Conversion (%)	C_3H_6 Selectivity (%)	C_3H_6 Yield (%)	CO_2 Selectivity (%)	CO_2 Yield (%)
1.5	45.3	28.0	12.7	7.1	3.2
6	24.0	37.8	9.1	2.8	0.7
30	24.6	34.0	8.4	2.5	0.6

Similar to that found with the 10VAl and 9.4MoAl catalysts, an enhancement in propene formation is observed in the PDH step of cycle 6 after holding the catalyst overnight under a continuous flow of argon. To further explore this effect, reaction profiles detailing the data obtained from the entire 30 min PDH step of cycle 5 versus cycle 6 have been compared. Figures 135 and 136 show propane conversion, propene and CO_2 selectivity plots and Figure 137 shows resulting propene and CO_2 yields.

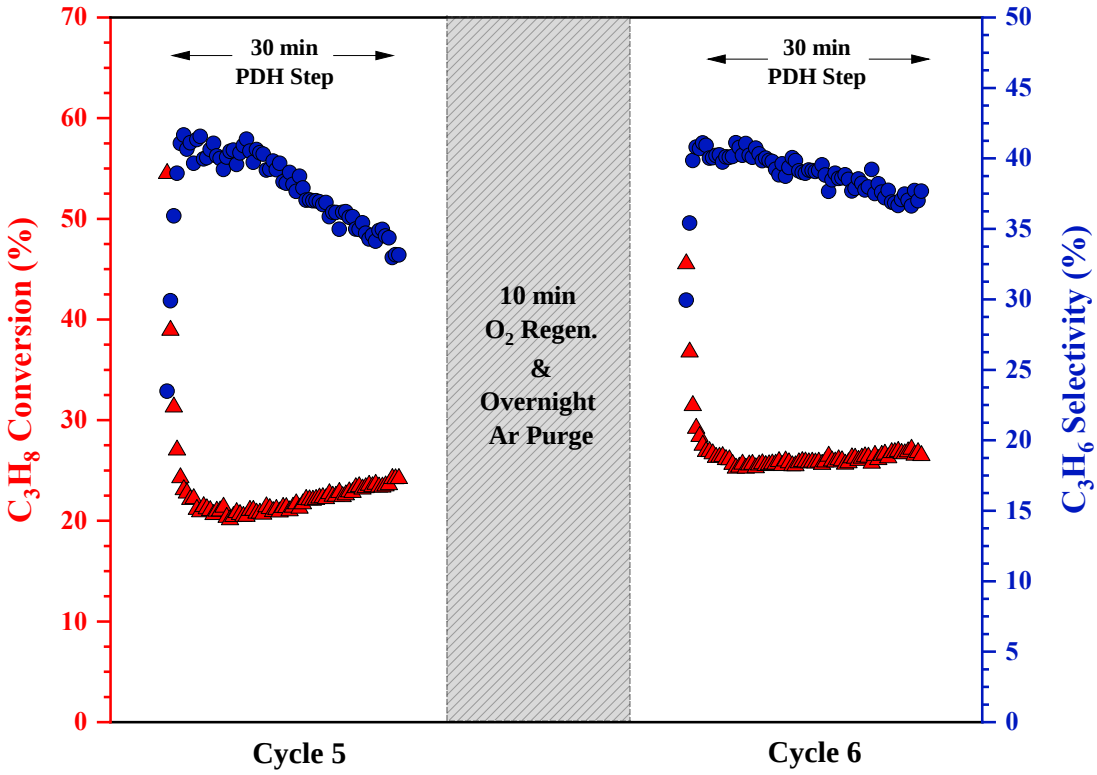

Figure 135: Reaction profile of C_3H_8 conversion and C_3H_6 selectivity during the PDH step of cycle 5 versus cycle 6: 10V9.4MoAl, O_2 oxidant, 773 K, 1 atm

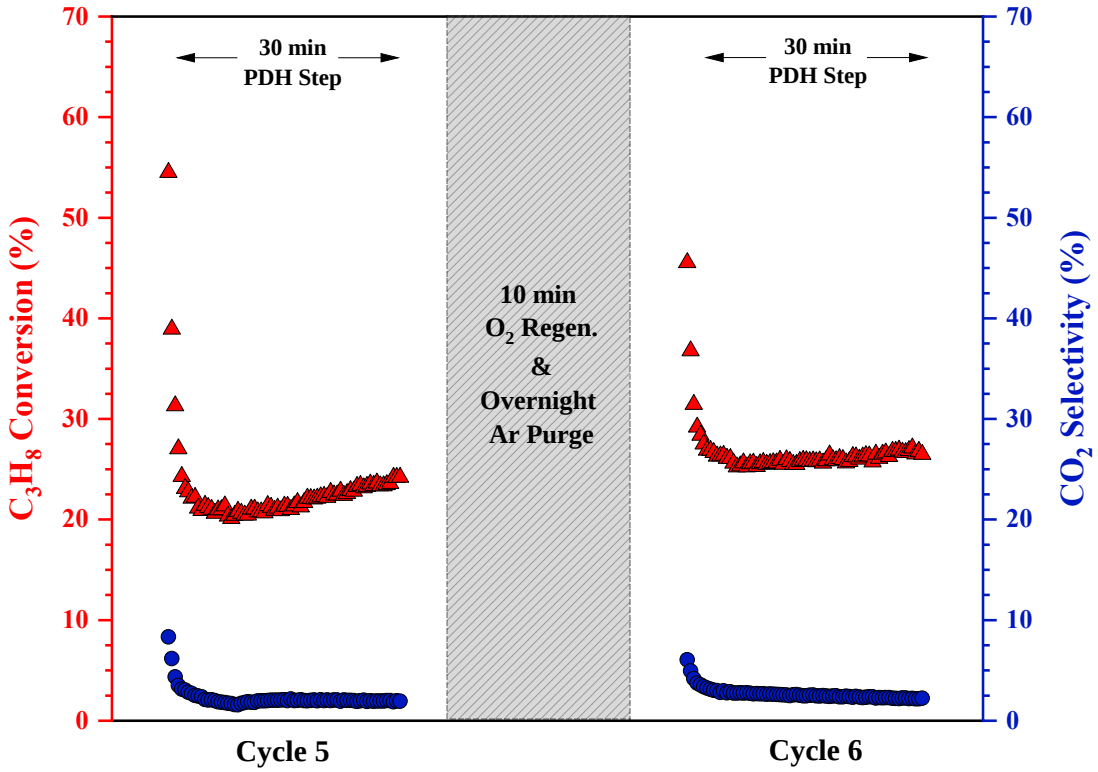

Figure 136: Reaction profile of C_3H_8 conversion and CO_2 selectivity during the PDH step of cycle 5 versus cycle 6: 10V9.4MoAl, O_2 oxidant, 773 K, 1 atm

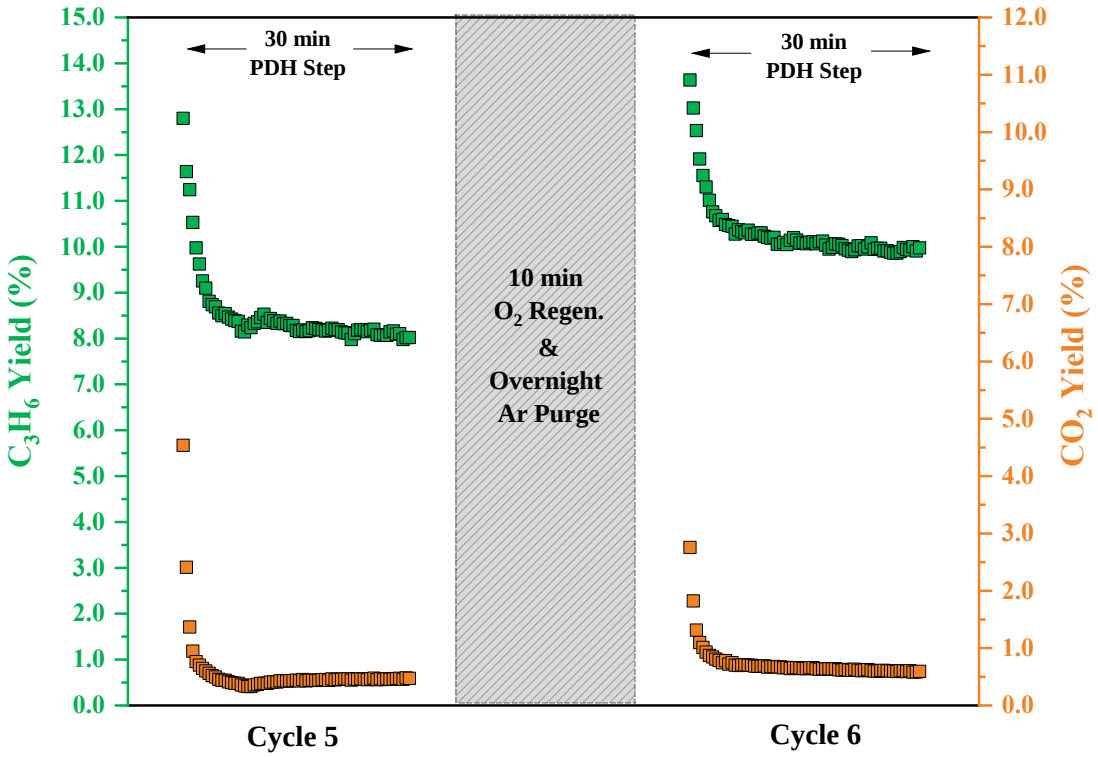

Figure 137: Reaction profile of C_3H_6 and CO_2 yields during the PDH step of cycle 5 versus cycle 6: 10V9.4MoAl, O_2 oxidant, 773 K, 1 atm

A similar trend is observed in cycles 5 and 6 regarding the different reactivity regions throughout the PDH step. Notably, maximum propene and CO_2 yields are achieved within the first ~1.5 min of switching on the propane feed. After this point, propene and CO_2 yields decay continually throughout the remainder of the PDH step concomitant with decreasing selectivity. Upon comparison of both cycles, the selectivity to both propene and CO_2 is further enhanced in the PDH step of cycle 6. This improvement consequently achieves higher propene and CO_2 yields, which increase from ~8.0 and 0.5 % to ~10.0 and 0.6 %, respectively.

Propane conversions, propene/CO_2 selectivities and the resulting propene/CO_2 yields achieved at these different reactivity regions in CL-PODH redox cycles 5 and 6 are summarised in Table 55 and Table 56.

Table 55: Summary of C_3H_8 conversions, C_3H_6 and CO_2 selectivities and yields obtained at the different reaction regions during the PDH step of cycle 5: 10V9.4MoAl, O_2 oxidant, 773 K, 1 atm

Time into PDH Step (min)	C_3H_8 Conversion (%)	C_3H_6 Selectivity (%)	C_3H_6 Yield (%)	CO_2 Selectivity (%)	CO_2 Yield (%)
1.5	54.5	23.5	12.8	8.3	4.5
6	21.4	40.0	8.6	2.1	0.5
30	24.2	33.1	8.0	1.9	0.5

Table 56: Summary of C_3H_8 conversions, C_3H_6 and CO_2 selectivities and yields obtained at the different reaction regions during the PDH step of cycle 6: 10V9.4MoAl, O_2 oxidant, 773 K, 1 atm

Time into PDH Step (min)	C_3H_8 Conversion (%)	C_3H_6 Selectivity (%)	C_3H_6 Yield (%)	CO_2 Selectivity (%)	CO_2 Yield (%)
1.5	45.5	29.9	13.6	6.1	2.8
6	26.4	39.7	10.5	3.0	0.8
30	26.5	37.6	10.0	2.2	0.6

6.3 Post-Reaction Characterisation

This section details the post-reaction characterisation results of spent VMoAl catalyst samples by BET, Raman, XRD and TGA-TPO.

6.3.1 BET Surface Area Determination

Table 57 summarises the surface area, pore volume and average pore diameter results for the spent 10V3.2MoAl, 10V4.7MoAl and 10V9.4MoAl catalysts.

Table 57: Surface area, pore volume and average pore diameter of spent 10V3.2MoAl, 10V4.7MoAl and 10V9.4MoAl catalysts from CL-PODH redox cycles utilising O_2 as the oxidant

Sample	S_{BET} ($m^2\ g^{-1}$)	V_{pore} ($cm^3\ g^{-1}$)	Avg. pore diameter (Å)
Fresh 10V3.2MoAl	117	0.48	61
Spent 10V3.2MoAl 10 Cycles, 773 K, O_2	97	0.43	61
Fresh 10V4.7MoAl	85	0.40	71
Spent 10V4.7MoAl 10 Cycles, 773 K, O_2	75	0.39	70
Fresh 10V9.4MoAl	76	0.38	84
Spent 10V9.4MoAl 10 Cycles, 773 K, O_2	65	0.35	71

With respect to the fresh VMoAl catalysts, post-reaction results obtained by BET analysis reveal a reduction in the surface area, pore volume and average pore diameter. This observation indicates either a degree of crystallite sintering due to elevated reaction temperatures or the formation of coke, despite employing an O_2 catalyst regeneration step.

6.3.2 Raman Spectroscopy

Post-reaction Raman spectra of spent VMoAl catalysts are presented in Figures 138-140.

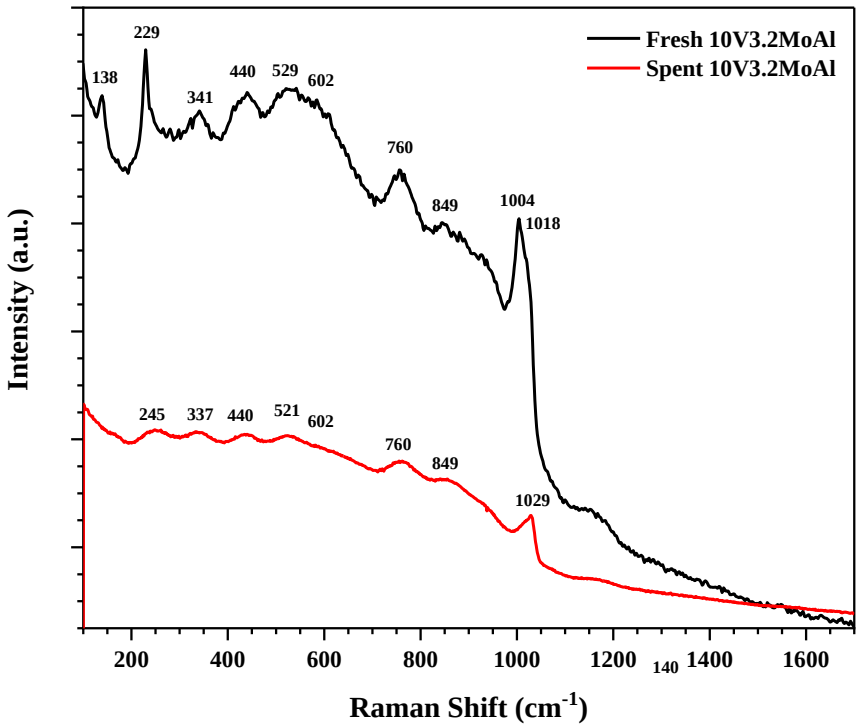

Figure 138: Raman spectra spent 10V3.2MoAl from CL-PODH redox cycles utilising O_2 as the oxidant

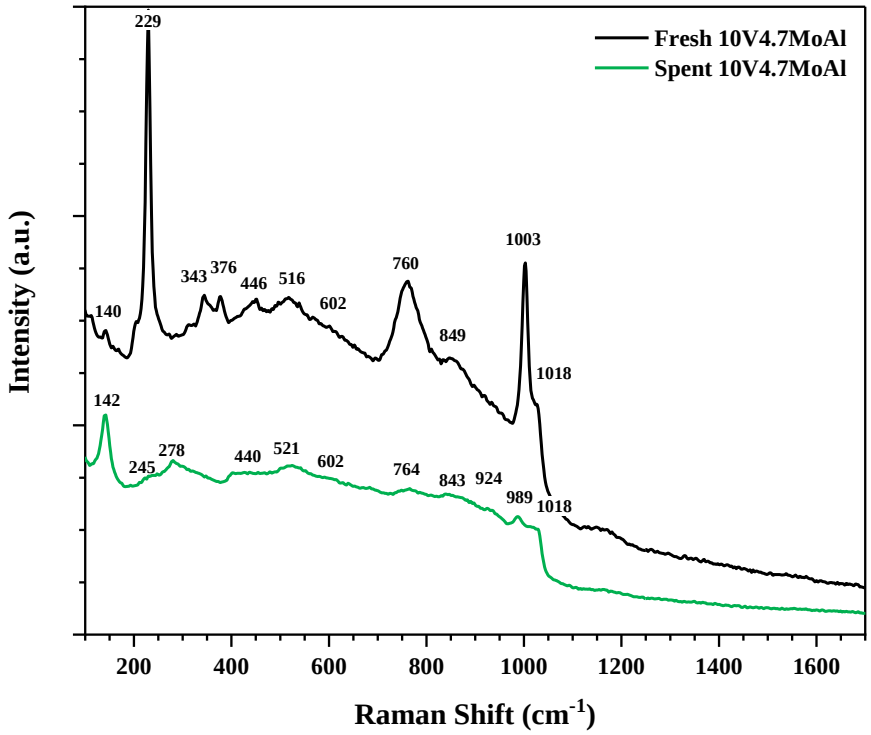

Figure 139: Raman spectra spent 10V4.7MoAl from CL-PODH redox cycles utilising O_2 as the oxidant

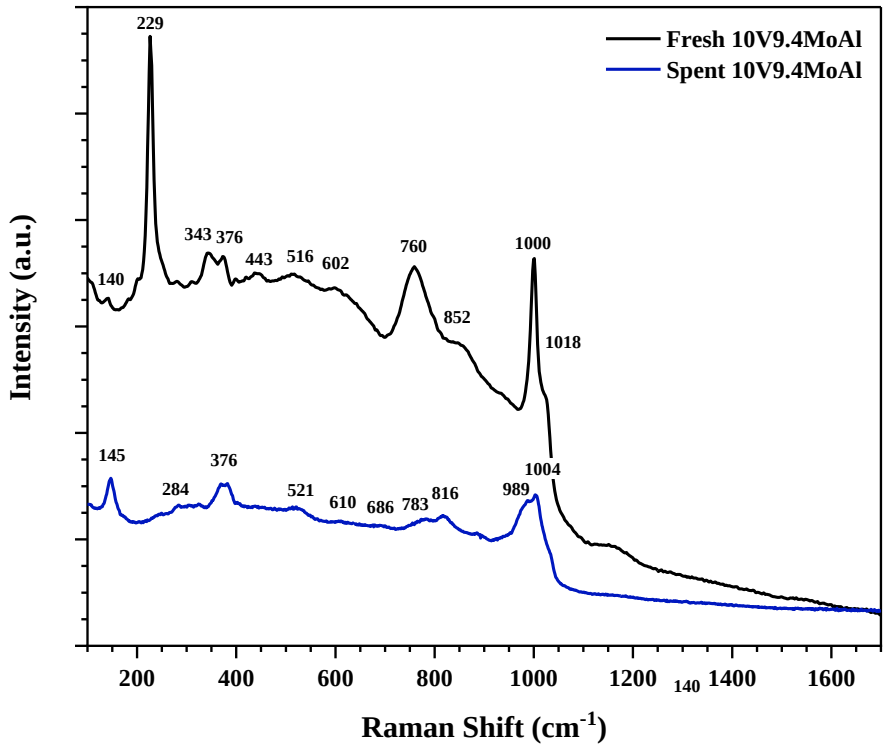

Figure 140: Raman spectra spent 10V9.4MoAl from CL-PODH redox cycles utilising O_2 as the oxidant

A clear disparity is observed between the Raman spectra of spent VMoAl catalysts and those obtained for the fresh catalyst samples. The prominent Raman feature at ~229 cm^{-1}, proposed to be characteristic of V-O-Mo species, is not detected in the post-reaction VMoAl samples. Notably however, a sharp and intense band appears at ~142 and 145 cm^{-1} in the spectra of spent 10V4.7MoAl and 10V9.4MoAl catalyst samples, which has previously been assigned to crystalline V_2O_5 species.

The spectra of the spent 10V3.2MoAl catalyst retains broad Raman bands in the region of ~200-900 cm^{-1}, which are characteristic of the bending modes, asymmetric and symmetric stretches of polyvanadate/polymolybdate species. The only observed change is the decreasing intensity of the band at ~1004 cm^{-1}, where it now shoulders the sharp band at ~1029 cm^{-1}, characteristic of the V=O vanadyl bond in monovanadate species.

The Raman feature at ~1003 cm^{-1} is absent in the spectra of the spent 10V4.7MoAl catalyst, with new bands featuring at ~989 and 278 cm^{-1}. These lie in similar regions to those observed in the spectra of the fresh 10VAl catalyst, which were previously assigned to crystalline V_2O_5 species. Studies performed by Wachs *et al.*, however, assign this feature to the symmetric stretch of the molybdenyl bond in isolated octahedral dioxo $(O=)_2MoO_4$ species, thus a conclusive assignment cannot be made. [49]

Raman bands present in the spectra of the fresh sample at ~343 and 376 cm^{-1}, previously assigned to MoO_3, are also not present in the post-reaction Raman of 10V4.7MoAl. This observation suggests the loss of crystalline MoO_3 species upon performing the CL-PODH redox cycling test.

The feature at 1004 cm^{-1} is retained in the post-reaction Raman spectra of the spent 10V9.4MoAl catalyst, however, the formation of Raman bands at ~989 at 284 cm^{-1} are observed once again. Furthermore, the Raman feature observed at ~1017 cm^{-1} , assigned to the V=O bond present in polyvanadate species in the spectra of the fresh catalyst, is no longer discernible; however, this may be as a result of its presence being masked by the prominence of the Raman bands at ~1004 and 989 cm^{-1}.

6.3.3 XRD

XRD patterns of spent VMoAl catalysts are presented in Figure 141. No significant change is observed in the pattern of the spent 10V3.2MoAl catalyst. Similar to those of the fresh 10V3.2MoAl sample, the XRD peaks relate primarily to the alumina support, indicating that vanadia and molybdena species are highly dispersed on the surface. Furthermore, the XRD pattern of spent 10V4.7MoAl and 10V9.4MoAl catalysts retain peaks assigned to crystalline V_2O_5, MoO_3 and the mixed oxide V_2MoO_8. [65, 116-118] Notably, however, the peaks attributed to V_2O_5 and MoO_3 have become less prominent in spent VMoAl samples, which implies a higher dispersion and/or lower crystallinity of these species exists.

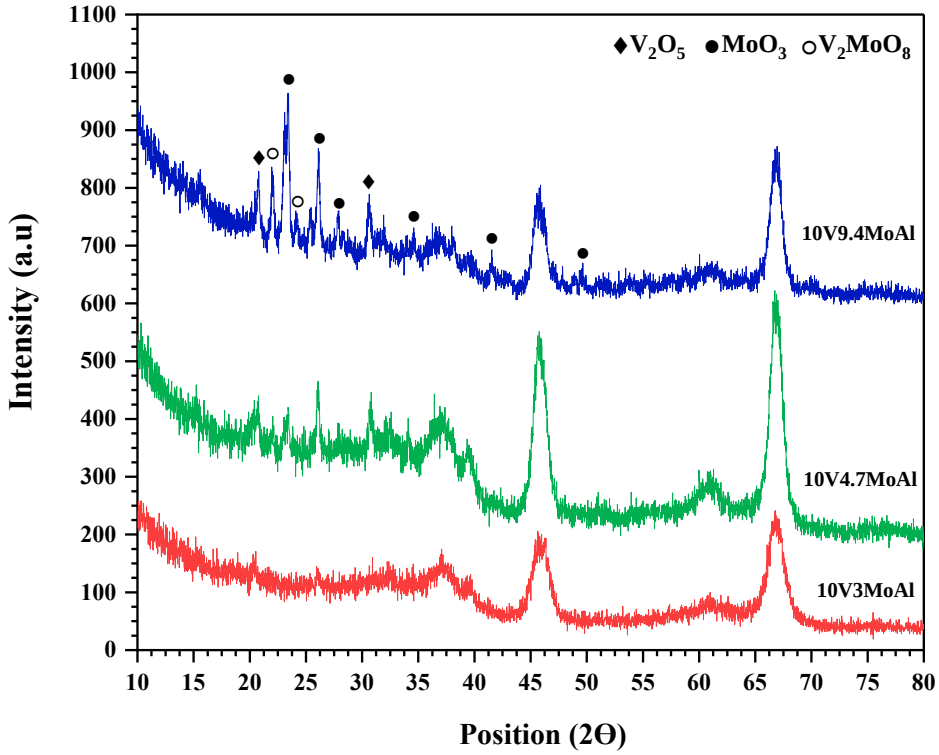

Figure 141: XRD patterns of spent VMoAl catalysts

6.3.4 TGA-TPO

TGA-TPO measurements were performed to investigate the extent of carbon laydown on spent VMoAl catalysts. Figure 142 presents the post-reaction TPO weight profile, which shows weight loss percentage between 300-1000 K. Notably, it is evident from the TPO profile that the weight loss observed arises mostly from H_2O evolution at lower temperatures. The absence of the higher temperature combustion event indicates that minimal carbon laydown occurs after performing ten CL-PODH redox cycles with an O_2 catalyst regeneration step.

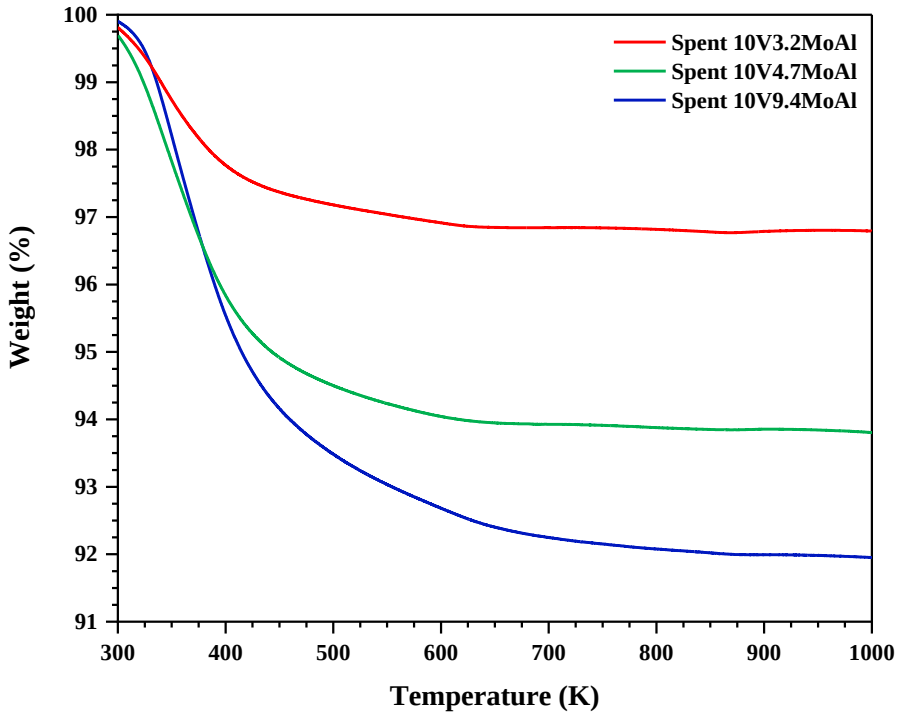

Figure 142: TPO weight loss profile of spent VMoAl catalysts, CL-PODH redox cycling test, O_2 oxidant, 773 K, 1 atm

7 Discussion

7.1 Pre-Reaction Characterisation

This section discusses the pre-reaction characterisation results obtained from the various techniques detailed throughout, drawing out any distinctions between the VAl, MoAl and VMoAl catalyst series.

BET measurements of the γ-Al_2O_3 support and fresh VAl, MoAl and VMoAl catalyst samples reveal characteristic Type IV isotherms with a H1-type hysteresis loop. This isotherm model is prevalent when multilayer adsorption and capillary condensation occurs on the catalyst surface, specifically in mesoporous solids with well-defined cylindrical pore channels and diameters ranging between 2 and 50 nm. [92] The surface area of the γ-Al_2O_3 support was 258 m^2 g^{-1}, which decreased with vanadium and molybdenum incorporation in VAl, MoAl and VMoAl catalyst samples. This observation is attributed to the blockage of the support micropores by vanadia and molybdena species upon impregnation, ultimately decreasing catalyst activity. Only a modest reduction in surface area is observed when going from the 5 to 7.5 V wt.% catalyst (175 to 171 m^2 g^{-1}, respectively). This observation may be explained through consideration of the vanadium surface density of the samples, which were calculated as described in Equation 17 and as shown in Figure 143.

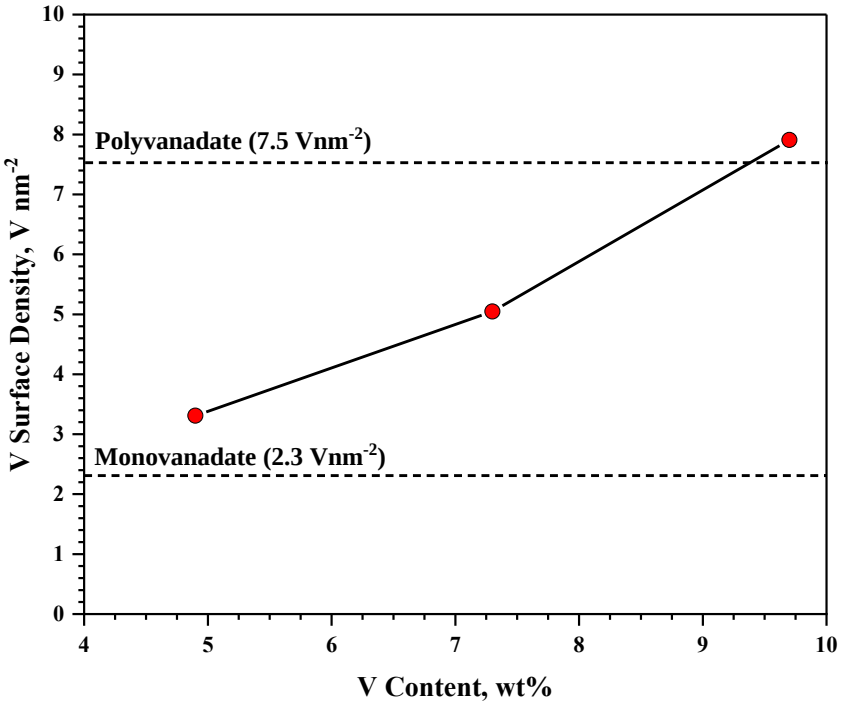

Figure 143: Vanadium surface densities for fresh VAl catalysts

As seen in Figure 143, vanadium surface density increases linearly with increasing vanadium content. Notably, the dashed lines illustrate surface densities corresponding to the theoretical monolayer coverage for isolated monomeric vanadia species (2.3 V nm^{-2}) and polymeric vanadia species (7.5 V nm^{-2}). [37, 119, 120] Studies performed by Bell and Iglesia suggest that isolated monovanadates dominate the surface at low surface densities below 2.3 V nm^{-2}. [37] The authors postulate, that when the surface density increases and surpasses the theoretical monolayer coverage for monovanadates, isolated VO_x structures react with neighbouring species to form two-dimensional structures comprising of polymeric V-O-V bonds. At higher surface densities exceeding the theoretical monolayer coverage for polyvanadates species, polymeric domains agglomerate to form three-dimensional structures which ultimately crystallise into bulk V_2O_5 species. [37, 120] Both 5VAl and 7.5VAl catalysts exhibit vanadium surface densities that lie within the theoretical monolayer coverage range for monomeric and polymeric vanadia entities. At these densities, it is possible that both species may exist simultaneously, with a varying degree of polymerisation. [121] Since there is only a modest reduction in the BET surface area and pore volume between 5 and 7.5VAl catalyst samples, one can assume that 5VAl and 7.5VAl catalyst samples comprise of similar vanadia structures, and that polyvanadates are the prevalent species, based on the calculated vanadium surface density. Comparatively, the 10VAl catalyst exhibits a vanadium surface density above the polyvanadate theoretical monolayer coverage, suggesting the possibility of V_2O_5 crystallite formation. The formation of three-dimensional vanadia species may explain the significant reduction in the BET surface area of the 10VAl catalyst to 145 m^2 g^{-1}.

With respect to the MoAl and VMoAl catalyst series, the BET surface area of the γ-Al_2O_3 support decreased from 258 to 155, 117, 85 and 76 m^2 g^{-1} in 9.4MoAl, 10V3.2MoAl, 10V4.7MoAl and 10V9.4MoAl samples, respectively. This observation was accompanied with an increase in average pore diameter, further suggesting an increase in bulk MoO_3 crystallite domains. To provide additional insight into the nature of molybdate species present in MoAl and VMoAl samples, molybdenum surface densities were also calculated, as described in Equation 21. Additional studies conducted by Bell *et al.* show the theoretical polymolybdate monolayer coverage to be ~5.0 Mo nm^{-2}, above which the formation of crystalline MoO_3 is detected by Raman spectroscopy and X-ray diffraction. [62] Moreover, Wachs *et al*. similarly investigated the effect of molybdenum surface density on the resulting surface species and found that, at monolayer coverage, both dioxo monomeric ($O_2Mo(=O)_2$) and mono-oxo polymeric molybdena species may co-exist on dehydrated γ-Al_2O_3 and ZrO_2 supports. [49]

The molybdenum surface density of the 9.4MoAl catalyst was calculated as 3.8 Mo nm^{-2}, therefore remaining below the reported theoretical monolayer coverage value, thus indicating a mixture of both monomeric and polymeric molybdena species on the support surface. Furthermore, the molybdenum surface density in co-impregnated VMoAl samples also increased linearly with increasing molybdenum incorporation (Figure 144), where 3.2MoAl and 10V4.7MoAl catalysts are shown to comprise a molybdenum surface density below the reported polymolybdate theoretical monolayer coverage. Notably, vanadium surface densities were also determined for co-impregnated VMoAl catalysts, and calculations reveal that all three samples exceed the polyvanadate theoretical monolayer coverage (7.5 V nm^{-2}), discussed previously. These results indicate that the predominant species in 10V3.2MoAl and 10V4.7MoAl samples may contain crystalline V_2O_5, in addition to monomeric and polymeric molybdena species. Comparatively, the 10V9.4MoAl catalyst exhibits a molybdenum surface density exceeding the theoretical polymolybdate monolayer coverage, thus suggesting the possibility of MoO_3 crystallite formation.

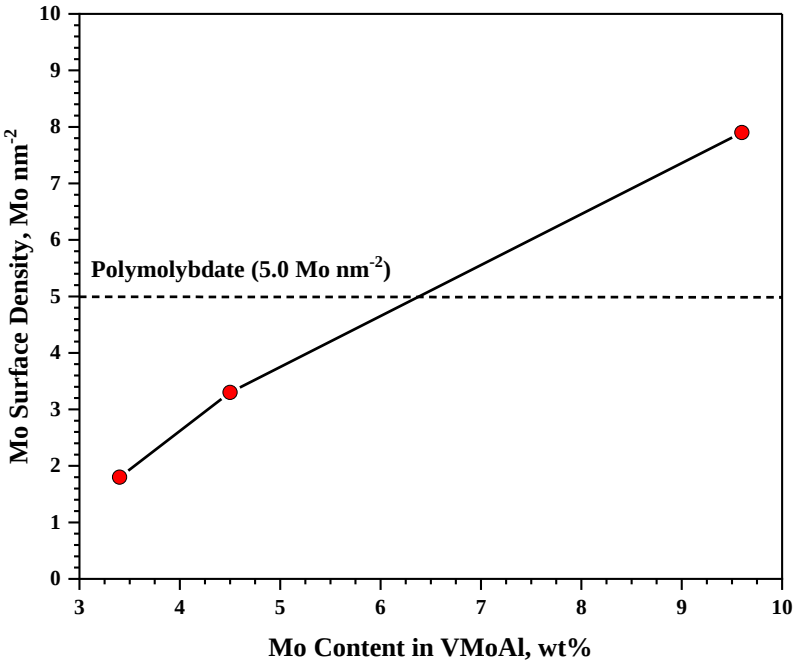

Figure 144: Molybdenum surface densities for fresh VMoAl catalysts

H_2-TPR measurements were performed to provide further insight into the reducibility of vanadia and molybdena sites present in fresh VAl, MoAl and VMoAl catalyst samples. Banãres *et al.* postulate the trend in H_2 reducibility of supported vanadia species is as follows: polymeric surface VO_x > isolated monomeric surface VO_x > crystalline V_2O_5. [93] In their studies, an increase in intensity in the Raman shift associated with the terminal

vanadyl (V=O) bond is observed as the surface coverage increases. This occurs simultaneously with surface vanadia sites becoming more easily reducible, therefore, the terminal V=O group is excluded in the rate-determining step involved in the reduction of supported vanadia species. [93] These findings correlate with the derivative weight (%/K) H_2-TPR profiles obtained for the fresh VAl series, where two distinct reduction events exist for all VAl catalysts. Comparably, the first reduction event shifts to lower temperatures, which indicates an increase in vanadia polymerisation as vanadium loading increases. The weight loss of oxygen during the second reduction event in fresh VAl catalysts was calculated and results indicate that approximately one oxygen atom was lost per one vanadium atom. This suggests that the higher temperature reduction event is ascribed to the reduction of crystalline V_2O_5 surface species, which is consistent with existing literature. [93, 94] Notably, the higher reduction event increases in intensity with respect to the first reduction event as the vanadium loading increases, which implies a growth in reducible V_2O_5 domains in the 10VAl catalyst. [94]

Similar to the VAl catalyst series, the 9.4MoAl catalyst reveals two distinct reduction events in the obtained derivative weight. As discussed in Section 5.1.3, the first reduction event occurring at ~601 K is assigned to the reduction of polymeric molybena species in the octahedral configuration, whilst the second reduction event correlates to the reduction of MoO_3 to MoO_2. The derivative weight H_2-TPR profile for the fresh VMoAl catalyst series detailed a lower temperature reduction event, which was comparable to that observed in the fresh VAl series, whilst the second reduction event shifted to even higher temperatures than those observed in the H_2-TPR profiles for both VAl and VMoAl catalysts. The weight loss of oxygen was calculated during this reduction event and the results show that less than one oxygen atom (~0.8) was lost per one vanadium and molybdenum site, which may evolve from newly formed mixed V-O-Mo phases.

Raman spectroscopy was conducted to probe the chemical structure of vanadium and molybdenum species in fresh VAl, MoAl and VMoAl catalysts and will further determine any comparisons between the data outlined in the BET, surface density and H_2-TPR profiles, discussed above. The calculated surface densities and BET measurements for the fresh 5 and 7.5VAl catalysts would suggest that the predominant species consists of both monomeric and polymeric vanadia domains. This correlates well with the obtained Raman spectra, which displays bands exclusively assigned to mono- and polyvanadate species. Furthermore, an increase in vanadia polymerisation is highlighted on going from the 5 to 7.5VAl catalyst, with a shift in the Raman band assigned as the symmetric vibration of terminal mono-oxo vanadyl (V=O) bond in isolated VO_4 species. Based on the calculated surface density, BET and H_2-TPR results for the fresh 10VAl catalyst, an increase in crystalline V_2O_5 domains is implied. This is consistent with results observed in the Raman spectra of fresh 10VAl as it exhibits characteristic features attributed to crystalline V_2O_5. These features dominate the spectra, however, broad bands relating to polymeric vanadia species are still detected, implying that crystalline V_2O_5 co-exists with polyvanadate domains.

Results from the pre-reaction Raman of the 9.4MoAl catalyst reveal characteristic features that are exclusively assigned to polymolybdate species. These results correlate well with the calculated molybdenum surface density which lies below the theoretical monolayer coverage of polymolybdates. As previously discussed, the H_2-TPR profile of 9.4MoAl displays a higher temperature reduction event assigned to the reduction of MoO_3 to MoO_2, however, it should be noted that crystalline MoO_3 domains were not detected via Raman spectroscopy or XRD. Despite the indication from the calculated surface densities that V_2O_5 crystallites are the predominant species in fresh VMoAl catalysts, sharp and intense features relating to V_2O_5 are less prominent in the obtained Raman spectra. The disparity between the calculated surface densities and the structural information obtained via the Raman spectroscopy simply highlights the complexities that exist when characterising mixed metal oxide catalysts. Nevertheless, results from the Raman further imply the formation of a newly formed V-O-Mo mixed phase, which correlates well with results obtained from H_2-TPR measurements.

XRD measurements were also performed to investigate the crystallinity and structure of vanadia and molybdena species in fresh VAl, MoAl and VMoAl catalysts. The lack of sharp and intense diffraction peaks in the XRD patterns of 9.4MoAl and VAl catalyst samples suggest that both molybdena and vanadia species do not exhibit long range order and remain highly dispersed on the alumina support. This includes crystalline V_2O_5 domains observed in the Raman spectra of the 10VAl catalyst. This observation is found in the XRD pattern for the 10V3.2MoAl sample, however, an increase in molybdenum content in the 10V4.7MoAl and 10V9.4MoAl catalyst results in a marked change. The XRD patterns of both 10V4.7MoAl and 10V9.4MoAl catalysts show sharp and intense diffraction peaks which have previously been assigned in literature to V_2O_5 and MoO_3 crystallites, in addition to a mixed oxide V_2MoO_8 phase. [65, 116-118] Confirmation of this mixed V-O-Mo phase has also been highlighted in the Raman spectra and H_2-TPR profiles of VMoAl samples, thus providing evidence that the molybdenum promoter acts in an interactive manner which coordinates chemically to the surface vanadium oxide species.

7.2 Thermodynamic Analysis

Thermodynamic analysis has been performed to provide further insight into reaction feasibility of chemical reactions which may occur during the CL-PODH tests. The basic thermodynamic data of key reactants and products has been used to determine the sign and value of the resulting Gibbs free energy value, which relates directly to the reaction spontaneity, as described in Section 4.2.

Stoichiometric equations which relate to the PDH step performed over supported V_2O_5 and MoO_3 catalyst sites are presented in Table 13 and Table 42, listed as reactions (1-10) and (36-40) respectively. Negative Gibbs free energy values are observed for the oxidation and over-oxidation of propane and propene using the lattice oxygen sites of V_2O_5, V_2O_4 and MoO_3, thus are thermodynamically feasible at our reaction conditions. Markedly, propane oxidation over V_2O_5 sites to produce CO_2 and H_2O displays a substantially more negative Gibbs free energy (ΔG_{800K} = -1394.6 kJ mol^{-1}) value than propane oxidising to the desired propene product (ΔG_{800K} = -111.9 kJ mol^{-1}). The former reaction occurs using higher stoichiometric quantities of V_2O_5, however, V_2O_5 sites transform to V_2O_4 as the PDH reaction proceeds, therefore, limited quantities of V_2O_5 may favour propene production which only requires a 1:1 stoichiometric ratio of C_3H_8 and V_2O_5. Comparably, propane oxidation over MoO_3 sites displays a similar trend.

Stoichiometric equations which relate to the regeneration of resulting V_2O_3, V_2O_4 and MoO_2 sites using O_2, N_2O and CO_2 oxidants are presented in Table 14 and Table 43, listed as reactions (11-16) and (41-43) respectively. At our reaction conditions, the re-oxidation of V_2O_3, V_2O_4 and MoO_2 sites with N_2O exhibit a higher negative Gibbs free energy, thus implying a greater reaction spontaneity than their O_2 counterparts. On the other hand, the re-oxidation of V_2O_3, V_2O_4 and MoO_3 sites with CO_2 demonstrates large positive Gibbs free energies ($\Delta G800K$ = +90.6, +139.7 and +114.4 kJ mol^{-1} respectively), which ultimately highlights the thermodynamic constraints of using the inherently inert CO_2 molecule as an oxidant in CL-PODH reactions. Recent studies performed by Djinović *et al.* analysed CO_2 -assisted PODH reactions. In CO_2-assisted PODH reactions using VO_x supported on activated carbon, the authors postulate from their activity results and data from C_3H_8-TPR and CO_2-TPO analysis that CO_2 activation is assisted by adsorbed propane and that the use of CO_2 to re-oxidise bulk V_2O_3 and VO_x catalysts samples was only initiated at temperatures exceeding 843 K. [72]

Stoichiometric equations relating to possible side reactions occurring during the PDH step of CL-PODH reactivity tests are presented in Table 15, listed as reactions (17-29). From the possible side reactions that have been listed, the most thermodynamically favourable reactions, exhibiting the lowest Gibbs free energy value at our reaction conditions, are carbon laydown reactions from propane and ethane (ΔG_{800K} = -132.1, and -66.5 kJ mol^{-1}) which result in the formation of surface carbon. A further observation worth noting is that carbon laydown from the propane reactant has lower Gibbs free energy than the oxidation of propane to propene utilising V_2O_5 lattice oxygen sites (ΔG_{800K} = -111.9 kJ mol^{-1}), which may dictate the reaction chemistry taking place in the PDH step of CL-PODH tests. Since the formation of carbon laydown is spontaneous, removal of carbon with both vanadia/molybdena lattice oxygen sites and O_2, N_2O and CO_2 oxidants has also been probed. The removal of carbonaceous deposits using łattice oxygen sites within V_2O_5, V_2O_4 and MoO_3 domains all display negative Gibbs free energies and are therefore thermodynamically feasible. Similarly, removal of carbonaceous deposits with O_2 and N_2O oxidants also display negative Gibbs free energies (ΔG_{800K} = -395.5 and -322.8 kJ mol^{-1}), whilst removal with the CO_2 oxidant exhibits a positive value (ΔG_{800K} = +30.6 kJ mol^{-1}) and is deemed non-spontaneous.

7.3 Reactivity Tests & Post-Reaction Analysis

The efficacy of VAl, MoAl and VMoAl catalysts within CL-PODH redox cycling tests has been investigated by conducting a series of ten propane dehydrogenation-regeneration redox cycles, as described in Section 3.3.3.

The effect of varying vanadium loading on catalyst activity and selectivity towards propene in bench-mark CL-PODH tests using O_2 has been established in Figures 32 and 33. Results show that both 5VAl and 7.5VAl catalysts exhibit comparable catalytic activities upon completion of the 1st PDH step (~13.2 and 13.6 C_3H_8 % conversion, respectively), despite an increase in vanadium loading. Given that both catalysts exhibit a similar vanadium surface density, and that only slight reductions in the BET surface area and pore volume are observed, these results support the conclusion that 5VAl and 7.5VAl samples comprise similar vanadia species. The subsequent oxidation step fails to regenerate both catalysts back to their initial activity, where propane conversions decrease to ~11.0 % in the 2nd PDH step.

As discussed, the pre-reaction Raman spectra indicates a higher presence of isolated monovanadate species in the 5VAl sample. An increased selectivity in the 1st PDH step is also observed (45.5 % versus 38.9 % for the 7.5VAl catalyst), which correlates well with the work performed by Zhang *et al.*, who attribute the increase in propene selectivity to the uniform dispersion of vanadia on the γ-Al_2O_3 support surface. [56] This results in an overall propene yield of ~5.9 % at the end of the 1st PDH step performed over the 5VAl catalyst, in comparison to ~5.3 % when utilising 7.5VAl. A considerable decline in propene selectivity to ~36 % is observed in cycles 2 to 5, and the overall propene yield ultimately suffers. The loss in selectivity indicates that the vanadia sites selective towards propene formation are not fully regenerated in the 5VAl catalyst, despite employing a catalyst re-oxidation step.

Within the VAl catalyst series, the most promising results for propene production are observed in CL-PODH tests using 10VAl. Pre-reaction characterisation results from BET, H_2-TPR and Raman spectroscopy suggest that the 10VAl catalyst most likely comprises of V_2O_5 crystallite species co-existing with polyvanadate domains. Nevertheless, the XRD pattern lacks sharp and intense peaks indicative of bulk crystallites, suggesting that the V_2O_5 present within the 10VAl sample is relatively dispersed and does not exhibit long-range ordering. When utilising 10VAl within the bench-mark CL-PODH-O_2 cycling

test, an overall propene yield of ~9.2 % is obtained by the end of the 1st PDH step. A combination of declining catalyst activity and propene selectivity however, results in a decrease in propene yield to ~7.3 % by the end of the 2nd PDH step.

To provide insight into the reaction chemistry taking place, reaction profiles detailing the data obtained from the entire PDH step of cycles 1 and 2, are presented in Figures 36-38. The distinctive trend in propane conversion and propene selectivity at different stages throughout the PDH step, imply different reactivity zones as the reaction proceeds. Notably, propene and CO_2 yields are maximised within ~1.5 min of switching on the propane feed in cycles 1 and 2. Thereafter, propane conversions begin to drop off significantly, which is met with an increase in propene selectivity. Propane conversions reach steady state with additional TOS as the activity of the 10VAl catalyst stabilises, and propene yields ultimately rise as the selectivity increases. Similarly, CO_2 yields also decrease as the PDH reaction progresses, however, the selectivity remains comparably low throughout, and the yield is not replenished as observed in the case of propene.

Further elucidation of the reaction chemistry taking place is feasible by monitoring the MS response of ions with m/z 2 and 18, corresponding to the evolution of hydrogen and water, respectively. The MS profile of the PDH step performed over the 10VAl catalyst is presented in Figure 145.

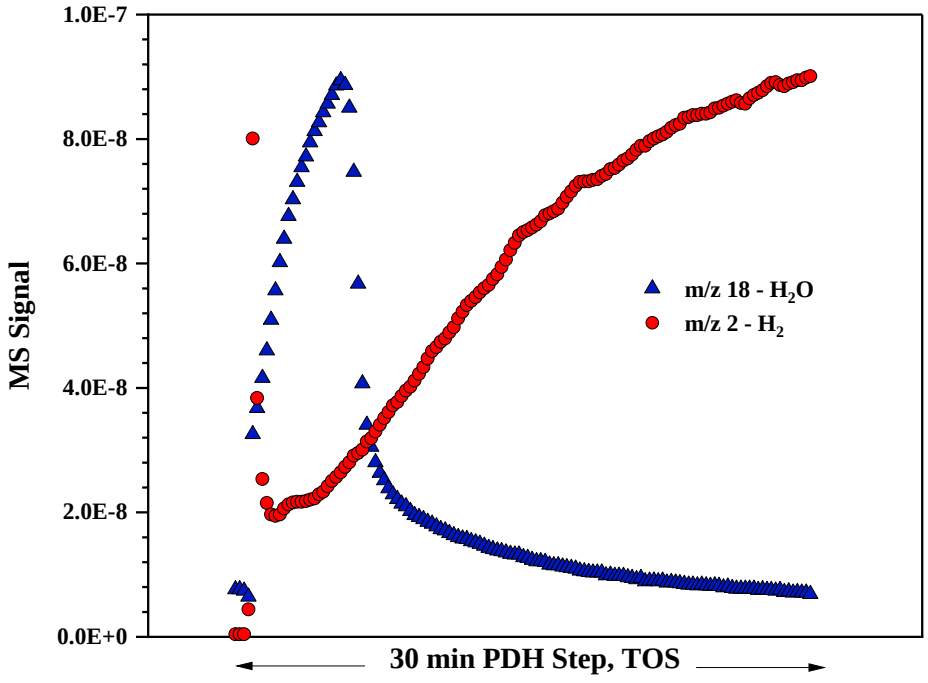

Figure 145: MS signal of m/z 2 and 18, corresponding to H_2 and H_2O evolution throughout the PDH step, 10VAl, 773 K, 1 atm

The trend in both hydrogen and water evolution in the initial stages (~1.5 min into the PDH step) highlights that competing reactions may be at play. Lattice oxygen sites present within the 10VAl catalyst are exploited; thus a maximum propene yield is obtained, presumably via the oxidative dehydrogenation pathway shown below:

$$C_3H_8 + \frac{1}{2}O_2 \longrightarrow C_3H_6 + H_2O$$

An initial spike in the m/z 2 response, and maximised CO_2 yields are also observed however, which suggests that a competing over-oxidation reaction may be occurring, involving the direct combustion of propane to CO_2 and H_2 (Equation 22). Weakly bound lattice oxygen and adsorbed oxygen species from the re-oxidation step are predominant on the vanadia surface in the initial stages, which seem to promote the over-oxidation reaction to form CO_2. Thermodynamic analysis reveals that the Gibbs free energy of the over-oxidation reaction displays a large negative value and is therefore feasible. As shown in Figures 28 and 29, a number of other side reactions are also viable under our reaction conditions, including various cracking, dry and steam reforming pathways. Limitations of the mass spectral analysis are such that gases such as carbon monoxide, ethane and methane cannot be reliably quantified due to coincident m/z with, for example residual nitrogen, nevertheless qualitatively no significant evolution of these gases was detected.

Equation 22: C_3H_8 reducing V_2O_5 to produce CO_2 and H_2

$$C_3H_8 + 6V_2O_5 \longrightarrow 3CO_2 + 4H_2 + 6V_2O_4 \quad (\Delta G°_{800K} = -873.9 \text{ kJ mol}^{-1})$$

As the reaction progresses, a significant rise in the MS response of m/z 18 is observed and the evolution of H_2O begins to dominate. This occurs in conjunction with a decline in the MS response of m/z 2 and propene yield, until the response of m/z 18 maximises ~6 min into the PDH step. At this stage, water evolution ceases, which is reflected by the rapid decrease in the response of m/z 18, indicating the complete removal of accessible lattice oxygen sites within the 10VAl catalyst. Adsorbed oxygen species that are selective to the over-oxidation reaction during the initial stages are exhausted, and the 10VAl catalyst is in a more reduced state. This results in an evident shift in the reaction chemistry, as the MS response of m/z 2, selectivity towards propene and overall propene yield rises with TOS whilst CO_2 yields remain comparatively low. This suggests that propane is reacting via the

direct propane dehydrogenation pathway, shown in Equation 1. These results compare with the recent work of Zhao *et al*. who utilised DFT calculations in conjunction with experimental work to determine the structure-activity relationship of monomeric, dimeric and crystalline vanadia domains for PDH. The authors concluded that PDH over VO_x/Al_2O_3 catalysts results in a reaction profile which can be segmented into two distinct regions. Initially the ODH reaction dominates, however, a loss in V=O bonds to H_2O formation initiates the direct dehydrogenation reaction which becomes the dominant reaction pathway. [122]

Both the catalyst activity and selectivity towards propene in CL-PODH redox cycling tests using VAl catalysts remain comparable in cycles 2 to 5. A marked increase in propene selectivity is observed, however, in the 6th PDH step performed after the overnight argon purge. Further interpretation of this enhancement is showcased in Figures 39-41, which compares the reaction profiles of the 5th and 6th PDH step employing the 10VAl catalyst. In comparison, the trend in catalyst activity during the 6th PDH step resembles that of cycle 1 as the reaction profile exhibits similar reactivity regions. As discussed previously, propene and CO_2 yields are maximised in the initial stages before decreasing to a minimal point. Furthermore, propane conversions obtained at the end of the 5th and 6th PDH step are comparable at ~16 %, however, an increase in propene selectivity from ~42.6 in cycle 5 to 51.2 % in cycle 6 is observed and the overall propene yield rises from ~7.0 to 8.3 %. The only difference between the 5th and 6th step is an extended period held under argon. Therefore, holding the catalyst at 773 K overnight under a continuous flow of argon alters the vanadium sites to become more selective for the desired olefin product. Under these conditions, the catalyst may undergo a degree of thermal reduction, where surface vanadia sites will be in a more reduced state with a decreased amount of labile oxygen. Thermodynamic analysis reveals that residual carbonaceous deposits not fully removed during the catalyst regeneration step, may be readily oxidised by the lattice oxygen sites within vanadia species during the overnight argon purge. The stoichiometric equations are presented below with their corresponding Gibbs free energy values, indicating their feasibility at similar temperature conditions.

$$C\,(s) + V_2O_5\,(s) \rightleftharpoons V_2O_4\,(s) + CO\,(g) \qquad (\Delta G_{800K} = -109.1\ kJ\ mol^{-1})$$

$$C\,(s) + V_2O_5\,(s) \rightleftharpoons V_2O_3\,(s) + CO_2\,(g) \qquad (\Delta G_{800K} = -199.7\ kJ\ mol^{-1})$$

$$C\,(s) + V_2O_4\,(s) \rightleftharpoons V_2O_3\,(s) + CO\,(g) \qquad (\Delta G_{800K} = -60.0\ kJ\ mol^{-1})$$

Propane pulsing tests were performed to investigate the reactivity during the initial stages of the bench-mark CL-PODH reaction. In these tests, a sequence of 20 propane pulses were directed over the 10VAl catalyst before resuming the continuous flow CL-PODH reaction. To further probe the shift in reaction chemistry directly after the O_2 regeneration step and the overnight argon purge, propane pulsing tests were performed at the initial stage of the 1st, 2nd and 6th PDH step.

Figures 60-62 display the reaction profiles from the pulsing test performed at the start of the 1st PDH step. Initial pulses show a full conversion of propane, which declines rapidly to ~30 % conversion by the 20th pulse. The selectivity profile for propene is directly inverse and propene selectivity increases as the conversion drops off, rising to ~54 % by the 20th pulse. Comparatively, the selectivity profile of CO_2 exhibits an immediate selectivity of ~20 %, subsequently declining to negligible values by the 12th propane injection. Confirming that over a fully oxidised catalyst, combustion of propane to carbon dioxide is the favoured reaction, with propene production enhanced as the catalyst is reduced. Figures 63-65 display the pulsing reaction profiles performed at the initial stage of the 2nd PDH step. Notably, the results are analogous to those obtained during the 1st cycle indicating that similar reaction chemistry is taking place after regenerating the catalyst with O_2.

Figures 66-68 detail the reaction profiles from the pulsing test performed after the overnight argon purge, where an enhancement in propene selectivity is observed. When comparing with the pulsing tests performed at the initial stages of the 1st and 2nd PDH step, a clear disparity in the reaction chemistry is observed during the initial stages of the 6th PDH step. An exponential decay in propane conversion occurs immediately, dropping from ~83.7 % to ~33 % by the 12th propane injection, whereafter, it stabilises with successive pulses. Furthermore, the selectivity to propene rises following a logarithmic growth, reaching ~62 % by the 20th pulse, whilst the selectivity profile for CO_2 is substantially lower during initial propane injections. An immediate selectivity to CO_2 of ~2.3 % is observed, declining to negligible levels thereafter. The resulting yield profile reveals an initial CO_2 yield of ~1.9 %, which decreases to nominal quantities. On the other hand, propene formation occurs immediately and reaches a maximum yield of ~20 % by reaction end. Following the enhancement observed in the PDH step of cycle 6, propene selectivity and yield are lower at similar propane conversions during the PDH step of cycle 7, before remaining relatively stable during successive cycles. This behaviour is in keeping with the difference in reactivity observed with vanadia in different states of reduction.

A similar trend is observed in the tests using the 5 and 7.5VAl catalyst, indicating that vanadia systems are relatively stable for propene production, with no significant deactivation as CL-PODH redox cycles proceed.

Both 5 and 7.5VAl catalysts were removed and analysed post-reaction after performing bench-mark CL-PODH tests. The obtained BET results of the fresh and spent 5VAl catalyst were analogous, however, a loss in both the surface area and pore volume of the 7.5VAl catalyst was observed. The BET surface area and pore volume decreased from 171 to 145 $m^2 g^{-1}$ and 0.62 to 0.45 $cm^3 g^{-1}$, respectively, whilst the average pore diameter increased from 48 to 54 Å. This observation is typically associated with pore blockage, which can be attributed to carbonaceous deposits or the sintering of the catalyst surface at elevated reaction temperatures. No observable changes were observed in the post-reaction Raman spectra of both 5 and 7.5VAl, and both catalysts retained their amorphous-like nature in the obtained XRD patterns, making it difficult to determine any structural changes resulting from CL-PODH redox cycling tests.

The 10VAl catalyst was also removed for post-reaction characterisation after performing the bench-mark CL-PODH-O_2 test. BET analysis reveals similar findings to those observed in the 7.5VAl sample, where a loss in both the surface area and pore volume was observed. The surface area and pore volume reduced from 145 to 129 $m^2 g^{-1}$ and 0.55 to 0.51 $cm^3 g^{-1}$, respectively, whilst the average pore diameter increased from 43 to 62 Å. As discussed above, this observation is typically associated with pore blockage by carbonaceous deposits, or the sintering of the catalyst surface. TGA-TPO measurements were also performed, and whilst CO_2 evolution could only be estimated due to coincident H_2O formation at similar temperatures, the MS response associated with m/z 44 was apparent in the 10VAl catalyst. This confirms the presence of residual carbon on the surface, despite the incorporation of a catalyst regeneration step within CL-PODH redox cycles.

Various structural changes were observed when comparing the pre- and post-reaction Raman spectra of the 10VAl catalyst, presented in Figure 146. Prominent bands at ~994, 408, 284 and 142 cm^{-1} assigned to V_2O_5 are less pronounced in the post-reaction spectrum, whilst the Raman band characteristic of the V=O bond in polyvanadates at ~1014 cm^{-1} increases in intensity with respect to the band at 994 cm^{-1}, suggesting a growth in polyvanadate domains. Furthermore, the Raman feature present at ~932 cm^{-1} in the fresh sample shifts to ~918 cm^{-1}, forming a broad shouldering band in the post-reaction spectra. This Raman shift has previously been attributed to the formation of V-O-Al linkages. It

should be noted that no bands were observed in the 1300-1800 cm^{-1} region, which would typically represent graphitic carbonaceous deposits.

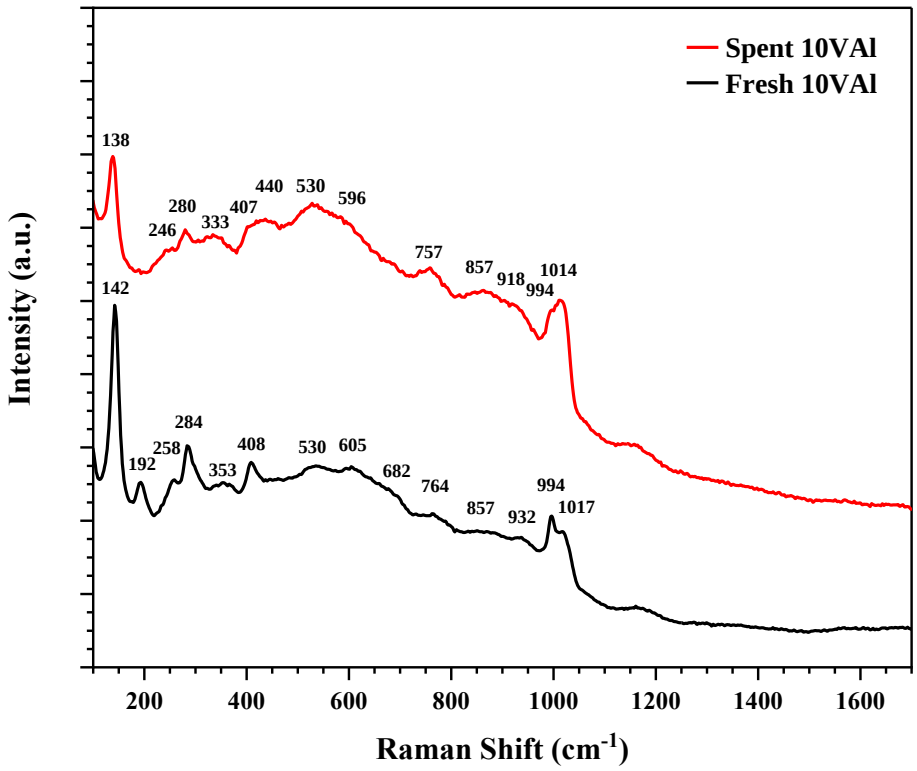

Figure 146: Pre- and post-reaction Raman spectra of the 10VAl catalyst

Additional post-reaction analysis was performed to characterise the 10VAl catalyst removed at various stages throughout the CL-PODH-O_2 cycling test. The BET results of fresh and spent 10VAl catalysts reveal an interchanging loss and regeneration of surface area and pore volume with sequential PDH and catalyst regeneration steps. The surface area and pore volume of the 10VAl sample, removed after the 1st PDH step, decreased from 145 to 119 $m^2\,g^{-1}$ and 0.55 to 0.46 $cm^3\,g^{-1}$. Upon re-oxidising the catalyst with O_2 in the subsequent regeneration step, an increase in both the surface area and pore volume to 132 $m^2\,g^{-1}$ and 0.49 $cm^3\,g^{-1}$ is observed, indicating the formation of coke within the catalyst pores. This trade-off is mirrored throughout subsequent PDH and catalyst regeneration steps in cycles 5 and 10, indicating the effectiveness of the O_2 oxidant for removing carbonaceous deposits and enhancing the catalysts surface area. Notably, a further increase in the surface area, pore volume and average pore diameter is observed for the catalyst sample removed after the overnight argon purge, which ultimately leads to enhanced selectivity towards propene in the PDH step of cycle 6. This indicates that removal of carbon by lattice oxygen is the most likely cause of the reduction of the vanadium oxidation state.

Post-reaction Raman analysis suggests that 10VAl samples removed after the 1st and 5th regeneration steps remain comparable to fresh 10VAl, whilst broad Raman features at ~1600 and 1378 cm^{-1}, attributed to coke formation, are present in the spectra of samples removed after the PDH step of cycles 1, 5, 6 and 10. The topology of coke formation has previously been investigated by comparing the intensity ratio (I_G/I_D) of both G and D bands in Raman spectroscopy.[104, 123] The intensities are relatively equal when the topology of the coke comprises of chain-like species. When the intensity of the G band is significantly larger than that of the D band however, the topology of the coke comprises of two-dimensional sheet-like structures. It has been proposed that these two-dimensional species can form entities with pre-graphitic character; a type of coke that reportedly deactivates dehydrogenation catalysts. [124-126]

To provide further insight into the nature of coke formed by the various PDH steps in sequential CL-PODH redox cycles, the I_G/I_D ratio of the G (~1609 cm^{-1}) to D (~1368 cm^{-1}) band has been calculated and is tabulated in Table 58. As observed, the I_G/I_D ratio of the G (~1598 cm^{-1}) to D (~1368 cm^{-1}) band is ~1.0 for the 10VAl samples removed after the PDH step of cycles 1, 5 and 6, which suggests that the coke formed from the dehydrogenation reaction comprises chain-like topology. Notably, an increase in the ratios is observed in the sample removed after the final PDH step of cycle 10, implying a higher degree of two-dimensional carbonaceous domains. This is in keeping with studies performed by S. D. Jackson *et al*., where species such as pyrene were detected as the catalyst aged. [127] Interestingly, the Raman spectra obtained after the corresponding regeneration cycles uncover an absence of both G and D bands, thus reinforcing the regenerative ability of the O_2 oxidant for the removal of coke.

Table 58: Intensity ratio of G and D bands in 10VAl catalysts removed after varying PDH steps

Sample	I_G/I_D
Spent 10VAl After 1st PDH Step	1.05
Spent 10VAl After 5th PDH Step	1.05
Spent 10VAl After 6th PDH Step	1.07
Spent 10VAl After 10th PDH Step	1.23

Moreover, the 10VAl samples have been analysed externally with XPS. The XPS spectra and V^{5+}/V^{4+} ratios of the fresh 10VAl catalyst indicate that V^{5+} species are prevalent on the surface. A considerable increase in surface V^{4+} species is observed after performing the PDH steps, where the V^{5+}/V^{4+} ratio decreases from 30.4 to 4.2 and 3.9. An increase in V^{4+} species is expected with TOS as the PDH step removes lattice oxygen species to form water, in turn reducing surface V^{5+} species. Subsequent catalyst regeneration steps result in increased surface V^{5+} species, however, ratios exhibit an overall decrease as the CL-PODH redox cycles proceed, suggesting that the catalyst is never fully regenerated back to its original state despite the reoxidation of the catalyst surface. Another interesting observation is that the V^{5+}/V^{4+} ratio in the sample removed after the overnight argon purge decreases further from 14.1 to 5.3. An increase in surface V^{4+} species at this stage agrees with our findings from the thermodynamics and post-reaction Raman that surface vanadia sites are oxidising and removing residual low-level carbonaceous deposits, hence the surface vanadium is in a more reduced state. An increase in propene selectivity is found in the PDH step performed following the overnight argon purge, which establishes a potential in enhancing propene production and crucially overcoming the selectivity limitations by obtaining specific V^{5+}/V^{4+} ratios.

Catalyst stability, and extent of catalyst deactivation with increasing TOS, has been investigated via a long duration 3 h PDH test utilising the 10VAl catalyst. The results presented in Figure 42 show that the activity of the 10VAl catalyst for PDH remains relatively stable until ~75 min, where propane conversion reaches ~19.8 %. Thereafter, catalyst deactivation becomes significant. After 180 min TOS, the conversion of propane is limited to ~13.8 %, which equates to a substantial loss of ~30 %.

The 10VAl catalyst was removed for post-reaction characterisation following the long-duration stability test. As expected, the BET results reveal a loss in the surface area and pore volume from 145 to 124 $m^2 g^{-1}$ and 0.55 to 0.42 $cm^3 g^{-1}$, respectively, whilst the average pore diameter increased from 43 to 58 Å. Interestingly, these results are less profound than those observed with the 10VAl sample removed after the CL-PODH-O_2 cycling test, despite the fact significant deactivation is observed. Notably, a stark contrast is observed with the pre- and post-reaction Raman spectra of the 10VAl catalyst removed after 180 min TOS. Post-reaction Raman provides evidence of significant coke formation with prominent G (~1600 cm^{-1}) and D (1368 cm^{-1}) bands. [104] Furthermore, Raman bands which relate to crystalline V_2O_5 are now essentially non-existent, with the spectra exhibiting bands at ~1027 and ~259-932 cm^{-1}, assigned exclusively to monomeric and polymeric vanadia species. The I_G/I_D ratio of G (~1609 cm^{-1}) and D (~1368 cm^{-1}) bands in the Raman was calculated as 1.05, which implies that the coke formed after 180 min TOS has a topology consisting of chain-like species.

Significant loss in catalyst activity and the presence of coke in the long-duration stability test highlights the advantage of sequential PDH and catalyst regeneration steps that are employed within CL-PODH cycling tests. Within the current literature, CL-PODH studies have focused exclusively in using molecular oxygen as the oxidant in the regeneration of lattice oxygen sites. [79-81, 84-86] Results have shown, however, that the strong oxidising character of molecular oxygen results in adsorbed oxygenates which limit propene selectivity by contributing to the over-oxidation of the alkane feed. Also, as cycling appeared to be slightly deleterious to the catalyst structure, the concept of using "softer" oxidants like CO_2 and N_2O in co-fed PODH studies has attracted substantial interest in recent years, therefore, it seemed appropriate to incorporate these alternative oxidants in the scope of our CL-PODH cycling tests.

The outcome of using N_2O and CO_2 in CL-PODH tests using the 10VAl catalyst has been established in Figures 43-47. As anticipated, the 10VAl catalyst exhibits analogous propane conversions, propene/CO_2 selectivities and yields during the PDH step of cycle 1. The 10VAl catalyst has been exposed to identical reaction conditions at this stage, thus the consistency in results demonstrates the reproducibility of the CL-PODH cycling test. The successive regeneration step that follows however, ultimately reveals a change in activity and productivity of propene when using the alternative oxidants. Overall, the 10VAl catalyst exhibits a similar activity when utilising N_2O. Upon completion of the 10th PDH step, the activity was only marginally lower with propane conversions of ~15.4 % and ~15.8 % when using N_2O and O_2 oxidants, respectively. At these similar conversions, an increase in propene selectivity is observed, which correlates well with the previously discussed work of Kondratenko and Baerns. [77] Theoretically, lower lattice oxygen concentrations are present when regenerating with the softer N_2O oxidant, which will directly influence the extent of reduction in surface vanadia species and consequently inhibit the over-oxidation reaction. A significant loss in catalyst activity is observed when using CO_2 as the oxidant, as propane conversions decay across the ten cycles. As a result, propene yields are considerably lower than observed when using O_2 and N_2O. By the end of the 10th PDH step, propane conversion decreases to ~9.2 %. At this conversion, the selectivity to propene is ~36.5 % and a propene yield of only ~3.4 % is achieved. These results confirm that N_2O could be used as an effective oxidant in the chemical looping PDH system over vanadia catalysts, with yield values similar to oxygen.

Post-reaction analysis was performed on 10VAl catalysts removed after performing the ten CL-PODH redox cycles utilising N_2O and CO_2 as the oxidants. BET results, summarised in Table 59, exhibit the same trend and reveal a loss of surface area and pore volume, whilst the average pore diameter increases. The decrease in surface area of the 10VAl sample removed from the CL-PODH-N_2O cycling test is observably less dramatic, whilst CL-PODH using CO_2 results in the most significant transformation with the lowest surface area. This result indicates a greater extent of pore blockage due to higher quantities of carbonaceous deposits, thus agreeing with the thermodynamic analysis that CO_2 as an oxidant is unable to remove the coke and regenerate the catalyst.

Table 59: Surface area, pore volume and average pore diameter of spent 10VAl catalysts from CL-PODH redox cycles utilising O_2, N_2O and CO_2 as the oxidant

Sample	S_{BET} ($m^2\ g^{-1}$)	V_{pore} ($cm^3\ g^{-1}$)	Avg. pore diameter (Å)
Fresh 10VAl	145	0.55	43
Spent 10VAl 10 Cycles, 773 K, O_2	129	0.51	62
Spent 10VAl 10 Cycles, 773 K, N_2O	137	0.49	54
Spent 10VAl 10 Cycles, 773 K, CO_2	120	0.49	61

Comparison of the pre- and post-reaction Raman spectra of the 10VAl catalyst suggests that the catalyst is completely re-oxidised back to crystalline V_2O_5-like species following the CL-PODH cycling test using N_2O. This is evident with the loss of broad features relating to bridging polyvanadate species, as well as the loss in intensity of the ~1021 cm^{-1} band, relating to the V=O bond in isolated monovanadates. Post-reaction Raman of the sample analysed after the CL-PODH cycling test using CO_2 reveals a significant transformation when comparison is made with the spectrum obtained for the fresh 10VAl sample. Ultimately, Raman features relating to vanadium oxide vibrations are masked, with the addition of two broad bands at ~1598 and 1353 cm^{-1} characteristic of the G and D bands present in coke. [104] The I_G/I_D ratio of the G (~1598 cm^{-1}) to D (~1368 cm^{-1}) band has been calculated as 1.02, which implies that the coke formed from the CL-PODH-CO_2 cycling test has chain-like topology.

TGA-TPO measurements were also performed, and whilst CO_2 evolution could only be estimated due to accompanying H_2O formation, the calculated weight loss varies considerably between samples which use N_2O and CO_2 oxidants. Where CO_2 is employed as the oxidant in the regeneration step, the weight loss associated with CO_2 evolution is significant and occurs at distinctively higher temperatures than those observed for H_2O evolution. In this case, the overall weight loss was > 5 %, implying that the extent of carbon laydown was substantial. The thermodynamic analysis discussed previously indicates that CO_2 would not act as a suitable oxidant in CL-PODH cycling tests, since the regeneration of lattice oxygen sites and the sufficient removal of carbon laydown exhibit positive Gibbs free energy values. Both experimental and post-reaction characterisation results reinforce the thermodynamic constraints, and whilst co-fed CO_2 assisted PODH may be successful, its use is ineffective in a chemical looping system where propane dehydrogenation and catalyst regeneration are isolated steps.

Numerous 10VAl catalyst samples were additionally removed at various stages throughout the CL-PODH-N_2O cycling test and analysed externally with XPS. In general, the samples exhibit a similar trend to tests utilising O_2 as the oxidant, where V^{4+} surface species increase after the PDH and V^{5+} surface species increase after regenerating with N_2O. Upon further evaluation, V^{5+}/V^{4+} ratios are lower when re-oxidising with N_2O, thus implying that the regeneration of V^{5+} with N_2O is less significant, owing to the fact that N_2O is a softer oxidant. Furthermore, the V^{5+}/V^{4+} ratio decreases once more from 10.3 to 3.0 in the 10VAl sample removed after the overnight argon purge, indicating a higher presence of surface V^{4+} species. Note that these differences in V^{5+}/V^{4+} ratio do not result in a significant change in propene yield between oxygen and N_2O as discussed above.

Molybdena catalysts have also been widely investigated in PODH studies, albeit less thoroughly than vanadia systems since PODH rates are reportedly lower. [35, 63, 128] Despite this, promising results for propene selectivity have been observed [63, 129, 130] thus it seemed appropriate to investigate the use of molybdena in the scope of our CL-PODH tests. Within this study, the MoAl catalyst sample was prepared with 9.4 wt.% Mo loading, which equates as a 2:1 molar V/Mo ratio to the promising 10VAl sample. As reported, pre-reaction characterisation results reveal that the predominant species in 9.4MoAl is a mixture of both monomeric and polymeric molybdates. An optimal ODH activity is reportedly observed when two-dimensional MoO_x oligomers are present, which has been attributed to the higher reducibility of MoO_x domains existing in the Mo^{6+} oxidation state. On the other hand, the same study postulates that three-dimensional MoO_3 crystallites led to inaccessible sites and subsequent decrease in PODH rates. [60, 62]

When utilising 9.4MoAl in the CL-PODH-O_2 cycling test, propane conversions reach ~15.9 %, which is a marked decrease to those obtained in tests performed over the 10VAl catalyst at ~19.5 %. Despite this, the overall trend across the cycle remains analogous as propane conversions decrease in the PDH step of cycle 2, before remaining relatively stable throughout successive cycles 2-5 and 7-10. Furthermore, the 9.4MoAl catalyst demonstrates an enhancement in activity during the PDH step of cycle 6, which indicates that the overnight argon purge is somewhat altering the molybdenum sites. This time however, it enhances catalyst activity as opposed to propene selectivity, which was observed in tests using the 10VAl catalyst. As previously discussed for the 10VAl system, thermodynamic analysis reveals that residual carbonaceous deposits may also be readily oxidised by the lattice oxygen sites within molybdena species. The stoichiometric equations of these reactions are presented below with their corresponding Gibbs free energy values, indicating their feasibility at similar temperature conditions.

$$C\ (s) + MoO_3\ (s) \rightleftharpoons MoO_2\ (s) + CO\ (g) \qquad (\Delta G_{800K} = -83.8\ kJ\ mol^{-1})$$

$$C\ (s) + 2MoO_3\ (s) \rightleftharpoons 2MoO_2\ (s) + CO_2\ (g) \qquad (\Delta G_{800K} = -198.2\ kJ\ mol^{-1})$$

The selectivity towards propene is also lower when using 9.4MoAl, reaching ~32.1 % by the end of the 1st PDH step. A subsequent decay is observed during the PDH step of cycle 2, resulting in a decrease in propene yield from ~5.1 % to ~4.0 %. Propene yields remain

comparable in cycles 2 to 5, with an enhancement again observed in the PDH step of cycle 6 due to this increase in catalyst activity. Both propene selectivity and yield decay during the PDH step of cycle 7, before remaining relatively stable during successive cycles, indicating that no significant catalyst deactivation had occurred.

To provide insight into the reaction chemistry taking place when using supported molybdena in the CL-PODH cycling test, reaction profiles showcasing the entirety of the PDH step in cycles 1 and 2 are presented in Figures 112-114. A clear disparity is observed in propane conversion and propene selectivity within the initial stages of the PDH reaction to those obtained when using the 10VAl catalyst. In contrast, both propene and CO_2 yields are not maximised within the ~1.5 min of 1st PDH step. These results would suggest that the oxygen species present in the fresh 9.4MoAl catalyst exhibit a different reactivity to the weakly bound oxygenates present in the 10VAl catalyst. Following the subsequent re-oxidation of the 9.4MoAl catalyst with O_2 however, propene and CO_2 yields become maximised at the initial stages, thus reinforcing that the catalyst regeneration step results in higher concentration of labile and weakly bound oxygenates which are selective towards competing over-oxidation and oxidative dehydrogenation pathways.

The 9.4MoAl catalyst was similarly removed and analysed post-reaction. BET results of the fresh versus spent 9.4MoAl catalyst reveal similar findings to those obtained in the VAl catalyst series with a loss in both the surface area and pore volume, indicative of pore blockage due to coke formation. Markedly, the BET surface area and pore volume decreased from 155 to 139 $m^2\,g^{-1}$ and 0.55 to 0.52 $cm^3\,g^{-1}$, respectively, whilst the average pore diameter increased from 48 to 54 Å. The post-reaction Raman also reveals structural changes as the sharp feature observed at ~952 cm^{-1}, previously assigned to the molybdenyl bond of octahedral polymolybdates, shifts to ~965 cm^{-1} and is significantly less prominent in the post-reaction spectrum. A prominent feature that is not present in the pre-reaction Raman appears at 832 cm^{-1}, which may be characteristic of the stretching frequency of Mo=O in tetrahedrally coordinated surface $[Mo^{VI}O_4]^{2-}$ moieties comprising two terminal Mo=O bonds and two bridging Mo-O-Al bonds. [112] MoO_x oligomers, in the Mo^{6+} oxidation state, exhibit a higher reducibility and have previously been associated with optimal ODH activity in studies performed by Bell *et al.* [60, 62] These findings correlate well with our results as catalyst activity within the PDH steps remains stable with no significant deactivation. Nevertheless, the molybdena system is less effective than the vanadia with an overall lower propene yield.

Molybdena incorporation into the 10VAl catalyst was also explored within this study to establish the synergistic effects of utilising Mo as a promoter in CL-PODH-O_2 cycling tests. Three VMoAl catalysts were prepared with a fixed vanadium loading of 10 wt.%, whilst molybdenum loadings varied from 3.2, 4.7 and 9.4 wt.% giving V: Mo molar ratios of 6:1, 4:1 and 2:1, respectively. Pre-reaction characterisation results imply the presence of bulk V_2O_5, MoO_3 and V_2MoO_8 crystallites in 10V4.7MoAl and 10V9.4MoAl catalyst samples via BET and XRD analysis. The presence of a mixed V-O-Mo phase has also been highlighted via Raman spectroscopy and H_2-TPR measurements in all three VMoAl samples, indicating that the molybdenum promoter acts in an interactive manner by chemically co-ordinating to the surface vanadium oxide species.

The effect of varying the loading of the molybdena promoter on catalyst activity and selectivity towards propene in CL-PODH-O_2 tests is outlined in Figures 127 and 128. Results show that both 10V3.2MoAl and 10V4.7MoAl catalysts reach propane conversions of ~21.9 and 23.3 % by the end of the 1st PDH step, decreasing to ~20.9 and ~22.4 % during the subsequent 2nd PDH step. Thereafter, propane conversions remain relatively stable, with no indication of significant deactivation during cycles 2-5 and 7-10. An enhancement in activity is observed in the PDH step of cycle 6 which was similarly observed in the VAl and MoAl catalyst series. This observation has been attributed to the removal of low-level carbonaceous deposits, which ultimately prompts the reduction of surface vanadia species; a key component which has the potential to overcome selectivity limitations associated with PODH reactions. A considerable decline in propene selectivity is observed after the 1st and 6th PDH step at similar propane conversions, resulting in an overall decrease in propene yield from ~8.0 and 8.8 % to ~5.7 and 7.0 % when using 10V3.2MoAl and 10V4.7MoAl catalysts, respectively. Propene selectivity increases and remains relatively stable throughout cycles 3-5 and 8-10 however, indicating the regeneration of vanadia and molybdena sites, selective towards the olefin product, which stabilise as CL-PODH cycles proceed.

When utilising the 10V9.4MoAl catalyst, a propane conversion of ~27.1 % is obtained by the end of the 1st PDH step. Considerable catalyst deactivation occurs with TOS however, as propane conversion declines to ~22.9 % in the PDH step of cycle 10. Comparison of catalyst activity in the tests utilising the 10VAl and 9.4MoAl catalysts, shows that 10V9.4MoAl exhibits a higher activity than that of the 10VAl sample, however, propene selectivities are lower. Nevertheless, the improvement in activity results in an overall higher propene yield of ~7.4 % by the end of cycle 10. It is possible that this enhancement

may result due to the formation of V-O-Mo species, which have previously been found to promote catalyst activity in studies performed by Iglesia *et al.* [69]

For further clarity, the obtained propene yields from CL-PODH cycling tests using the 10VAl, 9.4MoAl and 10V9.4MoAl catalysts have been compared below in Figure 147.

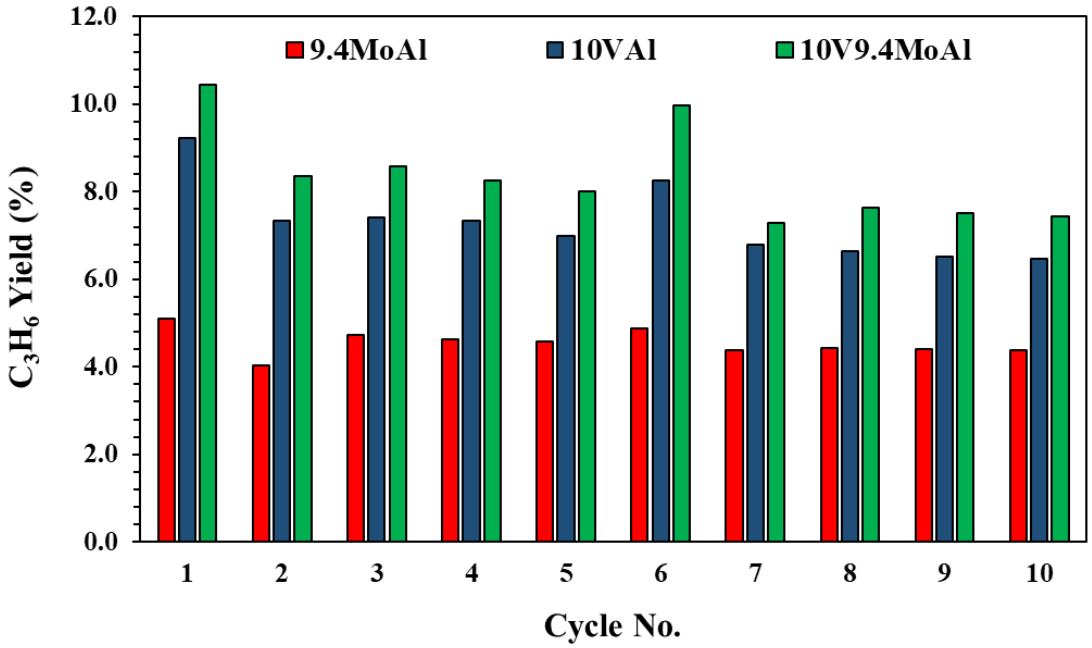

Figure 147: Instantaneous C_3H_6 and CO_2 yields using 9.4MoAl, 10VAl and 10V9.4MoAl catalysts, 773 K, 1 atm

Additional analysis was conducted to probe the reaction chemistry taking place when using the molybdena promoted 10V9.4MoAl catalyst. Reaction profiles showcasing the entirety of the PDH step in cycles 1 and 2 are presented in Figures 132-134. Within the initial stages of the PDH reaction, the trend in propane conversion and propene selectivity are comparable to those obtained when using the 10VAl catalyst. Both propene and CO_2 yields are maximised within the ~1.5 min of 1st PDH step, whereafter, the conversion begins to drop off significantly, which is met with an increase in propene selectivity. Notably, the initial propene yield ~1.5 min into the PDH reaction of cycle 1 is higher in the mixed 10V9.4MoAl catalyst (~13.4 %) than those observed in samples with separate molybdenum and vanadium entities (~3.2 and 12.0 %, respectively). These results would suggest that the oxygen species present in the fresh 10V9.4MoAl catalyst exhibit a similar reactivity to the weakly bound oxygenates present in the 10VAl catalyst. Subsequent propene yield begins to drop off until ~6 min into the PDH reaction, whereafter, it reaches steady state with TOS. Similarly, CO_2 yields decrease as the PDH reaction progresses

before reaching steady state, however, the selectivity remains comparably low and CO_2 yields remain below ~1 %.

VMoAl catalysts were similarly removed and characterised post-reaction after performing CL-PODH-O_2 tests. The BET results follow a similar trend to the post-reaction analysis of VAl and MoAl catalysts, whereby the surface area and pore volume decreases in comparison to the corresponding fresh VMoAl sample. A reduction in average pore diameter is observed however, which may imply a loss in the crystallite domains. A reduction in crystallinity and/or higher dispersion is further highlighted in the post-reaction XRD of 10V4.7MoAl and 10V9.4MoAl samples, whereby the reflections relating to V_2O_5, MoO_3 and mixed oxide V_2MoO_8 become significantly less prominent.

Upon completion of the CL-PODH-O_2 tests, various structural changes were observed in spent VMoAl catalysts. Markedly, a loss in the Raman features assigned to mixed V-O-Mo species is observed in the post-reaction spectra. Furthermore, prominent bands appear in the ~140 cm^{-1} region for the spent 10V4.7MoAl and 10V9.4MoAl catalyst, which were previously assigned to crystalline V_2O_5 in the Raman data obtained in the VAl catalyst series. Both G and D bands were discernibly absent in the post-reaction spectra, which suggests that the coke formed from the PDH step is successfully removed by the O_2 oxidant in the final catalyst regeneration step. This observation was reinforced in the TGA-TPO measurements, which show that the weight loss observed arises predominantly from H_2O evolution, with no evidence of carbon laydown. Reactivity tests show that catalyst activity is lost throughout the CL-PODH-O_2 cycling test using 10V9.4MoAl and analysis of the post-reaction characterisation would suggest that this is due to the speciation of vanadia and molybdena domains as opposed to the formation of coke.

8 Conclusions and Future Work

The previously stated main objective of this research project was to investigate the efficacy of VAl, MoAl and VMoAl catalysts for propene production in a series of CL-PODH redox cycling tests, using O_2, N_2O and CO_2 oxidants within the catalyst regeneration step. Specifically, the effect of varying vanadium loading and the incorporation of a molybdenum promotor at various V:Mo molar ratios has been investigated. Such tests have provided valuable insight into the relationship between the structure of vanadia and molybdena species and activity for propene production.

Within the VAl catalyst series, BET, H_2-TPR, Raman and XRD results imply that the prevalent species in fresh 5VAl and 7.5VAl catalysts are both monomeric and polymeric surface vanadia species, with increased polymerisation in the latter. There is evidence to suggest that polyvanadate species are present in the 10VAl catalyst, however, crystalline V_2O_5 domains are also identified in the Raman spectrum and their presence is backed by the significant reduction in the BET surface area on going from the 5VAl to the 10VAl sample. The XRD pattern lacks sharp and intense peaks indicative of bulk crystallites however, suggesting that the V_2O_5 present is highly dispersed on the surface. The resulting propane conversions, propene yields and propene selectivities that were obtained upon completion of the 1st PDH step of CL-PODH redox cycles are tabulated below in Table 60.

Table 60: Summary of C_3H_8 conversions, C_3H_6 selectivities and yields obtained during the PDH step of cycle 1: 5, 7.5 and 10VAl catalysts, O_2 oxidant, 773 K, 1 atm

Sample	C_3H_8 Conversion (%)	C_3H_6 Selectivity (%)	C_3H_6 Yield (%)
5VAl	13.2	45.5	5.9
7.5VAl	13.6	38.9	5.3
10VAl	19.5	47.4	9.2

Observably, the most promising results for propene production arise in benchmark CL-PODH redox cycling tests performed over the 10VAl catalyst. The regenerability of the catalyst has also been investigated, where both catalyst activity and selectivity towards propene decline in the 2nd PDH step, performed after re-oxidising the catalyst using the O_2 oxidant. Thereafter, catalyst activity and propene selectivity reach steady state in

successive cycles, where propene yields remain relatively stable upon completion of the CL-PODH test.

The reaction profile of the 1st PDH step performed over the 10VAl catalyst was further analysed to probe the reaction chemistry taking place. Further elucidation with propane pulsing tests reveals that both the oxidative dehydrogenation (ODH) of propane to propene and H_2O and the over-oxidation of propane to CO_2 and H_2 reactions are competing at initial stages. At this point, weakly bound lattice oxygenates are present, which promote the over-oxidation reaction. After this initial stage, water evolution appears to increase, implying that the ODH reaction begins to dominate. Water evolution then ceases ~6 min into the PDH step, indicating the complete removal of accessible lattice oxygen sites, which ultimately initiates the direct propane dehydrogenation reaction as the reaction proceeds. Additional *in-situ* Raman, XANES and EXAFS characterisation tests are required to establish the change in surface vanadia species. Such tests would be beneficial in establishing the effect of oxygen lability and reducibility of vanadia species on the reaction chemistry taking place throughout the entire PDH step.

Post-reaction characterisation of benchmark CL-PODH redox cycling tests performed over the 5VAl and 7.5VAl catalysts reveal no observable structural changes in the Raman or XRD spectra. The BET results of the spent 5VAl catalyst were analogous to the fresh sample, however, a notable change was observed when comparing the fresh and spent 7.5VAl catalyst, attributed to the pore blockage of support micropores. A similar trend in the BET results is observed for the spent 10VAl catalyst, in addition to various structural changes highlighted in the post-reaction Raman spectra. Raman bands relating to crystalline V_2O_5 become less prominent as the feature assigned to the V=O bond in polyvanadates increases in intensity, therefore implying an increase in polymeric vanadate domains post-reaction.

Additional post-reaction characterisation tests were conducted to probe the surface vanadia species present in the 10VAl catalyst removed at different stages throughout the ten cycles. Notably, the BET results of fresh and spent 10VAl catalysts reveal an interchanging loss and regeneration of surface area and pore volume with sequential PDH and catalyst regeneration steps, in line with the pore blockage and removal of carbonaceous deposits. Coke formation is further implied in the spectra of samples removed after the PDH step with broad Raman features at ~1600 and 1378 cm^{-1}. The Raman spectra obtained after the successive regeneration cycles uncover an absence of both G and D bands, thus reinforcing

the regenerative ability of the O_2 oxidant for coke removal. External analysis with XPS reveals an interchanging oxidation state of surface vanadia species after various PDH and O_2 regeneration steps. As would be expected, an increase in V^{4+} species results from the PDH step, as it removes lattice oxygen species and reduces surface V^{5+} species. Subsequent regeneration steps increase surface V^{5+} species, however, an overall decrease is observed as the cycles proceed, which suggests that the catalyst is not re-oxidised back to its original state.

Another significant observation in CL-PODH redox cycling tests performed across the VAl, catalyst series was the rise in propene production during the 6^{th} PDH step, brought about by an increase in selectivity at similar propane conversions. This is observed after holding the catalyst overnight under argon following the O_2 regeneration step of cycle 5. The 10VAl catalyst was similarly removed and characterised after this overnight argon purge. XPS results reveal an increase in surface V^{4+} species at this stage, which agrees with our findings from the thermodynamics and post-reaction Raman that surface vanadia sites are oxidising and removing residual low-level carbonaceous deposits, hence the surface vanadium is in a more reduced state. An increase in propene selectivity due to this reduced species establishes a potential in tuning specific V^{5+}/V^{4+} ratios, which may be crucial in overcoming the selectivity limitations to enhance propene production.

When removing the spent 10VAl catalyst from the benchmark test, we observe a profile along the catalyst bed with a colour gradient. As such, the top, middle and bottom of the catalyst bed were separated and characterised. A clear disparity is observed in the Raman spectra taken along the catalyst bed, where the top of the bed exhibits a significant loss in bands relating to crystalline V_2O_5 species and the bottom of the bed is comparable to the Raman of the fresh 10VAl sample. Additional reactions which utilise varying 10VAl catalyst bed lengths in CL-PODH redox cycling tests, or spatially resolved in situ Raman or XAFS studies, would be beneficial as it would provide further insight into the role each of these species plays in the oxidative dehydrogenation reaction.

A long duration 3 h PDH stability test was performed utilising the 10VAl catalyst. A substantial 30 % loss in catalyst activity is observed after 3 h TOS, as propane conversion declines from ~19.8 to 13.8 %. Post-reaction Raman analysis reveals significant coke formation and a profound loss in Raman bands characteristic of V_2O_5, thus highlighting the need for sequential PDH and catalyst regeneration steps.

Alternative softer N_2O and CO_2 oxidants were also employed as an oxidant in the catalyst regeneration step. The resulting propane conversions, propene yields and propene selectivities obtained upon completion of the 10th PDH step of CL-PODH redox cycles over the 10VAl catalyst are tabulated below in Table 61.

Table 61: Summary of C_3H_8 conversions, C_3H_6 selectivities and yields obtained during the PDH step of cycle 1: 10VAl, O_2, N_2O and CO_2 oxidants, 773 K, 1 atm

Oxidant	C_3H_8 Conversion (%)	C_3H_6 Selectivity (%)	C_3H_6 Yield (%)
O_2	15.8	40.8	6.5
N_2O	15.4	47.6	7.4
CO_2	9.2	36.5	3.4

At similar propane conversions, an increase in propene selectivity is observed in CL-PODH tests utilising N_2O, which has previously been attributed to lower lattice oxygen concentration, thus consequently inhibiting the over-oxidation reaction. Both the experimental results and the various post-reaction characterisation confirms that N_2O could be used as an effective oxidant in the chemical looping CL-PODH reaction system. A significant decline in catalyst activity is observed when using CO_2 as the oxidant however, and propene yields are considerably lower, indicating that CO_2 is not an effective oxidant in CL-PODH redox cycles. This is highlighted further in the post-reaction Raman spectrum with the presence of G and D bands, which reflects the inability of the CO_2 oxidant to remove the coke and regenerate the catalyst. Both experimental and post-reaction characterisation results reinforce the thermodynamic constraints of using the chemically inert CO_2 molecule. Whilst co-fed CO_2 assisted PODH may be successful, its use is ineffective in a chemical looping system where propane dehydrogenation and catalyst regeneration are isolated steps.

For the MoAl catalyst series, a 9.4MoAl catalyst was synthesised and BET, H_2-TPR, Raman and XRD results imply that the prevalent species is a mixture of both monomeric and polymeric molybdate species. An optimal ODH activity is reportedly observed when two-dimensional MoO_x oligomers are present, which has been attributed to the higher reducibility of MoO_x domains existing in the Mo^{6+} oxidation state. [60, 62] In comparison to the 10VAl catalyst however, a lower catalyst activity is observed in the 1st PDH step of the CL-PODH redox cycling test, as propane conversions reach ~15.9 %. Albeit the overall trend throughout the ten cycles is analogous as conversions reach steady state during successive cycles 2-5 and 7-10, with an enhancement in propene production observed again during the PDH step of cycle 6.

The reaction chemistry when using the 9.4MoAl catalyst was further investigated by analysing the reaction profiles obtained throughout the entirety of the PDH step. A clear disparity in catalyst activity and selectivity towards propene during the initial stages is found in comparison to those obtained when using the 10VAl catalyst, which implies that the oxygen species present exhibit a difference in reactivity to the weakly bound oxygen found in the 10VAl sample. Post-reaction characterisation of the 9.4MoAl catalyst was performed and the BET results reveal a loss in surface area and pore volume, attributed to the pore blockage of support micropores from carbonaceous deposits. Various structural changes were also found in the post-reaction Raman spectra, the most significant being the presence of a band at ~832 cm^{-1}, which has previously been assigned as the molybdenyl stretch in tetrahedrally coordinated surface $[Mo^{VI}O_4]^{2-}$ moieties.

In order to establish the synergistic effects of utilising Mo as a promoter within the 10VAl catalyst in CL-PODH-O_2 cycling tests, three 10VMoAl catalysts were prepared with V:Mo molar ratios of 6:1, 4:1 and 2:1, respectively. Pre-reaction characterisation results imply the presence of bulk V_2O_5, MoO_3 and V_2MoO_8 crystallites in 10V4.7MoAl and 10V9.4MoAl catalyst samples via BET and XRD analysis. The presence of a mixed V-O-Mo phase has also been highlighted in Raman spectroscopy and H_2-TPR measurements in all three VMoAl samples, indicating that molybdenum co-ordinates chemically to the surface vanadium oxide, thus acting as an interactive promotor.

The resulting propane conversions, propene yields and propene selectivities that were obtained upon completion of the 1st PDH step of CL-PODH redox cycles using the three 10VMoAl catalysts are tabulated in Table 62.

Table 62: Summary of C_3H_8 conversions, C_3H_6 selectivities and yields obtained during the PDH step of cycle 1: 10V3.2MoAl, 10V4.7MoAl, 10V9.4MoAl catalysts, O_2 oxidant, 773 K, 1 atm

Sample	C_3H_8 Conversion (%)	C_3H_6 Selectivity (%)	C_3H_6 Yield (%)
10V3.2MoAl	21.9	36.8	8.1
10V4.7MoAl	23.3	37.8	8.8
10V9.4MoAl	27.1	38.5	10.4

Evidently, an increase in molybdena incorporation into the 10VAl catalyst increases the catalyst activity, as propane conversions increases across the VMoAl series. In comparison to 10VAl and 9.4MoAl catalysts, a higher activity is observed in tests utilising 10V9.4MoAl. This results in an overall higher propene yield, which correlates well with studies performed by Iglesia *et al*., who concluded that the formation of the V-O-Mo interlayer had a promotional effect on catalyst activity. [69]

The three VMoAl catalysts were similarly removed and characterised post CL-PODH reaction tests. The BET results reveal a reduction in average pore diameter, which suggests a loss in the crystallite V_2O_5, MoO_3 and mixed oxide V_2MoO_8 species. A reduction in crystallinity and/or higher dispersion is implied in the post-reaction XRD of 10V4.7MoAl and 10V9.4MoAl samples as the reflections relating to the crystallite domains become significantly less prominent. Various structural changes were highlighted in the Raman spectra of spent VMoAl catalysts, the most significant being the loss in the Raman feature assigned to V-O-Mo domains in addition to a prominent band assigned to crystalline V_2O_5 species. Both G and D bands were absent in the spent VMoAl catalysts and post-reaction TPO measurements showed no evidence of carbon laydown, therefore, any carbonaceous deposits, which result from the PDH step, is successfully removed by the O_2 oxidant in the catalyst regeneration step. Additional *in-situ* Raman and XAFS characterisation tests would be beneficial to monitor the presence and fully establish the role of V-O-Mo domains throughout the PDH step.

The research detailed throughout this thesis has provided valuable insight into vanadia, molybdena and mixed vanadia/molybdena catalyst systems and their use within CL-PODH studies as an alternative route for propene production. Particularly, the relationship between the activity of vanadia and molybdena species as a function of varying vanadium loading and increased molybdenum incorporation has been highlighted. The incorporation of molybdenum displayed a promotional effect, where an enhancement in catalyst activity was observed across the VMoAl series. The presence of V-O-Mo domains were detected in the pre-reaction Raman and XRD, thereby inferring that the molybdenum counterpart behaved as an interactive promotor by chemically coordinating to active vanadia sites. Further investigation into the use of alternative promotors e.g. CrO_x and WO_x should be explored to determine their efficacy for propene formation within a CL-PODH system.

Furthermore, the use of N_2O and CO_2 within the catalyst regeneration step has also been explored to establish catalyst regenerability throughout the cycles when using alternative, softer oxidants. This work has shown both thermodynamically and experimentally that O_2 and N_2O are suitable oxidants for the catalyst regeneration step of CL-PODH cycles. The selectivity towards propene is, in fact, further enhanced when utilising N_2O as the oxidant, whereby XPS results reveal a higher presence of V^{4+} surface species than when using O_2 as the oxidant. Enhanced catalyst activity and propene yields are further observed during the PDH step of cycle 6 after holding the catalysts overnight under argon. Raman and XPS analysis reveal the catalyst is in a more reduced state, again with a higher presence of V^{4+} species. These findings establish a potential in enhancing propene production by obtaining specific V^{5+}/V^{4+} ratios, which may be crucial in overcoming the selectivity limitations. Future studies should focus on exposing the catalyst to various reducing H_2 atmospheres prior to the PDH step to determine the extent of reduction optimal for propene production.

Thermodynamically and experimentally, CL-PODH cycles utilising CO_2 have shown that it is not a suitable oxidant for the regeneration step. Whilst the softer oxidant has shown potential in PODH systems where CO_2/propane mixtures are co-fed, the loss in catalyst activity and significant carbonaceous deposits observed in the post-reaction Raman highlight the inability for CO_2 to regenerate active sites and sufficiently remove carbon laydown. The thermodynamics reveal that these findings are a direct result from the inherent inertness of the CO_2 molecule, therefore, a suitable catalyst that can overcome this thermodynamic barrier is required if CO_2 is to be utilised in CL-PODH redox cycling systems.

9 References

1. J. S. Plotkin, *Catal. Today*, 2005, **106**, 10-14.
2. M. Marsh and J. Wery, *Filling the Propylene Gap - Shaping the Future with On-Purpose Technologies*, Honeywell UOP, 2019, 1-10.
3. I. Amghizar, L. A. Vandewalle, K. M. Van Geem and G. B. Marin, *Engineering*, 2017, **3**, 171-178.
4. Z. Y. Wang, Z. H. He, L. Y. Li, S. Y. Yang, M. X. He, Y. C. Sun, K. Wang, J. G. Chen and Z. T. Liu, *Rare Metals*, 2022, **41**, 2129-2152.
5. *Global Propylene Capacity and Capital Expenditure Outlook to 2030 - Asia and Middle East to Lead Globally in Terms of Propylene Capacity Additions*, Global Data, 2020, 1-44.
6. A. M. Aitani, *Encyclopedia of Chemical Processing*, Taylor and Francis, 2006.
7. T. Ren, M. Patel and K. Blok, *Energy*, 2006, **31**, 425-451.
8. A. Akah and M. Al-Ghrami, *Appl. Petrochem. Res.*, 2015, **5**, 377-392.
9. *Shale gas, competitiveness, and new US chemical industry investment: An analysis based on announced projects.*, American Chemistry Council, Washington D.C, 2013, 5-47.
10. A. Akah, J. Williams and M. Ghrami, *Catal. Surv. Asia*, 2019, **23**, 265-276.
11. Y. M. John, R. Patel and I. M. Mujtaba, *Appl. Petrochem. Res.*, 2018, **8**, 79-95.
12. I. S. Han and C. B. Chung, *Chem. Eng. Sci*, 2001, **56**, 1951-1971.
13. N. Nesterenko, J. Aguilhon, P. Bodart, D. Minoux and J. P. Dath, in *Zeolites and Zeolite-Like Materials*, eds. B. F. Sels and L. M. Kustov, Elsevier, Amsterdam, 2016, ch. 5, pp. 189-263.
14. M. Stöcker, *Microporous Mesoporous Mater*, 1999, **29**, 3-48.
15. S. Kvisle, T. Fuglerud, S. Kolboe, U. Olsbye, K. P. Lillerud and B. V. Vora, in *Handbook of Heterogeneous Catalysis*, pp. 2950-2965.
16. M. Khanmohammadi, S. Amani, A. Bagheri Garmarudi and A. Niaei, *Chinese. J. of Catal.*, 2016, **37**, 325-339.
17. Y. Zhang, Z. Ren, Y. Wang, Y. Deng and J. Li, *Catalysts*, 2018, **8**, 570.
18. J. Q. Chen, A. Bozzano, B. Glover, T. Fuglerud and S. Kvisle, *Catal. Today*, 2005, **106**, 103-107.
19. M. Ibáñez, P. Pérez-Uriarte, M. Sánchez-Contador, T. Cordero-Lanzac, A. T. Aguayo, J. Bilbao and P. Castaño, *Catalysts*, 2017, **7**, 254.
20. X. Wu, M. G. Abraha and R. G. Anthony, *App. Cat. A: Gen.*, 2004, **260**, 63-69.
21. M. Monai, M. Gambino, S. Wannakao and B. M. Weckhuysen, *Chem. Soc. Rev*, 2021, **50**, 11503-11529.
22. S. Chen, X. Chang, G. Sun, T. Zhang, Y. Xu, Y. Wang, C. Pei and J. Gong, *Chem. Soc. Rev*, 2021, **50**, 3315-3354.
23. Z. Nawaz, *Rev. in Chem. Eng*, 2015, **31**, 413-436.
24. P. Chaiyavech, *Commercialization of the World's First Oleflex Unit*, J. R. Inst. Thail., 2002, 27, 1–7
25. J. Gregor and D. Wei, *UOP Oleflex process for light olefins production*, UOP LLC Des Plaine, Illinois, 2004.
26. H. Maddah, *Amer. Sci, Res, Journ. Eng. Tech. and Sci.*, 2018, **45**, 49-63.
27. D. E. Resasco and G. L. Haller, in *Catalysis: Catalytic dehydrogenation of lower alkanes*, Royal Society of Chemistry, 2007, vol. 11, ch. 9.
28. Clariant, *Clariant Catalysts & Lummus Technology expand CATOFIN® footprint with India's first PDH plant*, 2021.
29. C. A. Carrero, R. Schlögl, I. E. Wachs and R. Schomaecker, *ACS Catal.*, 2014, **4**, 3357-3380.

30. J. H. Carter, T. Bere, J. R. Pitchers, D. G. Hewes, B. D. Vandegehuchte, C. J. Kiely, S. H. Taylor and G. J. Hutchings, *Green Chem.*, 2021, **23**, 9747-9799.
31. S. A. Al-Ghamdi and H. I. de Lasa, *Fuel*, 2014, **128**, 120-140.
32. A. Dinse, S. Khennache, B. Frank, C. Hess, R. Herbert, S. Wrabetz, R. Schlögl and R. Schomäcker, *J. Mol. Catal. A Chem.*, 2009, **307**, 43-50.
33. K. Chen, A. T. Bell and E. Iglesia, *J. Phys. Chem. B*, 2000, **104**, 1292-1299.
34. H. H. Kung, in *Advances in Catalysis*, eds. D. D. Eley, H. Pines and W. O. Haag, Academic Press, 1994, vol. 40, pp. 1-38.
35. S. Albonetti, F. Cavani and F. Trifiro, *Catal. Rev. Sci. Eng*, 1996, **38**, 413-438.
36. A. Khodakov, J. Yang, S. Su, E. Iglesia and A. T. Bell, *J. Catal*, 1998, **177**, 343-351.
37. A. Khodakov, B. Olthof, A. T. Bell and E. Iglesia, *J. Catal*, 1999, **181**, 205-216.
38. O. V. Buyevskaya and M. Baerns, in *Catalysis: Volume 16*, ed. J. J. Spivey, The Royal Society of Chemistry, 2002, vol. 16, pp. 155-197.
39. M. A. Bañares, *Catal. Today*, 1999, **52**, 379.
40. D. L. Stern and R. K. Grasselli, *J. Catal*, 1997, **167**, 550-559.
41. I. E. Wachs and B. M. Weckhuysen, *App. Cat. A: Gen.*, 1997, **157**, 67-90.
42. K. Chen, A. Khodakov, J. Yang, A. T. Bell and E. Iglesia, *J. Catal*, 1999, **186**, 325-333.
43. Z. Pan, Y. Li, Y. Zhao, C. Zhang and H. Chen, *Catal. Today*, 2020, **364**, 2-6.
44. K. Alexopoulos, M.-F. Reyniers and G. B. Marin, *J. Catal*, 2012, **289**, 127-139.
45. Y. Wang, F. Rosowski, R. Schlögl and A. Trunschke, *J. Phys. Chem. C*, 2022, **126**, 3443-3456.
46. H. Kim, G. A. Ferguson, L. Cheng, S. A. Zygmunt, P. C. Stair and L. A. Curtiss, *J. Phys. Chem. C*, 2012, **116**, 2927-2932.
47. B. M. Weckhuysen and D. E. Keller, *Catal. Today*, 2003, **78**, 25-46.
48. T. V. Malleswara Rao, E. Vico-Ruiz, M. A. Bañares and G. Deo, *J. Catal*, 2008, **258**, 324-333.
49. H. Tian, C. A. Roberts and I. E. Wachs, *J. Phys. Chem. C*, 2010, **114**, 14110-14120.
50. Z. Wu, H.-S. Kim, P. C. Stair, S. Rugmini and S. D. Jackson, *J. Phys. Chem. B*, 2005, **109**, 2793-2800.
51. Y. T. Chua, P. C. Stair and I. E. Wachs, *J. Phys. Chem. B*, 2001, **105**, 8600-8606.
52. S. J. Khatib, R. Guil-López, M. A. Peña, J. L. G. Fierro and M. A. Bañares, *Catal. Today*, 2006, **118**, 353-359.
53. F. Klose, T. Wolff, H. Lorenz, A. Seidel-Morgenstern, Y. Suchorski, M. Piórkowska and H. Weiss, *J. Catal*, 2007, **247**, 176-193.
54. D. Siew Hew Sam, V. Soenen and J. C. Volta, *J. Catal*, 1990, **123**, 417-435.
55. A. Corma, J. M. López-Nieto, N. Paredes, M. Pérez, Y. Shen, H. Cao and S. L. Suib, in *Studies in Surface Science and Catalysis*, eds. P. Ruiz and B. Delmon, Elsevier, 1992, vol. 72, pp. 213-220.
56. J. Guo, X. Li, Y. Tang and J. Zhang, *ChemistrySelect*, 2019, **4**, 13576-13581.
57. T. Blasco and J. M. L. Nieto, *App. Cat. A: Gen.*, 1997, **157**, 117-142.
58. B. Wang, G. Ding, Y. Shang, J. Lv, H. Wang, E. Wang, Z. Li, X. Ma, S. Qin and Q. Sun, *App. Cat. A: Gen.*, 2012, **431-432**, 144-150.
59. F. Cavani, N. Ballarini and A. Cericola, *Catal. Today*, 2007, **127**, 113-131.
60. K. Chen, E. Iglesia and A. T. Bell, *J. Phys. Chem. B*, 2001, **105**, 646-653.
61. A. Christodoulakis, E. Heracleous, A. A. Lemonidou and S. Boghosian, *J. Catal*, 2006, **242**, 16-25.
62. K. Chen, S. Xie, A. T. Bell and E. Iglesia, *J. Catal*, 2001, **198**, 232-242.
63. K. Chen, S. Xie, E. Iglesia and A. T. Bell, *J. Catal*, 2000, **189**, 421-430.
64. M. Høj, T. Kessler, P. Beato, A. D. Jensen and J.-D. Grunwaldt, *App. Cat. A: Gen.*, 2014, **472**, 29-38.

65. S. Yang, E. Iglesia and A. T. Bell, *J. Phys. Chem. B*, 2005, **109**, 8987-9000.
66. B. Mitra, I. E. Wachs and G. Deo, *J. Catal*, 2006, **240**, 151-159.
67. S. C. Nayak, D. Shee and G. Deo, *Catal. Lett.*, 2010, **136**, 271-278.
68. H. Tian, E. I. Ross and I. E. Wachs, *J. Phys. Chem. B*, 2006, **110**, 9593-9600.
69. H. Dai, A. T. Bell and E. Iglesia, *J. Catal*, 2004, **221**, 491-499.
70. M. A. Atanga, F. Rezaei, A. Jawad, M. Fitch and A. A. Rownaghi, *Appl. Catal. B*, 2018, **220**, 429-445.
71. J. Kang, A. D. Czaja and V. V. Guliants, *Eur. J. Inorg. Chem.*, 2017, **2017**, 4757-4762.
72. P. Djinović, J. Zavašnik, J. Teržan and I. Jerman, *Catal. Lett.*, 2021, **151**, 2816-2832.
73. E. Nowicka, C. Reece, S. M. Althahban, K. M. H. Mohammed, S. A. Kondrat, D. J. Morgan, Q. He, D. J. Willock, S. Golunski, C. J. Kiely and G. J. Hutchings, *ACS Catal.*, 2018, **8**, 3454-3468.
74. S. Rogg and C. Hess, *J. CO2 Util*, 2021, **50**, 101604.
75. X. Jiang, L. Sharma, V. Fung, S. J. Park, C. W. Jones, B. G. Sumpter, J. Baltrusaitis and Z. Wu, *ACS Catal.*, 2021, **11**, 2182-2234.
76. G. Wu, F. Hei, N. Guan and L. Li, *Catal. Sci. Technol.*, 2013, **3**, 1333-1342.
77. E. V. Kondratenko and M. Baerns, *App. Cat. A: Gen.*, 2001, **222**, 133-143.
78. O. V. Buyevskaya and M. Baerns, *Catal. Today*, 1998, **42**, 315-323.
79. S. Rostom and H. de Lasa, *Catalysts*, 2020, **10**.
80. S. Rostom and H. I. de Lasa, *Ind. Eng. Chem. Res.*, 2017, **56**, 13109-13124.
81. S. Rostom and H. de Lasa, *Ind. Eng. Chem. Res.*, 2018, **57**, 10251-10260.
82. K. Fukudome, N.-o. Ikenaga, T. Miyake and T. Suzuki, *Catal. Sci. Technol.*, 2011, **1**, 987-998.
83. S. C. Kluiters, R. W. Van Den Brink and W. G. Haije, in *Developments and Innovation in Carbon Dioxide (CO2) Capture and Storage Technology*, ed. M. M. Maroto-Valer, Woodhead Publishing, 2010, vol. 1, pp. 320-357.
84. T. Wu, Q. Yu, K. Wang and M. van Sint Annaland, *Catalysts*, 2021, **11**, 1-18.
85. H. de Lasa, *Riser Simulator*, U.S. Patent 5,102,628, 1992.
86. S. Chen, L. Zeng, R. Mu, C. Xiong, Z.-J. Zhao, C. Zhao, C. Pei, L. Peng, J. Luo, L.-S. Fan and J. Gong, *J. Amer. Chem. Soc*, 2019, **141**, 18653-18657.
87. *United States Pat.*, 4,003,854, 1977.
88. I. E. Wachs and C. A. Roberts, *Chem. Soc. Rev*, 2010, **39**, 5002-5017.
89. N. Fairley, V. Fernandez, M. Richard‐Plouet, C. Guillot-Deudon, J. Walton, E. Smith, D. Flahaut, M. Greiner, M. Biesinger, S. Tougaard, D. Morgan and J. Baltrusaitis, *App. Surf. Sci. Adv*, 2021, **5**, 100112.
90. Hiden Analytical., Integrated Microreactor-Mass Spectrometer for Reaction Testing, TPD/R/O and Pulse Chemisorption, https://www.hidenanalytical.com/wp-content/uploads/2022/01/CATLAB-new-format.pdf, (accessed February, 2022).
91. V. K. Shen, D. W. Siderius, W. P. Krekelberg and H. W. Hatch, NIST Standard Reference Simulation Website - SRD 173, DOI: https://doi.org/10.18434/mds2-232).
92. A. M. Elfadly, A. M. Badawi, F. Z. Yehia, Y. A. Mohamed, M. A. Betiha and A. M. Rabie, *Egypt. J. Petrol*, 2013, **22**, 373-380.
93. M. V. Martínez-Huerta, X. Gao, H. Tian, I. E. Wachs, J. L. G. Fierro and M. A. Bañares, *Catal. Today*, 2006, **118**, 279-287.
94. J. Cheng, W. Li, X. Wang, H. Liu and Y. Chen, *Chem. Eng. J*, 2022, **431**, 133694.
95. G. G. Cortez and M. A. Bañares, *J. Catal*, 2002, **209**, 197-201.
96. S. Benomar, A. Massó, B. Solsona, R. Issaadi and J. M. López Nieto, *Catalysts*, 2018, **8**, 126.
97. A. Gennaro, A. A. Isse, M.-G. Severin, E. Vianello, I. Bhugun and J.-M. Savéant, *J. Chem. SOC Faraday. T*, 1996, **92**, 3963-3968.

98. G. Deo, F. D. Hardcastle, M. Richards, A. M. Hirt and I. E. Wachs, in *Novel Materials in Heterogeneous Catalysis*, Amer. Chem. Soc, 1990, vol. 437, ch. 29, pp. 317-328.
99. J. J. Hurly, *Int. J. Thermophys*, 2003, **24**, 1611-1635.
100. R. A. Robie, B. S. Hemingway and J. R. Fisher, *Thermodynamic properties of minerals and related substances at 298.15 K and 1 bar (105 pascals) pressure and at higher temperatures*, Report 1452, 1978.
101. D. R. Stull, E. F. Westrum and G. C. Sinke, *The chemical thermodynamics of organic compounds*, J. Wiley, New York, 1969.
102. C. E. Wicks and F. E. Block, *Thermodynamic properties of 65 elements - their oxides, halides, carbides, and nitrides*, 1963.
103. S. D. Jackson, S. Rugmini, P. C. Stair and Z. Wu, *Chem. Eng. J*, 2006, **120**, 127-132.
104. S. D. Jackson, P. C. Stair, L. F. Gladden and J. McGregor, in *Metal Oxide Catalysis*, 2008, pp. 595-612.
105. R. A. Lowden, J. J. O. Kiggans, S. D. Nunn, F. Montgomery, P. Menchhofer and C. D. Bryan, *Large-Batch Reduction of Molybdenum Trioxide*, Oak Ridge National Laboratory, 2015.
106. S. K. Maity, M. S. Rana, B. N. Srinivas, S. K. Bej, G. Murali Dhar and T. S. R. Prasada Rao, *J. Mol. Catal. A Chem.*, 2000, **153**, 121-127.
107. K. V. R. Chary, K. R. Reddy, G. Kishan, J. W. Niemantsverdriet and G. Mestl, *J. Catal*, 2004, **226**, 283-291.
108. D. A. Solís-Casados, L. Escobar-Alarcón, T. Klimova, J. Escobar-Aguilar, E. Rodríguez-Castellón, J. A. Cecilia and C. Morales-Ramírez, *Catal. Today*, 2016, **271**, 35-44.
109. J. Medema, C. Van Stam, V. De Beer, A. Konings and D. Koningsberger, *J. Catal*, 1978, **53**, 386-400.
110. T. L. Drake and P. C. Stair, *Top. Catal*, 2017, **60**, 1618-1630.
111. G. Mestl and T. K. K. Srinivasan, *Catal. Rev.*, 1998, **40**, 451-570.
112. H. Hu, I. E. Wachs and S. R. Bare, *J. Phys. Chem*, 1995, **99**, 10897-10910.
113. M. A. Vuurman, D. J. Stufkens, A. Oskam, G. Deo and I. E. Wachs, *J. Chem. SOC Faraday. T*, 1996, **92**, 3259-3265.
114. B. Solsona, A. Dejoz, T. Garcia, P. Concepción, J. M. L. Nieto, M. I. Vázquez and M. T. Navarro, *Catal. Today*, 2006, **117**, 228-233.
115. M. A. Bañares and S. J. Khatib, *Catal. Today*, 2004, **96**, 251-257.
116. F. A. Bezerra, H. O. Altino and R. R. Soares, *J. of the Brazilian. Chem. Soc.*, 2019, **30**, 1025-1033.
117. K. Hao, L. Zhang, L. Song, H. Y. Guan, C. M. Li, T. Liu, Q. Yu, J. M. Zeng and Z. W. Wang, *Inorg. Chem. Comm*, 2020, **116**, 107910.
118. A. Stoyanova, R. Iordanova, M. Gancheva and Y. Dimitriev, *J. Optoelectron. Adv. Mater.*, 2009, **11**, 1127-1131.
119. G. Centi, *App. Cat. A: Gen.*, 1996, **147**, 267-298.
120. M. D. Argyle, K. Chen, A. T. Bell and E. Iglesia, *J. Catal*, 2002, **208**, 139-149.
121. G.-Q. Yang, H. Wang, T. Gong, Y.-H. Song, H. Feng, H.-Q. Ge, H.-b. Ge, Z.-T. Liu and Z.-W. Liu, *J. Catal*, 2019, **380**, 195-203.
122. C. Xiong, S. Chen, P. Yang, S. Zha, Z.-J. Zhao and J. Gong, *ACS Catal.*, 2019, **9**, 5816-5827.
123. Y. T. Chua and P. C. Stair, *J. Catal*, 2003, **213**, 39-46.
124. S. M. Davis, F. Zaera and G. A. Somorjai, *J. Catal*, 1982, **77**, 439-459.
125. S. J. Tinnemans, M. H. F. Kox, T. A. Nijhuis, T. Visser and B. M. Weckhuysen, *Phys. Chem*, 2005, **7**, 211-216.
126. S. M. Airaksinen, M. A. Bañares and A. O. I. Krause, *J. Catal*, 2005, **230**, 507-513.

127. S. D. Jackson, J. Grenfell, I. M. Matheson, S. Munro, R. Raval and G. Webb, in *Studies in Surface Science and Catalysis*, eds. C. H. Bartholomew and G. A. Fuentes, Elsevier, 1997, vol. 111, pp. 167-174.
128. F. Meunier, A. Yasmeen and J. Ross, *Catal. Today*, 1997, **37**, 33-42.
129. L. Cadus, M. Gomez and M. Abello, *Catal. Lett.*, 1997, **43**, 229-233.
130. B. Barbero, R. Prada Silvy and L. Cadus, *Lat. Am. Appl. Res.*, 2005, **35**, 273-280.